2016

# Theoretical-Experimental Study of the Two-Photon Circular Dichroism of Helicenes and Aromatic Amino Acids in the UV Region: From the Structure-Property Relationship to the Final Implementation

Yuly Katherine Vesga Prada
*University of Central Florida*

# THEORETICAL-EXPERIMENTAL STUDY OF THE TWO-PHOTON CIRCULAR DICHROISM OF HELICENES AND AROMATIC AMINO ACIDS IN THE UV REGION: FROM THE STRUCTURE-PROPERTY RELATIONSHIP TO THE FINAL IMPLEMENTATION.

by

YULY VESGA
M.S. University of Central Florida 2016
M.S. Universidad Nacional de Colombia 2010
B.S. Universidad Industrial de Santander 2007

A dissertation submitted in partial fulfillment of the requirements
for the degree of Doctor of Philosophy
in the Department of Chemistry
of the College of Sciences
at the University of Central Florida
Orlando, Florida

Fall Term
2016

Major Professor: Florencio Hernández

# ABSTRACT

In chemistry, chiral molecules are the ones that are non-superimposible on their mirror image. They possess a very distinctive property known as optical activity, which refers to the rotation of the plane polarization when monochromatic light is passed through them. The use of chiral molecules has been extensively investigated due to the key role they play not only in chemistry but also in the development of new technologies and drugs.

Spectroscopy has been very interested in understanding and taking advantage of the potential application of the opposite signal obtained from enantiomers of chiral molecules when excited with a light source. Electronic Circular Dichroism (ECD), a clear representation of this, measures the differences in linear absorption when a chiral system is excited with circular polarized light of both handedness. Although the ECD technique has been the most popular method employed for the characterization of chiral molecules, it is limited by the presence of linear absorption from common solvents and buffers in the near and far-UV (FUV) region. For this reason, the ECD response signal from molecules that absorb in the same spectral region could be potentially masked by the absorption of solvents and buffers. Since one of the main motivation for this dissertation was to study chiral biomolecules that are linked to common illnesses such as Alzheimer's and Parkinson's diseases and these biomolecules mainly absorb in the near and FUV, ECD is not a potential candidate for this investigation. Consequently, there was an evident need to propose a new technique for studying chiral molecules that was going to overcome the existent limitations of ECD.

In 2008, Hernandez and co-workers proposed a new technique known as the Double-L scan technique. This is a reliable and versatile technique for the measurement of the nonlinear counterpart of ECD, Two-Photon Circular Dichroism (TPCD). The Double-L scan technique is a highly sensitive technique due to the use of "twin" pulses as its experimental approach for

accounting for fluctuations of the excitation source. The first TPCD spectra were obtained for the pair of enantiomers, R- and S-BINOL. After this important achievement, the TPCD spectra of multiple chiral molecules, i.e. BINAP, CN6, A6, have been measured. Also, theoretical calculation for all these molecules have been obtained in order to gain a better understanding of the structure-property relationship of TPCD. These results have been exhibiting an excellent overlapping between theoretical and experimental spectra. This led us to continue the study of the structure-property relationship of TPCD and expand the spectral capability of TPCD spectrometer down to the far-UV.

In **Chapter 2,** we present the expansion of the theoretical calculations and the experimental measurements of the two-photon absorption (TPA) and two-photon circular dichroism (TPCD) spectra of a series of optically active biaryl derivatives (R-BINOL, R-VANOL, and R-VAPOL) using femtosecond pulses. The comparative analysis of the experimental TPCD spectra obtained with our tunable amplified femtosecond system with those previously measured in our group on the same series of compounds in the picosecond regime, revealed a decrease in the amplitude of the signal and an improvement in matching with the theory in the former. Our results were explained based on the negligible contribution of excited state absorption and two-photon circular dichroism with femtosecond pulses compared to the picosecond regime, which could affect both the strength and the shape of the TPA and TPCD spectra.

Then, in **Chapter 3** we embark on the theoretical-experimental analysis of the TPA and TPCD spectra of 1-(2-pyridil)-4-methoxy[6]helicene derivative. The outcomes of our investigation indicated that i) when a molecular system exhibits a lower energy gap and a higher delocalization of electrons in the helicene core, the angular momentum increases, therefore, a higher magnetic dipole transition moment is observed, and ii) when the donor-acceptor combination on the molecule enhances the intramolecular charge transfer (ICT), the electric quadrupole transition

moment increases as well.

Subsequently, in **Chapter 4,** we display the calculation and the comparative analysis of the theoretical TPCD spectra of L-tryptophan (Trp), L-Histidine (His), L-phenylalanine (Phe), ana L-tyrosine (Tyr) residues in proteins with secondary structures (α-helix, β-strand, and random coil), down to the far-UV region. The examination of the TPCD spectra of the different conformers in each configuration revealed distinctive fingerprints in the FUV, a dark spectral region for ECD. Our investigation showed how FUV-TPCD can be used to study peptide and protein structures in a region never evaluated before but packed with important structural information.

Finally, in **Chapter 5** we report the pros and cons of the implementation of the Double-L scan technique in the far-UV, as well as the experimental TPA spectrum of tryptophan, our first targeted molecule. This measurement is promising because it shows the potential application of FUV-TPCD. However, from the many attempts to measure the TPCD spectrum of tryptophan we learned that chiral molecules, such as amino acids, undergo photochemical reactions when exposed to near-UV light (300-375 nm), tryptophan being the most susceptible amino acid to photooxidation.

In **summary**, the results presented in this dissertation provided us a deeper knowledge and understanding of the structure-property relationship of TPCD throughout the study of other helicenes derivatives and by changing the pulse width of the light source. Additionally, we realized that the implementation of the Double-L scan technique in the FUV was challenging because chiral molecules that absorb in this region experienced photoreaction when excited. In the future, we expect to implement an experiment based on the pump-probe technique in order to measure the TPCD signal associated to the excited state. We predict that TPCD will be used to investigate multiple chiral molecules that find a variety of application in biology, medicine, drug and food industry, nanotechnology, asymmetric catalysis, and photonics.

*To my husband, Carlos, my son, Nicolas, and my family. All of our efforts and sacrifices are summarized in this document. Carlos and Nicolas, the two of you have been my greatest support and inspiration. I love you!*

# ACKNOWLEDGMENTS

When I look back in time and ponder how I ended up obtaining a Chemistry PhD, I can only see God directing every decision and turn I have made. It has not been an easy path, but I certainly know that my Lord has carried me in His arms through each and every battle. I am truly thankful to Jesus because He has taught me patience, tolerance, and love with this experience.

I would like to express my deepest gratitude to Dr. Hernandez. He has been a great supervisor, advisor, communicator, mediator, mentor, and friend. I truly appreciate the opportunity he gave me to become a PhD student at the University of Central Florida and join his research team. Even though we have not always agreed on everything, he has always showed me a different perspective that helped me expand my knowledge and develop my scientific skills in order to reach my full potential. Dr. Hernandez has seen me change and grow from being a single, young, immigrant woman to becoming a married mother with a PhD and a bright future in the United States of America. I am very grateful for the way he has supported me throughout every single one of these important steps in my life. He has played a monumental part in my success and is one of the main reasons for me being where I am today. Needless to say, I could not have done all of this without him.

I must give credit and thanks to all the people that collaborated with our research during these years. Among them, I would specially like to mention my committee members (Dr. Zou, Dr. Tatulian, Dr. Torres, and Dr. Huo) for taking their time to be part of this journey, Dr. Stará, Dr. Stary, and Dr. Crassous, who synthesized beautiful chiral helicenes with nonlinear applications, Dr. Rizzo, who helped us with the theoretical calculations of TPCD, and Dr. Tatulian, for being very generous in assisting us with many experimental measurements of ECD spectra. I also want to acknowledge the National Science Foundation (Projects CHE-0832622 and CHE-0840431) for

providing the funds to perform our research, as well as STOKES ARCC at UCF for providing the computing time used throughout these years.

During my time in the Nonlinear Optics, Materials, and Sensors (NOMS) lab, I have had the pleasure of meeting some great people, who happen to be great scientists as well. Dr. Echevarria (Lorenciano) and Dr. Borras (Cubano) instilled in me that life is very short, so we must enjoy every minute of it. Dr. Diaz (Carlos) became a very close friend and taught me how to work with optics, computational chemistry, and lasers. He was also a vivid example of dedication to one's family. To say that I learned a lot from him would be quite an understatement. Julie has been a great co-worker and friend throughout the last several years and I am going to miss our conversations on how to be "the best mom" and life in general. She has been a great help with proofreading my publications and dissertation. Our lunches with Rashi, Casey, and Dom will be missed as well. Mary, who was the first undergraduate I had the opportunity to work with. Eduardo, who is the latest addition to the NOMS lab team, has also provided some valuable assistance.

This takes me to one of the most important people in life: my husband, Carlos. During these five years, he has had to be my editor, psychologist, husband, friend, coach, and cheerleader, among his many other responsibilities. When I felt like giving up on pursuing my PhD, he was always there to be my praying partner and to offer a helping hand. He always said "baby, I know you can do this" when many times I did not think I could. During those times, it was only his admiration for me and his encouraging words that kept me going and inspired me to continue working harder and harder. I am grateful that he never stopped believing in me.

Nicolas, my little Nico! If I had to, I would trade anything in my life for my precious son. Being a mom is truly the best experience anyone can have. I love him with every single millimeter of my body. Nico is the only one in this world that knows how I sound from the inside. He is my everything, which is why I tell him "te amo de aquí a la luna… times infinity" every chance I get.

Without my family, this would have been almost impossible. They have always been here by my side. Even though most of them live across the ocean, there was not a single day when I did not feel their presence through encouraging words or heartfelt expressions of love. After Nicolas was born, some of them rearranged their own lives so they could come to the United States to take care of my baby so I could complete my PhD. Words cannot express how thankful I am to the Lord for all His blessings, for giving me such an amazing family, and for surrounding me with people that love me and care so much about me.

# TABLE OF CONTENTS

# LIST OF FIGURES

# LIST OF TABLES

# LIST OF ACRONYMS AND ABREVIATIONS

| | |
|---|---|
| A6 | *P*-(+)-1-aza[6]helicene |
| B3LYP | Becke 3-parameter Lee-Yang-Parr hybrid functional |
| CAM-B3LYP | Coulomb attenuating method Becke 3-parameter Lee-Yang-Parr hybrid functional |
| CN6 | *M*-(-)-2-[4-(cyanophenyl)-1-ethynyl]carbo[6]helicene |
| *c* | Speed of light ($3x10^8$ m $s^{-1}$) |
| CARS | Coherent Anti-Stokes Raman Scattering |
| CD | Circular dichroism |
| $CH_2Cl_2$ | Dichloromethane |
| cm | Centimeter |
| CT | Charge transfer |
| D-trp | D-tryptophan |
| DFT | Density functional theory |
| DFWM | Degenerate Four-Wave Mixing |
| *e* | Electron charge ($1.602x10^{-19}$ Coulombs) |
| ECD | Electronic circular dichroism |
| ENDO-ICT | Intramolecular charge transfer within the helicene core. |
| EXO-ICT | Intramolecular charge transfer beyond the helicene core |
| *f* | Oscillator strength |
| fs | Femtosecond ($10^{-15}$ s) |
| FAR-UV | Far-ultraviolet |
| FWHM | Full width at half maximum |

| | |
|---|---|
| FMOs | Frontier molecular orbitals |
| FROG | Frequency-resolved optical gaiting |
| $g\left(n\omega,\omega_{0f},\Gamma\right)$ | Normalized lineshape for an *n*-photon excitation |
| GM | Goppert-Mayer unit for the TPA cross-section and TPCD |
| | (1 x$10^{-50}$ $cm^4$ s $photon^{-1}$ $molecule^{-1}$) |
| *h* | Planck's constant (6.626x$10^{-34}$ $m^2$ kg $s^{-1}$) |
| H | HOMO (highest occupied molecular orbital) |
| Hz | Hertz (unit of frequency) |
| His | L-histidine |
| ICT | Intramolecular charge transfer |
| kJ | Kilojoules |
| L | LUMO (lowest unoccupied molecular orbital) |
| L-trp | L-tryptophan |
| LCPL | Left circularly polarized light |
| LPL | Linearly polarized light |
| *m* | Mass of the electron (9.109 x$10^{-31}$ kg) |
| M | Molar (unit of concentration) |
| M1 | (S,S)-spiro[8.8]4,5(1,2),13,14(2,3)-tetranaphtalenaheptadecane |
| M2 | (Δ,S)-(1,1′-binaphthalene-2,2′diolato)(bis(1,2-benzenediolato)sulfate(VI)) |
| M | Two-photon magnetic transition dipole matrix element |
| MCD | Magnetic circular dichroism |
| MD | Molecular dynamics |
| MM | Molecular mechanics |

| | |
|---|---|
| MPA | Multi-photon absorption |
| mL | Milliliter |
| $n_0$ | Linear refractive index |
| $n_2$ | Nonlinear refractive index |
| Nd:YAG | Neodymium-doped yttrium aluminum garnet |
| nm | Nanometer ($10^{-9}$ m) |
| NLO | Nonlinear optical |
| NT | Normalized transmittance |
| NUV | Near ultraviolet |
| OPA | One-photon absorption |
| OPG | Optical parametric generator |
| ORD | Optical rotatory dispersion |
| P | Two-photon electric transition dipole matrix element |
| P6 | 1-(2-pyridil)-4-methoxy[6]helicene |
| PCM | Polarizable continuum model |
| Ph | Phenyl group |
| Phe | L-phenylalanine |
| ps | Picosecond ($10^{-9}$ s) |
| $q^d$ | Dynamic component of the solvent reaction field |
| $q^i$ | Delayed component of the solvent reaction field |
| QM | Quantum mechanics |
| $R_{0f}^{ECD}$ | Rotatory strength |
| R-BINOL | (R)-(+)-1,1'-bi(2-naphthol) |

| | |
|---|---|
| RCPL | Right circularly polarized light |
| ROA | Raman optical activity |
| R-VANOL | (R)–3,3’–Diphenyl–[2,2’–binaphthalene]– 1,1’–diol |
| R-VAPOL | (R)–2,2’–Diphenyl– [3,3’–biphenanthrene]–4,4’–diol |
| s | Seconds |
| $S_0$ | Ground state, singlet |
| $S_1$ | First excited state, singlet |
| $S_2$ | Second excited state, singlet |
| $S_n$ | $n^{th}$ excited state, singlet |
| $S_{ii}^{0f}$ | Two-photon transition matrix elements |
| S-BINAP | (S)-(+)-(1,1′-Binaphthalene-2,2′-diyl)bis(diphenylphosphine) |
| S-BINOL | (S)-(-)-1,1’-bi(2-naphthol) |
| SAS | Solvent accessible surface |
| SES | Solvent excluded surface |
| SFG | Sum frequency generation |
| SHG | Second harmonic generation |
| SCRF | Self-consistent reaction field |
| SRF | Solvent reaction field |
| S-VANOL | (S)–3,3’–Diphenyl–[2,2’–binaphthalene]– 1,1’–diol |
| S-VAPOL | (S)–2,2’–Diphenyl– [3,3’–biphenanthrene]–4,4’–diol |
| T | Two-photon electric transition quadrupole matrix element |
| TPA | Two-photon absorption |
| TPIF | Two-photon induced fluorescence |

| | |
|---|---|
| TD-DFT | Time dependent density functional theory |
| THF | Tetrahydrofuran |
| Trp | tryptophan |
| Tyr | L-tyrosine |
| UV | Ultraviolet |
| VCD | Vibrational circular dichroism |
| VIS | Visible |
| $w_0$ | Beam radius at the focal plane |
| XCF | Exchange correlation functional |
| $z_0$ | Rayleigh range |
| #CN | CN6-like helicenes |
| n-π* | Transition from a non-bonding orbital (n) to an antibonding π orbital (π*) |
| π-π* | Transition from a bonding π orbital to an antibonding π orbital (π*) |
| α | One-photon absorption coefficient |
| β | Two-photon absorption coefficient |
| γ | Three-photon absorption coefficient |
| Γ | Empirical linewidth parameter |
| $\delta^{TPA}$ | Two-photon absorption cross-section |
| $\delta_L^{TPA}$ | Two-photon absorption cross-section for left circularly polarized light |
| $\delta_R^{TPA}$ | Two-photon absorption cross-section for right circularly polarized light |
| $\Delta\delta^{TPCD}$ | Two-photon circular dichroism |
| $\Delta f$ | Lippert's function |

| | |
|---|---|
| $\Delta G_{sol}$ | Free energy of solvation |
| $\Delta G_{el}$ | Electrostatic contribution to the free energy |
| $\Delta G_{dr}$ | Dispersion-repulsion contribution to the free energy |
| $\Delta G_{cav}$ | Cavitation free energy |
| $\Delta\mu$ | Difference between ground and excited state dipole moment |
| $\varepsilon$ | Molar Absorptivity |
| $\varepsilon_0$ | Dielectric constant |
| $\varepsilon_{\beta\rho\alpha}$ | Levi-Civita alternating tensor |
| $\theta$ | Ellipticity |
| $\lambda_{max}$ | Maximum absorption wavelength |
| $\mu_{0f}$ | Transition moment (ground to final singlet state) |
| $\mu_E$ | Excited state permanent dipole moment |
| $\mu_G$ | Ground state permanent dipole moment |
| $\tilde{\nu}_A$ | Absorption frequency |
| $\tilde{\nu}_F$ | Emission frequency |
| $\chi^{(n)}$ | $n^{th}$ order nonlinear susceptibility tensor |
| $\Psi_0$ | Ground state wavefunction |
| $\Psi_f$ | Excited (final) state wavefunction |
| $\omega$ | Circular frequency |

# CHAPTER 1: INTRODUCTION

The sun is the Earth's main source of light, and light is the Earth's greatest form of energy. Approximately 44% of the solar radiation that reaches our planet is in the visible range. Every color that we see around us is a result of the interaction between visible light and matter. Researchers have investigated this interaction for several decades,[1, 2] and their interest has led to the development of new technologies such as the Internet, optical telecommunications, optical data storage,[3] human-cell bio-imaging,[4] and single-molecule imaging, [5] among many others. Additionally, a new area of research, photonics, emerged as a result of the scientists and engineers' efforts. This discipline studies the generation, detection, and manipulation of photons through emission, transmission, modulation, signal processing, switching, amplification, and detection/sensing[6, 7]. In order to reveal important information about the optical properties mentioned before, as well as the structural characteristics of materials, a series of spectroscopic techniques have been developed.

Before 1950, the spectroscopic techniques based on One-Photon Absorption (OPA), also known as linear spectroscopic techniques, were the most commonly used for research in photonics. After the introduction of laser systems in 1960, new nonlinear techniques were established in order to overcome the barriers faced by linear spectroscopy, such as scattering and sample photodamage. In multiphoton processes the excitation occurs at a longer wavelength equivalent to $1/n$ times that of the corresponding energy gap - degenerate case. The increase in the excitation wavelength compared to linear processes results in reduced absorption, scattering and sample photodamage, as well as an increase in penetration depth and spatial resolution.[8, 9] The benefits offered by multiphoton-based processes have drawn the attention of researchers working in the development of new optical devices. These efforts have produced multiple promising applications in the fields of bio-imaging and photodynamic therapy.[4, 10] However, along with the advances in photonics

technology, it is important to focus in the creation of new multiphoton characterization techniques, as well as the improvement of the existing ones.

Among all the possibilities for multiphoton spectroscopy, Two-Photon Absorption (TPA) has been unequivocally established as one of the foremost techniques in the analysis of optical properties induced in materials due to their interaction with intense optical fields.[11, 12] Z-scan, which is the most used technique for measuring TPA, takes advantage of this interaction through the movement of a sample across the focal plane of a focusing geometry[13]. TPA has been extensively employed in the characterization of materials with applications in microscopy,[14] optical limiting,[15] and 3D microfabrication,[16] among others. As a consequence of the successful emergence and acceptance of TPA as a nonlinear technique, in the past 20 years researchers have started developing state-of-the-art methods for characterizing molecular systems that display optical activity.[17-25]

Optical activity is an exclusively property exhibited by chiral molecules, which are asymmetric molecules with a non-superimposable mirror image. These types of molecules are appealing because of their implication in the origin of life, and their application in the investigation of many biological processes, the design of new drugs [26] and asymmetric catalysts.[27, 28] Up to this day, Electronic Circular Dichroism (ECD) has been the gold standard technique employed for the characterization of chiral systems.[29] ECD measures the differences in OPA when excitation is performed with right and left circularly-polarized light. Since the majority of the ECD measurements take place in the UV region, the ECD signal is hindered by strong OPA from solvents and buffers. Also, an enlargement in the scattering of heterogeneous samples can limit the application of ECD to homogeneous systems.[30] As mentioned before, these impediments can actually be surmounted by leveraging the advantages of multiphoton excitation. Many attempts

have been made to propose new nonlinear processes that can potentially be employed as ECD counterpart techniques. Processes such as Second Harmonic Generation (SHG),[17] Sum-Frequency Generation (SFG),[18] nonlinear optical activity,[19, 20] and multiphoton optical rotation have been proposed.[21-25] Unfortunately, none of these techniques are indeed a polarization-dependent method like ECD.

Fortunately, a truly nonlinear equivalent technique to ECD, known as Two-Photon Circular Dichroism (TPCD), was theoretically predicted by Tinoco and Power in the 1970s.[31, 32] In 1995, Richardson and co-workers reported the first experimental measurement of TPCD spectra[33] by using a technique known as Fluorescence-Detected Two-Photon Circular Dichroism (FD-TPCD). Approximately one decade later, Rizzo and co-authors successfully implemented TPCD computationally.[34] Although, many efforts had been made to create a fruitful nonlinear technique for measuring TPCD, it was not until the introduction of the novel double-L scan technique[35] that a reliable and reproducible method allowed the measurement of TPCD.

In 2008, Hernandez and co-workers launched the double-L scan technique for simultaneous measurements of polarization-dependent nonlinear absorption. The high sensitivity of this approach is linked to the use of "twin" laser pulses which synchronize the measurements by counterweighing for energy and mode fluctuations in the sample. This differential technique was successfully applied to the accurate measurement of TPA and TPCD in BINOL enantiomers.[36]

Afterward, they decided to study the TPCD structure-property relationship of optically active molecules with axial and helical chirality. This is the starting point of this dissertation in which we present a description of multiple theoretical and experimental investigations of the polarization dependence linear and nonlinear optical properties of molecules with different type of chirality.

## 1.1 Fundamentals of linear and nonlinear absorption processes.

### 1.1.1 One-Photon Absorption.

To understand the correlation between the electronic structure of a molecule and its properties, a great start would be to study linear absorption of electromagnetic radiation, also known as One-Photon absorption, which is one of the simplest and most common cases of light-matter interaction. In this process the absorption of one photon induces an electronic transition from an initial state ($S_0$) to a final excited state ($S_n$) (See Figure 1-1).

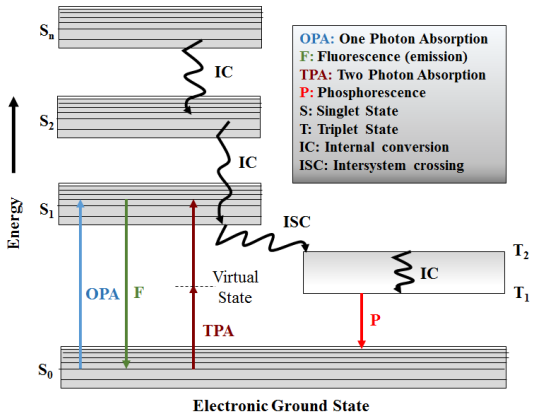


**Figure 1-1.** Jablonski Diagram

The electromagnetic radiation that impinges the molecular system usually creates a perturbation in its electron cloud. If the oscillation frequency of the incident photon's electric field is equal to one of the natural oscillation frequencies of the molecule, the photon and the molecule, which are the two interacting parts, are at a resonance condition. This results in the absorption of the incident photon, creating an oscillating electric dipole within the molecule, such as the transition dipole moment ($\mu_{0\,f}$), and taking the molecule to the excited state $S_n$. The likelihood of

an electronic transition to occur is limited to $\mu_{0\,f.}$ This is exhibited in the relationship between molar

absorptivity ($\varepsilon$) and $\mu_{0f}$ described below, where $\tilde{\nu}$ is the frequency of the light in $cm^{-1}$, $e$ is the electron charge, and $\left|\mu_{0f}\right|^2$ is the transition probability.[37]

$$\int \varepsilon d\tilde{\nu} = (2.512 \times 10^{19} l \cdot mol^{-1} cm^{-3}) \frac{\tilde{\nu}}{e^2} \left|\mu_{0f}\right|^2 \qquad (1-1)$$

In addition, OPA measurements are usually carried out in solutions. If the molecule being measured is polar, the solvent's dielectric properties can significantly modify the electronic cloud of the molecule's ground and excited states, with the latter experiencing the most impact. Thus, the energy gap between the ground and excited states is altered and can be determined using the Lippert equation,[38]

$$\widetilde{\nu_A} - \widetilde{\nu_F} = \frac{2}{hc}\left(\frac{\varepsilon - 1}{2\varepsilon + 1} - \frac{n^2 - 1}{2n^2 + 1}\right)\frac{(\mu_E - \mu_G)^2}{a^3} \qquad (1-2)$$

Here, $\widetilde{\nu_A}$ and $\widetilde{\nu_F}$ are the absorption and emission frequencies, respectively (in $cm^{-1}$), $\varepsilon$ is the solvent's dielectric constant, $n$ is refractive index, $c$ is the speed of light *in vacuo*, $h$ *is* the Planck's constant, $\mu_E$ and $\mu_G$ symbolize the permanent dipole moment of the molecules in their excited and ground state, respectively, and $a$ is the radius of the cavity in which the molecule is located. The difference between $\widetilde{\nu_A}$ and $\widetilde{\nu_F}$ is the energy separation between the ground and excited state.

In order to fully comprehend the processes involved in OPA, it is necessary to highlight the presence of additional rules, known as selection rules. These rules are originated merely from quantum mechanics and they govern the occurrence of electronic transitions.

### 1.1.2 Selection Rules

Based on what has been described so far, it would seem that, in order for an electronic state to occur, the energy of an incident photon must match the energy gap between $S_0$ and $S_f$. Although this statement is true, it is also important to highlight the presence of selection rules that have to be met for a molecular system in order to experience OPA. These rules are responsible for allowing or forbidding a particular electronic transition and are derived from the transition dipole moment integral,[37]

$$\mu_{0f} = \int \Psi_0^* \mu \Psi_f d\tau \qquad (1-3)$$

where $\Psi_0$ and $\Psi_f$ are the wave functions of the initial and final states, respectively. When the transition dipole moment integral approaches zero, the transition between that specific set of initial and final states is prohibited and it will not appear in the experimental spectrum. If the transition between states is allowed, the transition dipole moment integral will not vanish and will be observed in the experimental spectrum. Its strength will depend on the magnitude of $\mu_{0f}$ as expressed in equation 1-1.

There are two types of rules that typically apply to chromophores: i) The *spin* selection rules, where $\Delta S = 0$, which assume that both the dipole and the quadrupole moment operators have a negligible influence on the spin. This means that electronic transitions are allowed only when the multiplicity of the intervening states are the same. ii) The *spatial symmetry* selection rules, where $\Delta l = \pm 1$, which mainly relate to centrosymmetric molecules where electronic transitions between states with same symmetry are allowed and forbidden for states with different symmetry.[37]

Although the OPA spectra of molecular systems offer a substantial amount of structural information, it is also helpful to explore the spectroscopic information present in the nonlinear regime. In the following section, one of the most studied nonlinear process is presented.

### 1.1.3 Nonlinear Absorption

A multiphoton absorption or nonlinear absorption occurs when a chemical species is excited from one state ($S_0$) to a higher energy state ($S_f$) due to the simultaneous absorption of more than one photon. In this case, the energy difference between $S_0$ and $S_f$ is equal to the sum of the energy of the *n* photons responsible for the excitation (figure 1-1). This multiphoton absorption process was originally predicted by Göppert-Mayer in 1931 in her doctoral dissertation.[39] She explicitly referred to the theoretical probability of simultaneous absorption of two photons by proposing the presence of virtual states between real states. The first experimental verification of TPA was not possible until the advent of lasers in the 1960s,[40] when two-photon-excited fluorescence was detected in a europium-doped crystal.[41]

When certain material is exposed to a strong radiation, such as the one produced by a laser source, the polarization of the electron cloud starts to deviate from linearity and the electronic oscillations are better explained by an anharmonic oscillator. In this case, the polarization of the material can be expanded by a Taylor series as a function of the electric field

$$\vec{P} = \chi^{(1)} \cdot \vec{E} + \chi^{(2)} \cdot \vec{E}^2 + \chi^{(3)} \cdot \vec{E}^3 + \cdots + \chi^{(n)} \cdot \vec{E}^n, \qquad (1-4)$$

where $\chi^{(1)}$ is the susceptibility tensor of the first order, which describes the linear polarization of the medium. $\chi^{(2)}$ is the second-order susceptibility tensor and it is the first induced nonlinear polarization. Second order nonlinear interactions are only observed in noncentrosymmetric molecular systems and refers to the SHG process. $\chi^{(n)}$ is the susceptibility tensor of the $n^{th}$ order, describing the other induced nonlinear polarization. In general, the real and imaginary parts of the complex susceptibility tensor are related in the frequency domain through the Hilbert transform [42]. The real part of the $\chi^{(1)}$ refers to the refractive index of the medium and its imaginary part

represents the OPA coefficient of the molecular system.

The understanding of the third order susceptibility tensor ($\chi^{(3)}$) is crucial because it is part of this dissertation's mathematical foundation. Third-order nonlinear interactions can take place in both centrosymmetric and noncentrosymmetric molecules. They are composed of 81 independent terms, which are a function of the material's spatial symmetry through which the electrical field propagates. In general, when the frequencies of the applied field involved in the nonlinear process are different, the components of $\chi^{(3)}$obey [42]

$$\chi_{ijkl}^{(3)} = \chi_{1122}^{(3)}\delta_{ij}\delta_{kl} + \chi_{1212}^{(3)}\delta_{ik}\delta_{jl} + \chi_{1221}^{(3)}\delta_{il}\delta_{jk}, \qquad (1-5)$$

Here, $\delta_{uv}$ refers to the Kronecker delta. The indices i, j, k, l, 1, and 2 indicate the Cartesian components of the vectors. When the frequencies of the applied field involved in the nonlinear process are the same, $\chi_{1122}^{(3)}$ is equal to $\chi_{1212}^{(3)}$ and the equation (1-5) is reduced to:

$$\chi_{ijkl}^{(3)} = \chi_{1122}^{(3)}(\delta_{ij}\delta_{kl} + \delta_{ik}\delta_{jl}) + \chi_{1221}^{(3)}\delta_{il}\delta_{jk} \qquad (1-6)$$

If the total electric field is written as a superposition of waves, the nonlinear polarization can be expressed in terms of the electric field's frequencies and the equation (1-4) is obtained.

As mentioned previously, $\chi^{(3)}$ is a complex susceptibility tensor in which its real part ($\mathrm{Re}\chi^{(3)}$) is associated with the change in the refractive index, originated from the high intensity field applied to the material, and the imaginary part ($\mathrm{Im}\chi^{(3)}$) is linked to the TPA of the media.

Therefore, in addition to observing the refractive index of the material ($n_0$), a nonlinear refractive index coefficient ($n_2$) will appear and be responsible for the self-modulation of the incident light, generating two phenomena known as self-focusing ($n_2 > 0$) and self-defocusing ($n_2 < 0$).[43]

$$n(I) = n_0 + n_2 I, \qquad (1-7)$$

where

$$\mathrm{Re}\chi^{(3)} = \frac{4n_0^2\varepsilon_0}{3} n_2 \qquad (1-8)$$

The nonlinear absorption process results in a complex dependence of the radiation intensity as it propagates over the absorbing media (see Equation 1-9). $I(z)$ is the intensity of the incident light along the z-axis. $\alpha, \beta, \gamma,$ and $\eta$ are the one-, two-, three-, and four-photon coefficients of the medium.

$$\frac{dI(z)}{dz} = -\alpha I - \beta I^2 - \gamma I^3 - \eta I^4 - \cdots \qquad (1-9)$$

Here, $\alpha, \beta,$ and $\gamma$ are associated with $\mathrm{Im}\chi^{(1)}$, $\mathrm{Im}\chi^{(2)}$, and $\mathrm{Im}\chi^{(3)}$, respectively. For the purpose of this thesis, the focus will be centered on the relationship between $\mathrm{Im}\chi^{(3)}$ and $\beta$:

$$\mathrm{Im}\chi^{(3)} = \frac{n_0^2\varepsilon_0 c^2}{\omega}\beta \qquad (1-10)$$

In certain materials, it is possible to observe nonlinear responses that involve transitions *via* virtual states, with TPA being the most probable process to occur. In this case, the nonlinear absorption process is responsible for the in refractive index change in the material. These phenomena are mathematically described through the Kramers-Kronig (KK) relation, which associates the real

and imaginary parts of the susceptibility tensors, allowing the calculation of the nonlinear refractive index of the medium. The KK relations for the $\chi^{(3)}$ tensors are:[44]

$$Re\{\chi^{(3)}(\omega)\} = -\frac{2\omega'}{\pi}\wp\int_0^\infty \frac{\omega Im\{\chi^{(3)}(\omega)\}}{\omega^2 - \omega'^2}d\omega \qquad (1-11)$$

and

$$Im\{\chi^{(3)}(\omega)\} = -\frac{2\omega'}{\pi}\wp\int_0^\infty \frac{\omega Re\{\chi^{(3)}(\omega)\}}{\omega^2 - \omega'^2}d\omega, \qquad (1-12)$$

where $\wp$ means that the integral has to be calculated using the Cauchy principal value.[45]

Besides the two-photon absorption coefficient ($\beta$), TPA can be expressed in terms of a two-photon absorption cross-section ($\sigma_2$). This quantity is expressed as follows:[43]

$$\sigma_2 = \frac{\beta\hbar\omega}{N_0}. \qquad (1-13)$$

Here, $\omega$ is the frequency of the excitation radiation and $N_0$ is the total number of molecules that can be excited *via* TPA.

As mentioned previously, OPA and TPA processes are governed by different selection rules,[37] which are accountable for the differences between them. Specifically for centrosymmetric molecules, the symmetry selection rules determine that in order for a transition to take place *via* OPA, the two states involved in the transition must have opposite symmetry, also known as odd

parity. On the contrary, in TPA, the symmetry of the initial and final state must be the same (even parity) because the symmetry of the virtual state is opposite to the two states implicated (Fig. 1-1). Therefore, the set of excited states reached by OPA are completely different from the ones approached by two-photon spectroscopy.[46, 47]

## 1.2 Theoretical framework for the calculation of linear and nonlinear spectra

The use of computational methods in chemistry has been gaining popularity among the scientific community lately because it is very helpful to complement results, predict phenomena and solve problems associated with chemical experiments.[48] Linear and nonlinear spectroscopy have also benefited from the application of computational tools. Time-Dependent Density Functional Theory (TD-DFT)[49, 50] is the most commonly employed method to predict OPA and TPA [51] spectra because it allows for the performance of the calculations at a relatively low computational cost. The total success of the computational prediction is only possible if there is an appropriate combination of a functional and a basis set. The equations applied by TD-DFT to obtain OPA and TPA spectra are presented in this section.

### 1.2.1 One-Photon Absorption

When OPA takes place, an electronic transition occurs from a lower energy state to a higher energy state. The following equation expresses the relationship between the oscillator strength ($f_{0f}$), which depends on the electric transition dipole moment ($\mu_{0f}$) and the molar absorptivity, $\varepsilon^{OPA}(\omega)$, when electronic transitions are the only ones taken into consideration:[52]

$$\varepsilon^{OPA}(\omega) = \frac{2\pi^2 \omega N_A}{1000 \times \ln(10)(4\pi\varepsilon_0)\hbar C_0} \times \frac{1}{\hbar} \sum_f g\left(\omega, \omega_{0f}, \Gamma\right) \frac{f_{0f}}{\omega_{0f}}, \qquad (1-14)$$

$$\varepsilon^{OPA}(\omega) \approx 1.05495 \times 10^3 \times \omega \sum_f g\left(\omega, \omega_{0f}, \Gamma\right) \frac{f_{0f}}{\omega_{0f}}, \qquad (1-15)$$

where $\omega$, which equals $2\pi c_0/\lambda$, is the circular frequency of the incident radiation, $C_0$ is the speed of light *in vacuo*, $\varepsilon_0$ is the vacuum permittivity, and $N_A$ is Avogadro's number.

$f_{0f}$, which equals $2m_e\omega_{0f}\left|\mu_{0f}\right|^2/3\hbar e^2$, is the oscillator strength, and $g(\omega, \omega_{gv_gfv_f})$ is the line-broadening function, which is centered at $\omega = \omega_{0f}$ and a full width half-maximum (FWHM) ($\Gamma$). For a general n-photon absorption process, $g(\omega, \omega_{gv_gfv_f})$ is described by a Lorentzian function

$$g_L\left(n\omega, \omega_{0f}, \Gamma\right) = \frac{1}{\pi} \frac{\Gamma}{(\omega_{0f} - n\omega)^2 + \Gamma^2} \qquad (1-16)$$

or by a Gaussian function

$$g_G\left(n\omega, \omega_{0f}, \Gamma\right) = \frac{1}{\Gamma\sqrt{2\pi}} e^{\frac{(\omega_{0f} - n\omega)^2}{2\Gamma^2}} \qquad (1-17)$$

When $\varepsilon^{OPA}(\omega)$ is obtained from equation 1-15, $\varepsilon^{OPA}(\omega)$ units are l.mol$^{-1}$.cm$^{-1}$.

### 1.2.2 Two-Photon Absorption

The theoretical value of the two-photon absorption cross-section ($\sigma^{TPA}$) for two photons of equal frequency $\omega_1 = \omega_2 = \omega$ is represented by the following expression:[31, 53]

$$\sigma^{TPA}(\omega) = \frac{1}{30}\frac{(2\pi)^3\omega^2}{c_0^2(4\pi\varepsilon_0)^2} \times \sum_f g(2\omega, \omega_{0f}, \Gamma) \cdot \bar{\delta}^{TPA}(\omega_{0f}) \qquad (1-18)$$

$$\delta^{TPA}(\omega) \approx 8.35150 \times 10^{-4} \times \omega^2 \sum_f g(2\omega, \omega_{0f}, \Gamma) \cdot \bar{\delta}^{TPA}(\omega_{0f}). \qquad 1-19)$$

In the following mathematical relationship, the orientationally-averaged two-photon probability ($\bar{\delta}^{TPA}$) is termed as a function of the molecular parameters $A_1$ and $A_2$.

$$\sigma^{TPA}(\omega_{0f}) = F \times A_1(\omega_{0f}) + (G+H) \times A_2(\omega_{0f}). \qquad (1-20)$$

Here F, G, and H are scalars employed to express the polarization of the excitation radiation. In the specific case of using linearly-polarized light F=G=H=2,[31, 53] $A_1$ and $A_2$ are obtained from the two-photon transition matrix elements ($S_{ii}^{0f}$).

$$A_1(\omega_{0f}) = \sum_{\rho\sigma} S_{\rho\rho}^{0f}(\omega_{0f}) S_{\sigma\sigma}^{of^*}(\omega_{0f}) \qquad (1-21)$$

$$A_2(\omega_{0f}) = \sum_{\rho\sigma} S_{\rho\sigma}^{0f}(\omega_{0f}) S_{\rho\sigma}^{of^*}(\omega_{0f}) \qquad (1-22)$$

The unit for $\sigma^{TPA}$ is cm$^4$ s photon$^{-1}$ molecule$^{-1}$ when the values of $\omega$ and $\bar{\delta}^{TPA}$ are in atomic units. 1 Göppert-Mayer (GM) is equivalent to $10^{-50}$ cm$^4$ s photon$^{-1}$ molecule$^{-1}$. Next, the effect of adding solvents to the theoretical model will be presented.

### 1.2.3 Solvent Models

The addition of solvents to any chemical species can possibly alter their geometry and electronic structure. These changes are more frequently observed in the excited states due to their promptness to react to perturbations triggered by the addition of solvents. The main reason for this behavior is that there is a greater polarization of charges perceived in the excited states that can result in important changes in the absorption response of the molecule. Therefore, the use of theoretical models for describing solvent environments is highly recommended. These theoretical solvent models are divided into two main types: explicit approaches, also known as discrete, and implicit or continuum models.[54, 55]

Among the discrete models (Figure 1-2.a) that have practical applications, the Supramolecular approach, Molecular Mechanics (MM), Hybrid Quantum Mechanics/Molecular Mechanics (QM/MM), and Molecular Dynamics (MD) are the most popular. First, the Supramolecular approach evaluates the solute interacting with some of the nearest solvent molecules in a quantum mechanical routine. Second, the MM method describes the classical electrostatic interactions considering the charge distribution such as point charges, dipoles, etc. of solute and solvent molecules. Next, the QQ/MM model amalgamates both quantum mechanics for one or a few molecules and classical molecular mechanics for the rest of the surrounding molecules within the same system. Finally, MD uses Newton's classical equations to model the trajectories of the molecules from theoretically or empirically-fitted intramolecular potentials.

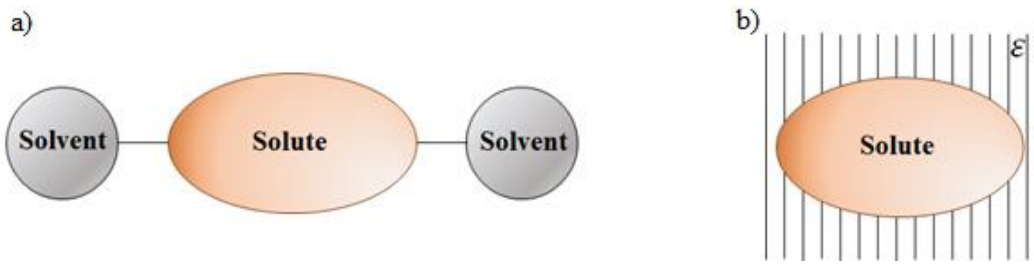


**Figure 1-2.** Graphical representation of a) discrete model and b) continuum approach

On the other hand, continuum methods consider both the solvent environment as a polarizable continuum characterized by its dielectric constant $\varepsilon$ and the solute molecule inside a cavity inserted in the continuum medium that is described by quantum mechanics (see Figure 1-2.b).[55] The Solvent Reaction Field (SRF) is one of the earliest continuum approaches proposed by Onsager in 1936.[56] This model simulates the molecule in a solution as a classical-point polarizable dipole confined in a spherical or ellipsoidal cavity surrounded by a dielectric continuum. The solute dipole induces a reaction field in the surrounding medium, which in turn produces an electric field in the cavity (reaction field), which in turn interacts with the dipole. The Polarizable Continuum Model (PCM) is a more modern way to deal with implicit solvation. [57, 58] PCM differs from SRF in that the latter uses a single sphere or ellipse to surround the molecule, which allows the prediction of a less accurate solute-solvent interaction energy. Since PCM is the model used to achieve solvent calculations in this dissertation, it will be expanded further in the next section.

#### 1.2.3.1 Polarizable Continuum Model

PCM is more advantageous than SRF because it uses a molecular-shaped cavity. In order to obtain the molecular-shaped cavity, PCM generates a series of coinciding spheres centered on the solute atoms at a certain radius, which is usually defined by van der Waals radii.[59] A graphical

representation of the PCM cavity is found in figure 1-3. It is worth noting the presence of two different surfaces: one of them is known as Solvent Excluded Surface (SES), which corresponds to the cavity surface and determines the smallest distance at which the solvent molecules can be located from the solute molecules. The second surface, Solvent Accessible Surface (SAS), is formed after the solvent radius is added to SES.

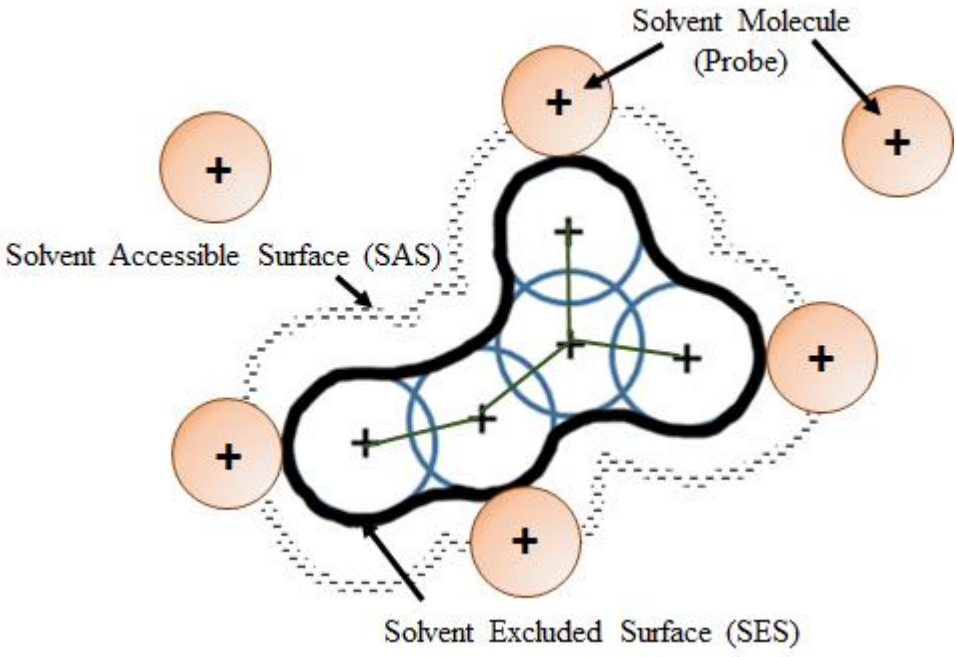


**Figure 1-3.** Graphical representation of the PCM cavity

In order to calculate the solvation free energy ($\Delta G_{sol}$), PCM uses the following formula:[60]

$$\Delta G_{sol} = \Delta G_{el} + \Delta G_{dr} + \Delta G_{cav}. \qquad (1-23)$$

Here, $\Delta G_{el}$ and $\Delta G_{cav}$ are the electrostatic contribution to the free energy and the cavitation energy,

respectively, both obtained from the SES. $\Delta G_{dr}$ is the dispersion-repulsion contribution to the free energy and is calculated from the SAS. The surface charges' localization and value are acquired by a systematic method where the SES is segmented in small pieces (tesserae) of a known area. Each one of those areas is considered to be a point charge.

Furthermore, when electronic transitions are simulated through PCM, non-equilibrium contributions must be considered for the model in order to take into account the fact that a sudden change in the charge distribution of the solute, such as an incident radiation, results in a non-instantaneous relaxation of the solvent molecules.[59] Figure 1-4 depicts a non-equilibrium process where there is an OPA process (blue line) followed by an emission (green line).

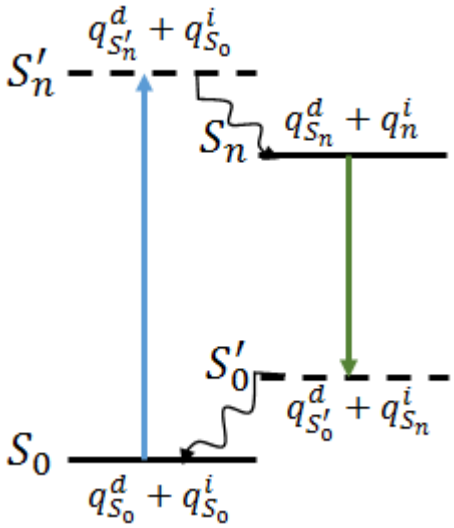


**Figure 1-4.** Illustration of the non-equilibrium process

The reaction field is portioned into two components: one fast and one slow. The fast one is also known as dynamic component ($q^d$) and it is associated to the electronic relaxation. $q^d$ is yielded from the optical or dynamic dielectric constant ($\varepsilon_{opt}$) that is given by the square of the refractive index of the solvent. The slow component, also known as delayed component ($q^i$), is

obtained from the static dielectric constant ($\varepsilon_{sta}$) and it is linked to the nuclear motions of the solvent molecules.

## 1.3 Experimental methods for the measurement of two-photon absorption coefficient

Nonlinear optics researchers have developed many techniques in order to obtain TPA coefficients ($\beta$) experimentally. These methods can be grouped in three different categories: wave-mixing techniques, indirect methods, and direct methods.[61] Among the mixing techniques, Coherent Anti-Stokes Raman Scattering (CARS),[62, 63] Optical Kerr effect,[64, 65] and Degenerate Four-Wave Mixing (DFWM)[66, 67] are the most popular methods. The use of these techniques for practical purposes has been limited because the experimental setup requires a careful control of temporal and spatial overlapping of the beams utilized.[61] On the other hand, most of the indirect techniques, which are based on monitoring various relaxation processes after TPA occurs, require less complicated experimental setups. The most common indirect technique is Two-Photon Induced Fluorescence (TPIF).[68, 69] The indirect techniques present two main challenges: one is the potential presence of uncertainty in the molar absorptivity, which can result in an inaccurate estimation of $\beta$; the other challenge is that they can only be used in molecules with a measurable fluorescence signal. In contrast, direct methods measure the absorption of the molecules. In 1989, Sheik-Bahae and co-workers[43] proposed the Z-Scan technique, which is the most simple and reliable technique for measuring $\beta$, as well as the nonlinear refractive index ($\eta_2$). In the following section, the bases of the Z-scan technique will be presented.

### 1.3.1 Z-scan technique

The experimental setup used for the Z-scan technique is presented in figure 1-5. A laser beam with a Gaussian spatial profile and fixed energy is focused using a lens ($L_1$) on the sample to be

analyzed. The sample is mounted in a translational stage in order to be moved along the propagation axis (z-axis).[43] The focusing geometry generates an intensity distribution by the z-axis that reaches the maximum level at the focal plane. At this point, the intensity is high enough to induce nonlinear processes, which modify not only the intensity of the beam but also its phase. These changes can be monitored by measuring the transmitted power as a function of the z position at the far field. This transmitted light is focused using a second lens ($L_2$), which is then collected by a photodetector. In order to investigate the nonlinear processes that occur in various materials, it is necessary to have two different setups: open aperture and closed aperture.

The open aperture setup (Figure 1-5.a) is implemented by letting all the transmitted light reach the far field detector. When the sample is close to the focal point, the beam intensity allows the material to experience an electronic transition due to the nonlinear absorption of two or more photons in a single event. The open aperture arrangement is used to measure $\beta$ in the case of TPA.

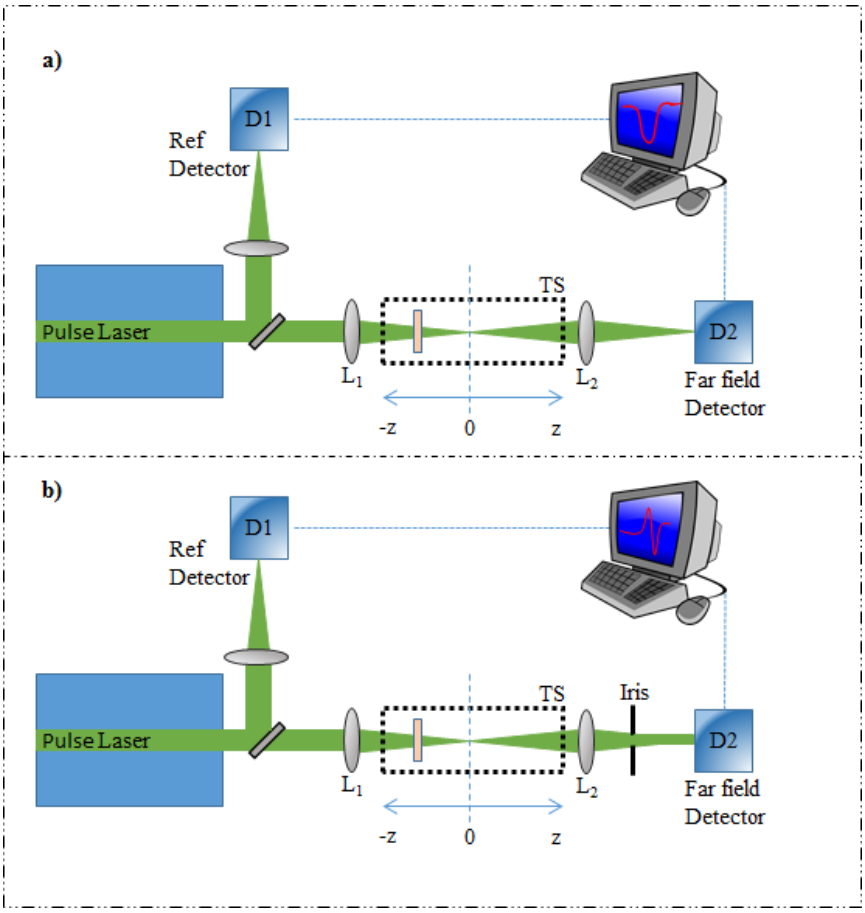


**Figure 1-5.** a) Open aperture Z-scan arrangement. b) Closed aperture Z-scan setup.

In the closed aperture setup (figure 1-5.b), a circular aperture (iris) is placed concentrically with the beam so that the light propagating close to the optical axis can be transmitted through it. The self-focusing process ($\eta_2 > 0$, green line in figure 1-6.a) is responsible for the material acting as a converging lens and the self-defocusing ($\eta_2 < 0$, blue line in figure 1-6.a) as a diverging lens, depending on the sign of $\eta_2$. The beam propagates either converging or diverging, depending on the previously mentioned lens effects. This results in an increase or decrease of the amount of light that is transmitted through the iris. The enlargement or reduction of the light is detected by the far-field detector and it can be observed in the change on the sample transmittance as a function of its position. The iris is usually placed at a distance roughly 20 to 100 times greater than $z_0$, in order

to satisfy the far-field approximation. Another important parameter in the closed aperture Z-scan technique is the transmittance factor (S). S is calculated by the fraction of the transmitted light that goes through the iris and it usually ranges between 0.1 and 0.5. The parameters that affect both open and closed aperture setups are the sample thickness (L) and the Raleigh range ($z_0$). $z_0$ is defined as the confocal parameter of the beam and equals $\pi w_0^2/\lambda$ for Gaussian beams, where $w_0$is the beam radius at the focal point. L must be less than $z_0$ to avoid any changes in the beam spatial distribution within the cell due to nonlinear absorption or diffraction. In order to guarantee that the nonlinear behavior is properly evaluated, a minimum scan length of $\pm 5z_0$ from the focal point must be used.

Figure 1-6.b presents the typical outcome of a sample exhibiting nonlinear absorption in an open aperture Z-scan measurement. Far from the focal point, the size of the beam does not have the adequate diameter to achieve the intensity needed to induce nonlinear absorption. Consequently, the Normalized Transmittance (NT) is adjusted to one. Then, the sample is translated to the focal plane of the focused beam, where z equals zero. When the nonlinear absorption process begins, the NT decreases until it reaches a minimum at the focal point. After the sample passes through the focal point, NT returns to its initial value. The following expression describes the transmittance as a function of the sample's position:

$$T_{OA} \cong 1 + -\frac{1}{2\sqrt{2}}\frac{\beta I_0 L}{(1+x^2)} \qquad (1-24)$$

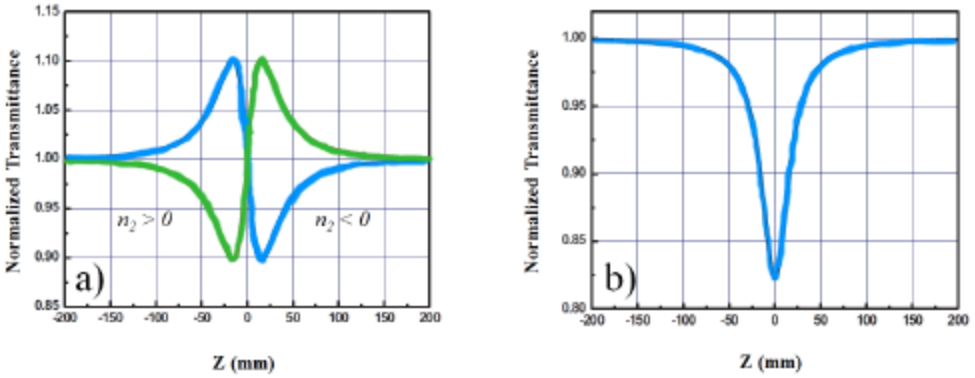


**Figure 1-6.** Typical outcome for a) closed aperture Z-scan and b) open aperture Z-scan

As shown in Figure 1-6.a, there is a common point for self-focusing and self-defocusing processes. At this point the transmittance is the same for both negative and positive $\eta_2$. This behavior is a result of assuming the thin lens approximation, which simplifies the calculations. $\eta_2$ can be obtained from

$$|\eta_2| = \left(\frac{\lambda}{2\pi}\right)\frac{|\Delta\Phi_0|}{I_0 L}. \qquad (1-25)$$

Here, $I_0$ is the irradiance at the focal point. $|\Delta\Phi_0|$ is the absolute value of the nonlinear pulse shift, which is calculated from equation 1-26,

$$|\Delta\Phi_0| = \frac{\Delta T_{pv}}{0.406(1-S)^{0.25}}, \qquad (1-26)$$

where $\Delta T_{pv}$ is the value for the separation between the peak and the valley transmittance.

Now that the Z-scan technique has been fully described, it is worth noting the existence of a group of molecules, known as chiral molecules, which exhibit additional optical properties not obtained directly from Z-scan measurements. The understanding of these additional properties is key to the comprehension of this disseminated work. The fundamentals and the experimental techniques for studying chiral molecules will be presented in the next section.

## 1.4 Fundamentals of linear and nonlinear circular dichroism

Chirality is a geometric property that certain molecules possess and it is responsible for the absence of a superimposable mirror image. [70] Chiral molecules exhibit specific optical features known as chiroptical properties. The observation of these properties depends on the polarization of the light source, which is why it is important to study the fundamentals of polarized light.

When light is linearly polarized, the electric field vector is confined to a particular plane along the propagation direction. Additionally, light presents various polarization states, most of which are based on two orthogonal linearly-polarized waves propagating in time (t) along the z axis.[71] In this case, the electric field ($\overrightarrow{E_\iota}$) of both waves is expressed as

$$\overrightarrow{E_x}(z,t) = \hat{\imath}E_{0x}\cos(kz - \omega t) \qquad (1-27)$$

and

$$\overrightarrow{E_y}(z,t) = \hat{\jmath}E_{0y}\cos(kz - \omega t + \varphi). \qquad (1-28)$$

Here, $k, \omega,$ and $\varphi$ are the light wave vector, the frequency of the light, and the relative phase difference, respectively. $E_{0x}$ and $E_{0y}$ are the amplitude of the electric field in the x and y direction.

The combination of the x and y components of the $\overrightarrow{E_t}$ yields

$$\vec{E}(z,t) = \overrightarrow{E_x}(z,t) + \overrightarrow{E_y}(z,t) \qquad (1-29)$$

or

$$\vec{E}(z,t) = \left(\hat{\imath}E_{0x} + \hat{\jmath}E_{0y}\right)\cos(kz - \omega t) \qquad (1-30)$$

when $\varphi = \pm n\pi$ and $n = 0, 1, 2, 3$ ....

The resultant wave from the combination of two linearly-polarized lights is not always linear. For example, when both waves have the same amplitude and $\varphi$ equals $(-\pi/2) + (2m\pi)$, the resultant quarter-wave phase difference changes the behavior of $\overrightarrow{E_y}(z,t)$ from cosinusoidal to sinusoidal as follows:

$$\vec{E} = E_0[\hat{\imath}\cos(kz - \omega t) + \hat{\jmath}\sin(kz - \omega t)]. \qquad (1-31)$$

Here, the amplitude of the electric field is constant but its direction rotates continuously in time around the z axis, resulting in circularly-polarized light. When the two terms in equation 1-31 are added together, the wave rotates in a clockwise direction and it is known as right circularly-polarized light. If the wave rotates in a counterclockwise direction, the terms of the equation 1-31 are subtracted one from the other and the light is said to be left circularly-polarized.[71]

### 1.4.1 Electronic Circular Dichroism

When chiral molecules are irradiated with polarized light, the circular polarized components present various chiroptical responses such us differences in refractive index (circular birefringence) and absorption coefficient (circular dichroism) between right and left circularly polarized light. Circular birefringence, also known as optical rotation, induces the rotation of the

polarization plane of linearly-polarized light as the beam travels through the chiral sample. The other chiroptical response, circular dichroism, manifests itself when one-handed circularly-polarized light exhibits a higher absorption than the other.

Before polarized light and chiral system interact, both left and right circularly-polarized components exhibit the same amplitude for the electric field vectors. After the interaction, both amplitudes decrease due to absorption, but one of them decreases even more as a result of circular dichroism (see figure. 1-7). For this reason, the polarization of the transmitted light is elliptical.[70]

$\theta$ (the degree of ellipticity) is calculated from the arctangent of the lower to the higher elliptical axis as shown in figure 1-7.b. $\theta$ relates to absorption through the following mathematical expression:[72]

$$\theta = 32.988\Delta A, \qquad (1-32)$$

Where $\Delta A$ corresponds to the circular dichroism and is equal to $A_L - A_R$. $A_L$ and $A_R$ are the absorbance of the left and right circularly-polarized light, respectively. If equation 1-32 is combined with Beer's law, an expression for molar ellipticity ($[\theta]$) is obtained:[72]

$$[\theta] = \frac{\theta}{c \cdot l} = \frac{32.988\Delta A}{c \cdot l} = 32.988\Delta\varepsilon. \qquad (1-33)$$

Here, $c$ is the molarity, $l$ is the path length in centimeters, and $\Delta\varepsilon$ is the circular dichroism in terms of molar absorptivity. $[\theta]$ and $\Delta\varepsilon$ are two common ways to report circular dichroism experimentally.

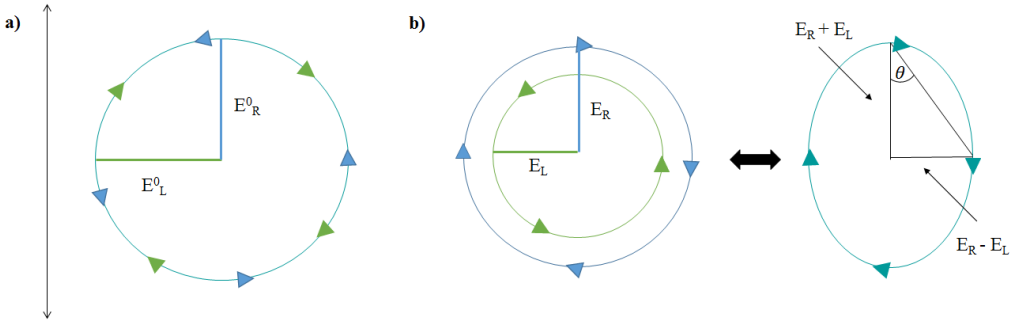


**Figure 1-7**. a) Linearly polarized light described by left (blue arrows) and a right (green arrows) circularly-polarized components with an electric field of equal amplitude. b) Both electric field components with a different amplitude after the interaction with a chiral system. The addition of these components results in an elliptical polarization state (teal ellipse). Note: the graphs shown here describe a complete oscillation ($2\pi$) of the electric field vector from a viewer's perspective located in front of the propagation axis.

The study of the circular dichroism phenomenon introduced a very useful technique known as Electronic Circular Dichroism (ECD). This method is widely employed for the assignment of absolute configurations of chiral molecules and macromolecules. Interesting to highlight is the fact that mirror images of chiral molecules (enantiomers) gives specular ECD spectra, i.e. same shape but the opposite sign.[29] ECD is a very sensitive technique used to study conformational and structural changes of molecular and macromolecular systems in biology and medicine. However, ECD finds barriers for measurements below 200 nm because its signal is hindered by the absorption of solvents and buffers in this spectral region.[30] Additionally, the scattering produced by inhomogeneous samples is clearly intensified in this region. In order to overcome these challenges, researches have proposed multiple approaches, such as Synchrotron Radiation Circular Dichroism (SRCD),[73] Magnetic Circular Dichroism (MCD),[74] Vibrational Circular Dichroism (VCD),[75] and Raman Optical Activity (ROA).[76] However, these techniques are not a feasible solution to obtaining access to the near and far UV region, where the ECD signal is obscured. The only polarization-dependent experimental technique that has presented a clear potential to gaining access to the spectral region below 200 nm is known as Two-Photon Circular Dichroism (TPCD).

### 1.4.2 Two-Photon Circular Dichroism

TPCD is the nonlinear counterpart of ECD (Figure 1-8) and it is defined as the difference between the TPA cross-section of left ($\delta_L^{TPA}$) and right ($\delta_R^{TPA}$) circular polarized light ($\Delta\delta^{TPCD}(\lambda) = \delta_L^{TPA} - \delta_R^{TPA}$).[31, 32] This method brings together two main advantages previously mentioned: First, it is a technique that is applicable only for chiral systems and it can discriminate between pairs of enantiomers. Second, it has all the advantages described in section 1.3 for TPA-based measurements. For this reason, TPCD has been proven to be an excellent complimentary technique for ECD.[77]

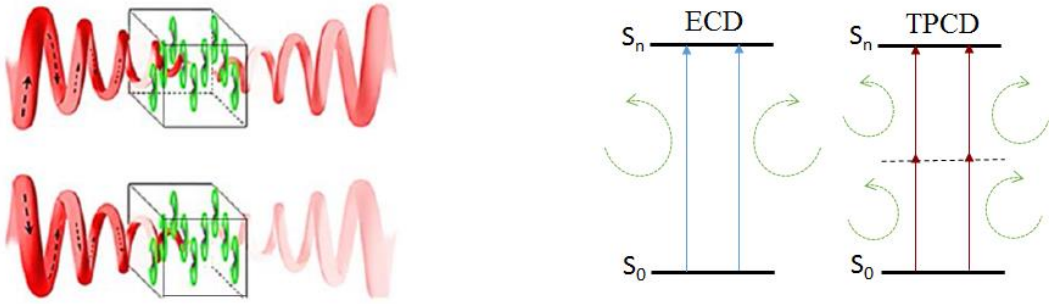


**Figure 1-8.** Graphical comparison between electronic circular dichroism and two-photon circular dichroism

## 1.5 Theoretical framework for the calculation of linear and nonlinear circular dichroism spectra

### 1.5.1 Electronic circular dichroism

The molar absorptivity ( $\Delta\varepsilon^{ECD}$) is defined as the difference in OPA from left and right circularly-polarized light and it is related to the ECD rotatory strength ($R_{0f}^{ECD}$) of each electronic excited state. $R_{0f}^{ECD}$ is proportional to the imaginary part of the scalar product of the electric dipole (μ) and the magnetic dipole (m) transition moments as shown here:[31, 52, 78]

$$\Delta\varepsilon^{ECD}(\omega) = \varepsilon_L(\omega) - \varepsilon_R(\omega) = \frac{64\pi^2 N_A \omega}{9 \times 1000 \times \ln(10) \times (4\pi\varepsilon_0) \times \hbar c_0^2} \sum_f g(\omega, \omega_{0f}, \Gamma) R_{0f}^{ECD}, (1-34)$$

$$\Delta\varepsilon^{ECD}(\omega) \approx 2.73719 \times 10^1 \times \omega \sum_f g(\omega, \omega_{0f}, \Gamma) R_{0f}^{ECD}, \quad (1-35)$$

where the circular frequency of the incident radiation ($\omega$) is equal to $2\pi c_0/\lambda$, $c_0$ is the speed of light *in vacuo*, $\varepsilon_0$ is the vacuum permittivity, $N_A$ is Avogadro's number, $g(\omega, \omega_{0f}, \Gamma)$ is the normalized lineshape centered at $\omega_{0f}$, and Γ is the full width half-maximum (FWHM). $R_{0f}^{ECD}$ is obtained from the following formula:[78, 79]

$$R_{0f}^{ECD} = \frac{3}{4}\Im[\langle 0|\mu|f\rangle\langle f|m|0\rangle]. \quad (1-36)$$

The units of $\Delta\varepsilon^{ECD}$ are mol$^{-1}$ cm$^{-1}$ L when $R_{0f}^{ECD}$ is used in a.u.

### 1.5.2 Two-Photon Circular Dichroism

In 1975, Tinoco[31] and Power,[32] simultaneously but independently, proposed TPCD theoretically. But it was not until 2005 that Rizzo and co-workers implemented TPCD computationally, allowing its calculation for complex molecular systems. The TPCD spectra can be obtained from the expressions proposed by Tinoco and presented here:[31, 52]

$$\Delta\delta^{TPCD}(\omega) = \delta_L^{TPA}(\lambda) - \delta_R^{TPA}(\lambda) = \frac{4}{15}\frac{(2\pi)^3\omega^2}{c_0^3(4\pi\varepsilon_0)^2} \times \sum_f g(2\omega, \omega_{0f}, \Gamma) \cdot R_{0f}^{TPCD}(\omega_{0f}), (1-37)$$

$$\Delta\delta^{TPCD}(\omega) \approx 4.87555 \times 10^{-5} \times \omega^2 \sum_f g(2\omega, \omega_{0f}, \Gamma) \cdot R_{0f}^{TPCD}(\omega_{0f}), \quad (1-38)$$

where $R_{0f}^{TPCD}(\omega_{0f})$ is calculated from

$$R_{0f}^{TPCD}(\omega_{0f}) = -b_1 B_1(\omega_{0f}) - b_2 B_2(\omega_{0f}) - b_3 B_3(\omega_{0f}). \qquad (1-39)$$

Here, $b_1$, $b_2$, and $b_3$are scalars determined by the experimental setup and are equal to 6, 2, and -2 for the specific case of two co-linear and co-propagating right or left circularly-polarized photons. The molecular parameters, $B_i(\omega_{0f})$, are obtained from[77]

$$B_1^{TI}(\omega_{0f}) = \frac{1}{\omega_{0f}^3} \sum_{\rho\sigma} M_{\rho\sigma}^{p,0f}(\omega_{0f}) P_{\rho\sigma}^{p*,0f}(\omega_{0f}), \qquad (1-40)$$

$$B_2^{TI}(\omega_{0f}) = \frac{1}{2\omega_{0f}^3} \sum_{\rho\sigma} T_{\rho\sigma}^{+,0f}(\omega_{0f}) P_{\rho\sigma}^{*,0f}(\omega_{0f}), \qquad (1-41)$$

$$B_3^{TI}(\omega_{0f}) = \frac{1}{\omega_{0f}^3} \left[ \sum_{\rho} M_{\rho\rho}^{p,0f}(\omega_{0f}) \right] \left[ \sum_{\sigma} P_{\sigma\sigma}^{p*,0f}(\omega_{0f}) \right]. \qquad (1-42)$$

Here, the tensors $T_{\alpha\beta}^{+,0f}(\omega_{0f})$, $M_{\alpha\beta}^{p,0f}(\omega_{0f})$, $P_{\alpha\beta}^{p*,0f}(\omega_{0f})$, are the quadrupole matrix elements in the velocity formulation, the magnetic transition dipole matrix element, and the electric transition dipole, respectively. These tensors are defined as follows:

$$P_{\alpha\beta}^{p*,0f}(\omega_\beta) = \frac{1}{\hbar} \sum_P \sum_{n\neq 0} \frac{\left(\mu_\alpha^p\right)^{0n} \left(\mu_\beta^p\right)^{nf}}{\omega_\alpha - \omega_{0n}}, \qquad (1-43)$$

$$M_{\alpha\beta}^{p,0f}(\omega_\beta) = \frac{1}{\hbar} \sum_P \sum_{n\neq 0} \frac{(\mu_\alpha^p)^{0n} (m_\beta^p)^{nf}}{\omega_\alpha - \omega_{0n}}, \qquad (1-44)$$

$$T_{\alpha\beta}^{+,0f}(\omega_\beta) = \frac{1}{\hbar}\mathcal{E}_{\beta\rho\alpha}\sum_P\sum_{n\neq 0}\frac{(T_{\alpha\rho}^{+})^{0n}(\mu_\beta^p)^{nf}}{\omega_\alpha - \omega_{0n}}, \qquad (1-45)$$

where $\mathcal{E}_{\beta\rho\alpha}$ is the Levi Civita alternating tensor, $\mu_\alpha^p$ is the $\alpha$ component of the dipole velocity operator, and $T_{\alpha\rho}^{+}$ is the $\alpha\beta$ component of the mixed length-velocity form of the quadrupole operator. $\mu_\alpha^p$, $m_\beta^p$ is the magnetic dipole operator, and $T_{\alpha\rho}^{+}$ are calculated from the following expressions:

$$\mu_\alpha^p = \sum_i \frac{q_i}{m_i} p_{i\alpha}, \qquad (1-46)$$

$$m_\beta^p = \sum_i \frac{q_i}{2m_i}(r_i \; x \; p_i)_\beta \qquad (1-47)$$

$$T_{\alpha\rho}^{+} = \sum_i \frac{q_i}{m_i}(p_{i\alpha}r_{i\beta} + r_{i\alpha}p_{i\beta}). \qquad (1-48)$$

Equation 1-37 yields units of cm$^4$ s photon$^{-1}$ molecule$^{-1}$ (1 G*ö*ppert-Mayer = $10^{-50}$ cm$^4$ s photon$^{-1}$ molecule$^{-1}$) when $\omega$ and $R_{0f}^{TPCD}(\omega_{0f})$are in atomic units.

Although TPCD was proposed in the 1970s,[31, 32] it was not until the advent of double-L scan that TPCD was experimentally feasible. In 2008, Hernandez and co-workers proposed the use of this differential method in order to experimentally measure TPCD.[35] This has been the most reliable and versatile technique for this application. All the details about the double-L scan technique will be covered in the next section.

## 1.6 Experimental measurements of two-photon circular dichroism

The first successful attempt to measure TPCD experimentally was made by Gunde and Richardson in 1995.[33] These scientists observed TPCD signal on a $Gd^{3+}$ complex using a method known as Fluorescence Detected TPCD (FD-TPCD). However, the entire TPCD spectrum only covered a maximum spectral region of approximately 20 nm. Additionally, this technique requires

that the system to exhibit fluorescence, which restricts its use. After this first attempt, many researchers proposed new alternatives to measure TPCD such as the use of pump-probe,[19] Z-scan with modulation of the polarization,[80] and resonance-enhanced multiphoton ionization.[81, 82] Unfortunately, none of these techniques yielded a pure TPCD spectrum of any optically-active system.

It was not until 2008 that a more reliable and versatile technique was proposed, when Hernandez and co-workers introduced the well-known double-L scan technique.[35] This method is primarily based on Z-scan measurements and perfectly allows the detection of the TPCD signal due to the use of "twin pulses".

### 1.6.1 Double-L scan

When Hernandez and co-workers decided to embark on the idea of measuring TPCD signals on chiral molecules, they started by measuring the TPA cross-section for linearly polarized light (LPL), right (RCPL) and left (LCPL) circularly-polarized light.[83] These measurements were done by keeping all the experimental variables constant. A pair of enantiomers, (S)-(-)-1,1'-bi(2-naphthol) (S-BINOL) and (R)-(+)-1, 1'-bi(2-naphthol (R-BINOL), were used on this first attempt. The excitation source was an Optical Parametric Generator (OPG) pumped by a third harmonic mode locked Nd:YAG laser (EKSPLA). The entire system was able to produce pulses of 25 ps (FWHM) at a 10 Hz repetition rate with less than 30% stability. Although extreme experimental conditions were employed to minimize the fluctuations from one measurement to the other, the instability ascribed to the laser source masked the small differences between RCPL and LCPL (see Figure 1-9).

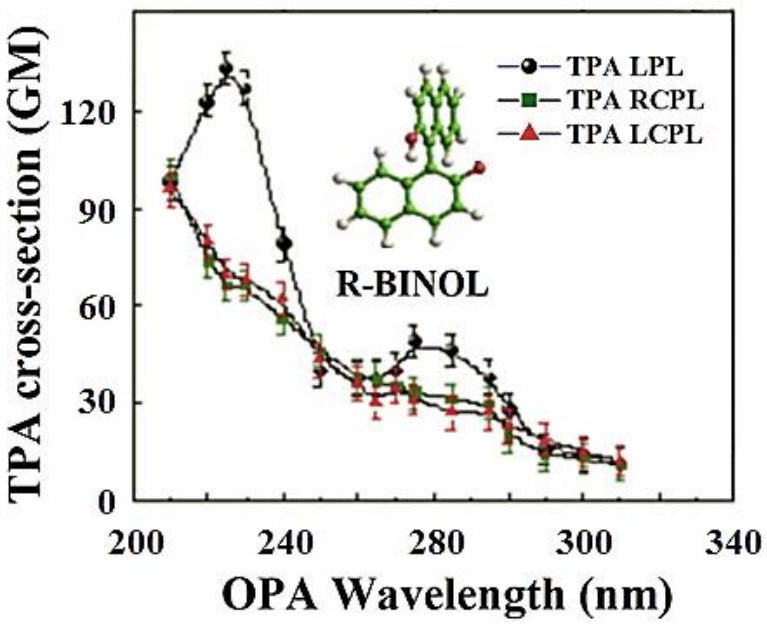


**Figure 1-9**. Z-scan TPA spectra of R-BINOL in THF, exciting with LPL (black spheres), RCPL (green squares), and LCPL (red triangles). Graph was taken from reference (83)

As a result of the observations made out of Figure 1-9, Hernandez and co-workers postulated the following hypothesis: "*Common changes observed in the beam size and shape, and even modal fluctuations can lead to significant changes in the spatial energy distribution that could create changes in irradiance for the different z positions, thus increasing the error of the measurement. This artifact can mask the TPCD signal."* In order to prove this hypothesis, they photographed pulse profiles for a series of pulses employing a CCD camera (Figure 1-10).[83] The snapshots of eight different pulses presented in Figure 1-10 exhibited the important variations in spatial profile, energy distribution, and size of the different pulses among them.

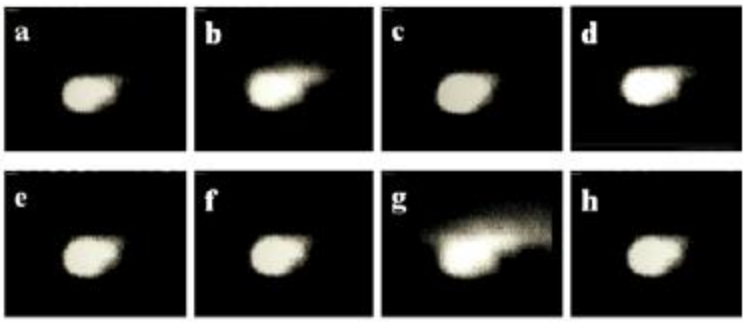


**Figure 1-10.** Snapshot of a sequence of eight laser pulses used in a Z-scan. Picture was taken from reference (83).

The solution that Hernandez and co-workers found to this challenge was to implement simultaneous measurements of $\delta_L^{TPA}(\lambda)$ and $\delta_R^{TPA}(\lambda)$ by employing a double-arm setup. In order to achieve the measurements with this new setup, it was necessary to fix the position of the sample and move the convergent lenses, which allowed them to scan the focal plane along z-axis. Figure 1-11 shows a graphical depiction of the main principal of the double-L scan technique.

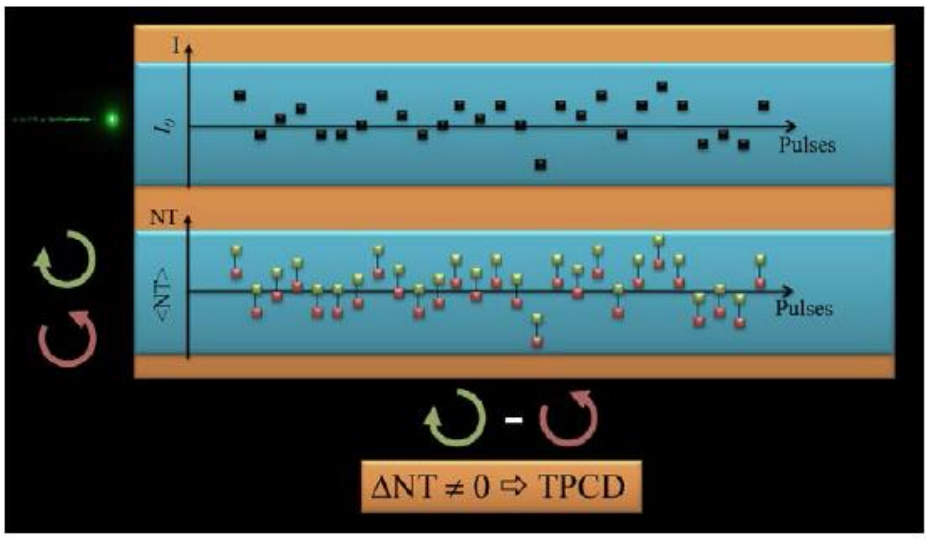


**Figure 1-11.** Graphical depiction of TPA measurements performed employing the double-L scan technique. Excitation is achieved by pulses with RCPL (green squares) and LCPL (red squares). The top section presents the intensity (I) of various laser pulses and the bottom one displays the NT of each pulse's sample for circular polarization of different handiness. Figure was taken from reference (83).

In the double-L scan technique, a seed beam is employed to generate two identical "twin beams" and they induce the TPA excitation using polarization states of different handedness. Each one of those "twin beams" travels through the same optical elements and path, ensuring that any fluctuations that occur during the measurement, due to a change in spatial profile, energy distribution, and size of the beam, will equally affect both arms. Therefore, any difference in signal ($\Delta NT \neq 0$) observed throughout the experiment is considered to be the TPCD signal associated to that specific chiral system.

Figure 1-12 presents the double-L scan setup.[83] It is worth noting that the two arms are identical in path and optical elements as previously referred.

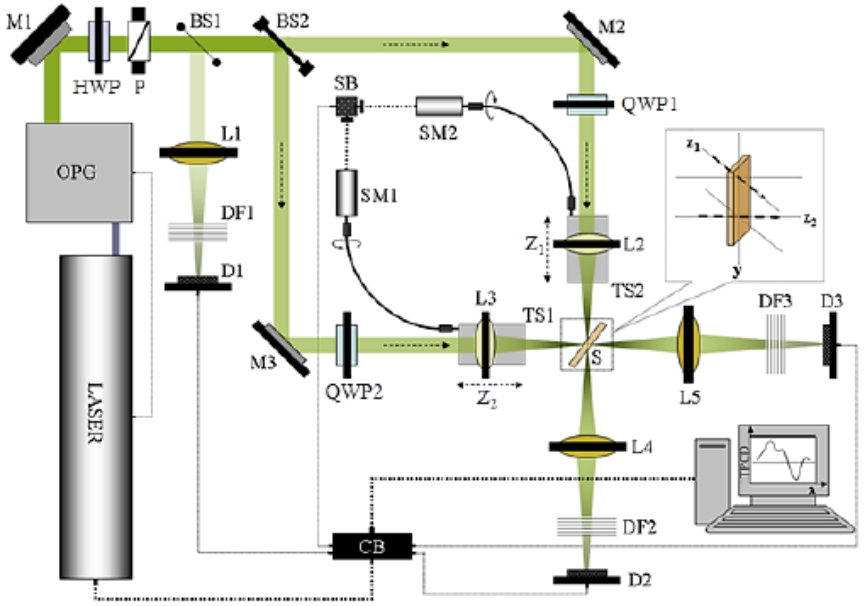


**Figure 1-12.** Double-L scan setup. Mirrors (M1, M2, M3); half wave plates (HWP); quarter wave plates (QWP1, QWP2); polarizer (P); beamsplitter (BS1, BS2); convergent lenses (L1, L2, L3, L4, L5); detectors (D1, D2, D3); neutral density filters (DF1, DF2, DF3); translation stages (TS1, TS2); step-motors (SM1, SM2); synchronization box (SB); sample (S), and control box (CB). Figure was taken from reference (83).

In order to confirm that the double-L scan setup would in fact produce "twin beams", the same CCD camera was used to capture a set of pulses profiles. The camera was placed right before the pulse hits the sample at a 45º angle from both beams. Twelve snapshots of a pair of pulses are shown in figure 1-13, where small variations in size can be observed. These differences are attributed to the location where the CCD camera was placed. Besides this, no other dissimilarities were observed. This means that the double-L scan setup compensates for all the variations produced by the laser source and makes it a reliable technique for measuring small TPCD signals.

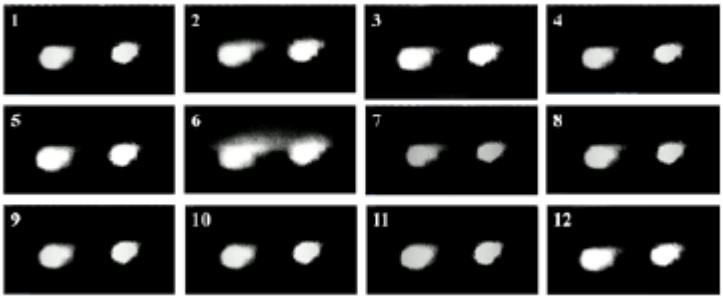


**Figure 1-13**. Snapshot of twelve pairs of pulses used in the double-L scan. The little variations in size within the pair of pulses is due to the angle used to capture the images with the CCD camera. Picture was taken from reference (83).

Since most of the chiral molecules generate a small TPCD signal, the required calibration of the double-L scan setup is very important. The calibration procedure resides on the measurements of the sample's TPA, employing LPL on both arms. The condition is to obtain exactly the same z-scan ($\Delta NT = 0$) for both arms, meaning that their energy is identical. Once this requirement is met, the TPCD measurements can be performed. Then, the extraordinary axis of the quarter waveplates in each arm (QWP1 and QWP2 in figure 1-13) are rotated 45º with respect to the polarization plane of the incident radiation in order to change the polarization state to RCPL and LCPL, respectively.

After all these changes were made, the double-L scan technique was used to measure the

TPCD spectrum of R-BINOL in THF. In figure 1-14.a, the experimental TPA spectra of R-BINOL in THF employing LPL (blue squares), RCPL (red triangles), and LCPL (green triangles) are presented, as well as the OPA spectrum. Two important observations can be made from this figure: first, the variations in shape and intensity of the spectra measured with LPL (blue squares) and the ones obtained with RCLP (red triangles) and LCPL (green triangles) are obvious. This effect is known as Circular Linear Dichroism (TPCLD) [36] and it will not be covered in this dissertation. Second, the obvious difference present between $\delta_L^{TPA}(\lambda)$ and $\delta_L^{TPA}(\lambda)$ allowed the measurement of TPCD in R-BINOL (Figure 1-14.b). The TPCD spectrum of the other enantiomer (S-BINOL) was also measured. Additionally, the measurement of the TPCD signal of a racemic mixture of 50% R-BINOL and 50% S-BINOL resulted in an experimental sensitivity of ≈1 GM, which corroborates that the TPCD signal for each enantiomer is different. To further confirm the results presented before, the theoretical TPCD spectra were obtained. Initially, both enantiomers were optimized using Density Functional Theory (DFT)[84] at the B3LYP[85-87] /6-31++G(d,p)[88, 89] level of theory in Gaussian 03. Then, excited state calculations were achieved through Time Dependent-DFT (TD-DFT)[84] in combination with the B3LYP/aug-cc-pVDZ[90] level of theory for the first 25 electronic excited states in Dalton 2.0.[91]

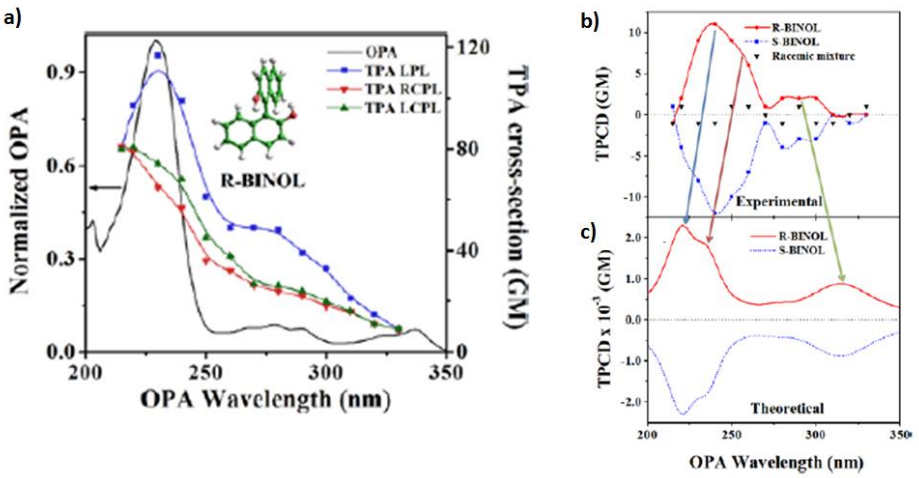


**Figure 1-14**. a) Double-L scan TPA spectra of R-BINOL in THF, pumping with LPL (black squares), RCLP (red triangles), and LCPL (green triangles). Normalized OPA (solid black line). b) Experimental and c) Theoretical TPCD spectra of R-BINOL (red) and S-BINOL (blue). The experimental TPCD for a racemic mixture of BINOL is also shown. This graphs were taking from references (83) and (36).

It is worth noting the great overlap between theory and experiment in Figure 1.14.b and c. All the spectra features were reproduced by the theoretical spectra. However, the experimental TPCD spectrum presents a magnitude that is almost three times larger than the theoretical spectrum. Up to this point, Hernandez and co-workers successfully proved the implementation of a versatile and reliable technique for measuring TPCD, known as the double-L scan technique. Then, they directed their attention towards a better understanding of the structure-property relationship of TPCD.

First, TPCD was measured on a series of molecules with axial chirality (S-BINOL, S-VANOL, and S-VAPOL).[92] The spectra of all biaryl derivatives were obtained in THF solutions and excited in the picosecond regime. TPA and TPCD spectra are presented in Figure 1-15 which exhibits the important tendency of the TPCD signal that varied according to $\Delta\delta^{TPCD}_{S-BINOL} < \Delta\delta^{TPCD}_{S-VANOL} < \Delta\delta^{TPCD}_{S-VAPOL}$. Then, the calculated spectra were obtained by initially optimizing all the

molecules with the B3LYP[85-87] and 6-31G(d)[93] level of theory with GAUSSIAN 09.[94] TPA and TPCD were calculated for the first 20 excited states using TD-DFT[49] with two different exchange-correlation functional (XCF), B3LYP[85-87] and Coulomb attenuating method-B3LYP (CAM-B3LYP),[95, 96] at 6-31G(d)[93] level of theory in DALTON 2.0.[91] As mentioned before, the TPCD signals directly rely on the different contributions from the electric transition quadrupole moment and the magnetic transition dipole moment through $R_{0f}^{TPCD}$.

A comparison of the contribution of the electronic transition quadrupole moment ($B_2$) and the magnetic transition dipole moment ($B_1 + B_3$) to the $R_{0f}^{TPCD}$ was achieved and led to the following important conclusion: *the effect of the magnetic transition dipole moment on the TPCD rotatory strength, and thus the TPCD signal, is strongly enhanced by the twist in the π-electron delocalization of chiral molecules.*

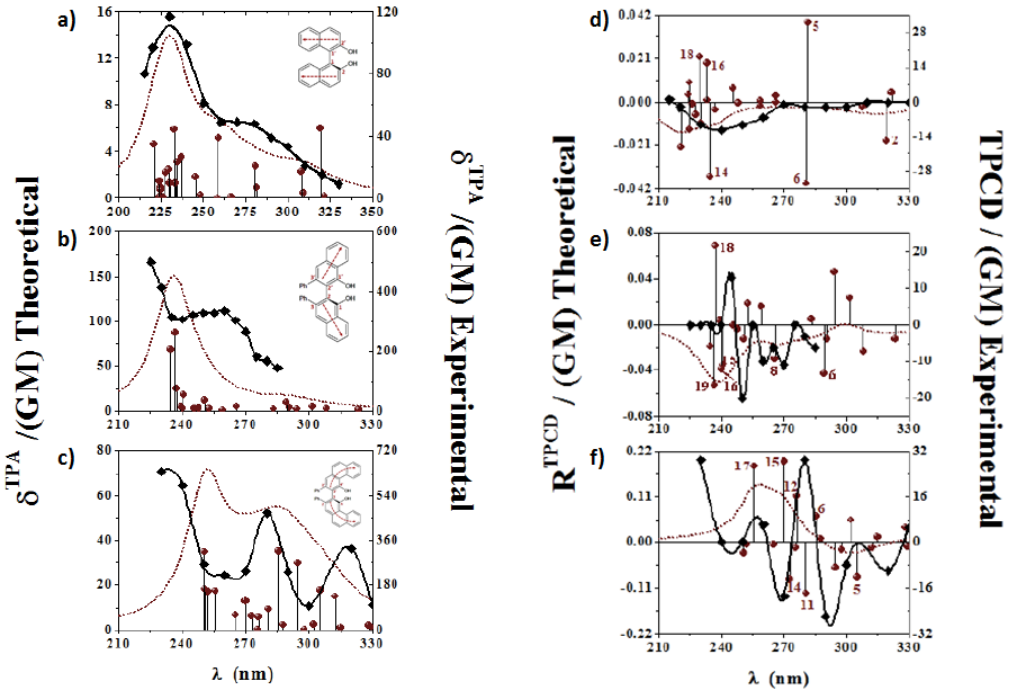


**Figure 1-15**. TPA spectra of a) S-BINOL, b) S-VANOL, and c) S-VAPOL. TPCD spectra of d) S-BINOL, e) S-VANOL, and f) S-VAPOL. The theoretical spectra are shifted +18nm, -17 nm, and -3 nm, respectively. Figures were taken from reference (92).

After TPCD was proven to be strongly affected by Intramolecular Charge Transfer (ICT), Hernandez and co-workers decided to investigate an axially dissymmetric diphosphine ligand (S-BINAP) in order to obtain a better perspective on the TPCD response influenced by the structure-property relationship.[97] The theoretical analysis of the TPCD spectrum of S-BINAP was accomplished by employing TD-DFT[49] calculations at two different levels of theory: first, B3LYP[85-87]/6-31G(d)[93] and second, CAM-B3LYP[95, 96]/6-31G(d).[93] The calculations were initially obtained for the first 40 excited states but they were extended to 80 excited states in order to properly assign the bands of the TPCD spectra. The experiments were carried out in THF solutions (see Figure 1-16). This study revealed that CAM-B3LYP is a more reliable XCF in molecules with ICT.

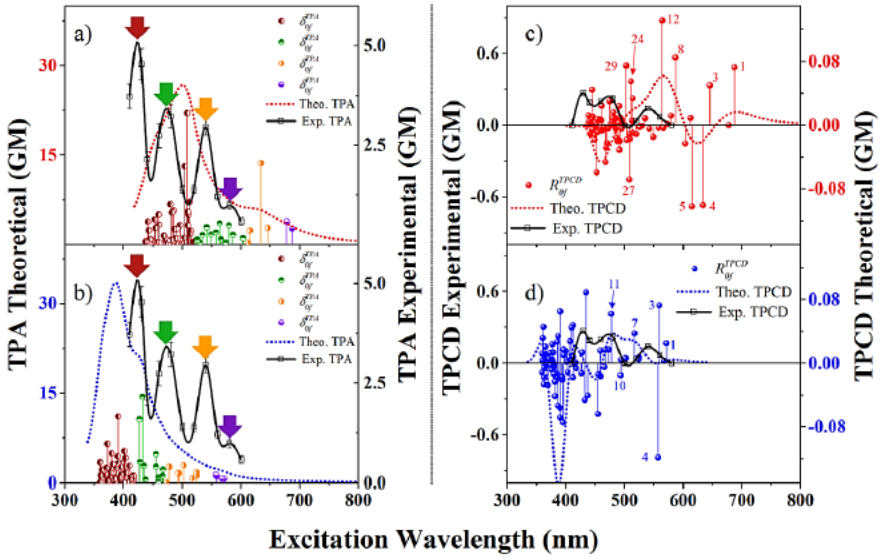


**Figure 1-16.** Experimental TPA (left, black squares) and TPCD (right, black squares) spectra of S-BINAP. a) Theoretical TPA calculated with B3LYP/6-31G(d) and b) Theoretical TPA calculated with CAM-B3LYP/6-31G(d). c) Theoretical TPCD calculated with B3LYP/6-31G(d) and b) Theoretical TPCD calculated with CAM-B3LYP/6-31G(d). 80 excited were calculated. Graph was taken from reference (97).

This finding was the main motivation for seeking a better understanding of this nonlinear property (TPCD) and its potential application. In order to accomplish that goal, the first theoretical-

experimental study of the effect of the nature of ICT of hexahelicenes derivatives was initiated.[98] Two interesting aromatic molecules, P-(+)aza[6]helicene (A6) and P-(+)-2-[4-(cyanophenyl)-1-ethynyl]carbo[6]-carbohelicene (CN6), with helical chirality and ICT, were selected. The theoretical calculations were achieved by optimizing the molecules with DFT[49] at a theory level of B3LYP[85-87]/6-311++G(d,p) using GAUSSIAN 09.[94] Then, TPA and TPCD were calculated employing TD-DFT [49] with CAM-B3LYP[95, 96] (already proven to be better for molecules with ICT) in combination with the 6-311++G(d,p) basis set. The number of TPA and TPCD excited states were 60 and 48 for A6 and 60 and 40 for CN6, respectively, using DALTON 2011.[99] Figure 1-17 presents the experimental TPA and TPCD spectra taken in THF solutions, as well as the theoretical spectra.

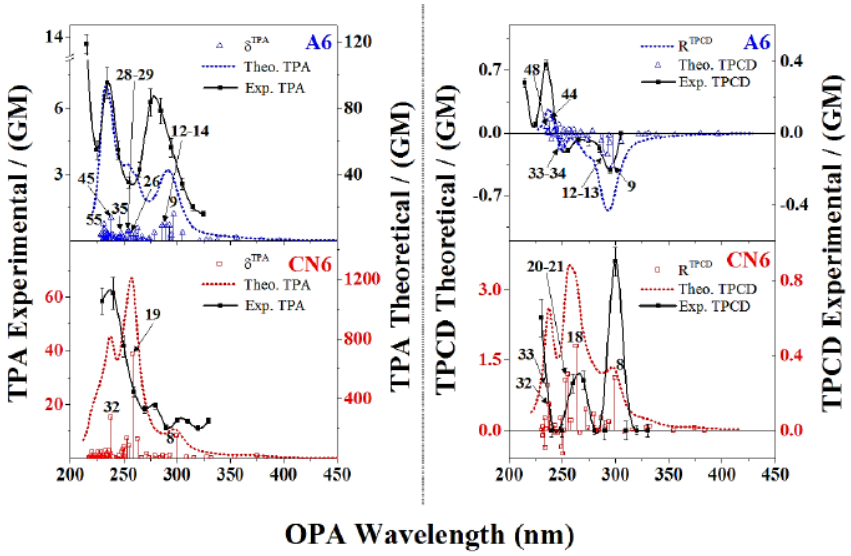


**Figure 1-17.** Experimental (black squares) and theoretical TPA (left) and TPCD (right) spectra of A6 and CN6 calculated in vacuo. The theoretical shifts are A6 (+22 nm) and CN6 (+26nm). All the experimental spectra were taken in THF solutions. Plot was taken from reference (98).

The most interesting outcome of the nonlinear characterization of A6 and CN6 is the evidently bigger TPA cross-section and TPCD signal observed in CN6. This result can be supported by the following two effects: first, the strong ICT character of the nitrile group ($-C \equiv N$) which is a

moderate electron-withdrawing group. Second, the extended electron delocalization over the (4-cyanophenyl)-1-ethynyl substituent outside the helical core in CN6. Although the CN6 compound experiences more ICT than A6, there is a mild ICT character in A6 that is only effective within the helical core, due to the presence of the aza group ($-N=$). A theoretical comparison between different ICT conjugation lengths outside the [6]carbohelicene core (EXO-ICT) and within the aromatic cluster (ENDO-ICT) was accomplished. Three important conclusion were drawn out of this evaluation: (1) the electric dipole transition moment, and consequently the TPA signal, is enhanced by increasing the EXO-ICT, (2) the magnetic dipole transition moment could cause a potential enhancement in the TPCD response of helical molecules due to its coupling with the induced molecular magnetic field, subsequent to the generation of molecular circular currents within the helical core and (3) the contribution of the electric quadrupole transition moment to the TPCD signal of helical molecules with enlarged EXO-ICT appreciably increases their nonlinear response. In summary, it was demonstrated that the amplitude of the TPCD signal in helicenes is altered by both the strength of the ICT and its nature.[98]

Until now, Hernandez and co-workers have proven to effectively measure and calculate the TPCD signal of multiple optically-active molecules with axial and helical chirality. The overall investigation has helped to understand how TPCD, a nonlinear property, responds to different structure–property conditions.

In the next four chapters, we will present the novel advances towards a deeper understanding of the structure-property relationship of TPCD, as well as the progress made to gain access to a spectral region that was never accessed before: the FAR-UV.

## 1.7 References


1. Sabra, A. I., *Theories of light, from Descartes to Newton*. CUP Archive: 1981.
2. Smith, A. M., Ptolemy's Theory of Visual Perception: An English Translation of the "Optics" with Introduction and Commentary. *Transactions of the American Philosophical Society* **1996,** *86* (2), iii-300.
3. Mustroph, H.; Stollenwerk, M.; Bressau, V., Current developments in optical data storage with organic dyes. *Angewandte Chemie International Edition* **2006,** *45* (13), 2016-2035.
4. Escobedo, J. O.; Rusin, O.; Lim, S.; Strongin, R. M., NIR dyes for bioimaging applications. *Current opinion in chemical biology* **2010,** *14* (1), 64-70.
5. Moerner, W., New directions in single-molecule imaging and analysis. *Proceedings of the National Academy of Sciences* **2007,** *104* (31), 12596-12602.
6. Quimby, R. S., *Photonics and lasers: an introduction*. John Wiley & Sons: 2006.
7. Yeh, C., *Applied photonics*. Academic Press: 1994.
8. Denk, W.; Strickler, J.; Webb, W., Two-Photon Laser Scanning Fluorescence Microscopy. *Science* **1990,** *248*, 73-76.
9. Cumpston, B. H.; Ananthavel, S. P.; Barlow, S.; Dyer, D. L.; Ehrlich, J. E.; Erskine, L. L.; Heikal, A. A.; Kuebler, S. M.; Lee, I.-Y. S.; McCord-Maughon, D., et al., Two-Photon Polymerization Initiators for Three-Dimensional Optical Data Storage and Microfabrication. *Nature* **1999,** *398*, 51-54.
10. Celli, J. P.; Spring, B. Q.; Rizvi, I.; Evans, C. L.; Samkoe, K. S.; Verma, S.; Pogue, B. W.; Hasan, T., Imaging and photodynamic therapy: mechanisms, monitoring, and optimization. *Chemical reviews* **2010,** *110* (5), 2795-2838.
11. Pawlicki, M.; Collins, H. A.; Denning, R. G.; Anderson, H. L., Two-Photon Absorption and

the Design of Two-Photon Dyes. *Angewandte Chemie International Edition* **2009,** *48* (18), 3244-3266.

12. He, G. S.; Tan, L.-S.; Zheng, Q.; Prasad, P. N., Multiphoton absorbing materials: molecular designs, characterizations, and applications. *Chemical Reviews* **2008,** *108* (4), 1245-1330.
13. Cumberbatch, E., Self-focusing in nonlinear optics. *IMA Journal of Applied Mathematics* **1970,** *6* (3), 250-262.
14. Helmchen, F.; Denk, W., Deep tissue two-photon microscopy. *Nature methods* **2005,** *2* (12), 932-940.
15. Spangler, C., Recent development in the design of organic materials for optical power limiting. *Journal of Materials Chemistry* **1999,** *9* (9), 2013-2020.
16. Sun, H.-B.; Kawata, S., Two-photon photopolymerization and 3D lithographic microfabrication. In *NMR• 3D Analysis• Photopolymerization*, Springer: 2004; pp 169-273.
17. Burke, B. J.; Moad, A. J.; Polizzi, M. A.; Simpson, G. J., Experimental confirmation of the importance of orientation in the anomalous chiral sensitivity of second harmonic generation. *Journal of the American Chemical Society* **2003,** *125* (30), 9111-9115.
18. Ji, N.; Ostroverkhov, V.; Belkin, M.; Shiu, Y. J.; Shen, Y. R., Toward Chiral Sum-Frequency Spectroscopy. *Journal of the American Chemical Society* **2006,** *128*, 8845-8848.
19. Mesnil, H.; Hache, F., Experimental evidence of third-order nonlinear dichroism in a liquid of chiral molecules. *Physical Review Letters* **2000,** *85*, 4257-4260.
20. Baranowska, A.; Rizzo, A.; Jansík, B.; Coriani, S., Nonlinear effects in the interaction of time-dependent fields and chiral systems: A computational investigation. *The Journal of chemical physics* **2006,** *125* (5), 054107.
21. Gedanken, A.; Tamir, M., Multiphoton optical rotary dispersion. *Review of scientific*

*instruments* **1987,** *58* (6), 950-952.

22. Power, E., *Developments in the theory of multiphoton absorption by molecules (bound-bound): Applications of a chirooptic character*. Plenum Press: New York, NY, USA: 1990.
23. Cameron, R.; Tabisz, G. C., Observation of Two-Photon Optical Rotation by Molecules. *Molecular Physics* **1997,** *90*, 159-164.
24. Cameron, R.; Tabisz, G. C., Characterization of intensity-dependent optical rotation phenomena in chiral molecules in solution. *Journal of Chemical Physics* **2007,** *126*.
25. Qu, W.; Tabisz, G. C., Ab initio calculations of nonlinear optical rotation by several small chiral molecules and by uridine stereoisomers. *The Journal of chemical physics* **2006,** *124* (18), 184305.
26. McConnell, O.; Bach, A.; Balibar, C.; Byrne, N.; Cai, Y.; Carter, G.; Chlenov, M.; Di, L.; Fan, K.; Goljer, I., et al., Enantiomeric Separation and Determination of Absolute Stereochemistry of Asymmetric Molecules in Drug Discovery: Building Chiral Technology Toolboxes. *Chirality* **2007,** *19*, 658-82.
27. Noyori, R., Asymmetric Catalysis: Science and Opportunities (Nobel Lecture). *Angew Chem Int Ed Engl* **2002,** *41* (12), 2008-22.
28. Tamura, K., Origin of Amino Acid Homochirality: Relationship with the RNA World and Origin of tRNA Aminoacylation. *Biosystems* **2008,** *92*, 91-98.
29. Nakanishi, K.; Berova, N.; Woody, R. W., *Circular Dichroism: Principles and Applications*. 2nd ed.; VCH: New York, 2000.
30. Tinoco, I., Jr.; Mickols, W.; Maestre, M. F.; Bustamante, C., Absorption, Scattering, and Imaging of Biomolecular Structures with Polarized Light. *Annu Rev Biophys Biophys Chem* **1987,** *16*, 319-49.

31. Tinoco, I., Two-Photon Circular Dichroism. *Journal of Chemical Physics* **1975,** *62*, 1006-1009.

32. Power, E. A., Two-Photon Circular Dichroism. *Journal of Chemical Physics* **1975,** *63*, 1348-1350.

33. Gunde, K. E.; Richardson, F. S., Fluorescence-Detected Two-Photon Circular Dichroism of $Gd^{3+}$ in Trigonal $Na_3[Gd(C_4H_4O_5)_3] \cdot 2NaClO_4 \cdot 6H_2O$. *Chemical Physics* **1995,** *194*, 195-206.

34. Jansik, B.; Rizzo, A.; Agren, H., Response Theory Calculations of Two-Photon Circular Dichroism. *Chemical Physics Letters* **2005,** *414*, 461-467.

35. De Boni, L.; Toro, C.; Hernandez, F. E., Synchronized Double L-Scan Technique for the Simultaneous Measurement of Polarization-Dependent Two-Photon Absorption in Chiral Molecules. *Optics Letters* **2008,** *33*, 2958-2960.

36. Toro, C.; De Boni, L.; Lin, N.; Santoro, F.; Rizzo, A.; Hernandez, F. E., Two-Photon Absorption Circular Dichroism: A New Twist in Nonlinear Spectroscopy. *Chemistry - A European Journal* **2010,** *16*, 3504-9.

37. Spencer, N. D.; Moore, J. H., *Encyclopedia of chemical physics and physical chemistry: Methods*. Taylor & Francis: 2001; Vol. 2.

38. Lakowicz, J. R., *Principles of fluorescence spectroscopy*. 3rd ed.; Springer Science & Business Media: 2007.

39. Goeppert-Mayer, M., Uber Elementarakte mit zwei Quantensprungen. *Annalen der Physik* **1931,** *8*, 273-294.

40. Maiman, T., Stimulated emission of radiation in ruby. *Nature* **1960,** *187*, 493-494.

41. Sovers, O.; Yoshioka, T., Fluorescence of trivalent-europium-doped yttrium oxysulfide.

*Journal of Chemical Physics* **1968,** *49*, 4945-4954.

42. Boyd, R. W., *Nonlinear optics*. Academic press: 2003.
43. Sheik-Bahae, M.; Said, A. A.; Wei, T. H.; Hagan, D. J.; Van Stryland, E. W., Sensitive measurement of optical nonlinearities using a single beam. *IEEE Journal of Quantum Electronics* **1990,** *26*, 760-769.
44. Peiponen, K.; Saarinen, J., Generalized Kramers–Kronig relations in nonlinear optical-and THz-spectroscopy. *Reports on Progress in Physics* **2009,** *72* (5), 056401.
45. Sheik-Bahae, M.; Hasselbeck, M. P., Third-order optical nonlinearities. *Handbook of Optics* **2000,** *4*, 16.1-16.36.
46. Bonin, K. D.; McIlrath, T. J., Two-Photon Electric-Dipole Selection Rules. *Journal of the Optical Society of America B* **1984,** *1*, 52-55.
47. McClain, W.; Harris, R.; Lim, E., Excited States. *Lim, EC, Ed* **1977**, 1-56.
48. Fernández, I.; Cossío, F. P., Applied computational chemistry. *Chemical Society Reviews* **2014,** *43* (14), 4906-4908.
49. Runge, E.; Gross, E. K. U., Density-Functional Theory for Time-Dependent Systems. *Physical Review Letters* **1984,** *52*, 997-1000.
50. Dierksen, M.; Grimme, S., A Theoretical Study of the Chiroptical Properties of Molecules with Isotopically Engendered Chirality. *The Journal of chemical physics* **2006,** *124*, 174301.
51. Masunov, A.; Tretiak, S., Prediction of two-photon absorption properties for organic chromophores using time-dependent density-functional theory. *The Journal of Physical Chemistry B* **2004,** *108* (3), 899-907.
52. Guillaume, M.; Ruud, K.; Rizzo, A.; Monti, S.; Lin, Z.; Xu, X., Computational Study of the One- and Two-Photon Absorption and Circular Dichroism of (L)-Tryptophan. *journal of*

*physical chemistry. B* **2010,** *114*, 6500-12.

53. McClain, W. M., 2-PHOTON MOLECULAR SPECTROSCOPY. *Accounts of Chemical Research* **1974,** *7*, 129-135.
54. Macák, P., *Solvent and vibrational effects on nonlinear optical properties*. Ph. D. thesis, Royal Institute of Technology: Stockholm: 2002.
55. Cammi, R.; Cappelli, C.; Mennucci, B.; Tomasi, J., Properties of Excited States of Molecules in Solution Described with Continuum Solvation Models. In *Practical Aspects of Computational Chemistry*, Springer: 2010; pp 19-36.
56. Onsager, L., Electric moments of molecules in liquids. *Journal of the American Chemical Society* **1936,** *58* (8), 1486-1493.
57. Tapia, O.; Goscinski, O., Self-consistent reaction field theory of solvent effects. *Molecular Physics* **1975,** *29* (6), 1653-1661.
58. Miertuš, S.; Scrocco, E.; Tomasi, J., Electrostatic Interaction of a Solute with a Continuum. A Direct Utilizaion of AB Initio Molecular Potentials for the Prevision of Solvent Effects. *Chemical Physics* **1981,** *55* (1), 117-129.
59. Tomasi, J.; Mennucci, B.; Cammi, R., Quantum Mechanical Continuum Solvation Models. *Chemical Reviews* **2005,** *105*, 2999-3093.
60. de O. Mendes, C. L.; da Silva, C. O.; da Silva, E. C., Parametrizing PCM to obtain solvation free energies from group contributions. 1. *The Journal of Physical Chemistry A* **2006,** *110* (11), 4034-4041.
61. Rumi, M.; Perry, J. W., Two-photon absorption: an overview of measurements and principles. *Advances in Optics and Photonics* **2010,** *2* (4), 451-518.
62. Anderson, R. J.; Holtom, G. R.; McClain, W. M., Absolute two-photon absorptivity of trans-

stilbene near the two-photon absorption maximum via three wave mixing. *The Journal of Chemical Physics* **1977,** *66* (8), 3832-3833.

63. Anderson Richard, J.; Holtom Gary, R.; McClain Wm, M., Two-photon absorptivities of the all transdiphenylpolyenes from stilbene to diphenyloctatetraenl via t hree wave m ixing. *J Chem Phys* **1979,** *70* (9), 4310-4315.
64. Orczyk, M.; Samoc, M.; Swiatkiewicz, J.; Manickam, N.; Tomoaia-Cotisel, M.; Prasad, P., Optical heterodyning of the phase-tuned femtosecond optical Kerr gate signal for the determination of complex third-order susceptibilities. *Applied physics letters* **1992,** *60* (23), 2837-2839.
65. Pfeffer, N.; Charra, F.; Nunzi, J. M., Phase and frequency resolution of picosecond optical Kerr nonlinearities. *Optics letters* **1991,** *16* (24), 1987-1989.
66. Zhao, M.; Cui, Y.; Samoc, M.; Prasad, P. N.; Unroe, M. R.; Reinhardt, B. A., Influence of two-photon absorption on third-order nonlinear optical processes as studied by degenerate four-wave mixing: The study of soluble didecyloxy substituted polyphenyls. *The Journal of chemical physics* **1991,** *95* (6), 3991-4001.
67. Sutherland, R.; Rea, E.; Natarajan, L.; Pottenger, T.; Fleitz, P., Two-photon absorption and second hyperpolarizability measurements in diphenylbutadiene by degenerate four-wave mixing. *The Journal of chemical physics* **1993,** *98* (4), 2593-2603.
68. Xu, C.; Webb, W. W., Measurement of two-photon excitation cross sections of molecular fluorophores with data from 690 to 1050 nm. *Journal of the Optical Society of America B-Optical Physics* **1996,** *13*, 481-491.
69. Birge, R. R., One-photon and two-photon excitation spectroscopy. *Ultrasensitive laser spectroscopy* **1983**, 109-174.

70. Eliel, E. L.; Wilen, S. H., *Stereochemistry of organic compounds*. John Wiley & Sons: 2008.

71. Hecht, E., *Optics*. Pearson Education, Inc.: San Francisco, 2002.

72. Polavarapu, P. L., Kramers-Kronig transformation for optical rotatory dispersion studies. *Journal of Physical Chemistry A* **2005,** *109*, 7013-7023.

73. Miles, A. J.; Wallace, B. A., Synchrotron Radiation Circular Dichroism Spectroscopy of Proteins and Applications in Structural and Functional Genomics. *Chemical Society reviews* **2006,** *35*, 39-51.

74. Mason, W. R. A., *Practical Guide to Magnetic Circular Dichroism Spectroscopy*. John Wiley & Sons: New Jersey, 2007.

75. Devlin, F. J.; Stephens, P. J.; Scafato, P.; Superchi, S.; Rosini, C., Determination of Absolute Configuration Using Vibrational Circular Dichroism Spectroscopy: The Chiral Sulfoxide 1-thiochromanone S-Oxide. *Chirality* **2002,** *14*, 400-6.

76. Barron, L. D., *Molecular Light Scattering and Optical Activity*. Cambridge University Press: Cambridge, 2004.

77. Jansik, B.; Rizzo, A.; Agren, H., Ab Initio Study of the Two-Photon Circular Dichroism in Chiral Natural Amino Acids. *Journal of Physical Chemistry B* **2007,** *111*, 446-460.

78. Thirunamachandran, T.; Craig, D. P., *Molecular Quantum Electrodynamics, An Introduction to Radiation Molecule Interaction*. Dover Publ., Inc., Mineaol, NY: 1998.

79. Condon, E. U.; Altar, W.; Eyring, H., Theories of Optical Rotatory Power. *Reviews of Modern Physics* **1937,** *9* (4), 432-457.

80. Markowicz, P. P.; Samoc, M.; Cerne, J.; Prasad, P. N.; Pucci, A.; Ruggeri, G., Modified Z-scan Techniques for Investigations of Nonlinear Chiroptical Effects. *Optics Express* **2004,** *12*, 5209-5214.

81. Li, R.; Sullivan, R.; Al-Basheer, W.; Pagni, R. M.; Compton, R. N., Linear and nonlinear circular dichroism of R-(+)-3-methylcyclopentanone. *Journal of Chemical Physics* **2006,** *125*.
82. Bornschlegl, A.; Logé, C.; Boesl, U., Investigation of CD effects in the multi photon ionisation of R-(+)-3-methylcyclopentanone. *Chemical Physics Letters* **2007,** *447*, 187-191.
83. Hernández, F. E.; Rizzo, A., Two-Photon Polarization Dependent Spectroscopy in Chirality: a Novel Experimental-Theoretical Approach to Study Optically Active Systems. *Molecules (Basel, Switzerland)* **2011,** *16*, 3315-37.
84. Runge, E.; Gross, E. K. U., Density-Functional Theory for Time-Dependent Systems. *Physical Review Letters* **1984,** *52* (12), 997-1000.
85. Becke, A. D., Density-Functional Exchange-Energy Approximation with Correct Asymptotic Behavior. *Physical Review A* **1988,** *38*, 3098-3100.
86. Becke, A. D., Density-Functional Thermochemistry. III. The Role of Exact Exchange. *Journal of Chemical Physics* **1993,** *98*, 5648-5652.
87. Lee, C.; Yang, W.; Parr, R. G., Development of the Colle-Salvetti Correlation-Energy Formula into a Functional of the Electron Density. *Physical Review B: Condensed Matter* **1988,** *37*, 785-789.
88. Krishnan, R.; Binkley, J. S.; Seeger, R.; Pople, J. A., Self-Consistent Molecular Orbital Methods. XX. A Basis Set for Correlated Wave Functions. *The Journal of Chemical Physics* **1980,** *72* (1), 650-654.
89. Clark, T.; Chandrasekhar, J.; Spitznagel, G. W.; Schleyer, P. V. R., Efficient Diffuse Function-Augmented Basis Sets for Anion Calculations. III. The 3-21+G Basis Set for First-Row Elements, Li–F. *Journal of Computational Chemistry* **1983,** *4* (3), 294-301.
90. Kendall, R. A.; Dunning, T. H.; Harrison, R. J., Electron affinities of the first-row atoms

revisited. Systematic basis sets and wave functions. *The Journal of Chemical Physics* **1992,** *96* (9), 6796-6806.

91. DALTON *A Molecular Electronic Structure Program, Release Dalton 2.0, see http://www.kjemi.uio.no/software/dalton/dalton.html*, 2005.
92. Diaz, C.; Lin, N.; Toro, C.; Passier, R.; Rizzo, A.; Hernández, F. E., The Effect of the π-Electron Delocalization Curvature on the Two-Photon Circular Dichroism of Molecules with Axial Chirality. *The Journal of Physical Chemistry Letters* **2012,** *3*, 1808-1813.
93. Rassolov, V. A.; Pople, J. A.; Ratner, M. A.; Windus, T. L., 6-31G* basis set for atoms K through Zn. *The Journal of chemical physics* **1998,** *109* (4), 1223-1229.
94. Frisch, M. J.; Trucks, G. W.; Schlegel, H. B.; Scuseria, G. E.; Robb, M. A.; Cheeseman, J. R.; Scalmani, G.; Barone, V.; Mennucci, B.; Petersson, G. A., et al., Gaussian 09, Revision A.1. Gaussian, Inc.: Wallingford CT, 2009.
95. Yanai, T.; Tew, D. P.; Handy, N. C., A new Hybrid Exchange-Correlation Functional using the Coulomb-Attenuating Method (CAM-B3LYP). *Chemical Physics Letters* **2004,** *393*, 51-57.
96. Peach, M. J. G.; Helgaker, T.; Sałek, P.; Keal, T. W.; Lutnaes, O. B.; Tozer, D. J.; Handy, N. C., Assessment of a Coulomb-attenuated exchange-correlation energy functional. *Physical chemistry chemical physics* **2006,** *8*, 558-62.
97. Diaz, C.; Frazer, A.; Morales, A.; Belfield, K. D.; Ray, S.; Hernández, F. E., Structural identification of a novel axially chiral binaphthyl fluorene based salen ligand in solution using electronic circular dichroism: a theoretical-experimental analysis. *The journal of physical chemistry A* **2012,** *116*, 2453-65.
98. Diaz, C.; Vesga, Y.; Echevarria, L.; Stará, I. G.; Starỳ, I.; Anger, E.; Shen, C.; Moussa, M. E.

S.; Vanthuyne, N.; Crassous, J., et al., Two-photon absorption and two-photon circular dichroism of hexahelicene derivatives: a study of the effect of the nature of intramolecular charge transfer. *RSC Advances* **2015,** *5* (23), 17429-17437.

99. DALTON *A Molecular Electronic Sstructure Program, Release Dalton 2011, see http://daltonprogram.org/*, 2011.

# CHAPTER 2: STUDY OF THE EFFECT OF THE EXCITATION SOURCE PULSE-WIDTH ON THE TWO-PHOTON ABSORPTION AND TWO-PHOTON CIRCULAR DICHROISM SPECTRA OF BIARYL DERIVATIVES



In this first chapter we present the expanded theoretical calculations and the experimental measurements of the two-photon absorption (TPA) and two-photon circular dichroism (TPCD) spectra of a series of optically active biaryl derivatives (R-BINOL, R-VANOL, and R-VAPOL) using femtosecond pulses. The comparative analysis of the experimental TPCD spectra obtained with our tunable amplified femtosecond system with those previously measured in our group on the same series of compounds in the picosecond regime, revealed a decrease in the amplitude of the signal and an improvement in matching with the theory in the former. Our findings are explained based on the negligible contribution of excited state absorption using femtosecond pulses compared to the picosecond regime, which could affect both the strength and the shape of the TPA and TPCD spectra.

TPA and TPCD spectra were performed using the double L-scan technique over a broad spectral range (450–750 nm) using 90 fs pulses at 50 Hz repetition rate produced by an amplified femtosecond system. The theoretical calculations were obtained using modern analytical response theory within the Time-Dependent Density Functional Theory (TD-DFT) approach using CAM-B3LYP and 6-311++G(d,p) basis sets.

## 2.1 Introduction

The understanding of chiral systems has been the focus of researchers in the last couple decades due to the key role of such molecules in optical and biological processes. Chiral molecules have found multiple applications in asymmetric catalysis[1], the pharmaceutical industry[2], nanotechnology[3], and photonics[4], among others.

BINOL is a chiral auxiliary in asymmetric catalysis that has found its application in the synthesis of highly enantiomerically pure compounds without further separation or purification[5]. Additionally, it has served as a starting point for the development of new optically active biaryl derivatives with a variety of applications in industry and research. VANOL and VAPOL are two of the main BINOL derivatives. They exhibit high degree of chiral selectivity due to the presence of a chiral axis at the center of their binaphtyl core as well as a $C_2$-symmetry.

In 2008, Hernandez and co-workers demonstrated TPCD experimentally by the development of the double L-scan technique[6]. In order to pursue a deeper knowledge of TPCD and its structure-property relationship, Hernandez *et al*. have been working on the theoretical-experimental analysis of the TPCD response for several systems[7-12]. However, in order to have a better understanding of this nonlinear optical property, there is a need to learn more about the effect of the excitation pulse-width on the TPCD signal.

In this chapter we show the theoretical-experimental comparative analysis of TPA and TPCD of R-BINOL, R-VANOL, and R-VAPOL when excited with femtosecond and picosecond pulses (previously reported in reference 13) [13]. Our discussion focuses on the reduced TPA and TPCD signal and the improvement in the theoretical-experimental matching using femtosecond pulses due to the negligible contribution of excited state absorption (ESA) to TPA and TPCD when using shorter (femtosecond) excitation pulses.

## 2.2 Experimental Section

(R)-(+)-1, 1'-Bi(2-naphthol) (R-BINOL) (99%), (R)-3,3′-Diphenyl-2,2′-bi-1-naphthalol, (R)-3,3′-Diphenyl-2,2′-bi-1-naphthol (R-VANOL) (97%), and (R)-2,2′-Diphenyl-3,3′-(4-biphenanthrol) (R-VAPOL) (97%) and THF (spectroscopic grade) were purchased from Sigma-Aldrich and used without further purification.

TPA and TPCD measurements were performed in THF solutions of R-BINOL, R-VANOL, and R-VAPOL at concentrations of 0.2 M, 0.12 M, and 0.1 M, respectively, using the double L-scan technique[6]. Two-photon excitation was generated with a computer-controlled femtosecond optical parametric amplifier (OPerA Solo) pumped by an amplified laser system from COHERENT. The whole system is capable of generating 90 fs (FWHM) pulses over a wavelength range covering from 240 nm to 2.6 μm, and with pulse energy of up to 350 μJ. Experiments were performed at a repetition rate of 50 Hz to avoid any contribution from cumulative effects. The pulse width was measured using a single-shot autocorrelator from COHERENT Inc. and a frequency-resolved optical gaiting (FROG) from Swamp Optics LLC.

## 2.3 Theoretical Methods

Section 1.2 and 1.5 of the introduction show all the theoretical background involved in this thesis document. In this part, we are only presenting the computational details relevant to this chapter specifically.

The molecular structures of R-BINOL, R-VANOL, and R-VAPOL were optimized using Density Functional Theory (DFT) [14], with the Becke's three-parameter exchange, Lee, Yang and Parr correlation (B3LYP) hybrid functional[15-17] and the 6-311++G(d,p) basis set[18, 19], employing Gaussian 09[20].

TPA probabilities ($\bar{\delta}_{0f}^{TPA}(\omega_{0f})$) and TPCD rotatory strength ($R_{0f}^{TPCD}(\omega_{0f})$) for all the biaryl derivatives were calculated using Time-Dependent DFT (TD-DFT)[14] in DALTON 2013[21], employing the Coulomb attenuating method-B3LYP (CAM-B3LYP) hybrid functional[22] and in combination with 6-311++G(d,p) basis set[18, 19]. CAM-B3LYP was selected because it is well-known to be a more reliable functional for molecules with Intramolecular Charge Transfer (ICT) - the results for the B3LYP functional are presented in Appendix E. For TPA and TPCD, the total number of electronic excited states selected for the biaryl derivatives (48) were decided based on the experimental spectral region (460-700 nm) required to be predicted. Solvents effects were not taken into consideration in the nonlinear calculations due to high computational costs. The convoluted theoretical TPA and TPCD spectra were obtained by Lorentzian broadening from $\bar{\delta}_{0f}^{TPA}(\omega_{0f})$ and $R_{0f}^{TPCD}(\omega_{0f})$ of the calculated electronic transitions using equations (1) and (2). The TPA and TPCD spectra for R-BINOL, R-VANOL, and R-VAPOL were obtained through equations 1-19 and 1-38 (see Chapter 1) employing a linewidth (Γ) of 0.2 eV, 0.1 eV, and 0.15 eV, respectively.

## 2.4 Results and Discussion

After having optimized the structures of all the biaryl derivatives, we computed their TPA and TPCD spectra within an extended two-photon excitation wavelength range that covered the range from 440 nm to 730 nm. In order to achieve a better theoretical-experimental overlap of bands, the TD-DFT calculations were extended to 48 excited states. i.e. approximately two fold more excited states than in reference 13. This effort resulted in large and computational intensive calculations where a tight control of the thresholds of the calculations became imperative[12]. Although 48 excited states in a TD-DFT calculation seem to be too many, mainly due to the

potential existence of Rydberg and ionic states, we have shown multiple times[9, 10, 13, 23, 24] that the prediction of the spectral features in relatively large molecules is acceptable. The convoluted spectra were calculated using CAM-B3LYP/6-311++G(d,p) in Dalton 2013 and with $\Gamma$ = 0.2, 0.1, and 0.15 eV (FWHM) for R-BINOL, R-VANOL, and R-VAPOL, respectively.

In Figure 2-1 we present the theoretical (isolated molecules) and experimental (in THF solution) TPA spectra of R-BINOL, R-VANOL, and R-VAPOL, employing linearly polarized light. To obtain the best theoretical-experimental spectral overlap, the theoretical spectra were shifted between 0.25 and 0.5 eV in the positive direction, i.e. +55 nm, +90 nm, and +90 nm for R-BINOL, R-VANOL, and R-VAPOL, respectively (this is a common practice in theoretical-experimental works) [7, 9, 10 23]. Interesting to highlight is the remarkable matching obtained for all three biaryl derivatives. In the case of R-BINOL the band located at 580 nm was successfully reproduced by the theoretical spectrum. Similarly for R-VANOL, the calculations yield important transitions ($4^{th}$, $34^{th}$ and $35^{th}$, among others) that replicate the two main peaks observed experimentally at 490 and 580 nm. For R-VAPOL, the distribution of two-photon transitions seems more complex, yet it still reproduces quite well the TPA spectrum measured with femtosecond pulses between 440-730 nm. The experimental spectral features observed at approximately 520, 580, 600, and 680 nm and the increase in intensity towards the blue-side of the interval are in agreement with electronic states that are mainly active in TPA.

With respect to the observe discrepancy between the theoretical and experimental TPA cross-sections in figure 2-1, it is hard to explain the disparity considering that the experiments were carried out in the femtosecond regime where the excited state absorption is almost negligible.[25, 26] We believe that the treatment of nonlinear absorption employed in sizeable molecules for which multiple excitation is of particular importance, with an inherently single-excitation based model

such as TD-DFT, limits the reach of our calculation to predict, accurately, TPA cross-sections[27, 28]. Nevertheless, the shape and position of the experimental spectra is well reproduced, and the TPA cross-sections follow the same trend predicted in the picosecond regime[13], i.e. $\delta^{TPA}_{R-VAPOL}(\lambda) > \delta^{TPA}_{R-VANOL}(\lambda) > \delta^{TPA}_{R-BINOL}(\lambda)$.

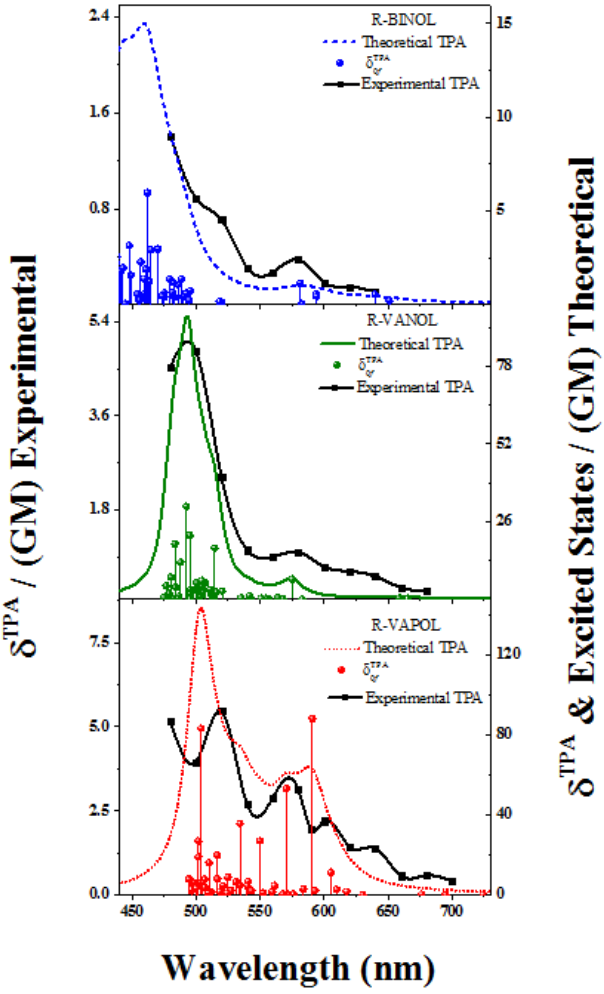


**Figure 2-1.** Experimental (black scattered squares) and theoretical TPA spectra of R-BINOL (top), R-VANOL (middle), and R-VAPOL (bottom) in vacuo using Dalton 2013. TPA was computed for the first 48 electronic excited states (colored scattered symbols) for all the molecules. The Lorentzian convolutions were obtained using a linewidth $\Gamma$ = 0.2, 0.1, and 0.15 eV for R-BINOL (top), R-VANOL (middle), and R-VAPOL (bottom), respectively. The theoretical spectra were calculated with CAM-B3LYP/6-311++G(d,p). The theoretical shifts are: R-BINOL (+55 nm), R-VANOL (+90 nm), and R-VAPOL (+90 nm). All the experimental spectra were taken in THF solutions.

Next, in Figure 2-2 we display the experimental TPCD spectra of R-BINOL, R-VANOL, and R-VAPOL, and their corresponding theoretical counterpart obtained using CAM-B3LYP/6-311++G(d,p). One can notice that the theoretical TPCD spectra reproduces remarkably well the shape, sign and relative intensities of the two positive bands in R-BINOL (500 and 580 nm), one main positive peaks in R-VANOL at 520 nm, and two negative bands in R-VAPOL (550 and 590 nm). Another interesting observation is that the TPCD signal in this family of compounds follow the same trend observed in the picosecond regime[13], and already reproduced in TPA where the nonlinear absorption is the strongest for R-VAPOL and the weakest for R-BINOL.

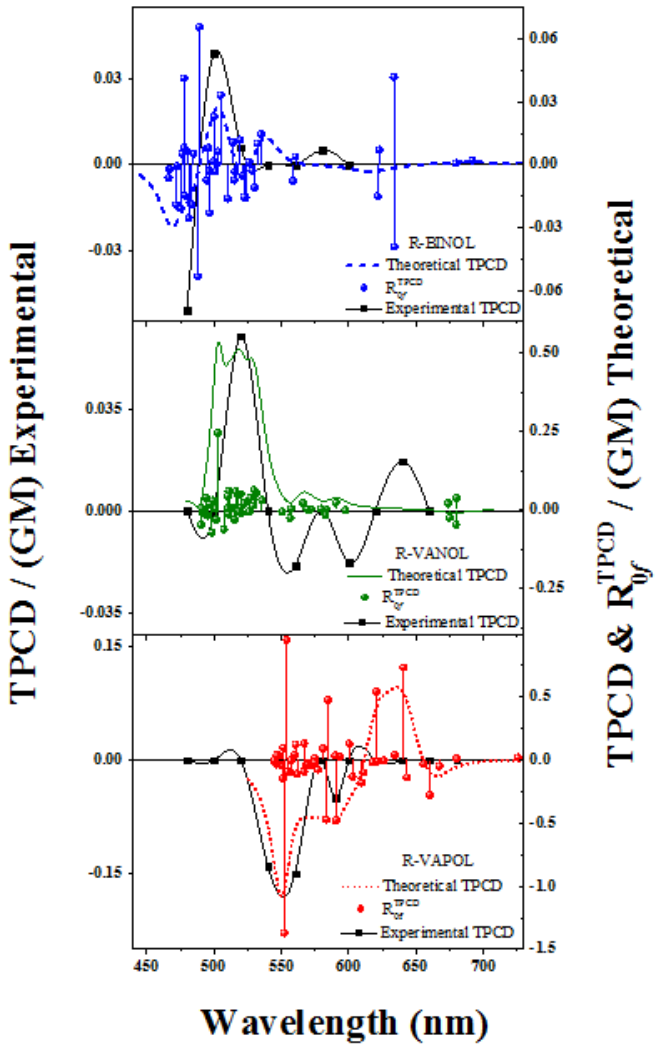


**Figure 2-2.** Experimental (black scattered squares) and theoretical TPCD spectra of R-BINOL (top), R-VANOL (middle), and R-VAPOL (bottom) in vacuo using Dalton 2013. TPCD was computed for the first 48 electronic excited states (colored scattered symbols) for all the molecules. The Lorentzian convolutions were obtained using a linewidth $\Gamma$ = 0.2, 0.1, and 0.15 eV for R-BINOL (top), R-VANOL (middle), and R-VAPOL (bottom), respectively. The theoretical spectra were calculated with CAM-B3LYP/6-311++G(d,p). The theoretical shifts are: R-BINOL (+95 nm), R-VAPOL (+105 nm), and R-VAPOL (+140 nm). All the experimental spectra were taken in THF solutions.

Finally, the most interesting result of the comparative nonlinear optical characterization presented in this chapter is the observed difference in magnitude and shape between the experimental TPA and TPCD spectra of the three biaryl derivatives, using femtosecond and

picosecond pulses[13]. In order to perform a fair comparison between the two regimes, we calculated the integrated area under the TPA and TPCD spectra within the specific experimental wavelength range measured for each molecule (see Table 2-1). From Table 2-1, it is worth highlighting two main aspects i) $\delta_R^{TPA}$ and $\delta^{TPCD}$ for all three biaryl derivatives were at least two orders of magnitude lower when performing the measurements using femtosecond, and ii) the TPCD cross-section ratio $\left(\delta_{ps}^{TPCD}/\delta_{fs}^{TPCD}\right)$ is more than three times larger than TPA cross-section ratio between the two temporal regimes $\left(\delta_{ps}^{TPA}/\delta_{fs}^{TPA}\right)$. This interesting phenomenon has already been explained for TPA and has been attributed to two primary effects: 1) exciton coupling for dimers undergoing electronically allowed transitions, and 2) the pulse-width of the excitation source (picosecond or nanosecond) which can lead to significant excited-state absorption.[7, 29-31] However, this is the first time this type of effect has been observed in TPCD. In this respect, F. Hache and co-workers have reported experimental measurements of excited state circular dichroism in BINOL, Ruthenium(II) Tris(phenanthroline), and carboxy-mioglobin.[32-34] In 2008, they measured the excited state CD signal of BINOL in the picosecond regime using time-resolved circular dichroism (TRCD) [32, 34]. After the photoexcitation of BINOL at two different wavelengths (237 nm and 245 nm), they probed the $^1B_b$ band at ca. 220 nm where the absorption of π-electrons along the naphthalene axis produced a strong CD structure due to Davydov excitonic coupling.[24] The results showed that the dominant process responsible for the CD signal were ground state absorption at 237, and excited state absorption at 245 nm.[33, 34] These results are in total agreement with our experimental observations and indicate that the TPCD signal, previously measured with picosecond pulses[13], was significantly enhanced by the contribution of important excited state absorption present in the picosecond regime, and modified by the corresponding circular dichroism of the excited state present in these chiral molecules (see figure 2-3).

**Table 2-1**. Comparative analysis of the integrated TPA and TPCD spectra of R-BINOL, R-VANOL, and R-VAPOL measured within the specific experimental wavelength range ($\lambda\Delta$) in the femtosecond (fs) and picosecond (ps) regime, and their ratio (ps/fs).

| Compound | λ (nm) | $\delta_i^{TPA}$ | | | $\delta_i^{TPCD}$ | | |
|---|---|---|---|---|---|---|---|
| | | **fs** | **ps$^{ref}$** | **(ps/fs)** | **fs** | **ps$^{ref}$** | **(ps/fs)** |
| R-BINOL | 480-600 | 67.6 | 6300 | 93 | 1.5 | 455 | 303 |
| R-VANOL | 480-560 | 201.1 | 19550 | 97 | 1.39 | 608 | 437 |
| R-VAPOL | 480-660 | 513.5 | 51350 | 100 | 6.3 | 2090 | 332 |

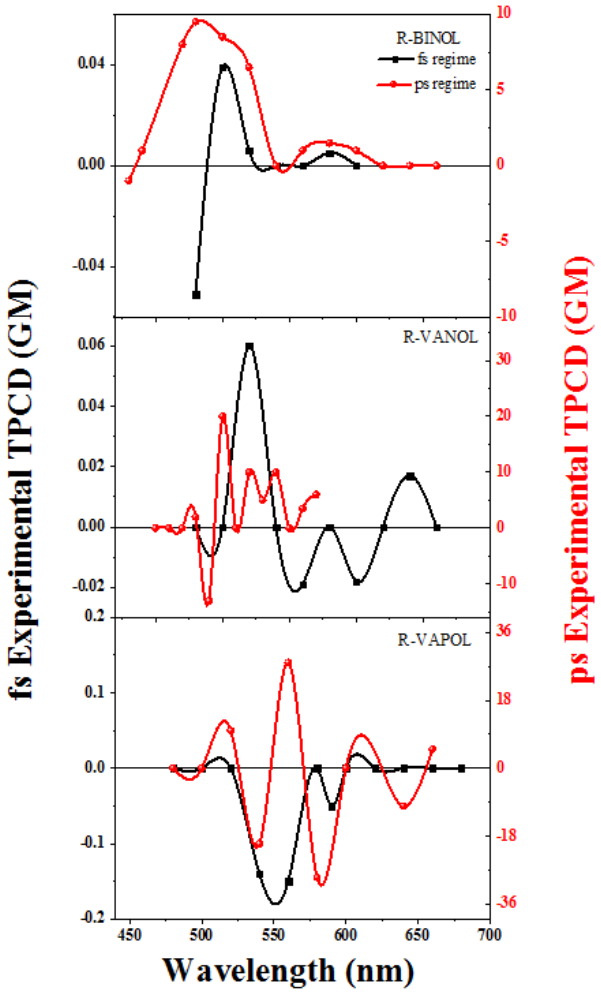


**Figure 2-3**. Experimental TPCD spectra of R-BINOL (top), R-VANOL (middle), and R-VAPOL (bottom) measured in femtosecond (black scattered squares) and picosecond[13] (red scattered circles) regimes.

## 2.5 Conclusion

In summary, the comparative analysis of the measured and calculated TPA and TPCD spectra on a series of biaryl derivatives compounds in the femtosecond and picosecond regime led us to understand discrepancies between TPA and TPCD spectra measured in two different pulse regimes, and help us explain the differences in amplitude obtained in TPCD signals using femtosecond and picosecond pulses based on the presence of significant excited state absorption in the latter as a consequence of excited state circular dichroism. Though, important differences where established between the two excitation regimens, the TPCD signal followed the same trend in the femtosecond and the picosecond regime[13] i.e. $\delta_{R-BINOL}^{TPCD} < \delta_{R-VANOL}^{TPCD} < \delta_{R-VAPOL}^{TPCD}$. This effect was already elucidated in reference 13 and correlated with the curvature in the π–electron delocalization existent in vaulted molecular structures and the contributions of the different transition moments to the overall TPA rotatory strength.

## 2.6 References


1. Noyori, R., Asymmetric Catalysis: Science and Opportunities (Nobel Lecture). *Angew Chem Int Ed Engl* **2002,** *41* (12), 2008-22.
2. McConnell, O.; Bach, A.; Balibar, C.; Byrne, N.; Cai, Y.; Carter, G.; Chlenov, M.; Di, L.; Fan, K.; Goljer, I., et al., Enantiomeric Separation and Determination of Absolute Stereochemistry of Asymmetric Molecules in Drug Discovery: Building Chiral Technology Toolboxes. *Chirality* **2007,** *19*, 658-82.
3. Zhang, J.; Albelda, M. T.; Liu, Y.; Canary, J. W., Chiral Nanotechnology. *Chirality* **2005,** *17*, 404-20.
4. Haupert, L. M.; Simpson, G. J., Chirality in Nonlinear Optics. *Annu Rev Phys Chem* **2009,** *60*, 345-65.
5. Brunel, J. M., Update 1 of: BINOL: a versatile chiral reagent. *Chemical reviews* **2007,** *107* (9), PR1-PR45.
6. De Boni, L.; Toro, C.; Hernandez, F. E., Synchronized Double L-Scan Technique for the Simultaneous Measurement of Polarization-Dependent Two-Photon Absorption in Chiral Molecules. *Optics Letters* **2008,** *33*, 2958-2960.
7. Toro, C.; De Boni, L.; Lin, N.; Santoro, F.; Rizzo, A.; Hernandez, F. E., Two-Photon Absorption Circular Dichroism: A New Twist in Nonlinear Spectroscopy. *Chemistry - A European Journal* **2010,** *16*, 3504-9.
8. Vesga, Y.; Diaz, C.; Higgs, M.; Hernandez, F. E., Two-Photon Circular Dichroism of Molecular Structures Simulating L-tryptophan Residues in Proteins with Secondary Structures. *Chemical Physics Letters* **2014,** *601* (0), 6-12.
9. Díaz, C.; Echevarria, L.; Rizzo, A.; Hernández, F. E., Two-Photon Circular Dichroism of an Axially Dissymmetric Diphosphine Ligand with Strong Intramolecular Charge Transfer. *The*

*Journal of Physical Chemistry A* **2014,** *118* (5), 940-946.

10. Díaz, C.; Echevarria, L.; Hernández, F. E., Conformational Study of an Axially Chiral Salen Ligand in Solution using Two-Photon Circular Dichroism and the Fragment-Recombination Approach. *The Journal of Physical Chemistry A* **2013,** *117*, 8416–8426.
11. Diaz, C.; Echevarria, L.; Hernández, F. E., Overcoming the Existent Computational Challenges in the Ab Initio Calculations of the Two-Photon Circular Dichroism Spectra of Large Molecules using a Fragment-Recombination Approach. *Chemical Physics Letters* **2013,** *568-569*, 176-183.
12. Lin, N.; Santoro, F.; Zhao, X.; Toro, C.; De Boni, L.; Hernández, F. E.; Rizzo, A., Computational Challenges in Simulating and Analyzing Experimental Linear and Nonlinear Circular Dichroism Spectra. R-(+)-1,1'-bis(2-naphthol) as a Prototype Case. *journal of physical chemistry. B* **2011,** *115*, 811-24.
13. Diaz, C.; Lin, N.; Toro, C.; Passier, R.; Rizzo, A.; Hernández, F. E., The Effect of the π-Electron Delocalization Curvature on the Two-Photon Circular Dichroism of Molecules with Axial Chirality. *The Journal of Physical Chemistry Letters* **2012,** *3*, 1808-1813.
14. Runge, E.; Gross, E. K. U., Density-Functional Theory for Time-Dependent Systems. *Physical Review Letters* **1984,** *52*, 997-1000.
15. Becke, A. D., Density-Functional Exchange-Energy Approximation with Correct Asymptotic Behavior. *Physical Review A* **1988,** *38*, 3098-3100.
16. Becke, A. D., Density-Functional Thermochemistry. III. The Role of Exact Exchange. *Journal of Chemical Physics* **1993,** *98*, 5648-5652.
17. Lee, C.; Yang, W.; Parr, R. G., Development of the Colle-Salvetti Correlation-Energy Formula into a Functional of the Electron Density. *Physical Review B: Condensed Matter* **1988,** *37*,

785-789.

18. Krishnan, R.; Binkley, J. S.; Seeger, R.; Pople, J. A., Self-Consistent Molecular Orbital Methods. XX. A Basis Set for Correlated Wave Functions. *The Journal of Chemical Physics* **1980,** *72* (1), 650-654.
19. Clark, T.; Chandrasekhar, J.; Spitznagel, G. W.; Schleyer, P. V. R., Efficient Diffuse Function-Augmented Basis Sets for Anion Calculations. III. The 3-21+G Basis Set for First-Row Elements, Li–F. *Journal of Computational Chemistry* **1983,** *4* (3), 294-301.
20. Frisch, M. J.; Trucks, G. W.; Schlegel, H. B.; Scuseria, G. E.; Robb, M. A.; Cheeseman, J. R.; Scalmani, G.; Barone, V.; Mennucci, B.; Petersson, G. A., et al., Gaussian 09, Revision A.1. Gaussian, Inc.: Wallingford CT, 2009.
21. Aidas, K.; Angeli, C.; Bak, K. L.; Bakken, V.; Bast, R.; Boman, L.; Christiansen, O.; Cimiraglia, R.; Coriani, S.; Dahle, P., et al., The Dalton Quantum Chemistry Program System. *Wiley Interdisciplinary Reviews: Computational Molecular Science* **2014,** *4* (3), 269-284.
22. Yanai, T.; Tew, D. P.; Handy, N. C., A new Hybrid Exchange-Correlation Functional using the Coulomb-Attenuating Method (CAM-B3LYP). *Chemical Physics Letters* **2004,** *393*, 51-57.
23. Diaz, C.; Vesga, Y.; Echevarria, L.; Stará, I. G.; Starỳ, I.; Anger, E.; Shen, C.; Moussa, M. E. S.; Vanthuyne, N.; Crassous, J., et al., Two-photon absorption and two-photon circular dichroism of hexahelicene derivatives: a study of the effect of the nature of intramolecular charge transfer. *RSC Advances* **2015,** *5* (23), 17429-17437.
24. Diaz, C.; Frazer, A.; Morales, A.; Belfield, K. D.; Ray, S.; Hernández, F. E., Structural identification of a novel axially chiral binaphthyl fluorene based salen ligand in solution using electronic circular dichroism: a theoretical-experimental analysis. *The journal of physical*

*chemistry A* **2012,** *116*, 2453-65.

25. Wu, F.; Zhang, G.; Tian, W.; Chen, W.; Zhao, G.; Cao, S.; Xie, W., Two-Photon Absorption and Two-Thoton Assisted Excited-State Absorption in $CdSe_{0.3}S_{0.7}$ quantum dots. *Journal of Optics A: Pure and Applied Optics* **2009,** *11* (6), 0652061-5.
26. Hernandez, F. E.; Belfield, K. D.; Cohanoschi, I.; Balu, M.; Schafer, K. J., Three- and Four-Photon Absorption of a Multiphoton Absorbing Fluorescent Probe. *Applied Optics* **2004,** *43*, 5394-5398.
27. Marques, M. A.; Maitra, N. T.; Nogueira, F. M.; Gross, E. K.; Rubio, A., *Fundamentals of time-dependent density functional theory*. Springer: 2012; Vol. 837.
28. Ullrich, C. A., *Time-dependent density-functional theory: concepts and applications*. Oxford University Press: 2011.
29. Liu, Z.; Wang, Y.; Zhang, X.; Xu, Y.; Chen, Y.; Tian, J., Nonlinear optical properties of graphene oxide in nanosecond and picosecond regimes. *Applied Physics Letters* **2009,** *94* (2), 021902.
30. Woody, R. W., The Exciton model and the circular dichroism of polypeptides. *Monatshefte Fur Chemie* **2005,** *136*, 347-366.
31. Di Bari, L.; Pescitelli, G.; Salvadori, P., Conformational Study of 2,2‘-Homosubstituted 1,1‘-Binaphthyls by Means of UV and CD Spectroscopy. *Journal of the American Chemical Society* **1999,** *121* (35), 7998-8004.
32. Fischer, P.; Hache, F., Nonlinear Optical Spectroscopy of Chiral Molecules. *Chirality* **2005,** *17*, 421-37.
33. Niezborala, C.; Hache, F., Excited-State Absorption and Circular Dichroism of Ruthenium(II) Tris(phenanthroline) in the Ultraviolet Region. *The Journal of Physical Chemistry A* **2007,** *111*

(32), 7732-7735.

34. Niezborala, C.; Hache, F., Conformational changes in photoexcited (R)-(+)-1, 1′-bi-2-naphthol studied by time-resolved circular dichroism. *Journal of the American Chemical Society* **2008,** *130* (38), 12783-12786.

# CHAPTER 3: TWO-PHOTON ABSORPTION AND TWO-PHOTON CIRCULAR DICHROISM OF AN HEXAHELICENE DERIVATIVE WITH A TERMINAL DONOR-ACCEPTOR MOTIF

After studying the influence of the excitation pulse width on the measurements of TPA and TPCD in a family of biaryl-derivatives and elucidating the origin of the experimental differences in amplitude and shape observed in TPCD, using femtosecond and picosecond pulses, we decided to investigate the effect that the intramolecular charge transfer on one end of the molecule has on the TPCD signal of a helical structure in the femtosecond regime.

To accomplish this goal, we performed the theoretical-experimental analysis of the TPA and TPCD spectra of 1-(2-pyridil)-4-methoxy[6]helicene derivative (P6). In this chapter we present the outcomes of our investigation on this particular helicene derivative with a donor-acceptor motive on one end, which led to two important conclusions: 1) The lengthening of the π-electron delocalization within the helical core of P6 predominantly increases the contribution of the magnetic transition dipole moment to the TPCD signal. 2) The electric transition quadrupole moment contribution to the TPCD signal is enhanced by the intramolecular charge transfer (ICT) produced by the donor-acceptor combination on one end of the molecule. In order to corroborate our results, we performed a comparative theoretical analysis of the effect of the energy gap and ICT on TPCD on a series of P6-like helicenes with different donor-acceptor combinations.

## 3.1 Introduction

Although in our group we have extensively worked on different molecular systems to gain a better understanding of the TPCD structure-property relationship[1-8], more chiral molecules with different architecture need to be investigated in order to advance the engineering of the nonlinear response of optically active molecules. Working towards this goal, our investigation in this part focused on the theoretical-experimental analysis of the TPA and TPCD spectra of 1-(2-pyridil)-4-methoxy[6]helicene derivative (hereafter P6 – Figure 3-1) with helical chirality and intramolecular charge transfer (ICT). Due to their extended $\pi$-electron conjugation with the twisted backbone, helicene derivatives combine high optical activity with other properties [9], such as strong absorption and emission in the visible spectral range, and redox activity [10-12]. These types of molecules are very popular because of their direct application in asymmetric catalysis[13], chiroptical photoswitches[14], enantioselective fluorescence detectors[15], circularly polarized luminescence for back-lightning in liquid crystals displays[16, 17], and nonlinear optical (NLO) devices[18, 19].

Here, we present the theoretical-experimental analysis of the effect of pseudo-localized intramolecular charge transfer on the TPA and TPCD signal of a specific organic molecule with extended $\pi$-electron delocalization, helical chirality, and different donor-acceptor group combinations on one end. We first demonstrate that the lengthening of the $\pi$-electron delocalization within the helical core of P6 due to the presence of the pyridine moiety, predominantly increases the contribution of the magnetic transition dipole moment to the TPCD signal. This is explained by the observed decrease in the corresponding energy gap HOMO-LUMO and its direct correlation with the molecular angular momentum. Next, we show that the replacement of the pyridine moiety present in P6 by stronger electron withdrawing substituents (eWS) enhances the electron transfer towards eWS. This effect results in a higher electric quadrupole transition moment contribution to the TPCD signal.

## 3.2 Experimental Section

1-(2-pyridil)-4-methoxy[6]helicene (P6) was synthesized by Crassous and co-workers. P6 was prepared by using a Suzuki-coupling/Wittig/photocyclization reaction sequence.

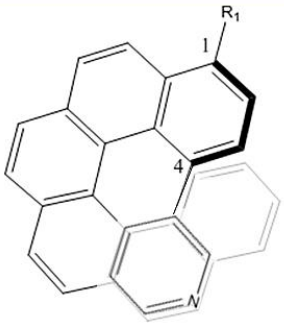


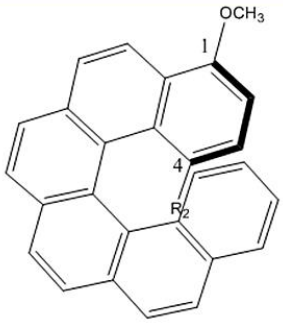


| Molecular System | R1 |
|---|---|
| 1 | H |
| 2 | OH |
| P6 | $OCH_3$ |
| 3 | $NHCOCH_3$ |
| 4 | $CH_3$ |

| Molecular System | R2 |
|---|---|
| 5 | CN |
| 6 | $SO_3H$ |
| P6 | Pyridine |
| 7 | Cl |
| 8 | OH |

**Figure 3-1.** Chemical structures of P-(+)-1-(2-pyridil)-4-methoxy[6]helicene (P6) and eight donor-acceptor P6 derivatives.

M-(-) and P-(+)-1-(2-pyridil)-4-methoxy[6]helicenes were obtained from a Wittig reaction and a subsequent photocyclization of 2-methoxy-5-(2-pyridil)-benzaldehyde and a commercially available benzanthracene. P and M enantiomers were separated through a chiral HPLC method.

OPA measurements were carried out in a single-beam spectrophotometer (Agilent 8453 Diode Array UV-Vis) from 190 to 600 nm in a 0.1 cm quartz cuvette in solutions with a concentration range from $2.0x10^{-5}$ to $2.0x10^{-4}$ M in THF. ECD spectra were performed in a J-815 CD spectropolarimeter (Jasco Corp., Tokyo, Japan). Solutions were prepared at a concentration of $1.0x10^{-5}$ M in THF, at 25 $^{o}$C, and in a 4 mm quartz cuvette. The ECD spectral region scanned

ranged from 190 nm to 600 nm with a 1 nm step and a scan speed of 50 nm/min.

TPA and TPCD experiments were completed by using the Double L-scan technique in solutions with concentration of $8.7x10^{-2}$ M in THF. Two-photon excitation was generated with a computer-controlled femtosecond optical parametric amplifier (OPerA Solo) pumped by an amplified laser system from COHERENT, Inc. The entire system is capable of generating 90 fs (FWHM) pulses over a wavelength range from 240 nm to 2.6 μm, and pulse energies of up to 350 μJ. Measurements were done at a repetition rate ranging from 2 to 50 Hz to avoid any contribution from cumulative effects. The pulse width was measured by a single-shot autocorrelator from COHERENT, Inc. and a frequency-resolved optical gaiting (FROG) from Swamp Optics, LLC.

## 3.3 Computational Methods

The theoretical background required for this section was explicitly exposed in sections 1.2 and 1.5 of this document's introduction. For this reason, we will only present the computational details pertaining the calculations of this chapter.

The molecular structure of M-(-) and P-(+)-P6 and the other donor-acceptor helicenes (Figure 3-1) were optimized using Density Functional Theory (DFT) [20], with the Coulomb attenuating method-Becke's three-parameter exchange, Lee, Yang and Parr correlation (CAM-B3LYP) [21] hybrid functional in combination with the 6-311++G(d,p) [22, 23] basis set, employing Gaussian 09[24]. Solvent effects were taken into consideration through the polarizable continuum model (PCM) [25]

Then, we calculated the oscillator strengths ($f_{0f}$) and velocity rotatory strengths ($R_{0f}^{ECD}$) for the first 100 electronic excited states for P6 and all the donor-acceptor helicene derivatives employing TD-DFT[20] at the CAM-B3LYP[21] /6-311++G(d,p) [22, 23] level of theory. CAM-B3LYP was selected as XCF because it has been proven to be more reliable than B3LYP in the prediction

of excited states of molecules with ICT. Solvent effects were included in the calculations by using PCM [25] in Gaussian 09[24]. The convoluted theoretical OPA and ECD spectra were obtained using Equations 1-15 and 1-35 with a Lorentzian shape and linewidth (Γ) of 0.28 eV (FWHM).

Finally, TPA probabilities ($\bar{\delta}_{0f}^{TPA}(\omega_{0f})$) and TPCD rotatory strength ($R_{0f}^{TPCD}(\omega_{0f})$) for P6 and all the eight theoretical donor-acceptor P6 derivatives were computed using TD-DFT [20] in DALTON 2013[26]. CAM-B3LYP [21] hybrid functional was employed in combination with 6-311++G(d,p) basis set[22, 23] for the calculation of the first 60 electronic excited states for all the molecules. The number of excited states was selected based on the experimental spectral range (200 to 450 nm) covered by the measurements. No solvent effects were taken into account in the nonlinear calculations due to the high computational cost. The convoluted theoretical TPA and TPCD spectra were obtained using Equations 1-19 and 1-38, respectively. A normalized Lorentzian shape was employed with a linewidth (Γ) of 0.2 eV (FWHM).

In order to justify the use of the CAM-B3LYP hybrid functional for P6 we calculated the molecular orbitals involved in the most important electronic excitation on the red side of the theoretical ECD (#3) spectrum. The obvious ICT observed in Figure 3-2, makes the selection of CAM-B3LYP reliable for our analysis. Similar evidences have already been reported by Rizzo and co-workers in various molecular systems [2, 6, 7, 28, 29].

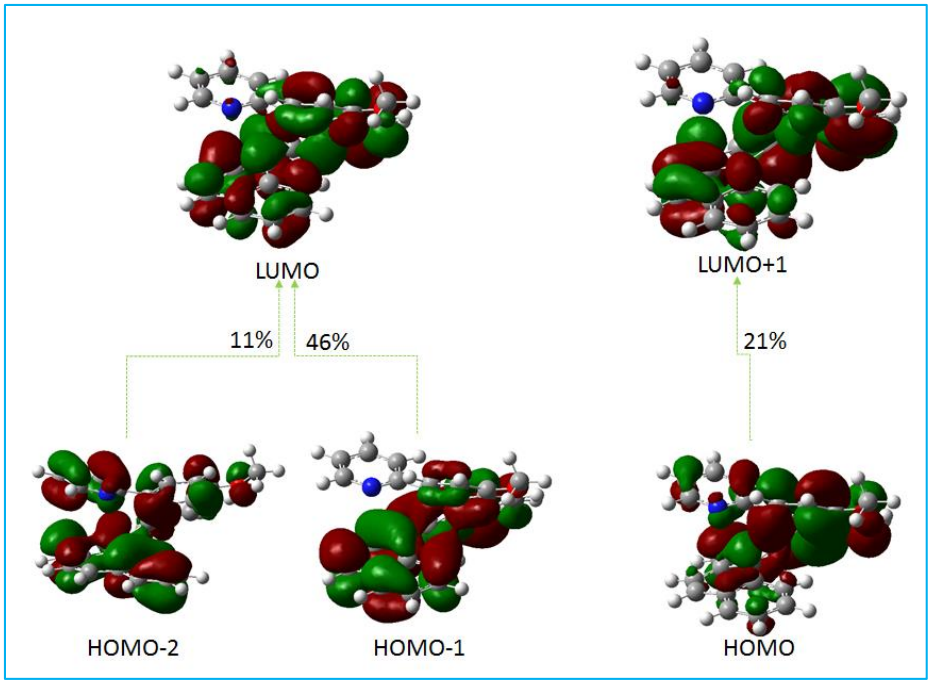


**Figure 3-2.** Molecular orbitals (MOs) involved in the 3rd electronic excited state of P6. The MOs were obtained from CAM-B3LYP/6-311++G(d,p) TD-DFT calculations in THF using PCM in Gaussian 09. The percent contribution from single excitations ([HOMO-x] → [LUMO + y]

## 3.4 Results and discussion

In Figure 3-3, we show the experimental ECD and TPCD spectra for both enantiomers of P6, M-(-) and P-(+)-P6. It can be noticed that the spectrum of one enantiomer is the specular image of the other, as expected. From this figure we can corroborate that TPCD is a sensitive technique for unequivocal enantiomeric identification. Now a more extensive elucidation of the TPCD spectrum of P6 can be completed. For this reason, from now on we will mainly focus our discussion on P-(+)-P6 since similar arguments apply to M-(-)-P6.

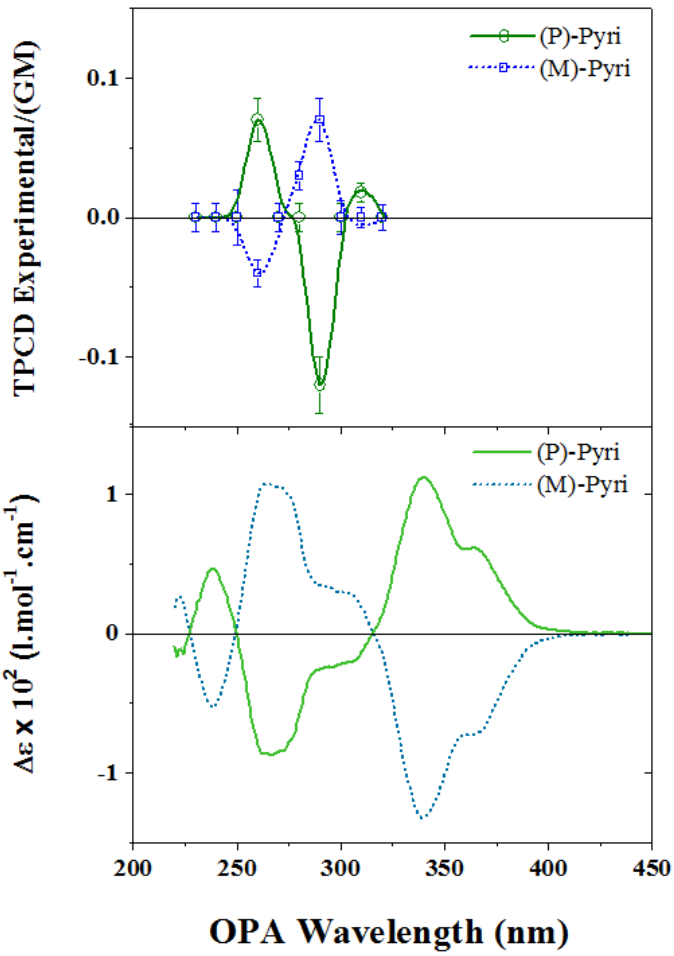


**Figure 3-3.** Experimental a) TPCD and b) ECD spectra for P-(+)-P6 and M-(-)-P6 in THF.

Then, the experimental OPA and ECD spectra (Figure3-4.a and b) and the experimental TPA and TPCD (see Figure3-4.c and d) spectra of P6 in THF solution are presented in Figure 3-4. This figure also display the corresponding convoluted theoretical linear (OPA and ECD) and nonlinear (TPA and TPCD) spectra - linear and nonlinear excited states were computed using TD-DFT with CAM-B3LYP hybrid functional in combination with the 6-311++G(d,p) basis set. For the linear calculations (100 electronic excited states), solvent effects were considered using PCM. For the nonlinear theoretical spectra, the lowest 60 excited states were obtained without taking solvents

effects into account due to high computational cost. In order to obtain a better overlapping between theoretical and experimental bands, the theoretical linear and nonlinear spectra were spectrally shifted by the amount reported in the caption of Figure 3-4, this is a common practice for theoretical-experimental works[2, 3, 5-8, 27].

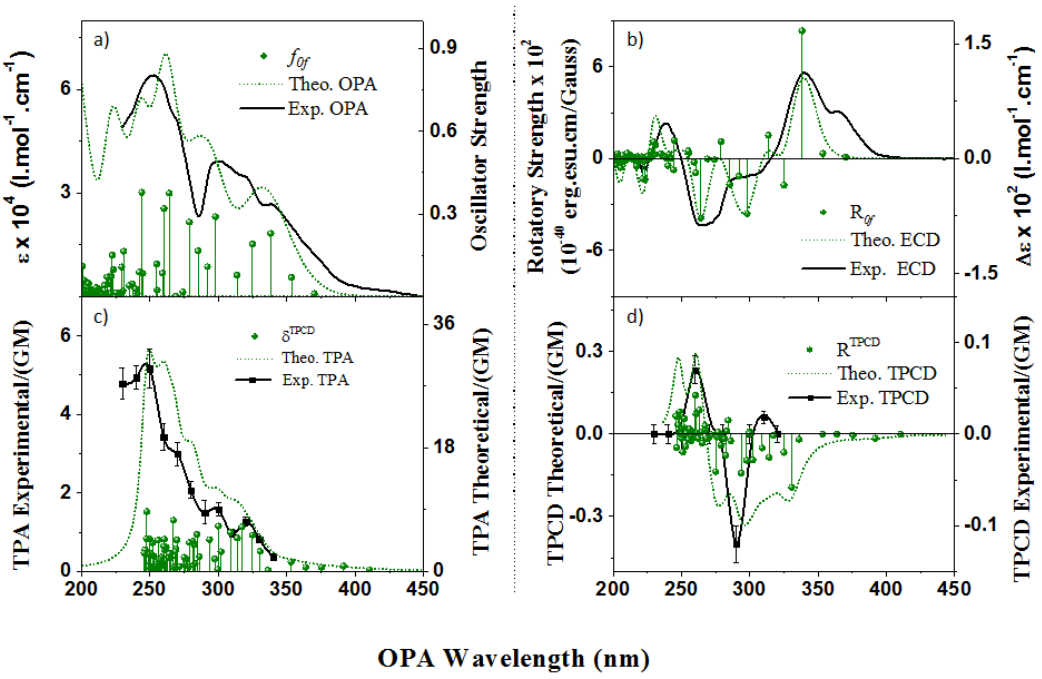


**Figure 3-4.** Experimental (black solid and scattered line) and theoretical (green dotted line) of: a) UV-Vis, b) ECD, c) TPA, and d) TPCD spectra of P6. Colored symbols display the oscillator strength in the case of UV-Vis and ECD and TPA probabilities and rotatory strength in the case of TPA and TPCD, respectively. The OPA and ECD were calculated for the 100 lowest electronic excited states at the CAM-B3LYP/6-311+ +G(d,p) level of theory using Gaussian 09 in THF employing PCM. The theoretical spectra are only shown within the measurable spectral range (200-450 nm) with +10 nm spectral shift. $\Gamma$ = 0.28 eV (FWHM) was used for OPA and ECD. The TPA and TPCD spectra were computed for the first 60 excited states at the same level of theory. The theoretical shift was +50 nm and the $\Gamma$ = 0.2 eV (FWHM).

The first interesting observation to highlight from Figure 3-4 is the remarkable theoretical-experimental overlapping in all four spectra. The theoretical spectra extraordinarily reproduced the shape, position of the bands, and the fano-type shape profile of the experimental spectra. As

mentioned before, the great performance of the chosen XCF is attributed to the presence of ICT in P6. The second important observation is the differences in TPA cross-sections between theoretical and experimental spectra, where the former is larger than the latter. This differences have been previously observed in other molecules[6, 27]. This result is very hard to explain considering the fact that measurements were performed in the femtosecond regime where excited state absorption is almost negligible[30, 31]. However, the relative intensities of the bands are well-reproduced allowing an accurate assignment of the bands without interferences. Next, it is worth noting that the shape, sign and relative intensities of the two main bands (290 and 260 nm) in TPCD were notably reproduced.

In previous publications, we reported the effect of different ICT conjugation length outside the [6]carbohelicene core (EXO-ICT) and within the aromatic cluster (ENDO-ICT) on the TPCD signal[6]. Since then, we have been trying to investigate the influence of having various combinations of donor-acceptor groups at the ends of the aromatic cluster. This has been experimentally challenging because the synthesis of the helicene derivatives has resulted in the symmetric functionalization on both ends of the molecule. To certify this statement, in Figure 3-5, we present the structures of the two helicene derivatives recently synthesized by our collaborator for us to characterize.

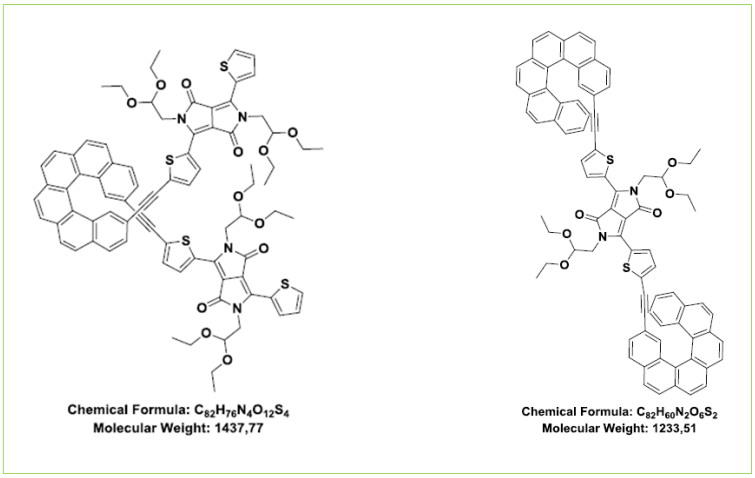


**Figure 3-5**. Recently synthesized symmetric helicene derivatives.

In order to overcome this challenge, we embark on a theoretical investigation of several molecular systems with different donor-acceptor combinations at one end of the helicene core of P6-like structures (see Figure 3-1).

In order to gain more insight about the effects of the structural motif on the linear and nonlinear chiroptical properties of conjugated organic molecules with helical chirality, we performed calculations of OPA, ECD, TPA, and TPCD on four different moieties on position 1 and four different substituents in position 4 (see Figure 3-1). The substituents were selected based on their ability to affect the electron density of the helicene core. In order to perform a systematic selection of the corresponding substituents, we used the Hammet parameter (σ), which provides a qualitative (negative σ for electron releasing and positive for electron withdrawing substituents) and quantifiable scale based on the electron withdrawing and releasing strength of the groups (see Tables 3-1 and 3-2) [32, 33].

**Table 3-1.** Hammet σ-constant for substituents of position 1.

| Substituent Position1 | Hammet σ-constant |
|---|---|
| **H** | 0 |
| **OH** | -0.37 |
| **P6** | -0.27 |
| **NHCOCH3** | -0.15 |
| **CH3** | 0.23 |

**Table 3-2.** Hammet σ-constant for substituents of position 4.

| Substituent Position4 | Hammet σ-constant |
|---|---|
| **CN** | 0.66 |
| **$SO_3H$** | 0.30 |
| **Cl** | 0.23 |
| **P6** | -0.05 |
| **OH** | -0.37 |

In Figure 3-6, we present the comparative plot of the OPA, ECD, TPA and TPCD theoretical spectra for all four different substituents for position 1, as well as the theoretical spectra for P6.

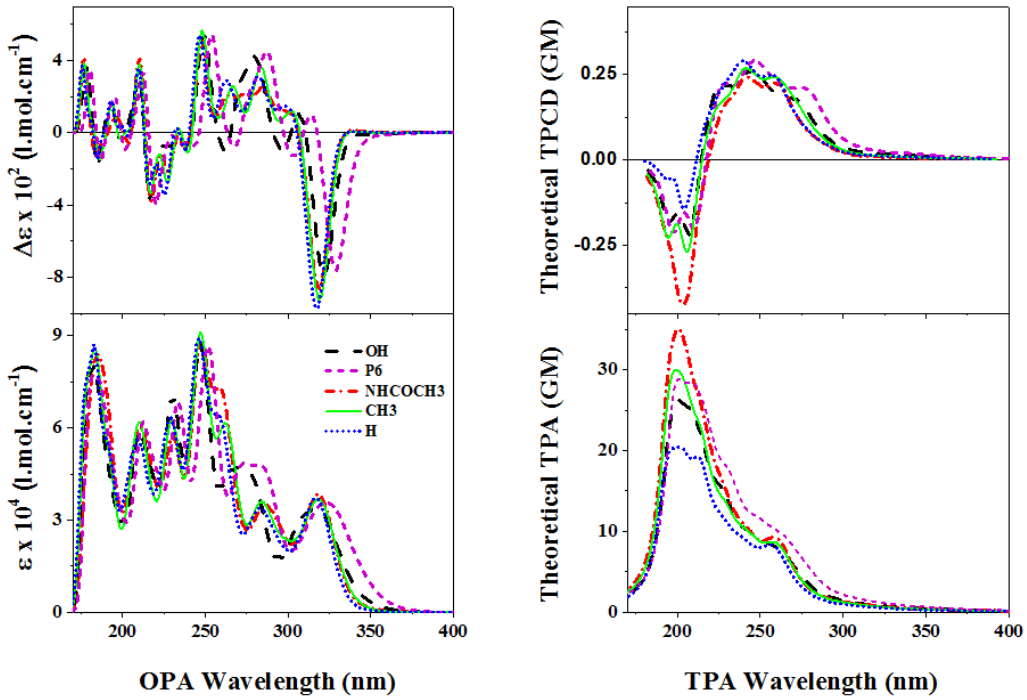


**Figure 3-6.** OPA, ECD, TPA, and TPCD theoretical spectra of all different substituents of position 1 including P6. OPA and ECD were obtained from the Lorentzian convolution (Γ = 0.2 eV FWHM) of the first 60 excited states of their optimized structures calculated at the CAM-B3LYP/6-311++G(d,p) level of theory in THF using PCM employing Gaussian 09. TPA and TPCD spectra of all optimized structures were obtained from the Lorentzian convolution ($\Gamma$ =0.2 eV (FWHM)) of the first 60 excited states. The nonlinear calculations were performed at CAM-B3LYP/6-311++G(d,p) level of theory in vacuo using Dalton 2013.

First, we decided to vary the substituent in position 1, keeping the substituent in position 4 as in P6 (see the combinations in Figure 3-1). The OPA and ECD signals are not strongly affected by the nature of the substituents in this position. In this figure, one can only observe an almost negligible increase in the amplitude and a red shift on the red side of the fano-type band of the ECD signal.

In TPA, one can identify two main bands, one at approximately 520 nm and the other at 400 nm. The intensity of the first band is similar in all five derivatives. However, the second band changes its intensity from 20 GM in H to 34 GM in $NHCOCH_3$. In the TPCD spectra, one can also notice that the first band is unaffected by the substitution in position 1. However, the apparent

change in intensity observed in the second band of the -NHCOCH3 derivative is attributed to the fusion of the double-peak band present in the other four molecules to produce an intense single-peak band.

Next, we varied the substituent in position 4, keeping the moiety in position 1 as in P6 (see the combinations in Figure 3-1). In Figure 3-7, we present the OPA spectra of the four derivatives of the second series. Interesting to highlight is the small red shift (30 nm) experienced by the band centered at approximately 320 nm in -CN, -$SO_3H$, and P6. Likewise in ECD, we see a similar shift in the same three derivatives. This interesting result reveals the extension of the conjugation length introduced by the pyridine moiety on the outside of the helicene core in P6, an effect not present in the other four derivatives.

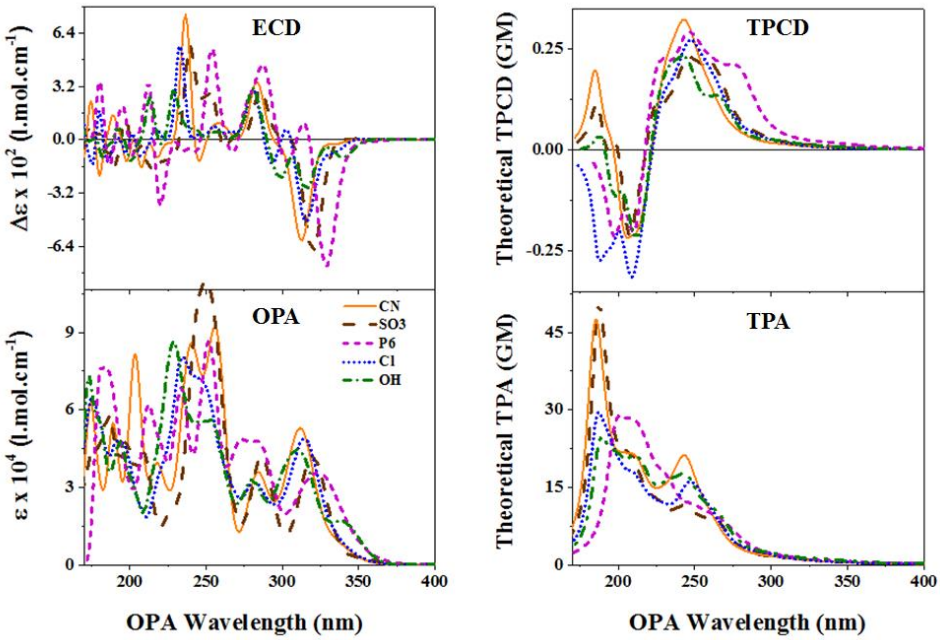


**Figure 3-7.** OPA, ECD, TPA and TPCD theoretical spectra of all five different substituents. OPA and ECD spectra were obtained from the Lorentzian convolution (Γ = 0.2 eV FWHM) of the first 100 electronic excited states of the optimized structures of all different five substituents at the CAM-B3LYP/6-311++G(d,p) level of theory in THF using PCM and employing Gaussian 09. TPA and TPCD spectra of the optimized structures were calculated from the Lorentzian convolution ($\Gamma$ = 0.2 eV FWHM) for the first 60 electronic excited states. TPA and TPCD calculations were performed at the CAM-B3LYP/6-311++G(d,p) level of theory in vacuo using Dalton 2013.

Another interesting point to highlight, only observed in the two strongest electron withdrawing groups, is the presence of a strong band at approximately 180 nm, which TPA cross section varies from 28 GM for P6 to 48 GM for the -$SO_3H$ substituted. This result is supported by previous theoretical results published by Yan and co-workers (2012) , where they demonstrate that conjugated molecules with a push-pull motive present an enhanced TPA cross section as a result of the intramolecular charge transfer, which increase the transition dipole moments between energy states[34]. To corroborate this finding, we calculated the resultant transition dipole moment for the 3rd electronic excited state (see table 3-3) - same electronic excited state selected previously for P6. As expected, one can clearly see that at least for this electronic excited state the resultant transition dipole moment is larger for CN and $SO_3H$ than for P6.

**Table 3-3.** Comparison of the resultant transition dipole moment of the two groups with the highest electron withdrawing character (CN and SO3H) and P6.

| State 3 | Resultant Transition Dipole Moment |
|---|---|
| CN | 2.14327 |
| $SO_3H$ | 2.00440 |
| P6 | 1.57353 |

The molecular orbitals presented in Figure 3-8, evidently expose the greater ICT observed in -$SO_3H$ when compared to P6 (see Figure 3-3). On the one hand, in the HOMO and HOMO-1 energy levels, one can see that the electrons are mainly delocalized in the aromatic ring of the molecular system. On the other hand, in the LUMO and LUMO+1 energy levels, the electron density goes more towards the -$SO_3H$ group due to its higher electron withdrawing character. Consequently, the ICT effect is more evident in the helicene with the -$SO_3H$ substituent than in P6.

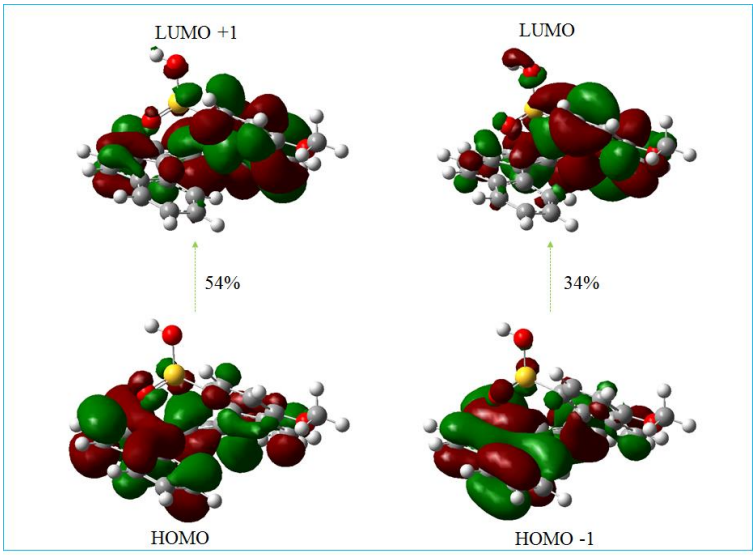


**Figure 3-8.** Molecular orbitals (MOs) involved in the 3rd electronic excited state of SO3H. The MOs were obtained from CAM-B3LYP/6-311++G(d,p) TD-DFT calculations in THF using PCM in Gaussian 09. The percent contribution from single excitations ([HOMO-x] → [LUMO + y]) to the excited state is indicated next to each arrow.

Finally, we analyze the TPCD spectra of all five substituents in position 4 (Figure 3-7). Once again, the positive band that appears towards the red side of the spectra seems to be unaffected by the donor-acceptor combination of the substituents. However, the band located at approximately 200 nm changed in shape and sign. In the case of P6 and -Cl, one can notice a negative double-peak band in this region. For -CN and -$SO_3H$, this band emerges as a negative single-peak band at 210 nm that turns into a positive band at 180 nm. Knowing that TPCD signal directly depends on the different contributions from the electric transition quadrupole moment ($B_2$) and the magnetic transition dipole moment ($B_1 + B_3$), a comparison of the sum of the absolute values of molecular parameters $B_1 + B_3$ and $B_2$ for all five substituents in position 1 and 4 is presented in Figure 3-9.

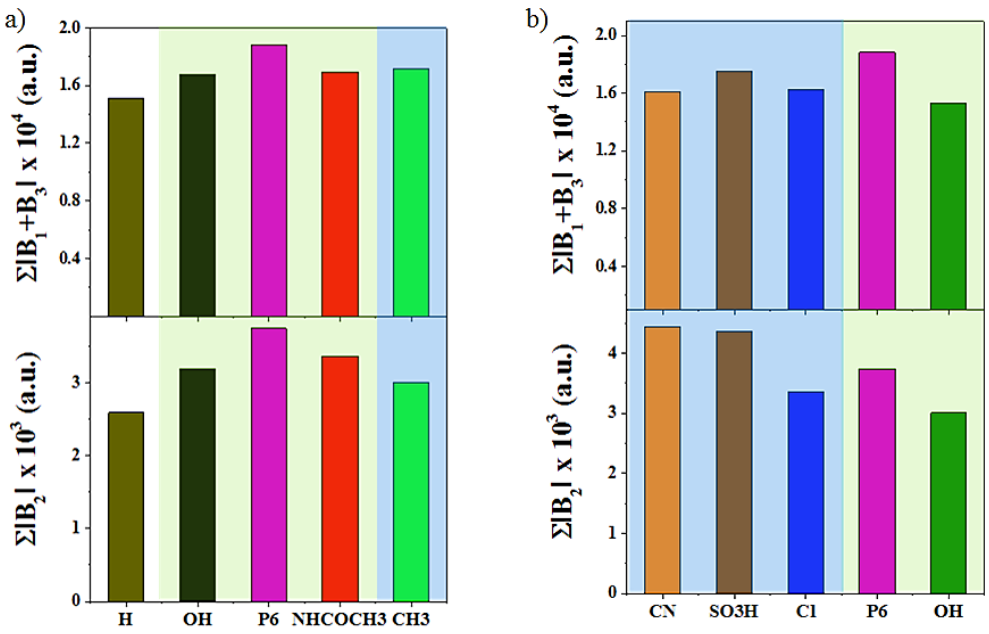


**Figure 3-9.** Comparative bar graph of a) $\sum|B_1+B_3|$ and b) $\sum|B_2|$ for all substituents of a) position 1 and b) position 4.

In Figure 3-9, one can identify three main shaded areas: the green one indicates that these substituents act as electron releasing groups based on their negative Hammet constant, the blue area designates the electron withdrawing groups with positive Hammet constants, and the clear area correspond to -H, which was used as a reference (see tables 3-1 and 3-2) [32].

In this figure, we first show a clear trend on the contribution of the magnetic transition dipole moment ($B_1+B_3$) to the TPCD spectra with respect to their donor-acceptor character. One can observe that the $B_1+B_3$ molecular parameter is always greater for P6 than the P6-like molecules with different substituents. However, the contribution of the electric transition quadrupole moment ($B_2$) to the TPCD spectra is larger for P6 on the electron releasing moieties and larger for –CN on the electron withdrawing series. In order to explain this trends, we calculated the HOMO and LUMO energies for each P6-like derivative, P6 included, employing DFT at the CAM-B3LYP/6-311++G(d,p) level of theory. The calculated energies, as well as the energy gaps of these molecules are presented in Figure 3.10.

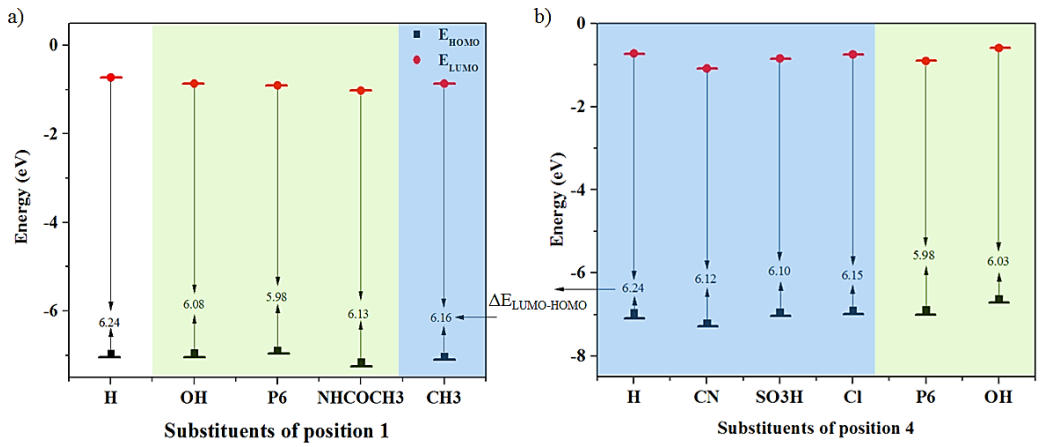


**Figure 3-10**. Calculated HOMO energies, LUMO energies, and energy gaps of all the donor-acceptor combinations substituents for a) position 1 and b) position 4.

From Figure 3-10.a, which compare the effect of the strength of donor groups in position 1, one can deduce that electron releasing groups tend to increase the LUMO energy of the helicene derivatives. This is corroborated by the change in tendency observed in a weak electron withdrawing substituent such as -$CH_3$) (the LUMO energy increases again, Figure 3-10.a). Now, in Figure 3-10.b, which assess the effect of the strength of attractor groups in position 4, one can observe an overall decrease of the LUMO energy as the electron withdrawing character increases.

After completing the examination of the effect of contributions of $\sum|B_1+B_3|$ and $\sum|B_2|$ to the TPCD spectra of both series of P6-like derivatives (Figure 3-9), and the effect of energy gap (HOMO-LUMO) in the same two series, we proceeded to evaluate the existing correlations between the two. Through this analysis, an inverse dependency between the magnetic transition dipole moment contribution to the TPCD and the energy gap was noticed, i.e. the lower the energy gap the higher $\sum|B_1+B_3|$. This can be explained based on previous works reporting that a decrease in energy gap causes and increase in the angular momentum [35]. Therefore, because the angular momentum is directly correlated with the magnetic moment, an increase in the angular momentum results in a higher magnetic transition dipole moment [36].

In order to corroborate the established correlation between $\sum|B_1+B_3|$ and $\sum|B_2|$ and the donor-acceptor combination in P6 derivatives, we calculated the frontier molecular orbitals (FMOs) of all nine molecules (see Figure 3-11). The FMOs were obtained using DFT at the CAM-B3LYP/6-311++G(d,p) level of theory. In Figure 3-11.a, one can observe, in most of the derivatives, that the electron density over the substituents on one end of the molecule is higher in the HOMO than in the LUMO. This reveals the strong electron withdrawing character of the helical core in P6-like derivatives with different electron donating moieties. On the contrary, the FMOs presented in Figure 3-11.b show a strong ICT between the two moieties with push-pull arrangement on one end on the derivatives rather than through the helicene core. In summary, the presence of strong withdrawing substituents such as –CN and $–SO_3H$ in position 4 tend to originate a larger contribution to TPCD through the electric transition quadrupole moment, while the pure existence of an aromatic ring like pyridine in P6 that can extend the length of the π–electron delocalization beyond the helical core creates a stronger contribution to TPCD through the magnetic transition dipole moment.

## 3.5 Conclusions

The analysis of the effect of localized ICT on one end of helicene derivatives on the contribution transition moments of TPA and TPCD revealed that: a) the lengthening of the π-electron delocalization, within the helical core of P6, predominantly increases the contribution of the magnetic transition dipole moment to the TPCD signal, and b) the electric transition quadrupole moment contribution to the TPCD signal is enhanced by the localized ICT produced by the donor-acceptor combination on one end of the molecule. These two effects were certified by the analysis of FMOs in all the nine derivatives.

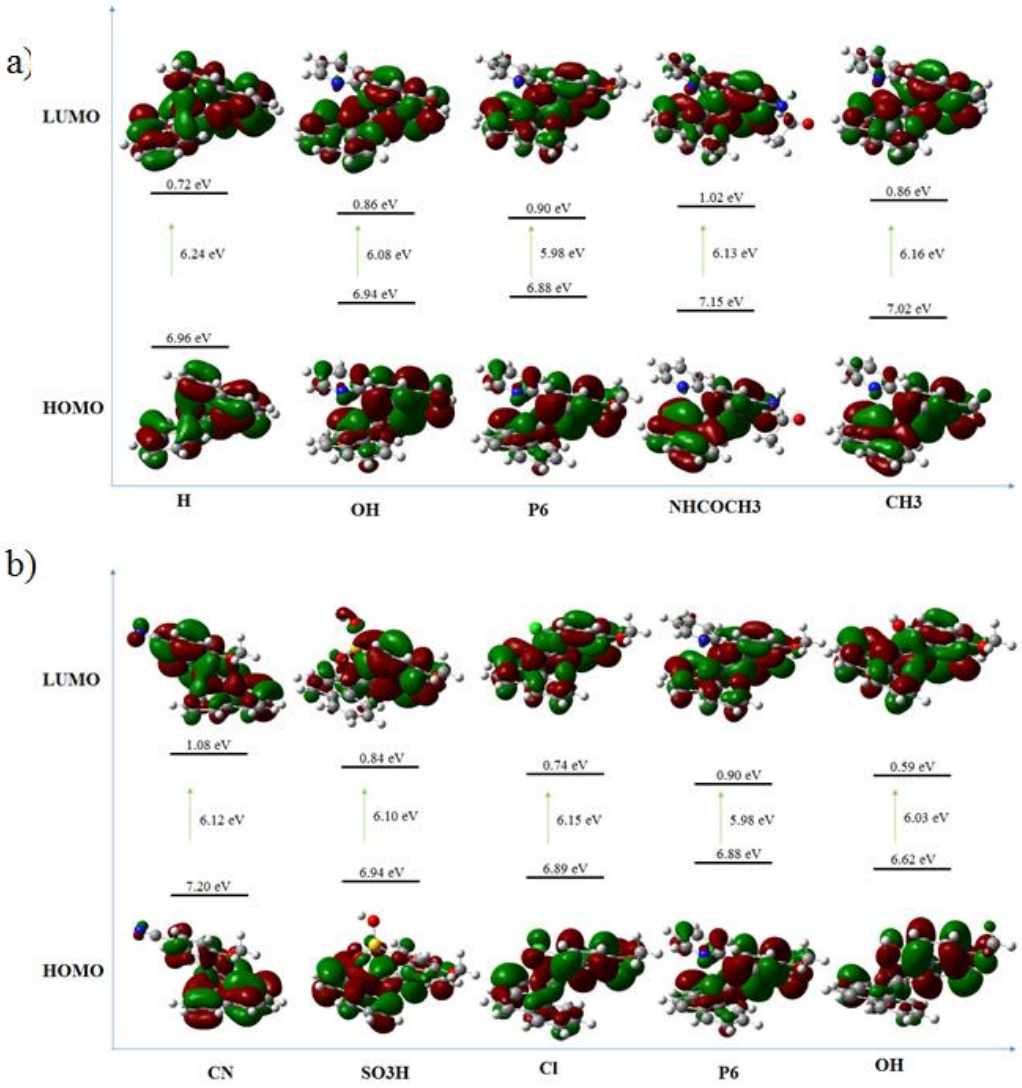


**Figure 3-11.** The frontier molecular orbitals (FMOs) of all substituents of a) position1 and b) position 4. The molecular orbitals were obtained using DFT at the CAM-B3LYP/6-311++G(d,p) level of theory.

## 3.6 References


1. Vesga, Y.; Diaz, C.; Hernandez, F. E., Theoretical study of two-photon circular dichroism on molecular structures simulating aromatic amino acid residues in proteins with secondary structures. *RSC Advances* **2014,** *4* (105), 60974-60986.
2. Díaz, C.; Echevarria, L.; Rizzo, A.; Hernández, F. E., Two-Photon Circular Dichroism of an Axially Dissymmetric Diphosphine Ligand with Strong Intramolecular Charge Transfer. *The Journal of Physical Chemistry A* **2014,** *118* (5), 940-946.
3. Díaz, C.; Echevarria, L.; Hernández, F. E., Conformational Study of an Axially Chiral Salen Ligand in Solution using Two-Photon Circular Dichroism and the Fragment-Recombination Approach. *The Journal of Physical Chemistry A* **2013,** *117*, 8416–8426.
4. Tiburcio-Moreno, J. A.; Alvarado-Gil, J.; Diaz, C.; Echevarria, L.; Hernández, F. E., Polarization dependent two-photon absorption spectroscopy on a naturally occurring biomarker (curcumin) in solution: A theoretical–experimental study. *Chemical Physics Letters* **2013,** *583*, 160-164.
5. Diaz, C.; Lin, N.; Toro, C.; Passier, R.; Rizzo, A.; Hernández, F. E., The Effect of the π-Electron Delocalization Curvature on the Two-Photon Circular Dichroism of Molecules with Axial Chirality. *The Journal of Physical Chemistry Letters* **2012,** *3*, 1808-1813.
6. Diaz, C.; Vesga, Y.; Echevarria, L.; Stará, I. G.; Starỳ, I.; Anger, E.; Shen, C.; Moussa, M. E. S.; Vanthuyne, N.; Crassous, J., et al., Two-photon absorption and two-photon circular dichroism of hexahelicene derivatives: a study of the effect of the nature of intramolecular charge transfer. *RSC Advances* **2015,** *5* (23), 17429-17437.
7. Lin, N.; Santoro, F.; Zhao, X.; Toro, C.; De Boni, L.; Hernández, F. E.; Rizzo, A., Computational Challenges in Simulating and Analyzing Experimental Linear and Nonlinear Circular Dichroism Spectra. R-(+)-1,1'-bis(2-naphthol) as a Prototype Case. *journal of*

*physical chemistry. B* **2011,** *115*, 811-24.

8. Toro, C.; De Boni, L.; Lin, N.; Santoro, F.; Rizzo, A.; Hernandez, F. E., Two-Photon Absorption Circular Dichroism: A New Twist in Nonlinear Spectroscopy. *Chemistry - A European Journal* **2010,** *16*, 3504-9.
9. Gingras, M.; Félix, G.; Peresutti, R., One hundred years of helicene chemistry. Part 2: stereoselective syntheses and chiral separations of carbohelicenes. *Chemical Society Reviews* **2013,** *42* (3), 1007-1050.
10. Aillard, P.; Voituriez, A.; Marinetti, A., Helicene-like chiral auxiliaries in asymmetric catalysis. *Dalton Transactions* **2014,** *43* (41), 15263-15278.
11. Bosson, J.; Gouin, J.; Lacour, J., Cationic triangulenes and helicenes: synthesis, chemical stability, optical properties and extended applications of these unusual dyes. *Chemical Society Reviews* **2014,** *43* (8), 2824-2840.
12. Narcis, M. J.; Takenaka, N., Helical-Chiral Small Molecules in Asymmetric Catalysis. *European Journal of Organic Chemistry* **2014,** *2014* (1), 21-34.
13. Dreher, S. D.; Katz, T. J.; Lam, K.-C.; Rheingold, A. L., Application of the Russig-Laatsch reaction to synthesize a bis [5] helicene chiral pocket for asymmetric catalysis. *The Journal of Organic Chemistry* **2000,** *65* (3), 815-822.
14. Wigglesworth, T. J.; Sud, D.; Norsten, T. B.; Lekhi, V. S.; Branda, N. R., Chiral Discrimination in Photochromic Helicenes. *Journal of the American Chemical Society* **2005,** *127* (20), 7272-7273.
15. Reetz, M. T.; Sostmann, S., 2,15-Dihydroxy-hexahelicene (HELIXOL): Synthesis and use as an Enantioselective Fluorescent Sensor. *Tetrahedron* **2001,** *57* (13), 2515-2520.
16. Field, J. E.; Muller, G.; Riehl, J. P.; Venkataraman, D., Circularly Polarized Luminescence

from Bridged Triarylamine Helicenes. *Journal of the American Chemical Society* **2003,** *125* (39), 11808-11809.

17. Hassey, R.; Swain, E. J.; Hammer, N. I.; Venkataraman, D.; Barnes, M. D., Probing the Chiroptical Response of a Single Molecule. *Science* **2006,** *314* (5804), 1437-1439.
18. Verbiest, T.; Elshocht, S. V.; Kauranen, M.; Hellemans, L.; Snauwaert, J.; Nuckolls, C.; Katz, T. J.; Persoons, A., Strong Enhancement of Nonlinear Optical Properties Through Supramolecular Chirality. *Science* **1998,** *282* (5390), 913-915.
19. Verbiest, T.; Sioncke, S.; Persoons, A.; Vyklicky, L.; Katz, T. J., Electric-Field-Modulated Circular-Difference Effects in Second-Harmonic Generation from a Chiral Liquid Crystal. *Angew Chem Int Ed Engl* **2002,** *41* (20), 3882-4.
20. Runge, E.; Gross, E. K. U., Density-Functional Theory for Time-Dependent Systems. *Physical Review Letters* **1984,** *52*, 997-1000.
21. Yanai, T.; Tew, D. P.; Handy, N. C., A new Hybrid Exchange-Correlation Functional using the Coulomb-Attenuating Method (CAM-B3LYP). *Chemical Physics Letters* **2004,** *393*, 51-57.
22. Krishnan, R.; Binkley, J. S.; Seeger, R.; Pople, J. A., Self-Consistent Molecular Orbital Methods. XX. A Basis Set for Correlated Wave Functions. *The Journal of Chemical Physics* **1980,** *72* (1), 650-654.
23. Clark, T.; Chandrasekhar, J.; Spitznagel, G. W.; Schleyer, P. V. R., Efficient Diffuse Function-Augmented Basis Sets for Anion Calculations. III. The 3-21+G Basis Set for First-Row Elements, Li–F. *Journal of Computational Chemistry* **1983,** *4* (3), 294-301.
24. Frisch, M. J.; Trucks, G. W.; Schlegel, H. B.; Scuseria, G. E.; Robb, M. A.; Cheeseman, J. R.; Scalmani, G.; Barone, V.; Mennucci, B.; Petersson, G. A., et al., Gaussian 09, Revision

A.1. Gaussian, Inc.: Wallingford CT, 2009.

25. Tomasi, J.; Mennucci, B.; Cammi, R., Quantum Mechanical Continuum Solvation Models. *Chemical Reviews* **2005,** *105*, 2999-3093.
26. Aidas, K.; Angeli, C.; Bak, K. L.; Bakken, V.; Bast, R.; Boman, L.; Christiansen, O.; Cimiraglia, R.; Coriani, S.; Dahle, P., et al., The Dalton Quantum Chemistry Program System. *Wiley Interdisciplinary Reviews: Computational Molecular Science* **2014,** *4* (3), 269-284.
27. Vesga, Y.; Hernandez, F. E., Study of the Effect of the Pulse-Width of the Excitation Source on the Two-Photon Absorption and Two-Photon Circular Dichroism Spectra of Biaryl Derivatives. *The Journal of Physical Chemistry A* **2016**.
28. Lin, N.; Santoro, F.; Rizzo, A.; Luo, Y.; Zhao, X.; Barone, V., Theory for Vibrationally Resolved Two-Photon Circular Dichroism Spectra. Application to (R)-(+)-3-Methylcyclopentanone. *The journal of physical chemistry A* **2009,** *113*, 4198-207.
29. Guillaume, M.; Ruud, K.; Rizzo, A.; Monti, S.; Lin, Z.; Xu, X., Computational Study of the One- and Two-Photon Absorption and Circular Dichroism of (L)-Tryptophan. *journal of physical chemistry. B* **2010,** *114*, 6500-12.
30. Wu, F.; Zhang, G.; Tian, W.; Chen, W.; Zhao, G.; Cao, S.; Xie, W., Two-Photon Absorption and Two-Thoton Assisted Excited-State Absorption in $CdSe_{0.3}S_{0.7}$ quantum dots. *Journal of Optics A: Pure and Applied Optics* **2009,** *11* (6), 0652061-5.
31. Hernandez, F. E.; Belfield, K. D.; Cohanoschi, I.; Balu, M.; Schafer, K. J., Three- and Four-Photon Absorption of a Multiphoton Absorbing Fluorescent Probe. *Applied Optics* **2004,** *43*, 5394-5398.
32. Leffler, J. E.; Grunwald, E., *Rates and equilibria of organic reactions: as treated by statistical, thermodynamic and extrathermodynamic methods*. Courier Corporation: 2013.

33. Pandith, A. H.; Islam, N., Electron transport and nonlinear optical properties of substituted aryldimesityl boranes: a DFT study. *PloS one* **2014,** *9* (12), e114125.
34. Hu, Z.; Khadka, V. S.; Wang, W.; Galipeau, D. W.; Yan, X., Theoretical study of two-photon absorption properties and up-conversion efficiency of new symmetric organic π-conjugated molecules for photovoltaic devices. *Journal of Molecular Modeling* **2012,** *18* (8), 3657-3667.
35. Dalafi, H., Theoretical investigation of anomalies in 162 Er. *Lettere Al Nuovo Cimento (1971–1985)* **1978,** *23* (7), 247-249.
36. Cullity, B. D.; Graham, C. D., *Introduction to magnetic materials*. John Wiley & Sons: 2011.

# CHAPTER 4: THEORETICAL STUDY OF TWO-PHOTON CIRCULAR DICHROISM ON MOLECULAR STRUCTURES SIMULATING AROMATIC AMINO ACID RESIDUES IN PROTEINS WITH SECONDARY STRUCTURES

*Reproduced with permission of Elsevier from: Vesga, Y.; Diaz, C.; Higgs, M.; Hernandez, F.E.,Chem. Phys. Lett.* ***2014,*** *601* (0), 6-12.
*And RSC publications from: Vesga, Y.; Diaz, Hernandez, F.E.,RSC Advances* ***2014,*** *4 (105), 60974-60986*

After completing the systematic study of the effect localized ICT on one end of helicene derivatives has on the contribution of transition moments that determine the intensity and shape of TPA and TPCD spectra of chiral systems, we decided to embark in a new, and perhaps, a more powerful purpose of TPCD in the biomedical field, i.e. the application of this unique nonlinear chiroptical property in the Far-UV region.

In this chapter we present the theoretical comparative analysis of the TPCD spectra of the four aromatic amino acids found in mammals, L-trytophan (Trp), L-histidine (His), L-phenylalanine (Phe), and L-tyrosine (Tyr), simulating their corresponding residues in proteins with secondary structures (α–helix, β-strand and random coil). Our results reveal unique signatures in the FUV for each conformer in each configuration. The outcomes of this research show how FUV-TPCD can be used to study peptide and protein structures in a region never evaluated before but packed with important structural information.

## 4.1 Introduction

We have already discussed, throughout this dissertation, how TPCD opens new paths for novel structural and conformational studies of biological and chemical chiral systems in the visible and near-IR spectral region[1-6]. However, the potential implementation of TPCD in the near- and far-UV, which is of great interest for the scientific community, has not been explored yet. Before incursioning this spectral region with sophisticated experimental setups, the theoretical TPCD analysis in model systems of interest such as natural amino acids should be performed.

With the aim of reveal the great potential TPCD has in the identification of conformers and configurations even at shorter wavelengths, we have started the determination of the contribution of side- and main-chains conformation of aromatic amino acid residues to the TPCD spectra of proteins, in the NUV and FUV region. In order to accomplish this objective, we have decided to calculate and evaluate conformational changes on the side-chain aromatic amino acids in the main three secondary structure configurations, i.e. α-helix, β-strand and random coil.

In this chapter we present the calculation and analysis of the theoretical TPA and TPCD of molecular structures imitating Tryptophan (Trp), Phenylalanine (Phe), Tyrosine (Tyr), and Histidine (His) residues in proteins with secondary structure configurations using Ramachandra's lower energy conformers. The comparative examination of the TPCD spectra of various conformers in each configuration exposed unique fingerprints down to the FUV, a blind spectral region for ECD. Results exhibited in this chapter confirm the potential of FUV-TPCD to identify and study the structures of proteins in a region where intrinsic solvent absorption and sample scattering cover the ECD signal.

## 4.2 Computational Methods

The theoretical background needed in this dissertation has been clearly exposed in sections 1.2 and 1.5 of the introduction of this document. Therefore, in this chapter we will only cover the computational details related to this specific section.

The molecular structure of the L-stereoisomers of the six primary Trp residues Trp11, Trp12, Trp21, Trp22, Trp31, Trp32, the main six Histidine residues (His11, His12, His21, His22, His31 and His32), the six primary Tyrosine residues (Tyr11, Tyr12, Tyr21, Tyr22, Tyr31 and Tyr32), and the three principal Phenylalanine residues (Phe1, Phe2 and Phe3), were optimized using Density Functional Theory (DFT) [7], employing the Becke's three-parameter exchange, Lee, Yang and Parr correlation (B3LYP) hybrid functional[8-10] in combination with the 6-311G(d) basis set[11, 12], employing Gaussian 09[13]. The establishment and optimization of all the Trp, His, Tyr, and Phe conformers, in their corresponding α-helix, β-strand and random coil configuration, were performed using, initially the well-known Ramachandran dihedral angles for such structures[14]. These angles account for the relative configuration of the two groups about the $C_\alpha$ atom which are specified by $\psi$ and $\phi$ (main-chain angles). The relative positioning of these two groups with respect to the $C_\alpha$–$C_\beta$ and $C_\beta$–$C_\gamma$ bonds were accounted by angles $\chi_1$ and $\chi_2$ (side-chain angles). Main- and side-chain angle values for all the amino acids investigated here were taken from reference 15[15].

The TPA and TPCD response for the lowest 80 electronic excited states of all optimized structures were computed using Time-Dependent DFT (TD-DFT) [7], employing B3LYP[8-10] and the Coulomb Attenuated Method variant of B3LYP (CAM-B3LYP)[16] exchange correlation functionals (XCF), and the 6-311G(d) basis set[11, 12] using Dalton 2011[17]. All the calculations were carried out in gas phase. The convolution of the TPA and TPCD spectra were obtained employing Equations 1-19 and 1-38 (see dissertation introduction), respectively.

In order to gain some initial validation of our theoretical approach we first performed linear calculations of the OPA and ECD spectra of all the molecular structures simulating all the Trp, His, Tyr, and Phe residues in α-helix, β-strand and random coil conformation, see Appendix D. Although, we were aware that this is not totally adequate to make a definite selection of a prefer XCF, in some cases it can be helpful. Briefly OPA and ECD for the lowest 80 electronic excited states were computed of all optimized structures at the B3LYP[8-10]/6-311G(d) [11, 12] and CAM-B3LYP[16]/6-311G(d) [11, 12] level of theory using Gaussian 09[13] in gas phase. All convoluted spectra were calculated using $\Gamma$ = 0.124 eV (FWHM) in agreement with ref. 18[18]. The comparative theoretical-experimental fitting performed with B3LYP[8-10] and CAM-B3LYP[16], on the experimental measurements of the FUV-ECD spectrum of L-alanine (down to 140 nm) reported by Meierhenrich and collaborators using Synchrotron Radiation CD[19], surprisingly give a better match for B3LYP[8-10] than CAM-B3LYP[16] (see Appendix D). This result is in agreement with previous calculation on Trp using similar XCF but performed only over the first six excited states[20] instead of the 80 employed herein which extend the calculation to much higher energy excited states. As demonstrated in reference 21, CAMB3LYP surpasses B3LYP on the prediction of highly excited, long range and charge transfer diffuse states because the HOMO energy determined with this XCF is usually lower than for B3LYP[21]. Therefore, we believe that CAMB3LYP should predict more accurately the TPCD spectra of Trp residues in the FUV. Anyhow, because within the short wavelengths region of the spectra the results are affected by the strong state diffusion, high density of states and the possibility of intermediate state resonances, we should consider to recourse to complex damped response theory when working with molecules such as Trp, His, Tyr, and Phe [22, 23]. Unfortunately, this approach is available for TPA[24] but not for TPCD yet. Obviously, because we cannot totally discard the theoretical results obtained with B3LYP[8-10] until the

experimental TPCD spectrum of this and other amino acids are measured in the FUV, in Appendix D we provide all the theoretical TPA and TPCD spectra of Trp, His, Tyr, and Phe residues obtained with this exchange-correlation functional (XCF).

## 4.3 Results and Discussion

In order to understand better the origin of all the angles contemplated for the establishment of the primary six conformers of Trp (as example), in Figure 4-1 we show the complete molecular structure of a standard configuration of Trp residue (a), a zoom of the atoms, bonds and planes involved in the establishment $\psi$ and $\phi$ (b), and a partial view of the primary atoms and bonds that define the rotatory axes for determining the $\chi_1$ and $\chi_2$ angles (c). First, $\psi$ and $\phi$ are defined as the dihedral angles of the main-chain amide groups, i.e. $N_{(+1)}$–C–$C_\alpha$–N and $C_{\alpha(+1)}$–N–$C_\alpha$–C, respectively (Figure 4-1.b). Initial values of $\psi$ and $\phi$ for α-helix, β-strand and random coil configuration were ($-40^0$, $-60^0$), ($160^0$, $-150^0$) and ($70^0$, $-80^0$), in that order[18]. Second, $\chi_1$ and $\chi_2$ are defined as the angle of rotation around the $C_\alpha$–$C_\beta$ and $C_\beta$–$C_\gamma$, respectively. While $\chi_1$ can adopt three different relative positions through a rotation of $120^0$, $\chi_2$ lead to two opposite relative orientations through a $180^0$ rotation[18].

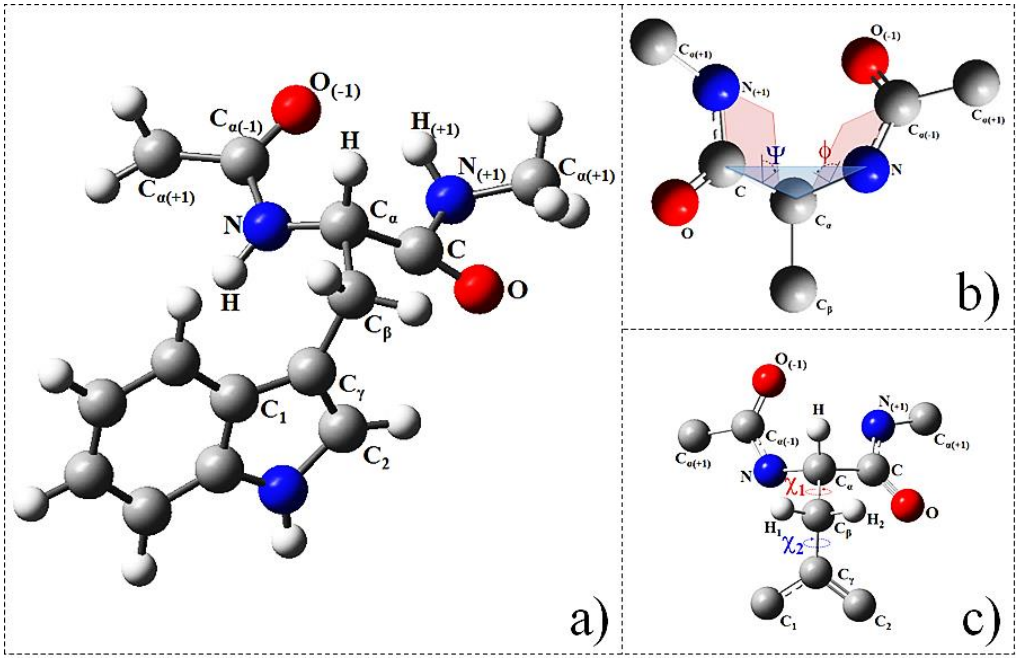


**Figure 4-1.** Most stable conformation of a Trp residue (a), standard configuration of the two peptide residues depicting the dihedral angles of the main-chain ψ and ϕ in (b), and representation of the rotating angles $\chi_1$ ($C_\alpha$–$C_\beta$) and $\chi_2$ ($C_{-\beta}C_\gamma$) (c) on the same the two peptide residues. $C_\beta$ position corresponds to that of residues of L-configuration.

Figure 4-2 displays the optimized stereochemical structures of Trp, His, Tyr, Phe residues in random coil configuration to illustrate differences between configurations. Similar type of structures were obtained for the α-helix and β-strand (these structures can be found in Appendix D). The classification of the different conformers respects the following convention in all main-chain configuration, Trp$\chi_1\chi_2$.

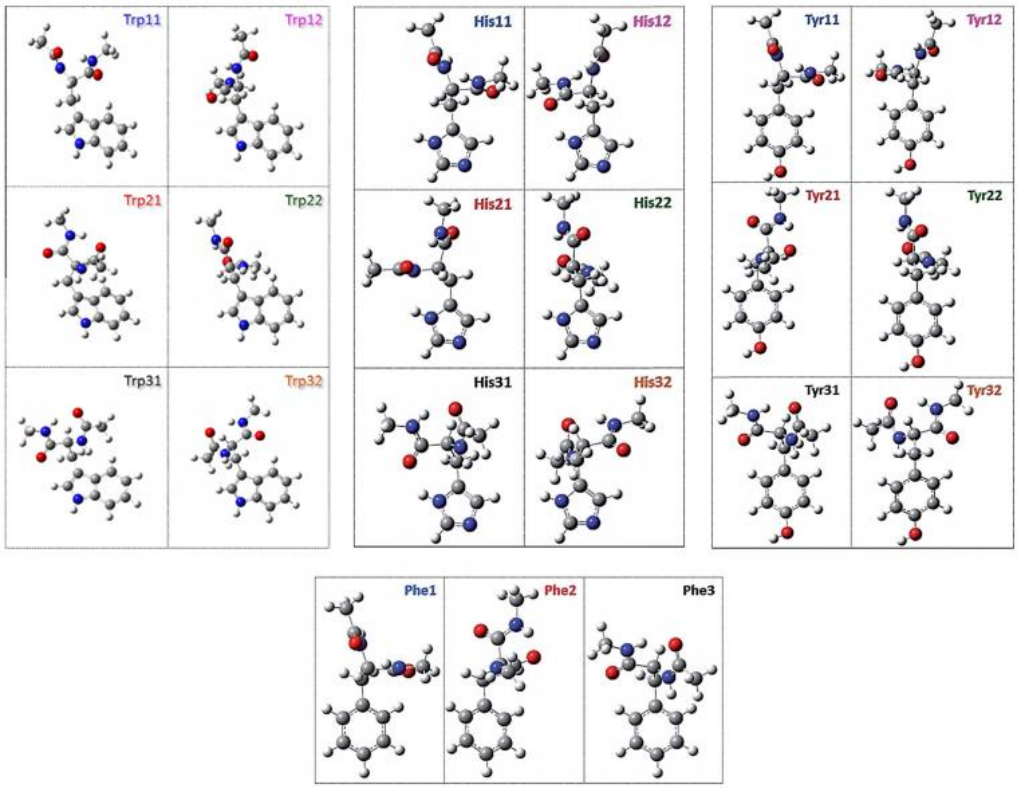


**Figure 4-2.** Stereochemical structures of L-tryptophan (left), L-histidine (middle), L-tyrosine (right), and L-phenylalanine (down) models in a random coil configuration. Optimizations were performed with DFT/B3LYP/6-311G(d) in gas phase using Gaussian 09.

All the optimized angles for each conformer are presented in Table 4-1, 4-2, 4-3, and 4-4. In these four tables, it is possible to observe rather important differences in the main-chain angles for different configurations of Trp, His, Tyr, and Phe residues within each conformation. This indicates that the main-chain angles are unquestionably modified by the side-chain configuration and *vice versa*. It is also noticeable that the differences in $\psi$ and $\phi$ are more significant in the β-strand conformation. All these distortions can be explained in terms of the allowable van der Waals distances which demarcate the areas of permissible $\psi$ and $\phi$[14]. In di-, tri-, and polypeptide chains, $\psi$ and $\phi$ configurations always take place inside the outer boundaries of the minimum contact distance assumed, and a clustering configuration can emerge. Every time the $C_\alpha$ atom under

analysis belongs to a glycyl residue the configuration is close to $180^0$ and 0, and whenever there is a $C_\beta$ atom the clustering is nearly $150^0$ and $120^0$ [14].

**Table 4-1.** Optimized Ramachandran dihedral angles ($\psi$ and $\phi$) for the main-chain amide group in L-tryptophan and the corresponding angles ($\chi_1$ and $\chi_2$) for the rotational conformers defining the residues (all in degree). Angles are reported for Trp residues in random-coil, α-Helix, β-Strand conformation.

| Main-Chain Configuration | Side-Chain Configuration | $\phi$ | $\Psi$ | $\chi_1$ | $\chi_2$ |
|---|---|---|---|---|---|
| Random-Coil | 11 | -83.471 | 82.593 | -158.563 | 91.512 |
| | 12 | -82.966 | 77.512 | -166.272 | -87.283 |
| | 21 | -84.319 | 74.654 | -48.569 | 115.644 |
| | 22 | -84.399 | 74.047 | -50.670 | -81.611 |
| | 31 | -82.982 | 61.423 | 47.298 | 82.202 |
| | 32 | -82.647 | 57.483 | 33.246 | -100.766 |
| β-Strand | 11 | -158.160 | 166.002 | -162.578 | 76.536 |
| | 12 | -156.552 | 167.449 | -159.615 | -112.542 |
| | 21 | -116.519 | 141.830 | -66.684 | 93.533 |
| | 22 | -122.377 | 148.637 | -69.516 | -69.516 |
| | 31 | -161.652 | 165.113 | 54.005 | 84.706 |
| | 32 | -152.524 | 166.940 | 63.883 | -81.269 |
| α-Helix | 11 | -60.228 | -41.015 | -170.505 | 91.407 |
| | 12 | -53.748 | -48.877 | -178.043 | -150.542 |
| | 21 | -60.895 | -40.981 | -57.735 | 112.973 |
| | 22 | -62.037 | -41.505 | -57.973 | -56.698 |
| | 31 | -64.587 | -36.570 | 37.802 | 81.708 |
| | 32 | -55.821 | -45.188 | 45.484 | -64.102 |

**Table 4-2**. Optimized Ramachandran dihedral angles ($\psi$ and $\phi$) for the main-chain amide group in L-hisditine and the corresponding angles ($\chi_1$ and $\chi_2$) for the rotational conformers defining the residues (all in degree). Angles are reported for His residues in random-coil, α-Helix, β-Strand configuration.

| Main-Chain Configuration | Side-Chain Configuration | $\phi$ | $\Psi$ | $\chi_1$ | $\chi_2$ |
|---|---|---|---|---|---|
| **Random-Coil** | **11** | -83.487 | 80.634 | -165.003 | 85.845 |
| | **12** | -83.211 | 70.474 | -170.189 | 110.403 |
| | **21** | -80.309 | 77.357 | -73.281 | 51.317 |
| | **22** | -84.619 | 72.924 | -49.889 | 113.134 |
| | **31** | -82.622 | 68.860 | 49.524 | -111.039 |
| | **32** | -83.272 | 65.803 | 43.188 | -117.085 |
| **β-Strand** | **11** | -162.708 | 171.775 | -125.454 | 61.882 |
| | **12** | -157.729 | 152.839 | -179.823 | 76.793 |
| | **21** | -118.667 | 136.089 | -65.477 | -14.878 |
| | **22** | -132.038 | 153.333 | -57.576 | -26.088 |
| | **31** | -149.376 | 132.726 | 60.646 | -49.944 |
| | **32** | -150.902 | 175.458 | 68.070 | -60.460 |
| **α-Helix** | **11** | -61.041 | -41.509 | -165.419 | 139.644 |
| | **12** | -61.932 | -41.118 | -171.243 | 176.085 |
| | **21** | -60.080 | -41.501 | -73.144 | -4.945 |
| | **22** | -63.000 | -40.556 | -71.054 | 31.273 |
| | **31** | -58.168 | -46.167 | 56.581 | -110.636 |
| | **32** | -61.461 | -40.596 | 52.179 | -99.841 |

**Table 4-3**. Optimized Ramachandran dihedral angles (ψ and ϕ) for the main-chain amide group in L-tyrosine and the corresponding angles ($\chi_1$ and $\chi_2$) for the rotational conformers defining the residues (all in degree). Angles are reported for Tyr residues in random-coil, α-Helix, β-Strand configuration.

| Main-Chain Configuration | Side-Chain Configuration | ϕ | Ψ | $\chi_1$ | $\chi_2$ |
|---|---|---|---|---|---|
| Random-Coil | 11 | -83.172 | 79.274 | -163.680 | 91.593 |
| | 12 | -83.164 | 78.822 | -163.729 | 90.941 |
| | 21 | -84.599 | 73.952 | -54.497 | -67.299 |
| | 22 | -84.605 | 73.564 | -55.577 | 109.712 |
| | 31 | -82.998 | 60.807 | 42.379 | -101.330 |
| | 32 | -82.938 | 60.709 | 41.995 | -102.427 |
| β-Strand | 11 | -158.147 | 164.174 | -161.169 | 71.103 |
| | 12 | -157.355 | 161.546 | -164.719 | 70.301 |
| | 21 | -117.278 | 140.859 | -61.060 | 96.373 |
| | 22 | -124.004 | 143.438 | -57.805 | 98.939 |
| | 31 | -153.901 | 166.312 | 59.342 | -91.861 |
| | 32 | -154.404 | 167.351 | 59.864 | -91.742 |
| α-Helix | 11 | -56.374 | -41.444 | -179.701 | 109.164 |
| | 12 | -55.709 | -41.421 | -179.407 | 89.914 |
| | 21 | -58.532 | -40.313 | -48.846 | 97.869 |
| | 22 | -58.947 | -40.619 | -43.136 | 102.711 |
| | 31 | -55.253 | -41.267 | 54.833 | -75.374 |
| | 32 | -53.901 | -41.385 | 61.283 | -89.946 |

**Table 4-4.** Optimized Ramachandran dihedral angles ($\psi$ and $\phi$) for the main-chain amide group in L-phenylalanine and the corresponding angles ($\chi_1$ and $\chi_2$) for the rotational conformers defining the residues (all in degree). Angles are reported for Phe residues in random coil, α-Helix, β-Strand configuration.

| Main-Chain Configuration | Side-Chain Configuration | $\phi$ | $\Psi$ | $\chi_1$ | $\chi_2$ |
|---|---|---|---|---|---|
| Random-Coil | 1 | -83.220 | 79.360 | -163.256 | 89.235 |
| | 2 | -84.603 | 73.399 | -55.295 | 111.016 |
| | 3 | -83.005 | 60.863 | 41.819 | -101.829 |
| β-Strand | 1 | -157.892 | 161.490 | -164.491 | 70.138 |
| | 2 | -116.854 | 139.585 | -60.891 | 96.454 |
| | 3 | -154.392 | 166.737 | 60.085 | -90.473 |
| α-Helix | 1 | -72.924 | -41.633 | 173.254 | -109.940 |
| | 2 | -57.545 | -40.589 | -69.998 | 131.189 |
| | 3 | -61.588 | -40.714 | 52.867 | -95.292 |

After having optimized the structures of all residues of the left-handed isomers of Trp, His, Tyr, and Phe, in each backbone configuration (α-helix, β-strand and random coil), we computed their TPA and TPCD spectra within the two-photon excitation wavelength range comprising 220 nm to 500 nm (in the OPA scale this range corresponds to a wavelength range from 110 nm to 250 nm). The convoluted spectra were calculated using CAM-B3LYP[16]/6-311G(d)[11, 12] in Dalton 2011[17] and with $\Gamma$ = 0.124 eV (FWHM) (theoretical spectra calculated with B3LYP[8-10]/6-311G(d)[11, 12] can be found in SI).

First, we examine the effect of the side-chains onto the TPA and TPCD spectra of Trp, His, Phe, and Tyr residues, in their corresponding β-strand, α-helix, and random coil configurations (see Figures 4–3 to 4-12).

The direct comparison between the corresponding spectra of pair of conformers (Figures 4-3 to 4-5) with equal $\chi_1$ revealed relatively mild differences for TPA opposed to significantly large variations for TPCD. The only exceptions in TPA were Trp31 and Trp32 in α-helix, and Trp21 and Trp22 in β-strand, which presented significant dissimilarities on the red side of the spectrum. However, in TPCD we could see specific bands with opposite sign (spectral signatures) between pairs of residues for all the structures. This was not totally unexpected after having recognized that TPCD is very sensitivity to small peptide structural distortions such as side-chain conformational angles and bond lengths of residues[26], and Ramachandran dihedral angles[14]. Second, the characteristic fingerprints became more apparent and numerous in the ECD blind region, i.e. $\lambda_{TPA}$ < 400 nm ($\lambda_{OPA}$ < 200 nm). In fact, it is in this region where the TPA cross-section of typical aromatic amino acid and their residues becomes the largest, thus making it possible to measure the relatively small TPCD signals[2]. Third, the comparison between TPA and TPCD spectra of all the conformers (Trp11, Trp12, Trp21, Trp22, Trp31 and Trp32) in each protein configuration (Figures 4-3 to 4-5) showed remarkable differences in specific spectral ranges that would allow to identifying particular conformation and specific amino acid residues in relatively complex structures such as peptides and proteins.

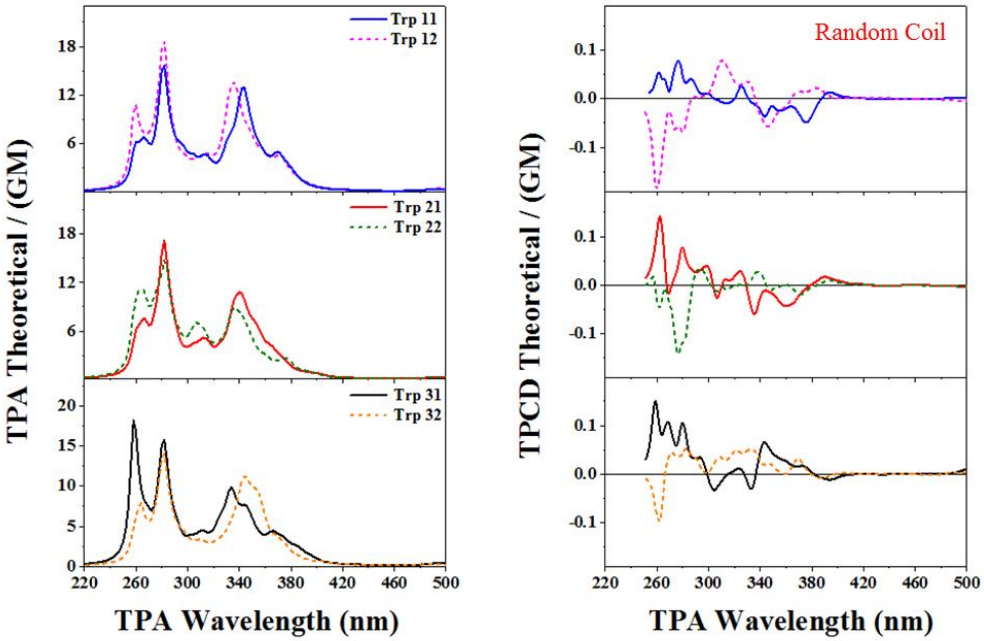


**Figure 4-3**. Comparative plots of TPA (left) and TPCD (right) spectra of L-tryptophan models in random-coil configuration. Trp11 and Trp12 (top), Trp21 and Trp22 (middle), Trp31 and Trp32 (bottom). TPA and TPCD response for the lowest 80 electronic excited states of all optimized structures were computed with TD-DFT/CAM-B3LYP/6-311G(d) in gas phase using Dalton 2011.

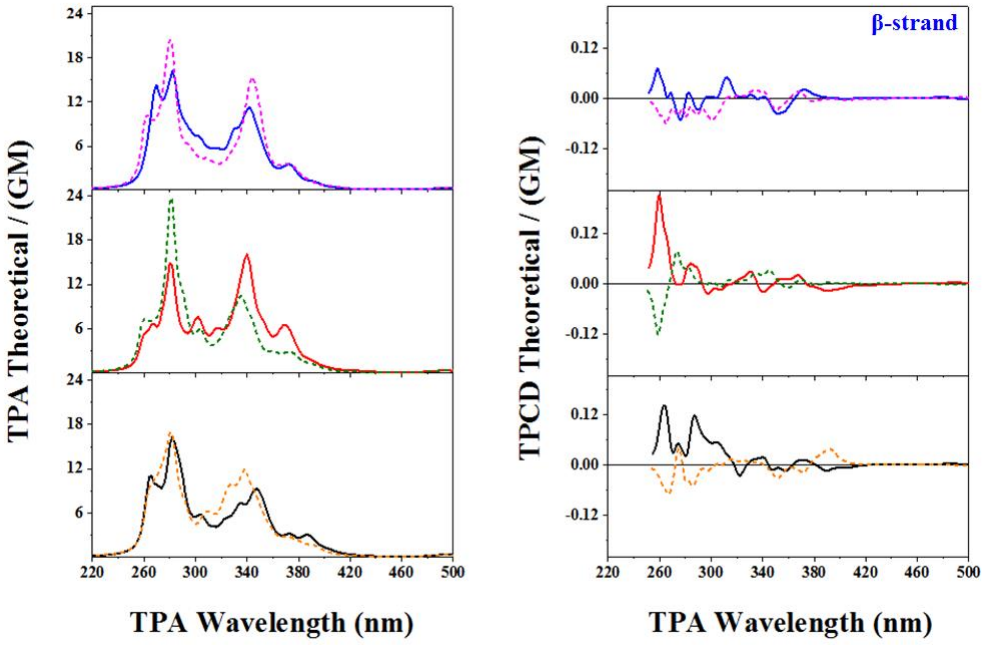


**Figure 4-4.** Comparative plots of TPA (left) and TPCD (right) spectra of L-tryptophan models in $\beta$-strand configuration. Trp11 and Trp12 (top), Trp21 and Trp22 (middle), Trp31 and Trp32 (bottom). TPA and TPCD response for the lowest 80 electronic excited states of all optimized structures were computed with TD-DFT/CAM-B3LYP/6-311G(d) in gas phase using Dalton 2011.

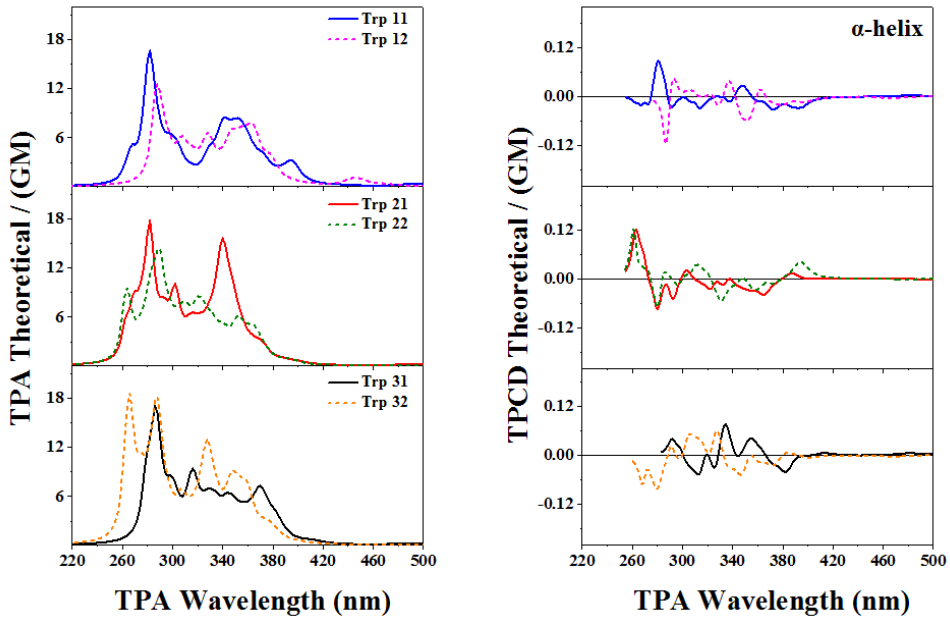


**Figure 4-5.** Comparative plots of TPA (left) and TPCD (right) spectra of L-tryptophan modelsin α-helix configuration. Trp11 and Trp12 (top), Trp21 and Trp22 (middle), Trp31 and Trp32 (bottom). TPA and TPCD response of all optimized structures were computed with TD-DFT/CAM-B3LYP/6-311G(d) in gas phase using Dalton 2011.

In the case of His (Figure 4-6 to 4-8), the same straight comparison uncovered moderately mild differences for TPA, in contrast to considerably big variations in TPCD. The largest difference in TPA is noticed between His11 and His12 in β-strand, which exhibited a noteworthy variation in the peak located at 252 nm. The fact that TPCD is a technique recognized for its sensitivity to small peptide structural distortions can be certified one more time by the occurrence of bands with opposite signs (spectral signatures) among residues of His. For instance, between His11 and His12 at 328 nm and 380 nm, and between His31 and His32 within the spectral region 280-350 nm, there were clear variations in β-strand. In α-helix and random coil, the residues of His look very similar. This made it challenging to distinguish between a pair of conformers with same $\chi_1$. These TPCD spectra also presented some exceptions, specifically in His31 and His32 in α-helix within a wavelength range of 300-340 nm as well as in His11 and His12 in the region between 240 and 260 nm in random coil, where the TPCD signal acquired an opposite sign.

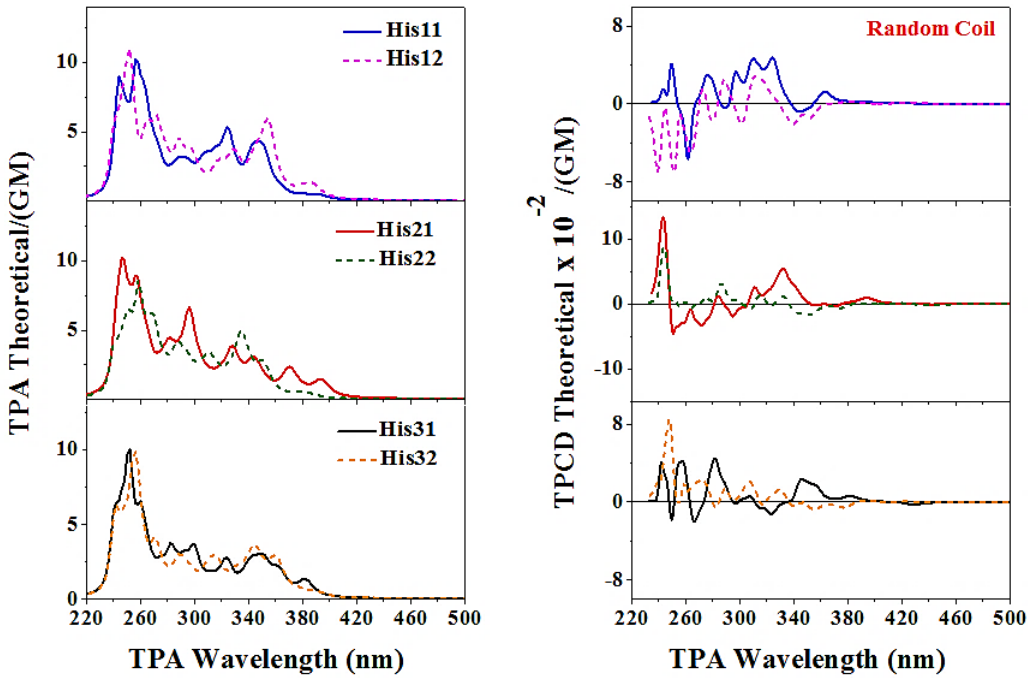


**Figure 4-6.** Comparative plots of TPA (left) and TPCD (right) spectra of L-histidine models in random coil configuration. His11 and His12 (top), His21 and His22 (middle), His31 and His32 (bottom). TPA and TPCD response for the lowest 80 electronic excited states of optimized structures were computed with TD-DFT/ CAM-B3LYP/6-311G(d) in gas phase using Dalton 2011.

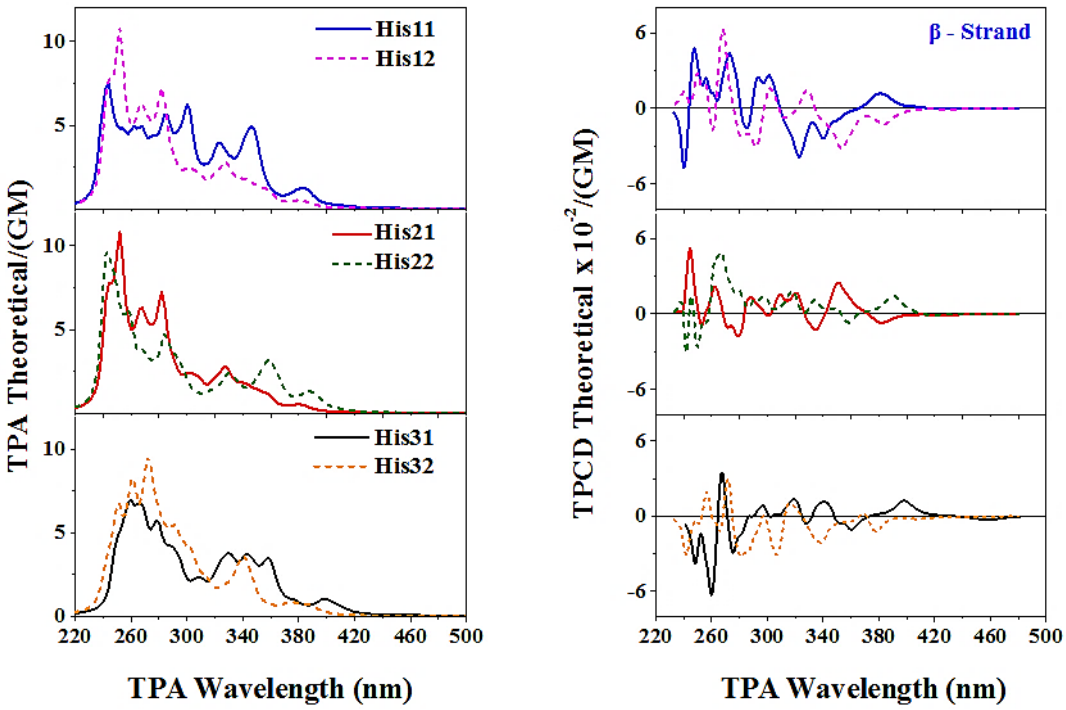


**Figure 4-7**. Comparative plots of TPA (left) and TPCD (right) spectra of L-histidine modelsin β-strand configuration. His11 and His12 (top), His21 and His22 (middle), His31 and His32 (bottom). TPA and TPCD response for the lowest 80 electronic excited states of all optimized structures were computed with TD-DFT/ CAM-B3LYP/6-311G(d) in gas phase using Dalton 2011.

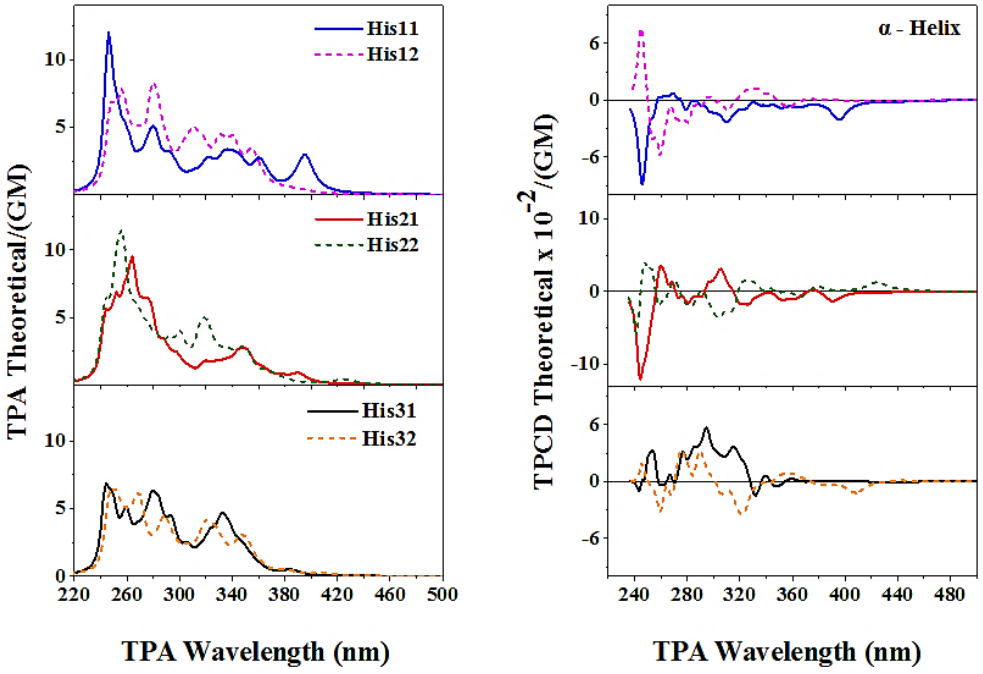


**Figure 4-8.** Comparative plots of TPA (left) and TPCD (right) spectra of L-histidine modelsin α-helix configuration. His11 and His12 (top), His21 and His22 (middle), His31 and His32 (bottom). TPA and TPCD response for the lowest 80 electronic excited states of all optimized structures were computed with TD-DFT/ CAM-B3LYP/6-311G(d) in gas phase using Dalton 2011.

With regard to Phe, in Figure 4-9 we could see differences in the TPA and TPCD spectra of the three conformers in each configuration. First, in the TPA spectra of all the conformers in β-strand, α-helix, and Random coil, we distinguished the following different spectral features between 280 and 340 nm: i) β-strand: a strong band centered at 330 nm for Phe1 and two strong bands at approximately 300 nm and 340 nm for Phe2, ii) α-helix: a strong band centered at ~ 300 nm for Phe2, and iii) Random coil: a double band with peaks at ca. 300 nm and 315 nm for Phe1. Second, the TPCD spectra of this amino acid in β-strand revealed evident differences in spectral signatures between the three residues, i.e. alternating sign signals for each conformer within the wavelength range between 300 nm to 380 nm. In α-helix, though, the situation was slightly different, while Phe1 was distinguishable from the rest of the residues through specific negative

sign features observed at 250 nm and 280 nm, in Phe2 the differentiation was more obvious at ca. 300 nm where the sign of the characteristic TPCD spectra was opposite for analogous conformers. The same trend could be notorious in random coil where the identification of the Phe1 residue was possible through its opposite sign TPCD signals between 260 nm and 290 nm.

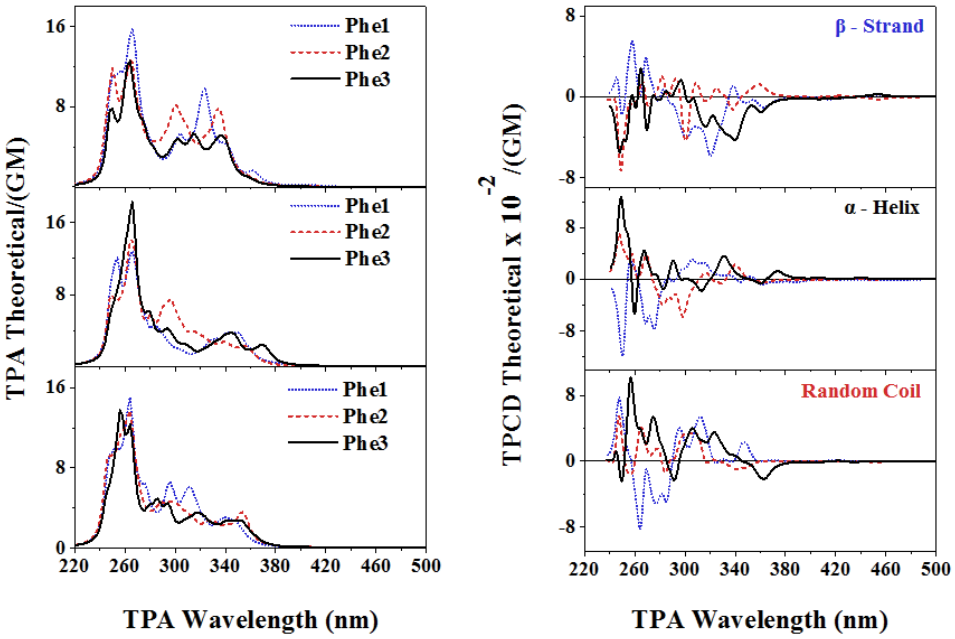


**Figure 4-9.** Comparative plots of TPA (left) and TPCD (right) spectra of L-phenylalanine models in β-strand(top), α-helix (middle), and random coil (bottom) configuration. TPA and TPCD response for the lowest 80 electronic excited states of all optimized structures were computed with TD-DFT/ CAM-B3LYP/6-311G(d) in gas phase using Dalton 2011.

Concerning Tyr (Figures 4-10 to 4-12), it was interesting to highlight the fact that the TPA spectra of all its residues were virtually identical. Likewise, the TPCD spectra of Tyr residues in β-strand and Random coil were very similar between pairs of conformers. However, the TPCD spectra of equivalent conformers in α-helix revealed small but noticeable differences between Tyr11 and Tyr12, and Tyr31 and Tyr32 - distinct peaks between 300 nm and 380 nm.

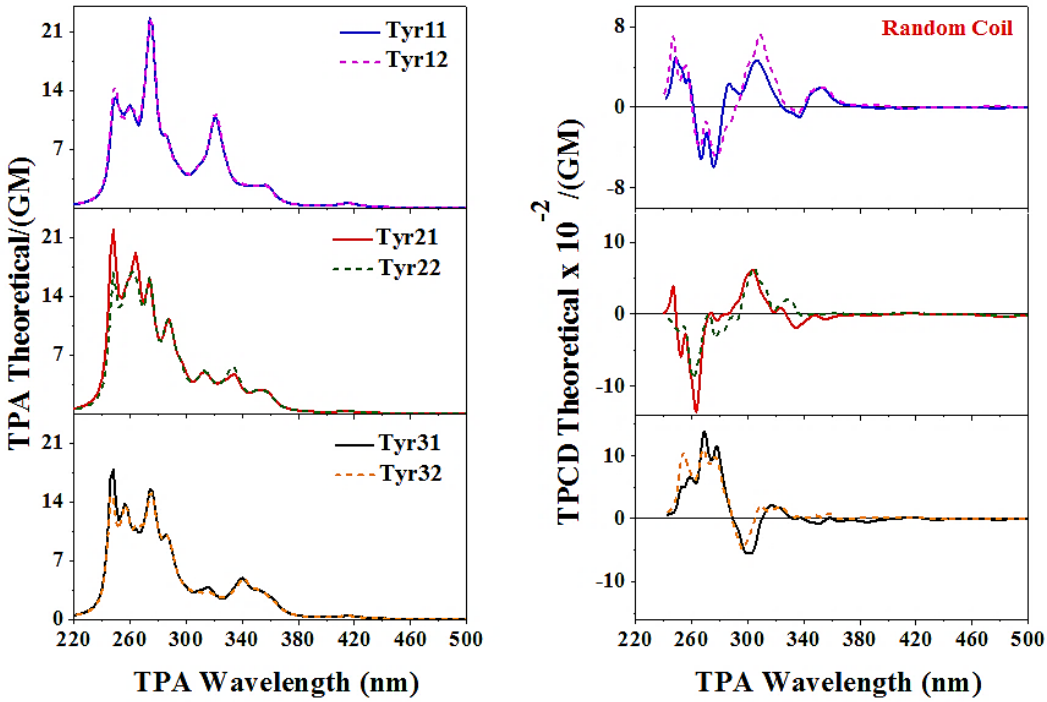


**Figure 4-10.** Comparative plots of TPA (left) and TPCD (right) spectra of L-tyrosine models in random coil configuration. Tyr11 and Tyr12 (top), Tyr21 and Tyr22 (middle), Tyr31 and Tyr32 (bottom). TPA and TPCD response for the lowest 80 electronic excited states of all optimized structures were computed with TD-DFT/ CAM-B3LYP/6-311G(d) in gas phase using Dalton 2011.

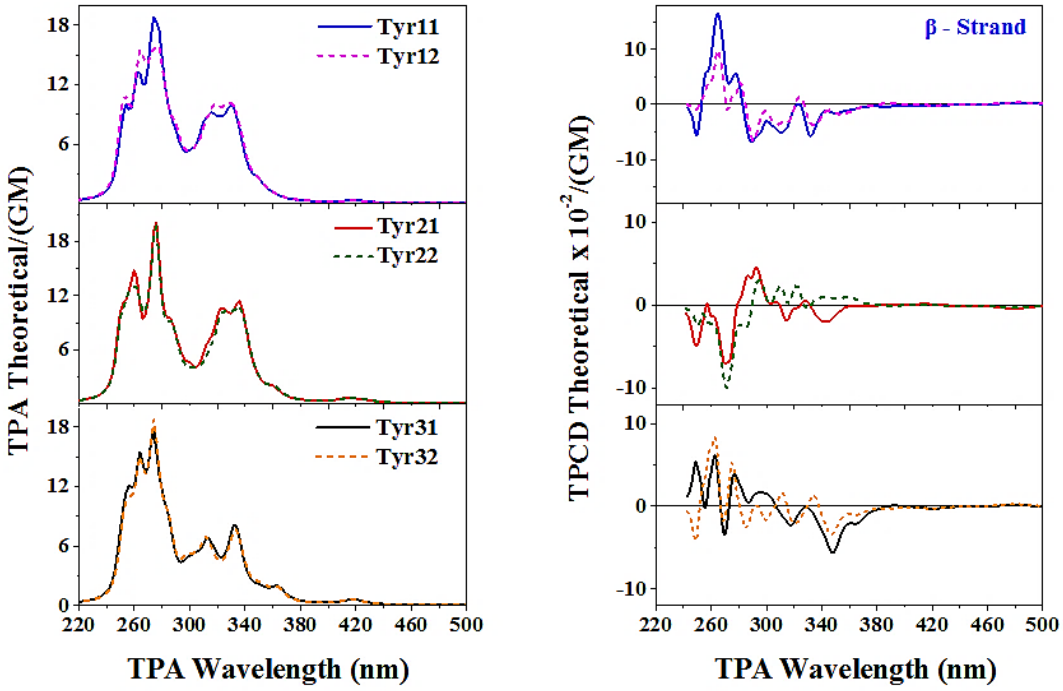


**Figure 4-11.** Comparative plots of TPA (left) and TPCD (right) spectra of L-tyrosine modelsin β-strand configuration. Tyr11 and Tyr12 (top), Tyr21 and Tyr22 (middle), Tyr31 and Tyr32 (bottom). TPA and TPCD response for the lowest 80 electronic excited states of all optimized structures were computed with TD-DFT/CAM-B3LYP/6-311G(d) in gas phase using Dalton 2011.

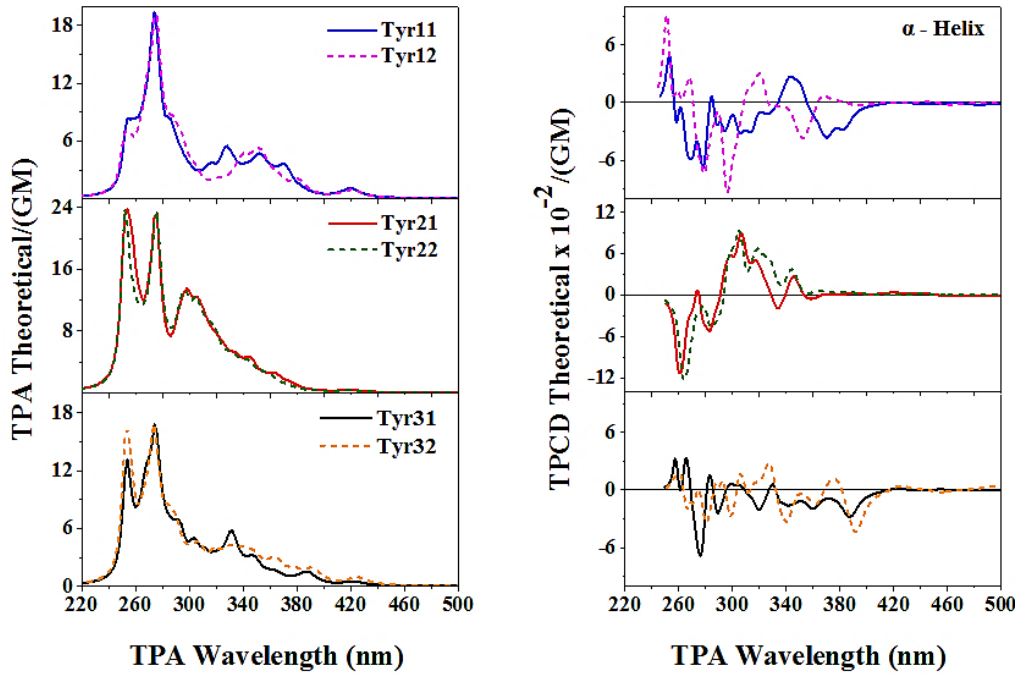


**Figure 4-12.** Comparative plots of TPA (left) and TPCD (right) spectra of L-tyrosine modelsin α-helix configuration. TPA and TPCD response for the lowest 80 electronic excited states of all optimized structures were computed with TD-DFT/ CAM-B3LYP/6-311G(d) in gas phase using Dalton 2011.

In summary, we recognized that TPCD, contrary to standard ECD [18], allows us to distinguish between pairs of conformers of amino acid residues in different secondary protein configurations, mainly in Trp and His.

Afterward, we analyzed the effect of the main-chains onto the TPA and TPCD spectra of Trp, His, Phe, and Tyr residues in α-helix, β-strand, and random coil conformations. In Figures 4-13 to 4-16, we present, in a comparative fashion, the corresponding linear and nonlinear absorption and CD spectra of Trp11, His11, Phe1, and Tyr11 residues calculated with CAM-B3LYP (the comparative plots of all the remaining His$\chi_1\chi_2$, Phe$\chi_1$, and Tyr$\chi_1\chi_2$ residues, calculated with CAM-B3LYP and B3LYP can be found in Appendix D). In order to facilitate the comparison between the linear and nonlinear spectra, OPA wavelength is used for both cases throughout the discussion

of Figures 4-13 to 4-16.

Before beginning the discussion in this section, it is worth noting that all four amino acids present more distinguishable and measurable variations in the nonlinear absorption spectra, TPA and TPCD, of the different conformations than in their corresponding linear counterpart, OPA and ECD.

First, in Figure 4-13 we display a comparative plot of all the mentioned spectra of the Trp11 residue in α-helix, β-strand and random coil conformations (the same analysis for all the remaining Trp$\chi_1\chi_2$ residues can be found in Appendix D). The TPA spectra of this amino acid in all three conformations look very similar regarding spectral features. On the contrary, the TPCD spectra exposed very specific spectral features that allowed us to identify them. Among the most important characteristics, we can mention: i) a negative band in the red side of the spectrum at ~ 200 nm in α-helix, ii) a specific positive band at approximately 200 nm in β-strand, and iii) two clear strong bands at ~ 150 nm and 190 nm in random coil. The presence of these specific bands, that allowed the recognition of the different configurations using Trp residues, revealed the applicability of TPCD as a complementary technique to ECD for the study of complex protein structures.

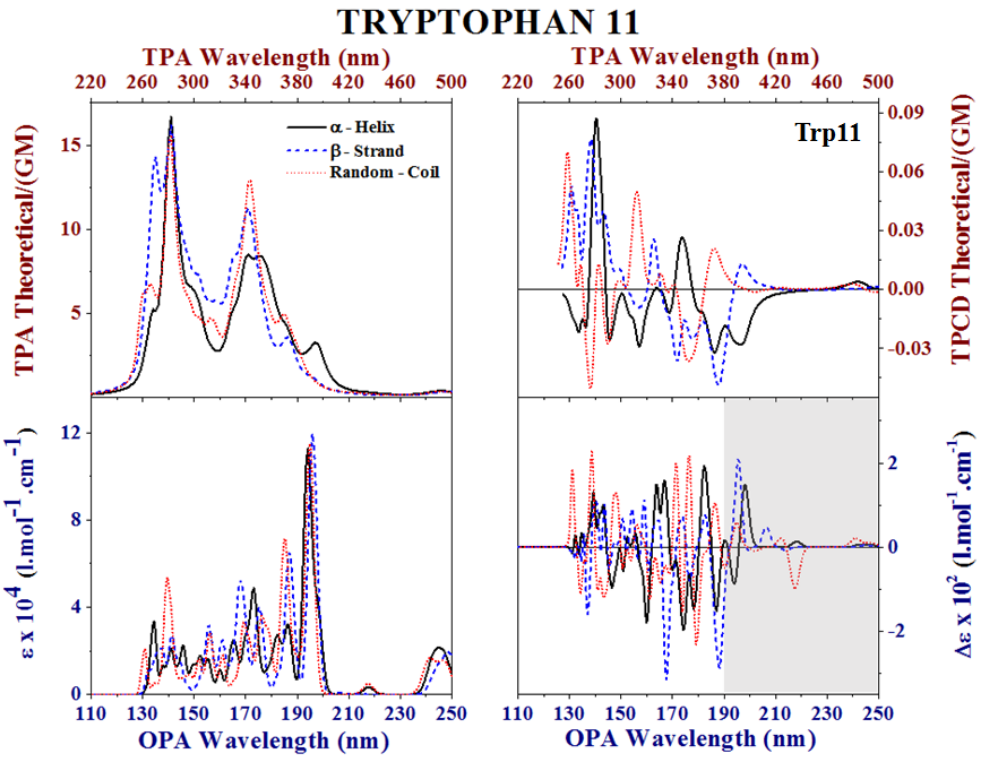


**Figure 4-13**. Comparative plots of TPA (top left), TPCD (top right), OPA (bottom left), and ECD (bottom right) spectraof Trp11 in random coil (red dotted line), α-helix (black solid line) and β-strand (blue dashed line) configuration. TPA and TPCD response for the lowest 80 electronic excited states of all optimized structures were computed with TD-DFT/ CAM-B3LYP/6-311G(d) in gas phase using Dalton 2011. OPA and ECD for the lowest 80 electronic excited states were computed of all optimized structures at the CAM-B3LYP/6-311G(d) level of theory using Gaussian 09 in gas phase. Shaded area indicates where ECD is truly functional.

Second, in the TPA spectra of His11 (Figure 4-14) (the same analysis for all the remaining His$\chi_1\chi_2$ residues can be found in Appendix D) we precisely identified its presence in all three different conformations through: i) the longer wavelength band at ~ 200 nm in the α-helix, ii) a double peak broad band between 140 nm and 160 nm in β-strand, and iii) the very specific band in the blue side of the spectrum at ~ 130 nm in random coil. On the other hand, in the TPCD spectra of the same amino acid residue, in all three different configurations, the following spectral fingerprints were observed: i) a strong negative band in the red side of the spectrum at ~ 200 nm

in α-helix, ii) a specific negative double band between 160 nm and 180 nm in β-strand, and iii) a clearly strong double peak band between 150 nm and 170 nm in random coil. Once more, the most noteworthy observations of this section are: first, the unique and identifiable fingerprints in all three configurations down to 110 nm, and second the accessibility to additional conformational information in the FUV.

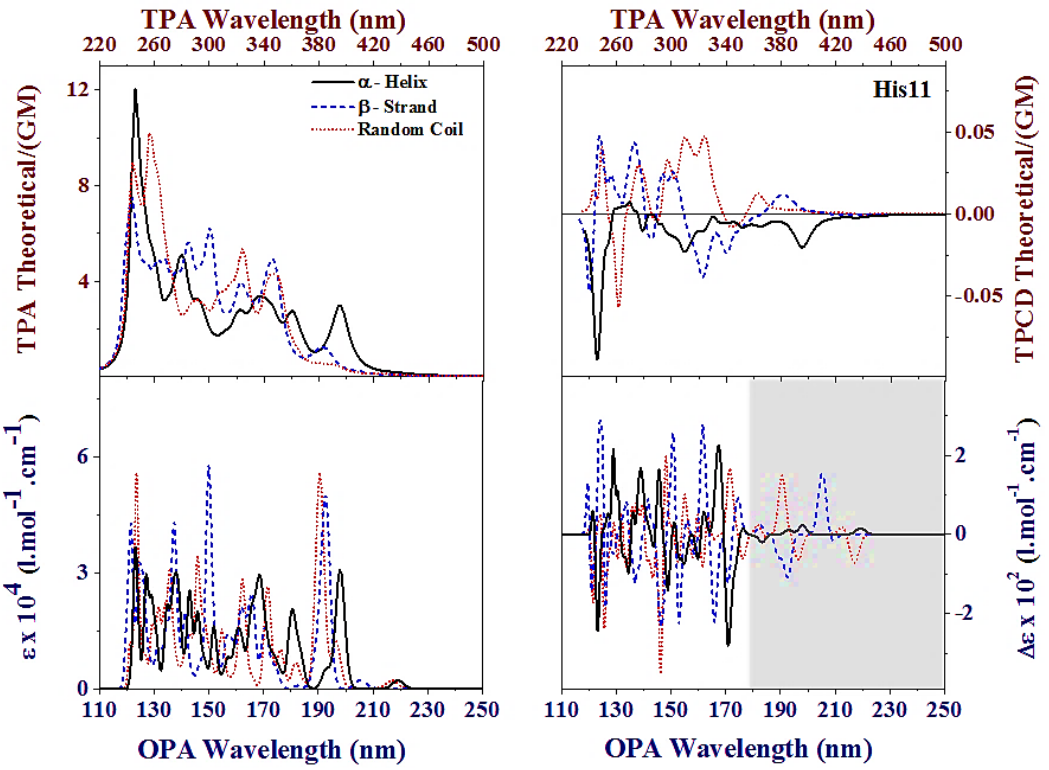


**Figure 4-14.** Comparative plots of TPA (top left), TPCD (top right), OPA (bottom left), and ECD (bottom right) spectra of His11in random coil (red dotted line), α-helix (black solid line) and β-strand (blue dashed line) configuration. TPA and TPCD response for the lowest 80 electronic excited states of all optimized structures were computed with TD-DFT/ CAM-B3LYP/6-311G(d) in gas phase using Dalton 2011. OPA and ECD for the lowest 80 electronic excited states were computed of all optimized structures at the CAM-B3LYP/6-311G(d) level of theory using Gaussian 09 in gas phase. Shaded area indicates where ECD is truly functional.

Third, in Phe1, (Figure 4-15) (the same analysis for all the remaining Phe $\chi_1$ residues can be found in Appendix D) we distinguished similar characteristics to those observed for Trp11 and

His11, i.e. less intricate nonlinear spectra down to 110 nm and the presence of specific bands for each conformation, mostly in the TPCD plot, that allowed the identification of one from another. Although, in TPA only the β-strand was distinguished from the other two configurations through a strong peak at ~ 165 nm, in TPCD characteristic signals with opposite sign allowed the identification of all three conformations independently. For instance, while β-strand presented a unique negative broad TPCD band between 150 nm and 180 nm, the other two configurations presented a positive one. To differentiate between α-helix and random coil, it is better to look at longer wavelengths (small positive band at ~ 175 nm) for the former and at very short wavelengths (sharp negative peak at ~ 125 nm) for the latter. Again, the most remarkable aspects of this analysis are, i) the unique and identifiable spectral signatures in all three configurations down to 110 nm, and ii) the accessibility to additional conformational information in the FUV. Even in the event were ECD becomes applicable for the conformational study of proteins in the FUV, the number of convoluted bands, overlapping with each other in that region, would limit its use in that spectral region - ECD is truly functional above ~ 180 nm.

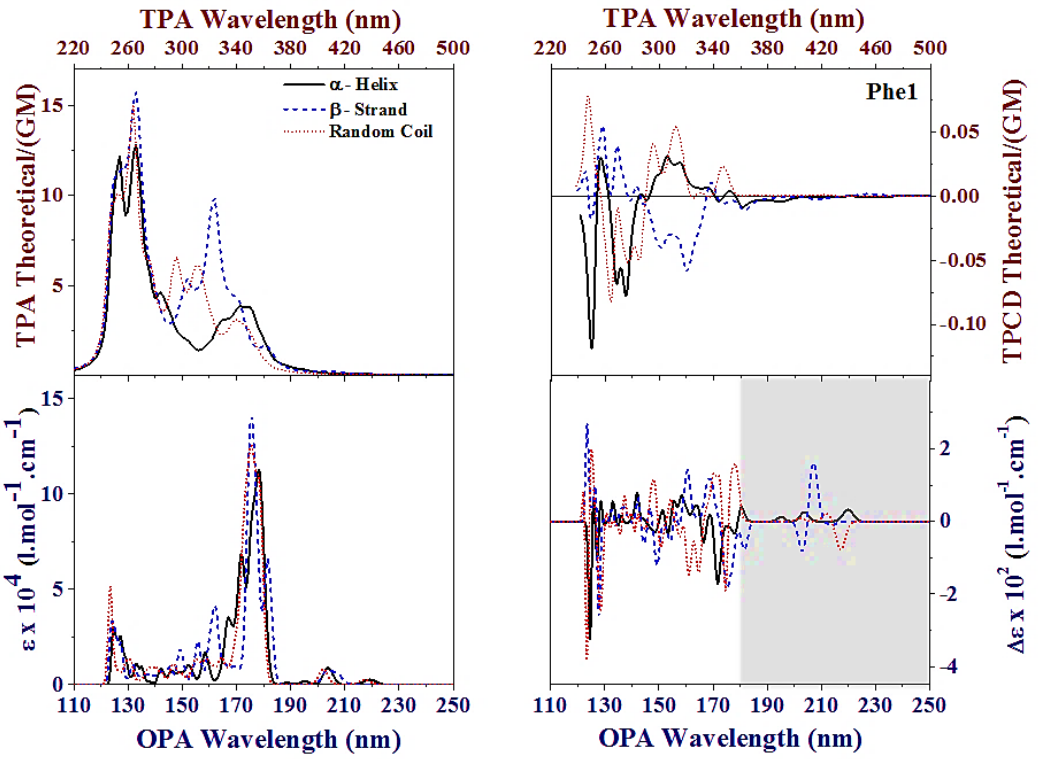


**Figure 4-15.** Comparative plots of TPA (top left), TPCD (top right), OPA (bottom left), and ECD (bottom right) spectra of Phe1 in random coil (red dotted line), α-helix (black solid line) and β-strand (blue dashed line) configuration. TPA and TPCD response for the lowest 80 electronic excited states of all optimized structures were computed with TD-DFT/ CAM-B3LYP/6-311G(d) in gas phase using Dalton 2011. OPA and ECD for the lowest 80 electronic excited states were computed of all optimized structures at the CAM-B3LYP/6-311G(d) level of theory using Gaussian 09 in gas phase. Shaded area indicates where ECD is truly functional.

Fourth, besides the already discussed characteristic nonlinear absorption fingerprints observed in Trp, His and Phe, we found that TPA in Tyr (Figure 4-16) (the same analysis for all the remaining Tyr$\chi_1\chi_2$ residues can be found in Appendix D) was not reliable for the differentiation between main-chain "back-bone" conformations. However, TPCD showed obvious differences in certain spectral regions to specifically identify all three conformations: i) α-helix: negative broad band in the red side of the spectrum above 170 nm, ii) β-strand: positive sharp peak at ~ 125 nm, and iii) random coil: positive broad band between 140 nm and 170 nm. One more time, it has been

proven that TPCD has all the potential as a tool for the identification between α-helix, β-strand, and random coil utilizing aromatic amino acid residues.

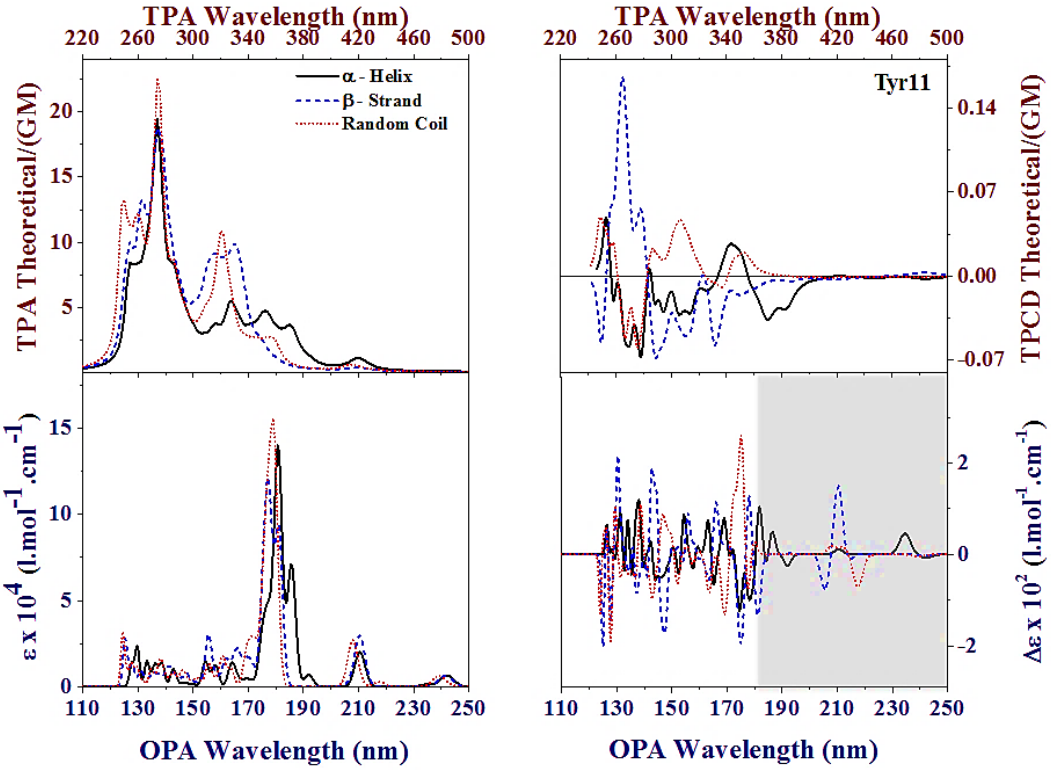


**Figure 4-16.** Comparative plots of TPA (top left), TPCD (top right), OPA (bottom left), and ECD (bottom right) spectraof Tyr11 in random coil (red dotted line), α-helix (black solid line) and β-strand (blue dashed line) configuration. TPA and TPCD response for the lowest 80 electronic excited states of all optimized structures were computed with TD-DFT/ CAM-B3LYP/6-311G(d) in gas phase using Dalton 2011. OPA and ECD for the lowest 80 electronic excited states were computed of all optimized structures at the CAM-B3LYP/6-311G(d) level of theory using Gaussian 09 in gas phase. Shaded area indicates where ECD is truly functional.

Finally, we present the direct comparison of the TPA and TPCD spectra on a set of two amino acid residues of Trp, His, Phe and Tyr (Trp11-His11-Phe1-Tyr11 and Trp21-His21-Phe2-Tyr21), in their corresponding β-strand, α-helix, and random coil configurations. As it was observed in Figures 4-17 to 4-19, they all exhibited clear spectral differences in TPA and TPCD, in each configuration. These signatures could be used, synergistically, for the conformational analysis of peptides and proteins in the FUV.

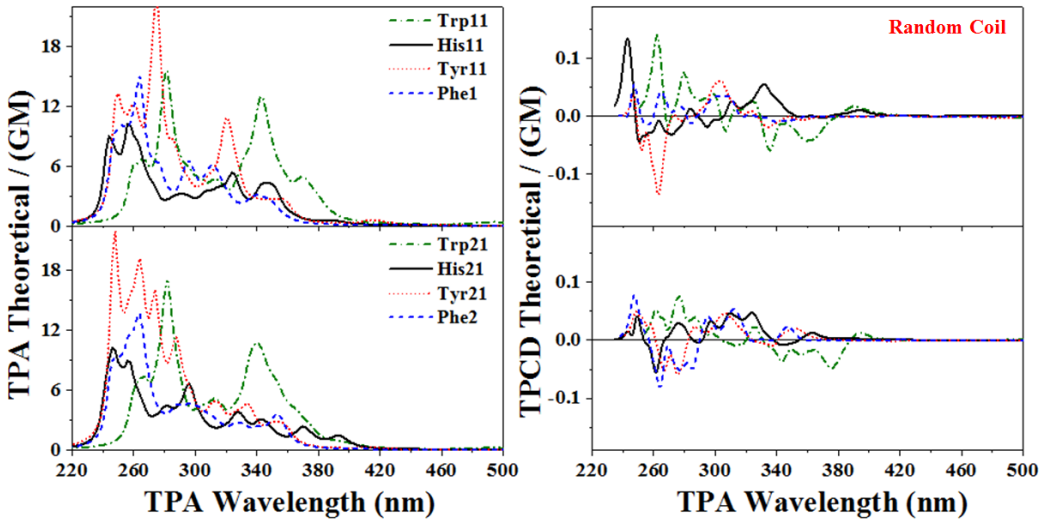


**Figure 4-17.** Comparative plots of TPA (left) and TPCD (right) spectra of Trp11 (green dashed-dotted line), His11 (black solid line), Phe1 (blue dashed line), and Tyr11 (red dotted line) (Top), and Trp21 (green dashed-dotted line), His21 (black solid line), Phe2 (blue dashed line), and Tyr21 (red dotted line) (Bottom), in random coil configuration. TPA and TPCD response for the lowest 80 electronic excited states of all optimized structures were computed with TD-DFT/ CAM-B3LYP/6-311G(d) in gas phase using Dalton 2011.

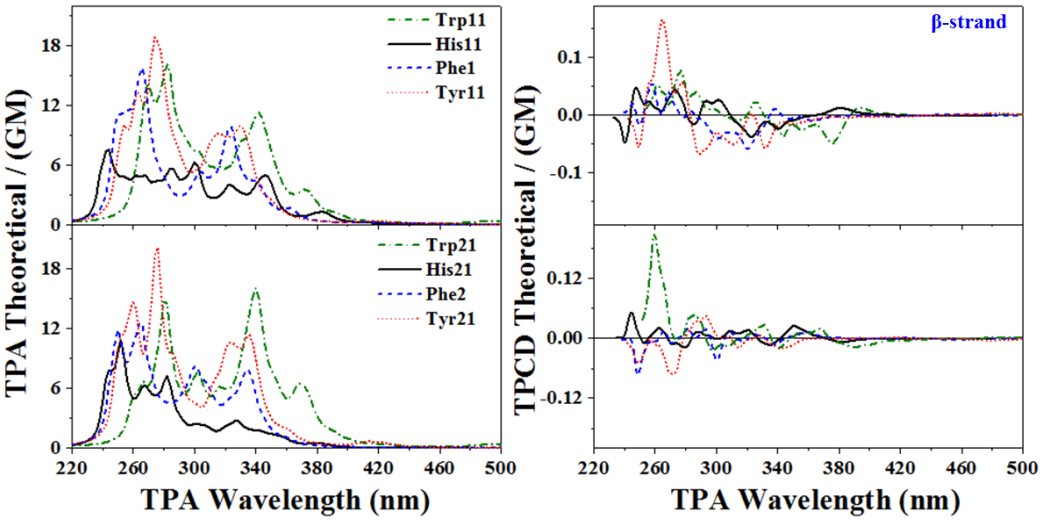


**Figure 4-18.** Comparative plots of TPA (left) and TPCD (right) spectra of Trp11 (green dash-dot line), His11 (black solid line), Phe1 (blue dashed line), and Tyr11 (red dotted line) (Top), and Trp21 (green dash-dot line), His21 (black solid line), Phe2 (blue dashed line), and Tyr21 (red dotted line) (Bottom), in β-strand configuration. TPA and TPCD response for the lowest 80 electronic excited states of all optimized structures were computed with TD-DFT/ CAM-B3LYP/6-311G(d) in gas phase using Dalton 2011.

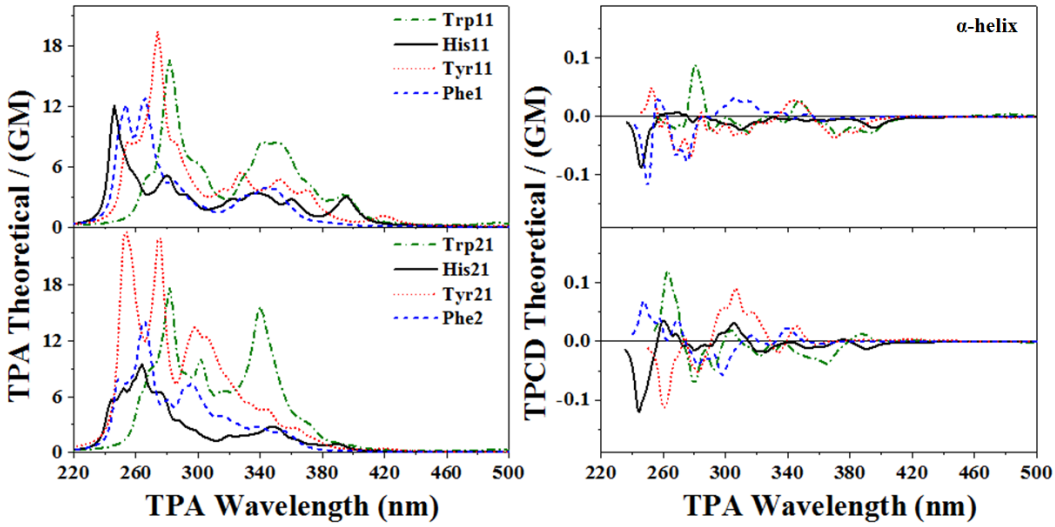


**Figure 4-19**. Comparative plots of TPA (left) and TPCD (right) spectra of Trp11 (green dash-dot line), His11 (black solid line), Phe1 (blue dashed line), and Tyr11 (red dotted line) (Top), and Trp21 (green dash-dot line), His21 (black solid line), Phe2 (blue dashed line), and Tyr21 (red dotted line) (Bottom), in α-helix configuration. TPA and TPCD response for the lowest 80 electronic excited states of all optimized structures were computed with TD-DFT/ CAM-B3LYP/6-311G(d) in gas phase using Dalton 2011.

Here, we assessed the potential of TPA spectroscopy for the conformational analysis of peptides and proteins examining the specific spectral signatures of aromatic amino acids in different configurations. In random coil it was possible to distinguish the following spectral signatures: two strong peaks centered at ~ 280 nm and 330 nm in Tyr11, a very broad band with defined spectral structure between 240 nm and 300 nm in Tyr21, a weak double band above ~ 360 nm in His21, and a peak at approximately 340 nm for Trp11 and Trp12. In β-strand, it was observed, simultaneously, the following complementary spectral fingerprints: a strong peak at ~ 270 nm in Tyr11, a small band at ~ 380 nm in His11, a sharp peak at ~ 280 nm in Tyr21, and a relatively intense band at ~ 370 nm in Trp21. In α-helix, the following complementary spectral features were detected: a strong peak at ~ 270 nm in Tyr11, a strong peak at approximately 280 nm in Trp11, a small band at ~ 390 nm in His11, an intense band at ~ 340 nm in Trp21, and a

broad band with two strong peaks at ~ 260 nm and 280 nm in Tyr21. Although, some peaks/bands are similar for different amino acid residues in different configurations, several others are very specific for each structural arrangement. Our outcome showed the limited but still useful potential of TPA for the targeted analysis.

Next, we present the examination of the TPCD spectra of the same amino acid residues, in the same protein secondary structures. As shown subsequently, our results revealed the exceptional spectroscopic ability of TPCD, compared to the traditional ECD, for the analysis of protein structures in a region where the overcrowded ECD spectra make the identification of complex structures using linear spectroscopy very difficult.

Using TPA we attempted to differentiate between protein secondary structures by looking for the following specific fingerprints in Tyr, i.e. a) β-strand: a band centered at ~ 340 nm with one shoulder on the red side of the spectrum in Trp11; b) Random coil: strong broad band with structure between ~ 240 nm and 300 nm in Tyr21; c) α-helix: broad band with two sharp peaks at ~ 250 nm and 280 nm in Tyr21. Other amino acid residues do not present such clear and differentiable signatures in TPA.

Using TPCD we clearly gathered conformational information from all three amino acids. For instance, β-strand could selectively be identified through specific positive or negative signatures at ~ 260 nm in Tyr11, 270 nm in Tyr21, 300 nm in His11 and 380 nm in Trp11; b) Random coil by measuring TPCD at ~ 260 nm and 300 nm in Tyr11, 240 nm and 330 nm in His11, and 260 nm and 360 nm in Trp11; c) α-helix through spectral bands at ~ 360 nm in Trp21, 240 nm in His21 and in Phe2, 260 nm in Tyr21. TPCD exposed its remarkable capability for the identification of molecules within the same protein structure using specific signatures of different aromatic amino acids, simultaneously.

## 4.4 Conclusions

The potential of TPCD for the study and analysis of complex chemical structures such as peptides and proteins in a region that is impenetrable using linear absorption processes was demonstrated. The specific signatures found in L-tryptophan, L-histidine, L-phenylalanine, and L-tyrosine residues, in β-strand, α–helix, and random coil configurations, validated the distinguishing ability of TPCD to differentiate between: i) very similar species with equal $\chi_1$, and ii) between equal or dissimilar species in different conformational configuration. The evaluation of the TPCD spectra of the re-optimized structures demonstrated that the main-chain angles are undeniably influenced by the side-chain configuration and *vice versa*. Through the determination of the TPCD signal of multiple amino acids simultaneously we gathered multi-parametric data to certify the existence of a specific conformation and assessed a small distortion of the same in the FUV. Finally, we should mention that in some cases the TPA spectra provide additional conformational information that can be used for the study of amino acid residues.

## 4.5 References


1. De Boni, L.; Toro, C.; Hernandez, F. E., Synchronized Double L-Scan Technique for the Simultaneous Measurement of Polarization-Dependent Two-Photon Absorption in Chiral Molecules. *Optics Letters* **2008,** *33*, 2958-2960.
2. Toro, C.; De Boni, L.; Lin, N.; Santoro, F.; Rizzo, A.; Hernandez, F. E., Two-Photon Absorption Circular Dichroism: A New Twist in Nonlinear Spectroscopy. *Chemistry - A European Journal* **2010,** *16*, 3504-9.
3. Díaz, C.; Echevarria, L.; Rizzo, A.; Hernández, F. E., Two-Photon Circular Dichroism of an Axially Dissymmetric Diphosphine Ligand with Strong Intramolecular Charge Transfer. *The Journal of Physical Chemistry A* **2014,** *118* (5), 940-946.
4. Diaz, C.; Lin, N.; Toro, C.; Passier, R.; Rizzo, A.; Hernández, F. E., The Effect of the π-Electron Delocalization Curvature on the Two-Photon Circular Dichroism of Molecules with Axial Chirality. *The Journal of Physical Chemistry Letters* **2012,** *3*, 1808-1813.
5. Diaz, C.; Vesga, Y.; Echevarria, L.; Stará, I. G.; Starỳ, I.; Anger, E.; Shen, C.; Moussa, M. E. S.; Vanthuyne, N.; Crassous, J., et al., Two-photon absorption and two-photon circular dichroism of hexahelicene derivatives: a study of the effect of the nature of intramolecular charge transfer. *RSC Advances* **2015,** *5* (23), 17429-17437.
6. Vesga, Y.; Hernandez, F. E., Study of the Effect of the Pulse-Width of the Excitation Source on the Two-Photon Absorption and Two-Photon Circular Dichroism Spectra of Biaryl Derivatives. *The Journal of Physical Chemistry A* **2016**.
7. Runge, E.; Gross, E. K. U., Density-Functional Theory for Time-Dependent Systems. *Physical Review Letters* **1984,** *52*, 997-1000.
8. Becke, A. D., Density-Functional Exchange-Energy Approximation with Correct Asymptotic Behavior. *Physical Review A* **1988,** *38*, 3098-3100.
9. Becke, A. D., Density-Functional Thermochemistry. III. The Role of Exact Exchange. *Journal of*

*Chemical Physics* **1993,** *98*, 5648-5652.

10. Lee, C.; Yang, W.; Parr, R. G., Development of the Colle-Salvetti Correlation-Energy Formula into a Functional of the Electron Density. *Physical Review B: Condensed Matter* **1988,** *37*, 785-789.
11. Krishnan, R.; Binkley, J. S.; Seeger, R.; Pople, J. A., Self-Consistent Molecular Orbital Methods. XX. A Basis Set for Correlated Wave Functions. *The Journal of Chemical Physics* **1980,** *72* (1), 650-654.
12. McLean, A. D.; Chandler, G. S., Contracted Gaussian basis sets for molecular calculations. I. Second row atoms, Z=11–18. *The Journal of Chemical Physics* **1980,** *72* (10), 5639-5648.
13. Frisch, M. J.; Trucks, G. W.; Schlegel, H. B.; Scuseria, G. E.; Robb, M. A.; Cheeseman, J. R.; Scalmani, G.; Barone, V.; Mennucci, B.; Petersson, G. A., et al., Gaussian 09, Revision A.1. Gaussian, Inc.: Wallingford CT, 2009.
14. Ramachandran, G. N.; Ramakrishnan, C.; Sasisekharan, V., Stereochemistry of polypeptide chain configurations. *Journal of molecular biology* **1963,** *7*, 95-99.
15. Miles, A. J.; Wallace, B. A., Synchrotron Radiation Circular Dichroism Spectroscopy of Proteins and Applications in Structural and Functional Genomics. *Chemical Society reviews* **2006,** *35*, 39-51.
16. Yanai, T.; Tew, D. P.; Handy, N. C., A new Hybrid Exchange-Correlation Functional using the Coulomb-Attenuating Method (CAM-B3LYP). *Chemical Physics Letters* **2004,** *393*, 51-57.
17. DALTON *A Molecular Electronic Sstructure Program, Release Dalton 2011, see* http://daltonprogram.org/, 2011.
18. Tanaka, T.; Kodama, T. S.; Morita, H. E.; Ohno, T., Electronic and vibrational circular dichroism of aromatic amino acids by density functional theory. *Chirality* **2006,** *18* (8), 652-61.
19. Meierhenrich, U. J.; Filippi, J.-J.; Meinert, C.; Bredehöft, J. H.; Takahashi, J.-i.; Nahon, L.; Jones,

N. C.; Hoffmann, S. V., Circular Dichroism of Amino Acids in the Vacuum-Ultraviolet Region. *Angewandte Chemie International Edition* **2010,** *49* (42), 7799-7802.

20. Jansík, B.; Rizzo, A.; Agren, H., Ab Initio Study of the Two-Photon Circular Dichroism in Chiral Natural Amino Acids. *journal of physical chemistry. B* **2007,** *111*, 446-60.
21. Lin, N.; Santoro, F.; Zhao, X.; Toro, C.; De Boni, L.; Hernández, F. E.; Rizzo, A., Computational Challenges in Simulating and Analyzing Experimental Linear and Nonlinear Circular Dichroism Spectra. R-(+)-1,1'-bis(2-naphthol) as a Prototype Case. *journal of physical chemistry. B* **2011,** *115*, 811-24.
22. Kristensen, K.; Kauczor, J.; Kjærgaard, T.; Jørgensen, P., Quasienergy formulation of damped response theory. *The Journal of Chemical Physics* **2009,** *131* (4), 044112.
23. Barone, V., *Computational Strategies for Spectroscopy: from Small Molecules to Nano Systems*. John Wiley & Sons: Hoboken, NJ, 2012; p 77-135.
24. Kristensen, K.; Kauczor, J.; Thorvaldsen, A. J.; Jørgensen, P.; Kjærgaard, T.; Rizzo, A., Damped Response Theory Description of Two-Photon Absorption. *The Journal of Chemical Physics* **2011,** *134* (21), 214104.
25. Aidas, K.; Angeli, C.; Bak, K. L.; Bakken, V.; Bast, R.; Boman, L.; Christiansen, O.; Cimiraglia, R.; Coriani, S.; Dahle, P., et al., The Dalton quantum chemistry program system. *Wiley Interdisciplinary Reviews: Computational Molecular Science* **2013**.
26. Jansik, B.; Rizzo, A.; Agren, H., Ab Initio Study of the Two-Photon Circular Dichroism in Chiral Natural Amino Acids. *Journal of Physical Chemistry B* **2007,** *111*, 446-460.

# CHAPTER 5: IMPLEMENTATION OF THE DOUBLE-L SCAN TECHNIQUE IN THE FAR-UV, A SPECTRAL REGION NEVER ACCESSED BEFORE…*WHEN SCIENCE GOES WRONG*!

Having completed the full TPA and TPCD theoretical characterization of the four aromatic amino acids found in mammals, in the Far-UV (FUV), we began working on the implementation of the Double-L scan technique in that spectral region.

In this chapter, we first present the implementation of the Double-L scan technique in the FUV, then we report on the measurements of the TPA spectrum of Trp in solution, and finally we discuss the *pros* and *cons* of the implementation of the technique in a region never attempted before, using tryptophan as our first targeted molecule. The initial validation of the Double L-scan technique, as well as the promising results obtained in the Near-UV (NUV)-FUV region, revealed that chiral molecules in solution, such as Trp/DMSO, can undergo photochemical reactions in front of prolonged exposition to UV radiation, being tryptophan the most susceptible amino acid to photooxidation according to the literature.

## 5.1 Introduction

Gaining access to the NUV and FUV region is of great interest in biology because chiral molecules related to the origin of life exhibit relevant structural and conformational information. In this region one can recover unique spectral fingerprints related to the structure of proteins, nucleic acids, and neurotransmitters, as well as information associated with interactions among them (ligand-receptor, enzyme-substrate) and with their environment (pH, salt conditions, and temperature). For instance, peptide bond absorption (n-$\pi^*$ and $\pi$-$\pi^*$ transitions) in the FUV produces specific secondary structural features for α-helix and β-sheet[1, 2]. Also, the signal from aromatic amino acid side chains of polypeptides in the NUV provides important information about their rigidity and environment (hydrogen bonds, polar groups, and polarizability) that can be related to proteins' tertiary structures[3-5]. In addition, co-factors' environment and interactions with ligands can be determined in the NUV and FUV[6-9].

With the aim of gaining access to the NUV and FUV, in this chapter we present a combination of specific UV optical elements and sensors in a Double-L scan geometry that could potentially result in the development of a unique TPCD spectrometer with capabilities in a spectral region otherwise impenetrable by existing techniques for the identification, analysis, and quantification of crucial biological structures in vitro.

## 5.2 Experimental Section

In order to test and validate the proposed instrument within the FUV region, we selected tryptophan as the best candidate for this purpose. Tryptophan was chosen based on its significance in biology and its already existent experimental and/or theoretical data.

Highly pure enantiomeric L- (L-trp) and D-tryptophan (D-trp) (≥98%) were purchased from Sigma-Aldrich Co. and used without further purification. The TPA and TPCD measurements were performed in a 65 mM solution of L-tryptophan/water in a 1 mm thick quartz cuvette, employing the Double-L scan technique[10]. Two-photon excitation was induced with a computer-controlled femtosecond optical parametric amplifier (OPerA Solo) pumped by an amplified laser system from COHERENT, Inc. The entire system is capable of generating 90 fs (FWHM) pulses over a wavelength range from 240 nm to 2.6 μm, and with pulse energies of up to 3 mJ at a 1-kHz repetition rate. Experiments were performed between 300 nm to 400 nm, using pulse energies ranging from 0.3 to 1 μJ and a repetition rate ranging from 5 to 50 Hz to prevent cumulative effects and sample degradation. The pulse width was determined using a single-shot autocorrelator from COHERENT Inc. and a frequency-resolved optical gaiting (FROG) from Swamp Optics, LLC.

## 5.3 Computational Methods

The theoretical background involved in this chapter has already been covered in detail in sections 1.2 and 1.5 of this dissertation's introduction. Here, we only present the computational features relevant to this chapter. The molecular structures of L-trp and D-trp were optimized employing Density Functional Theory (DFT) [11], using the Becke's three-parameter exchange, Lee, Yang and Parr correlation (B3LYP) [12-14] hybrid functional in combination with the aug-cc-VDZ basis set[15], employing Gaussian 09[16]. Solvent effects were not taken into account for this specific calculation. OPA and ECD calculations for L-trp and D-trp spectra were obtained with TD-DFT[11] at the B3LYP[12-14]/aug-cc-pVDZ[15] level of theory for the lowest 200 electronic excited states in Gaussian 09[16]. TPA and TPCD spectra calculations were computed employing TD-DFT[11] in combination with B3LYP[12-14]/6-311G(d) [17] level of theory for the lowest 80 electronic excited

states in Dalton 2011[18]. The convoluted theoretical TPA and TPCD spectra were accomplished by using Equations 1-19 and 1-38 (see introduction), respectively, employing a normalized Lorentzian lineshape with a linewidth (Γ) of 0.15 eV (FWHM).

## 5.4 Discussion of the implementation of the FUV-TPCD spectrometer and Results

### 5.4.1 Description of the implementation of the FUV-TPCD spectrometer

In this part we discuss all the aspects related to the implementation, calibration and characterization of this novel spectrometer.

#### 5.4.1.1 Implementation of the FUV-TPCD spectrometer

The same Double-L scan geometry employed for the visible and near-infrared TPCD signal measurements[10, 19-22] was used for the FUV-spectrometer set-up (see Figure 5.1). In this geometry the sample (S) is held fixed while the focuses of two "twin" beams with identical energy and profile are moved across the sample by translating the lenses L2 and L3.

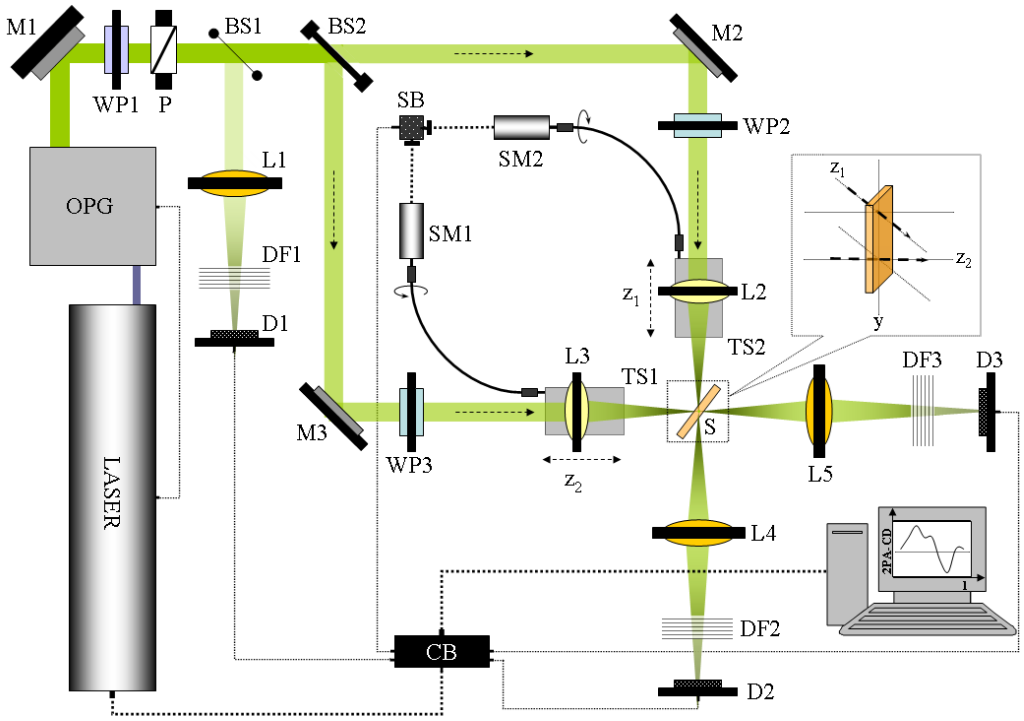


**Figure 5-1.** Double-L scan geometry. Mirrors (M1, M2, and M3), waveplates (WP1, WP2 and WP3), Glan polarizer (P), beam splitters (BS1 and BS2), convergent lenses (L1, L2, L3, L4 and L5), silicon detectors (D1, D2 and D3), neutral density filters (DF1, DF2 and DF3), translation stages (TS1 and TS2), step-motors (SM1 and SM2), synchronization box (SB), Sample (S) and control box (CB). Figure taken from reference (10)

The excitation beam was produced by a 1 kHz amplified femtosecond system. The experiments were performed between 300 nm to 380 nm, using the wavelength range generated by the second harmonic of the signal's second harmonic in the amplified system. The generation of lower wavelengths than 300 nm is not possible with the combinations of dichroic filters and crystals available for this system in our lab. We performed our measurements employing pulse energies ranging from 0.3 to 1 μJ and a repetition rate ranging from 5 to 50 Hz to prevent cumulative effects and sample degradation.

Several optical elements were placed between the laser system (OPG) and mirror M1 in order to generate a Gaussian and collimated beam with the spot size required for the accomplishment of the measurements. The power of the excitation beam was attenuated through a combination of an

achromatic zero-order broadband (spectral range ≈ 260-410 nm) half-wave plate and a broadband Glan polarizer (P). P also converts the incident light into a beam of well-defined polarization, usually vertically-polarized light. Then, a beam splitter (BS1) was used to deviate approximately 10% of the radiation towards an UV silicon detector (D1) (spectral range from 200 to 1100 nm) employed as an energy reference to constantly monitor the laser light. The remaining 90% of the incident beam was once again split into two beams with a 50/50 beam splitter (BS2). To control the alignment of the "twin" beams and deliver them in the sample, two broadband UV enhanced aluminum mirrors (M2 and M3) were used in each individual arm.

Two achromatic convergent lenses, L2 and L3, with a focal length of 100.3 mm, were moved in the same direction and displacement, via two translational stages (TS1 and S2), in order to make $z_1$ equal to $z_2$ (see Figure 5-1). This ensures that S is scanned at the same time by both focal plane positions. TS1 and TS2 were moved by coordinating two step-motors (SM1 and SM2) employing a synchronization box (SB). Achromatic zero-order broadband quarter-waveplates (260–410 nm), WP2 and WP3, were placed between M2 and L2 and M3 and L3 to convert the incident linearly-polarized light into left and right circularly-polarized light, respectively. Due to the nature of the geometry of the Double-L scan technique, S is located at a 45° angle with respect to the incident beam's propagation axes (see Figure 5-1). Therefore, the effective path length is equal to 1.4 mm for a 1 mm-thick quartz cuvette. The two incident beams are parallel to the table and approximately 1 cm apart on the vertical axis, in order to avoid interference effects due to beam overlapping (see inset, Figure 5-1). The detection lenses, L4 and L5, were used to fully collect the total energy of the beams into the detection system (two UV silicon detectors D2 and D3). Neutral density filters (DF1, DF2, and DF3) were used to adjust the input energy into the different detectors. The entire setup is synchronized by a control box (CB) and controlled with a LABVIEW program.

### 5.4.1.2 Calibration of the FUV-TPCD Spectrometer

The calibration procedure followed during the implementation of the Vis and near IR TPCD consisted of three main steps: i) Align both arms with the same experimental energy and geometry conditions. ii) Measure the Double-L scan curves with linearly-polarized light in both focusing geometries. Same shape and amplitudes in signals from both arms will confirm identical experimental conditions, resulting in zero-delta normalized transmittance (ΔNT = 0) (See Figure 5-2.a). iii) Proceed to change the polarization of light from linear to circular polarized light in both arms and measure the Double-L scan curves. Since the experimental conditions are the same in both arms, any positive or negative value of ΔNT will indicate the achievement of the measurement of the TPCD signal (see Figure 5-2.b)[23].

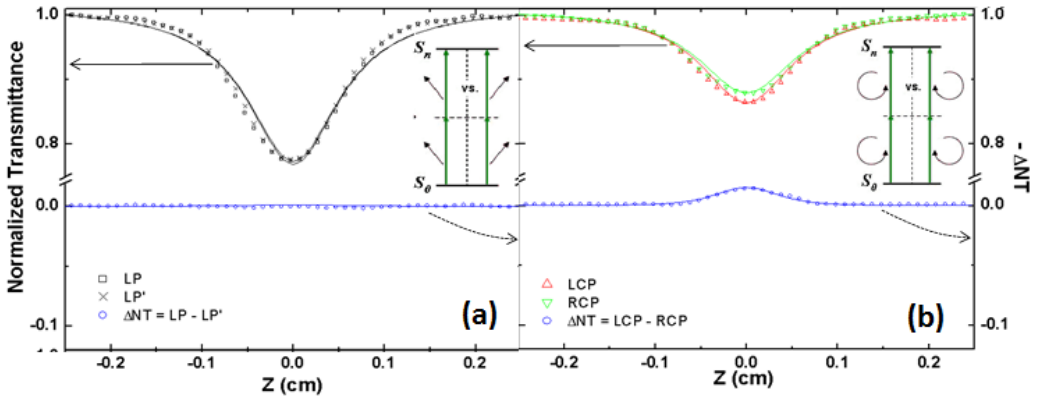


**Figure 5-2.** L-scan signatures and difference between normalized transmittance vs. z position on a THF solution of S-BINOL, using different polarization state combinations and pumping at 460 nm: a) linear-linear and b) circular-circular (left-right). Figure taken from reference (23).

The same calibration process was pursued for the Far-UV region. In fact, in Figure 5-3, we display experimental curves of the Double-L scan signatures such as the normalized transmittance achieved using two different polarization state combinations at 400 nm. The experimental error bars are within the size of the symbols (<1%) [23]. Figure 5-3.a presents the results of the measurements obtained with both beams linearly polarized. The fact that the two curves are

virtually identical means that the same experimental and geometric parameters were used. Figure 5-3.b shows the Z-scan curves measured with right and left circular polarizations. A positive value of ΔNT corroborates that the nonlinear effect is indeed susceptible to changes in the handiness of the excitation beam.

Additionally, it is important to highlight that the calibration and measurement of a complete TPA spectrum takes approximately one hour, depending on the external conditions, and at least 8 hours for the measurement of a TPCD signal at a specific wavelength.

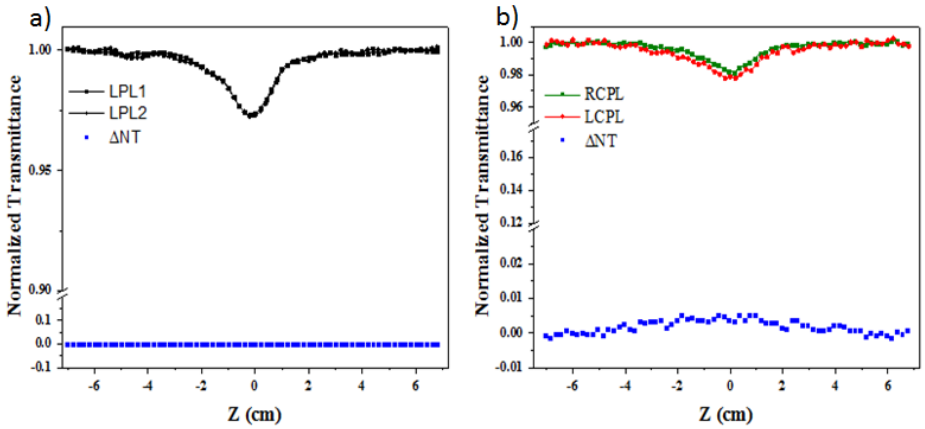


**Figure 5-3.** L-scan signatures and difference between normalized transmittance vs. z position on a water solution of L-trp, using different polarization state combinations and pumping at 400 nm: a) linear-linear and b) circular-circular (left-right).

### 5.4.1.3 Characterization of the sensitivity and reproducibility of the instrument

The high sensitivity of the Double-L scan geometry resides on the synchronized measurements of "twin" laser pulses that accounts for changes in laser performance. By splitting the original pulse into twin pulses, we assure that both incident beams are subject to the same type of spatial and temporal fluctuations of the pulsed source. As a consequence, this approach alleviates the concerns associated with changes in the pulse profile between runs.

Figure 5-4 displays the experimental TPCD spectra of R-BINOL and S-BINOL, certifying once again the ability of the Double-L scan technique to measure slight differences between nonlinear absorption cross-sections for left and right circularly-polarized light. It can also be noticed that the spectrum of one isomer is the specular image of the other, as expected. Additionally, measurements of TPCD attempted on a racemic mixture of S-BINOL and R-BINOL did not give any significant signal, demonstrating once again that TPCD is an optical property distinctly featured by enantiomeric chiral molecules. This figure also shows that this approach can determine TPCD with a sensitivity of ± 1GM [23].

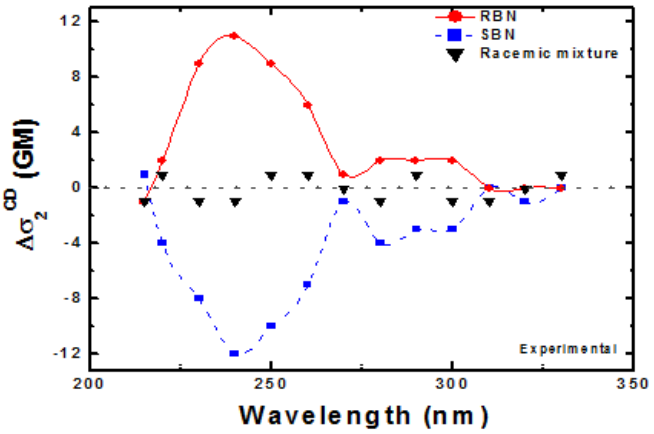


**Figure 5-4.** Experimental two-photon absorption circular dichroism spectra for S-BINOL and R-BINOL. The experimental signal for a racemic mixture is also depicted. Figure taken from reference (23).

### 5.4.1.4 Validation of the FUV-TPCD spectrometer

In order to test and validate the proposed instrument within the FUV region, we selected tryptophan as the best candidate for this purpose. We first prepared aqueous solutions of the two enantiomers of tryptophan at the maximum concentration experimentally allowed (65 mM). Then, we proceeded to start the nonlinear characterization of L- and D-trp by measuring their TPA spectra. Since low TPA cross-sections were expected within the excitation region (320-400 nm), the energies employed for the measurements were relatively high (.7 and 1 µJ). Consequently, a

change in refractive index was immediately noticed, making the acquisition of data challenging (Figure 5-5). In an effort to decrease the excitation energies, we considered changing the solvent of the sample (dioxane, THF, DMSO, dichloromethane) to increase the concentration solutions and decrease solvent effects in the NUV and FUV regions[24, 25]. In 1970, Tanford and co-workers reported that the aromatic side chains are the most hydrophobic among the naturally-occurring amino acid side chains due to the large size of the aromatic groups [26]. They concluded that the incorporation of a percentage of an inorganic solvent, such as dioxane, to the solution stabilizes the hydrophobic moiety. In fact, the publication suggests that the highest concentration of tryptophan is accomplished through the use of a 40/60 dioxane/water solvent ratio [26]. By employing this mixture of solvents, the concentration of the solution was increased by approximately 40%. However, the same shape presented in Figure 5-5 was observed. This result indicated that, although the concentration of the solution was increased, the incident beam's energies remained high for experimental purposes.

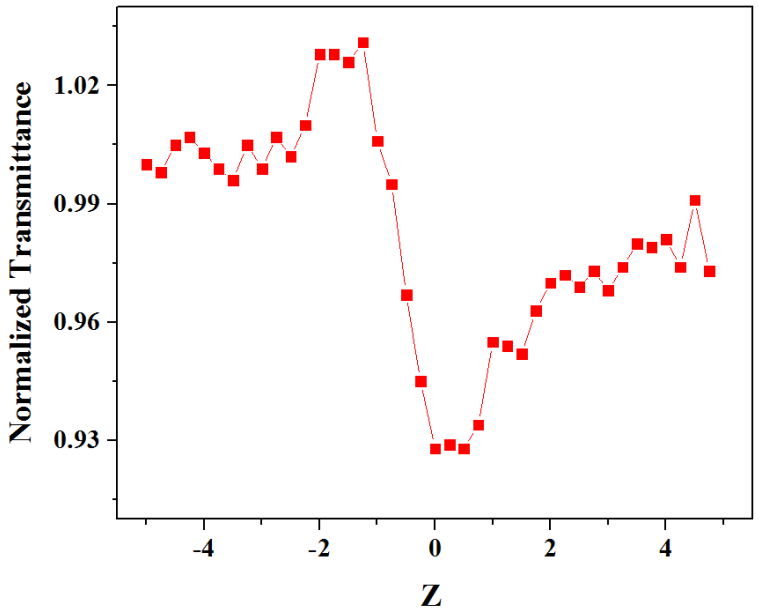


**Figure 5-5.** Experimental Z-scan of L-trp solution in water, measured at an energy of 0.7 μJ.

Next, L- and D-trp were dissolved in dimethyl sulfoxide (DMSO) in order to determine if a similar behavior as in water and dioxane/water was observed. The experimental outcome finally exhibited a typical Z-scan curve with a higher signal-to-noise ratio than the one observed in aqueous Trp solutions (see Figure 5-6).

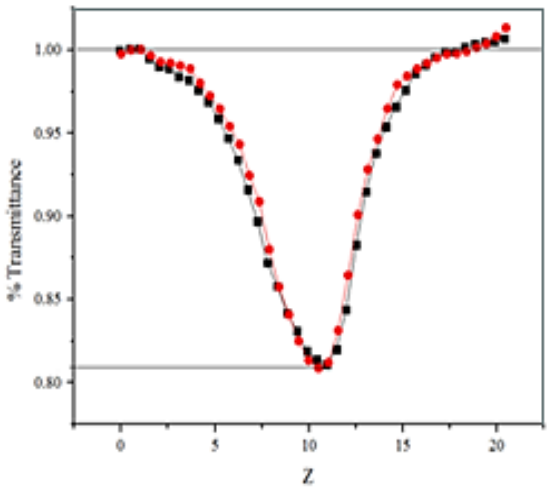


**Figure 5-6.** Experimental Z-scan measurements of DMSO at 355 nm, using linearly-polarized light in both arms of the Double-L scan geometry.

Then, we accomplished the measurement of the TPCD signal at 400 nm (see Figure 5-7). From this figure we concluded that, indeed, the FUV-TPCD spectrometer allows obtaining pure TPCD signal in the Far-UV region. Additionally, a tendency of remarkable agreement between theory and experiment is observed in Figure 5-7, where the TPCD data point measured at 400 nm perfectly overlaps with the theoretical spectrum. Finally, and probably the most important outcome of this study is the fact that we were able to measure, for the very first time, the TPCD of Trp/DMSO at an excitation wavelength of 400 nm, i.e. a wavelength corresponding to a transition in the FUV, an area never accessed before.

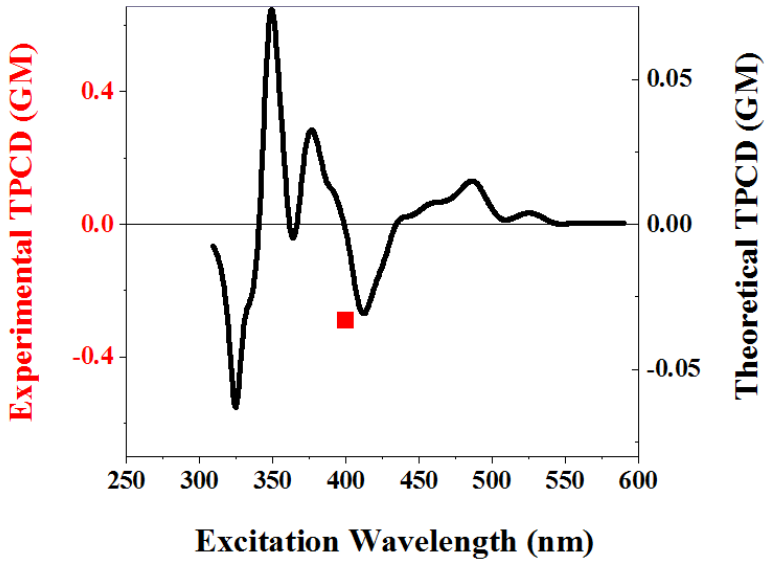


**Figure 5-7.** Theoretical and the first experimental point of TPCD signal of L-tryptophan in DMSO solution.

### 5.4.2 Results

After the optimization of both enantiomers, employing DFT[11] at B3LYP[12-14]/aug-cc-pVDZ[15] level of theory, we calculated the OPA and ECD spectra for the lowest 200 electronic excited states and plotted them with the experimental spectra (see Figure 5-8). To obtain a better theoretical and experimental spectral overlapping, the theoretical spectra were slightly shifted by + 5 nm, which is a common practice in theoretical-experimental work[19-22]. The initial observation from Figure 5-8 was the excellent theoretical-experimental spectral matching throughout the entire region. Next, one should highlight the fact that the amplitudes of the OPA and ECD signals between theory and experiment are virtually identical, as well as the relative intensities of the bands. Finally, the experimental ECD spectra of L-trp and D-trp are mirror images from each other, as expected for a pair of enantiomers.

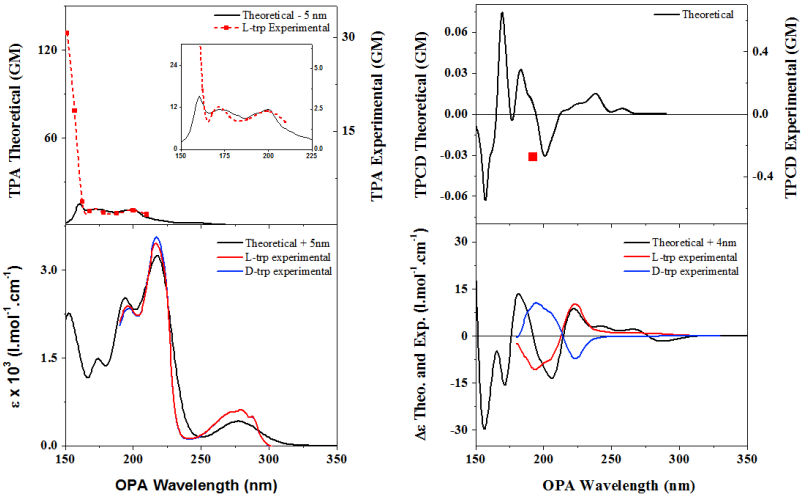


**Figure 5-8.** Linear absorption (bottom-left), electronic circular dichroism (bottom-right), two-photon absorption (top-left), and two-photon circular dichroism (top-right) spectra of L-Trp in an aqueous solution. The solid black line represents the corresponding theoretical spectra. OPA and ECD spectra were obtained at B3LYP/aug-cc-pVDZ level of theory for the lowest 200 electronic excited states in Gaussian 09. The theoretical spectra were shifted +5 nm and a $\Gamma$=0.3 eV (FWHM) was used. TPA and TPCD were computed with B3LYP/6-311G(d) for the first 50 excited states in Dalton 2011. The Lorentzian convolution was obtained using a linewidth $\Gamma$=0.15 eV (FWHM). The theoretical TPA spectrum was shifted -5 nm.

In Figure 5-8, we also present our initial results of the nonlinear optical characterization of L-Trp. The TPA and TPCD calculations were obtained with TD-DFT[11] at the B3LYP[12-14]/6-311G(d) [17] level of theory for the lowest 80 electronic excited states. We show the first measurements of the TPA of L-Trp down to 150 nm (TPA spectrum of D-Trp is not displayed because it is identical to that of L-Trp). The inset in the top-left plot evidences the excellent agreement between the theoretical calculations and the experimental results, corroborating the reliability of both the theory and technique. It is also worth highlighting the great enhancement of the TPA signal observed between 300 nm and 320 nm, which is attributed to the enhanced TPA typically observed as the excitation approaches the linear absorption region.

In the case of the experimental TPCD, we followed the protocol for the calibration of the instrument mentioned previously. After several attempts to measure TPCD at lower wavelengths

than 400 nm, we faced new challenges, i.e. the lack of reproducibility on the experimental TPCD curves. In order to circumvent this obstacle we decided to slightly modify the protocol for the calibration of the instrument by setting the quarter waveplate at 45º and performing the calibration with right and left circularly-polarized light at 355 nm. In Figure 5-9.a, we can see the Z-scan of both arms when we only measured the solvent (DMSO) as a reference for the calibration. Due to the differential nature of TPCD, we were able to measure the TPA of Trp in DMSO. The subtraction of the right TPCD cross-section from the left TPCD cross-section results in a pure TPCD signal. Since the exact same TPA is experienced in both arms, this technique has the advantage of subtracting contributions from impurities, as well as mild refractive index changes effects from the solvent. This type of approach have been using before. For instance, in 1994, Hernandez and co-workers proposed a differential technique known as the differential thermal lensing that accounts for the linear absorption contribution of solvents [27]. To subtract this contribution, they used a two-channel differential scheme, in which both channels are identical and have equal pump light power. Cells filled with solution and pure solvent were placed in the first and the second channels, respectively [27]. More recently, Van Stryland and co-authors presented a technique known as dual-arm Z-scan, in which small solute nonlinearities were extracted from large solvent signals by operating simultaneous Z-scans in solvent and solution [28]. These publications showed that it is possible to measure a specific nonlinear property in the presence of nonlinear contributions from solvents. Once we observed that the % transmittance was exactly the same for both arms, we proceeded to measure L-Trp/DMSO (see Figure 5-9.b). Immediately, we noticed that there was a slightly lower % transmittance (approximately 3%) in both arms in L-Trp/DMSO. This was promising because it was the first experimental evidence of the gained access to the NUV. However, both curves revealed exactly the same transmittance, even

at a higher energy (see Figure 5-9.c), which means that the difference in absorption between left and right circularly-polarized light was unmeasurable. Considering the possibility of the TPCD signal being higher at another point in the spectrum, we decided to change the incident wavelength. However, the same observations were made throughout the entire wavelength range, 320nm to 380 nm (see Figure 5-9.d).

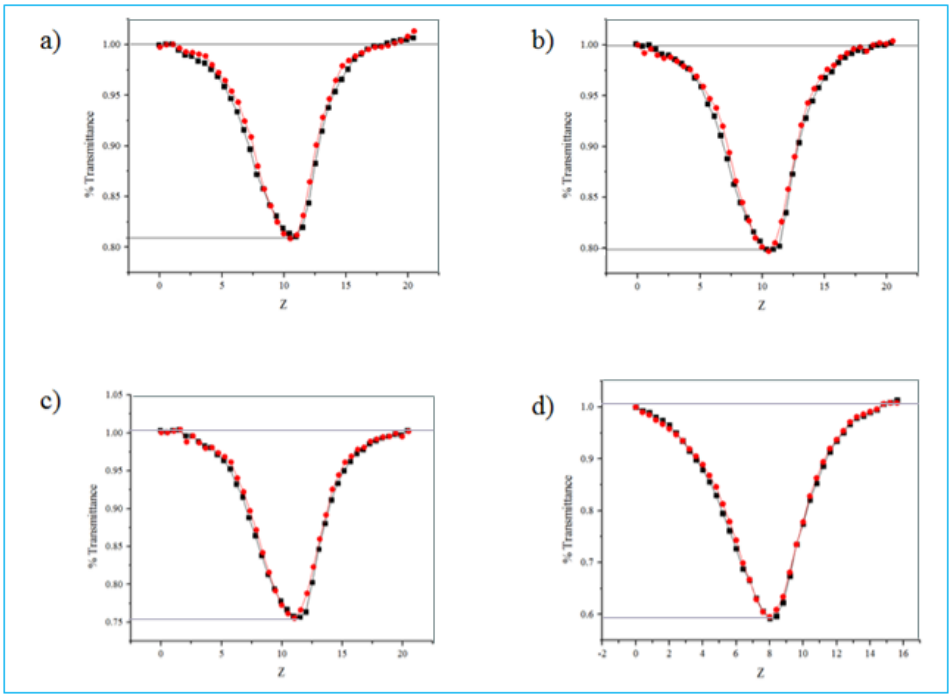


**Figure 5-9.** Experimental Z-scan measurements with left and right circularly polarized light in a) DMSO solvent at 355 nm, b) L-trp dissolved in DMSO at 355 nm, c) L-trp+DMSO at a higher energy (3μJ) at 355 nm, and d) L-trp+DMSO at 365 nm.

At this point, we observed that when the sample was exposed to radiation for a long period of time (4-6 hours), the Trp solution turned into a brownish color, indicating that a chemical change might have been occurring. In order to corroborate this hypothesis, we performed a bibliographic search and found that amino acid residues like tryptophan undergo a photochemical reaction when exposed to prolonged irradiation with UV/Vis light[30]. These amino acid residues react with $^1O_2$ *via* either a chemical reaction or physical quenching. Trp has been proven to undertake a physical

quenching method, known as singlet oxygen-mediated oxidation[31, 32]. This type of reaction can result in a variety of effects, including oxidation of the side-chains, backbone fragmentation, dimerization/aggregation, unfolding, or conformational changes, among others[31-34].

Singlet oxygen-mediated oxidation of Trp is believed to proceed either *via* initial formation of a dioxetane on the heterocyclic ring across the C2-C3 bond or a hydroperoxide at the C3 position (see Figure 5-10) [30].

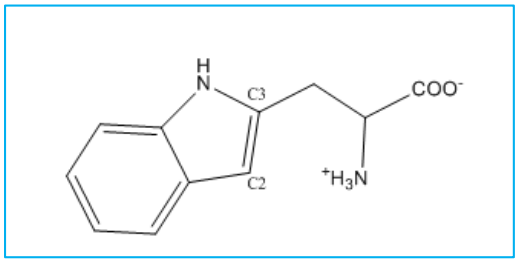


**Figure 5-10.** Molecular structure of tryptophan (Trp) showing the positions of C2 and C3, where the reactions occur.

In figure 5-11, a proposed mechanism[30] for both reaction paths is presented, where we can see that if the reaction proceeds via the initial formation of dioxetane ring, it will end up in the formation of 3α-hydroperoxypyrrolindole and 3α-hydroxypyrrolindole. Whereas, if the reaction proceeds *via* the heterocyclic ring, it will follow a subsequent decomposition and a C2-C3 bond cleavage, resulting in the formation of N-formylkynurenine (NFK). No matter which way the reaction takes, it would end up primarily in the formation of NFK[30].

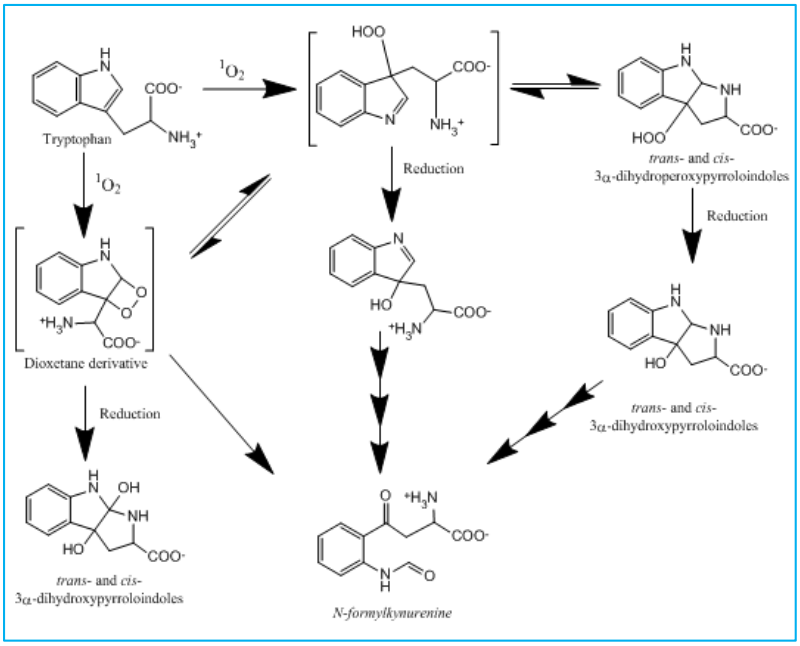


**Figure 5-11**. Proposed mechanism of the reaction of Trp with $^1O_2$ taken from ref (26).

This photoreaction begins as soon as the solution start being irradiated with UV light. However, the change in color of the Trp/DMSO solution from clear to brownish, which indicated the transformation of Trp into NFK, was not noticeable until after approximately four hours of continuum irradiation. This result explains why measuring the full experimental TPA spectrum in Trp/DMSO was possible while for TPCD only one point at 400nm was attainable. Considering the fact that single wavelength Double L-scan curves measurements of TPA are relatively fast experiments (approximately 15 min) while those for TPCD are very long (approximately eight hours), the total number of pulses irradiating the sample in the former is 32 times smaller than in the latter (# pulse in TPA ≈ 9,000 vs. # pulse TPCD ≈ 288,000). Therefore, the lack of reproducibility in TPCD measurements is not surprising noticing that during the measurement of one experimental point requires ≈ 279,000 more pulses for completion.

Our results demonstrate the possibility of performing NUV-TPCD for the study of a vast variety of biological molecules. However, to perform the complete analysis of samples such as natural amino acids, that can undergo a photochemical reaction when exposed to prolonged radiation in the Near to Far-UV range, the experimental approach needs to be considerably improved - the acquisition time needs to be reduced at least one order of magnitude. In order to overcome the current obstacle, it is imperative to optimize the external conditions (temperature, humidity, and air currents) in the room where the experiment is run. Nevertheless, looking for a more immediate solution we considered using a flow cell to continuously refresh the sample in the focusing geometry. However, to run an experiment for eight continuous hours, at a very low flow of 1.0 mL/min, we will need approximately 1.0 to 1.5 L of solution per wavelength, assuming we do not need to do more than three runs per point. This is an enormous amount of solution of Trp/DMSO.

## 5.5 Conclusions

In summary, we have expanded the spectral range, and consequently, the application of the Double- L-scan technique to the NUV and FUV, to perform polarization dependent TPA measurements of chiral molecules. We determined experimentally, and for the very first time, the complete TPA spectrum of Trp/DMSO down to 300 nm (equivalent to 150nm in the OPA scale), and measured the TPCD signal of this amino acid at 400nm. The observed limitation of the application of the Double L-scan technique in the NUV and FUV, below 400nm, was explained based on the required temporal length for completing a TPCD measurement, and consequently, the significant photodecomposition of the sample due to photochemical reactions in the UV region.

## 5.6 References


1. Greenfield, N. J., Applications of circular dichroism in protein and peptide analysis. *TrAC Trends in Analytical Chemistry* **1999,** *18* (4), 236-244.
2. Venyaminov, S. Y.; Yang, J. T., Determination of Protein Secondary Structure. In *Circular Dichroism and the Conformational Analysis of Biomolecules*, Fasman, G. D., Ed. Plenum Press, LLC: New York, 1996; pp 69-108.
3. Woody, R. W.; Dunker, K. A., Aromatic and Cystine Side-Chain Circular Dichroism in Proteins. In *Circular Dichroism and the Conformational Analysis of Biomolecules*, Fasman, G. D., Ed. Plenum Press: New York, 1996; pp 109-158.
4. Strickland, E. H., Aromatic contributions to circular dichroism spectra of proteins. *CRC Crit Rev Biochem* **1974,** *2*, 113-75.
5. Kahn, P. C., The interpretation of near-ultraviolet circular dichroism. *Methods Enzymol* **1979,** *61*, 339-78.
6. Johnson, L. N.; Barford, D., Glycogen phosphorylase. The structural basis of the allosteric response and comparison with other allosteric proteins. *J Biol Chem* **1990,** *265*, 2409-12.
7. Macheroux, P., UV-Visible Spectroscopy as a Tool to Study Flavoproteins. In *Flavoprotein Protocols*, Chapman, S. K.; Reid, G. A., Eds. Humana Press: New Jersey, 1999; Vol. 131, pp 1-7.
8. Andersson, L. A.; Peterson, J. A., Active-site analysis of ferric P450 enzymes: hydrogen-bonding effects on the circular dichroism spectra. *Biochem Biophys Res Commun* **1995,** *211*, 389-95.
9. Coleman, J. E., Carbonic anhydrase-azosulfonamide complexes. Spectral properties. *J Biol Chem* **1968,** *243*, 4574-87.
10. De Boni, L.; Toro, C.; Hernandez, F. E., Synchronized Double L-Scan Technique for the

Simultaneous Measurement of Polarization-Dependent Two-Photon Absorption in Chiral Molecules. *Optics Letters* **2008,** *33*, 2958-2960.

11. Runge, E.; Gross, E. K. U., Density-Functional Theory for Time-Dependent Systems. *Physical Review Letters* **1984,** *52* (12), 997-1000.
12. Becke, A. D., Density-Functional Exchange-Energy Approximation with Correct Asymptotic Behavior. *Physical Review A* **1988,** *38*, 3098-3100.
13. Becke, A. D., Density-Functional Thermochemistry. III. The Role of Exact Exchange. *Journal of Chemical Physics* **1993,** *98*, 5648-5652.
14. Lee, C.; Yang, W.; Parr, R. G., Development of the Colle-Salvetti Correlation-Energy Formula into a Functional of the Electron Density. *Physical Review B: Condensed Matter* **1988,** *37*, 785-789.
15. Kendall, R. A.; Dunning, T. H.; Harrison, R. J., Electron affinities of the first-row atoms revisited. Systematic basis sets and wave functions. *The Journal of Chemical Physics* **1992,** *96* (9), 6796-6806.
16. Frisch, M. J.; Trucks, G. W.; Schlegel, H. B.; Scuseria, G. E.; Robb, M. A.; Cheeseman, J. R.; Scalmani, G.; Barone, V.; Mennucci, B.; Petersson, G. A., et al., Gaussian 09, Revision A.1. Gaussian, Inc.: Wallingford CT, 2009.
17. Rassolov, V. A.; Pople, J. A.; Ratner, M. A.; Windus, T. L., 6-31G* basis set for atoms K through Zn. *The Journal of chemical physics* **1998,** *109* (4), 1223-1229.
18. DALTON *A Molecular Electronic Sstructure Program, Release Dalton 2011, see* *http://daltonprogram.org/*, 2011.
19. Diaz, C.; Vesga, Y.; Echevarria, L.; Stará, I. G.; Starỳ, I.; Anger, E.; Shen, C.; Moussa, M. E. S.; Vanthuyne, N.; Crassous, J., et al., Two-photon absorption and two-photon circular

dichroism of hexahelicene derivatives: a study of the effect of the nature of intramolecular charge transfer. *RSC Advances* **2015,** *5* (23), 17429-17437.

20. Díaz, C.; Echevarria, L.; Rizzo, A.; Hernández, F. E., Two-Photon Circular Dichroism of an Axially Dissymmetric Diphosphine Ligand with Strong Intramolecular Charge Transfer. *The Journal of Physical Chemistry A* **2014,** *118* (5), 940-946.
21. Diaz, C.; Lin, N.; Toro, C.; Passier, R.; Rizzo, A.; Hernández, F. E., The Effect of the π-Electron Delocalization Curvature on the Two-Photon Circular Dichroism of Molecules with Axial Chirality. *The Journal of Physical Chemistry Letters* **2012,** *3*, 1808-1813.
22. Vesga, Y.; Hernandez, F. E., Study of the Effect of the Pulse-Width of the Excitation Source on the Two-Photon Absorption and Two-Photon Circular Dichroism Spectra of Biaryl Derivatives. *The Journal of Physical Chemistry A* **2016**.
23. Toro, C.; De Boni, L.; Lin, N.; Santoro, F.; Rizzo, A.; Hernandez, F. E., Two-Photon Absorption Circular Dichroism: A New Twist in Nonlinear Spectroscopy. *Chemistry - A European Journal* **2010,** *16*, 3504-9.
24. Bailey, J.; Beaven, G.; Chignell, D.; Gratzer, W., An analysis of perturbations in the ultraviolet absorption spectra of proteins and model compounds. *European Journal of Biochemistry* **1968,** *7* (1), 5-14.
25. Auer, H. E., Far-ultraviolet absorption and circular dichroism spectra of L-tryptophan and some derivatives. *Journal of the American Chemical Society* **1973,** *95* (9), 3003-3011.
26. Nozaki, Y.; Tanford, C., The solubility of amino acids, diglycine, and triglycine in aqueous guanidine hydrochloride solutions. *Journal of Biological Chemistry* **1970,** *245* (7), 1648-1652.
27. Kozich, V. P.; Hernández, F. E.; Aristides, M. O., Pulse-induced thermal lensing in Kerr

media. *Applied spectroscopy* **1995,** *49* (12), 1804-1808.

28. Ferdinandus, M. R.; Reichert, M.; Ensley, T. R.; Hu, H.; Fishman, D. A.; Webster, S.; Hagan, D. J.; Van Stryland, E. W., Dual-arm Z-scan technique to extract dilute solute nonlinearities from solution measurements. *Opt. Mater. Express* **2012,** *2* (12), 1776-1790.
29. Doni, E.; Girlanda, R.; Parravicini, G. P.; Quattropani, A., *Progress in Electron Properties of Solids: Festschrift in Honour of Franco Bassani*. Springer Science & Business Media: 2012; Vol. 10.
30. Gracanin, M.; Hawkins, C. L.; Pattison, D. I.; Davies, M. J., Singlet-oxygen-mediated amino acid and protein oxidation: formation of tryptophan peroxides and decomposition products. *Free radical biology and medicine* **2009,** *47* (1), 92-102.
31. Matheson, I.; Lee, J., Chemical reaction rates of amino acids with singlet oxygen. *Photochemistry and photobiology* **1979,** *29* (5), 879-881.
32. Palumbo, M.; Garcia, N.; Argüello, G. A., The interaction of singlet molecular oxygen O 2 (1 Δ g) with indolic derivatives. Distinction between physical and reactive quenching. *Journal of Photochemistry and Photobiology B: Biology* **1990,** *7* (1), 33-42.
33. Davies, M. J., Singlet oxygen-mediated damage to proteins and its consequences. *Biochemical and biophysical research communications* **2003,** *305* (3), 761-770.
34. Davies, M. J.; Truscott, R. J., Photo-oxidation of proteins and its role in cataractogenesis. *Journal of Photochemistry and Photobiology B: Biology* **2001,** *63* (1), 114-125.

# CHAPTER 6: FUTURE WORK

The research presented in this manuscript constitutes the continuation of the comprehensive and systematic theoretical-experimental study of the structure-property relationship of TPCD, as well as the implementation of the Far-UV TPCD spectrometer and the first attempt to measure the TPCD signal in the NUV and FUV regions. The investigation presented in this dissertation was primarily focus on: i) the study of the effect of the excitation source pulse-width on TPCD, ii) the investigation of the effect of electron-releasing and electron-withdrawing substituents of a helicene core on TPCD, and iii) the theoretical and experimental approaches for the implementation of the Far-UV TPCD spectrometer.

Although we have made a great progress on the extension of the application of TPCD to the Far-UV by implementing the FUV-TPCD spectrometer, we still need to explore the option of reducing the acquisition time of the TPCD spectra. For this reason, it is important to optimize the external conditions (temperature, humidity, and air currents) in the room where the experiment is run. Naturally occurring amino acids solutions turn undergo photochemical reaction when exposed to UV irradiation for more than 4 hours, therefore, the acquisition time has to be kept within the 4 hours range. Another experimental possibility to assess is the use a flow cell, but before the evaluation of this option, the acquisition time needs to be reduced.

Additionally, the implementation of the pump-probe experiment would open a way to start measuring the circular dichroism associated with the excited state. This set-up can also be used for detecting changes in lifetime of chromophores, depending on the polarization of the light used as a pump and/or probe.

Finally, it is imperative to continue the study of the ICT effect on the TPCD signal of chiral molecular systems with various combinations of donor-acceptor substituents at both ends of the molecular core.

# APPENDIX A: **PUBLICATIONS FROM DISSERTATION WORK**

**1.** Vesga, Y.; Diaz, C.; Higgs M.; Hernandez, F.E., "*Two-photon circular dichroism of molecular structures simulating L-tryptophan residues in proteins with secondary structures",* Chem. Phys. Lett. **2014,** 601, 6-12.

**2.** Vesga, Y.; Diaz, C.; Hernandez, F.E., "*Two-photon circular dichroism of molecular structures simulating L-Tyr, L-Phe, and L-His residues in proteins with secondary structures",* RSC Adv. **2014,** 4, 60974-60986.

**3.** Diaz, C.; Vesga, Y.; Echevarria L.; Stará,, I. G.; Stary, I.; Anger, E.; Shen, C.; Moussa, M. E. S.; Vanthuyne, N.; Crassous, J.; Rizzo, A.; Hernandez, F. E., "*Two-photon absorption and two-photon circular dichroism of hexahelicene derivatives: a study of the effect of the nature of intramolecular charge transfer",* RSC Adv. **2015,** 5, 17429-17437.

**4.** Donnelly, J; Vesga, Y.; Hernandez, F. E., "*Enhanced two-photon absorption and fluorescence upconversion in Thioflavin T micelle-type aggregates in glycerol/water solution",* Chem. Phys. **2016**.

**5.** Vesga, Y.; Hernandez, F. E., "*Study of the effect of the pulse-width of the excitation source on the two-Photon absorption and two-photon circular dichroism spectra of biaryl derivatives",* J. of Phys. Chem. A **2016**.

# APPENDIX B: **CONTRIBUTION TO CONFERENCES AND RESEARCH FORUMS FROM DISSERTATION WORK**

1. Yuly Vesga, Carlos Diaz, Mary Higgs, Florencio E. Hernandez (March 2015), *Theoretical study of two-photon circular dichroism on molecular structures simulating aromatic amino acid residues in proteins with secondary structures*, 11th UCF Graduate Research Forum. Orlando, Florida. Poster Session.

2. Yuly Vesga, Carlos Diaz, Mary Higgs, Florencio E. Hernandez (March 2015), *Theoretical study of two-photon circular dichroism on molecular structures simulating aromatic amino acid residues in proteins with secondary structures*, 249th ACS National Meeting & Exposition. Denver, Colorado. Poster Session.

3. Yuly Vesga, Carlos Diaz, Mary Higgs, Florencio E. Hernandez (May 2015), *Theoretical study of two-photon circular dichroism on molecular structures simulating aromatic amino acid residues in proteins with secondary structures*, Southeast Theoretical Chemistry Association Annual Meeting 2015. Orlando, Florida. Poster Session.

4. Julie Donnelly, Yuly Vesga, Florencio E. Hernandez (March 2016), *Multiphoton spectroscopy on Thioflavin T: a nonlinear approach for Amyloid detection*, 251th ACS National Meeting & Exposition. San Diego, California. Poster Session.

# APPENDIX C: **GAUSSIAN BEAMS**

# GAUSSIAN BEAMS

One of the approximations that is made when third order nonlinearities are determined from Z-scan curves is that the excitation beam has a Gaussian spatial profile.[1] In this appendix a brief description of the main characteristics that describe these types of beams is presented. [2,3]

The transverse profile of a Gaussian beam (see Figure below) is described by,

$$I = I_0 e^{-2r^2/w^2},$$

where $I_0$ is the intensity at the propagation axis (maximum intensity), $r$ is the distance measured from the propagation axis and $w$ is the beam waist, that is defined as the value $r$ for which the intensity drops to $I_0 / e^2$.

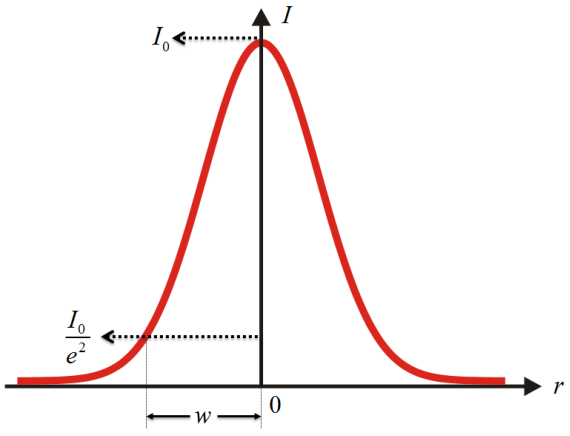


When the Gaussian beam is focused (see Figure below), the parameter $w$ varies along the propagation axis according to:

$$w(z) = w_0 \left[ 1 + \left( \frac{\lambda z}{\pi w_0^2} \right)^2 \right]^{1/2},$$

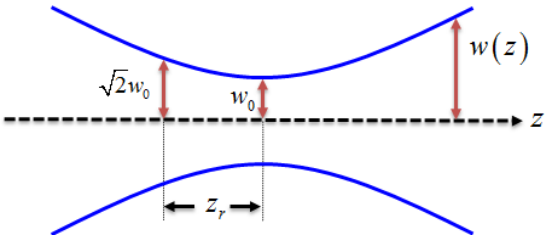


here, $w_0$ is the beam waist measured at the focal point (z = 0), $\lambda$ is the wavelength of the light, and $z$ is the position along the propagation axis. An important parameter that characterizes the focused Gaussian beam is the Rayleigh range $(z_r)$ that is defined as the distance from the beam waist to the position where the cross-sectional area of the beam is doubled. This condition occurs when the beam waist is equal to $\sqrt{2}w_0$. The expression for the calculation of the Rayleigh range is,

$$z_R = \frac{\pi w_0^2}{\lambda}.$$

Finally, an important parameter that is used to describe the focused Gaussian beam is its radius of curvature as it propagates, which is given by,

$$R(z) = z\left[1+\left(\frac{z_R}{z}\right)^2\right].$$

## References


1. Sheik-Bahae, M.; Said, A. A.; Wei, T. H.; Hagan, D. J.; Van Stryland, E. W., Sensitive measurement of optical nonlinearities using a single beam. *IEEE J. Quantum Electron.* **1990,** *26*, 760-769.
2. Hecht, E. *Optics*, Pearson Education, Inc., San Francisco, 2002.
3. Born, M.; Wolf, E. *Principles of Optics*, Cambridge University Press, Cambridge, 1999.

# APPENDIX D: **DENSITY FUNCTIONAL THEORY**

## DENSITY FUNCTIONAL THEORY

One of the main issues for treating large molecular systems with Hartree-Fock (HF) and post HF methods is that these approaches deal with a large number of variables that result in a tremendous computational problem. This is due to the fact that these methods are based on complicated many-electron wavefunctions that are dependent on each of the three spatial coordinates of all the *n* electrons that comprise the system. In order to simplify this problem, in 1964 Hohenberg and Kohn [1] proposed that all the information from the system could be obtained from the ground state electron density that only depends on three spatial coordinates. They provided proof of two theorems that supported their approach:

***Theorem I:*** The ground state density $\rho_0(r)$ of any system of electrons is uniquely determined by the external potential $V_{ext}(r)$ and a constant.

Which means that once the electron density of the system is known, the external potential, and in consequence the Hamiltonian can be directly determined. Then from the Hamiltonian the wavefunction can be determined, thus making every quantum mechanical observable into a functional of the ground state density.

***Theorem II:*** There exists a universal functional for the energy $E$ that can be defined in terms of $\rho(r)$. The global minimum value of this functional is equal to the exact ground state density $\rho_0(r)$.

In other words, the exact ground state density minimizes the energy as a functional of the density. These two theorems constitute the basis the so-called Density Functional Theory (DFT).

The Hohenberg-Kohn (HK) Hamiltonian for a many particle system can then be expressed in terms of the external potential as,

$$H = -\frac{1}{2}\sum_i \nabla_i^2 + \sum_i V_{ext}\left(r_i\right) + \frac{1}{2}\sum_{i\neq j}\frac{1}{\left|r_i - r_j\right|}$$

And the associated energy functional is,

$$E_{HK}\left[\rho\right] = T\left[\rho\right] + U\left[\rho\right] + \int d^3 r V_{ext}\left(r\right)\rho\left(r\right)$$

here, $U\left[\rho\right]$ is the potential energy of the interaction of the system and $T\left[\rho\right]$ is the kinetic energy of the system. Unfortunately, expressions for the calculation of the latter two quantities are unknown for the case of a system with interacting electrons, such as the one considered in the HK theory.

In 1965, Khon and Sham [2] proposed an elegant solution to this new problem. Instead of considering a system of interacting electrons their approach was to create a fictitious system composed by non-interacting electrons whose density would be identical to that of the system of interacting electrons. Using this approach the Khon-Sham (KS) equation was proposed,

$$\left(-\frac{1}{2}\nabla^2 + v_{ext}\left(r\right) + v_H\left(r\right) + v_{xc}\left(r\right)\right)\phi_i = \varepsilon_i\phi_i$$

here, $v_{ext}(r)$, $v_H(r)$ and $v_{xc}(r)$ are the external, the Hartree and the exchange correlation (XC) potentials, respectively. $v_{xc}(r)$ is a functional of the electron density that is known as the XC Functional (XCF).

In order to solve time-dependent problems, in 1984 Runge and Gross [3] proposed a time dependent analogue of the first HK theorem that set the basis for what is known today as Time Dependent DFT (TD-DFT). Using this formalism, the Time-Dependent (TD) KS equation can be expressed as,

$$\left(-\frac{1}{2}\nabla^2 + v_{ext}(r,t) + v_H(r,t) + v_{xc}(r,t)\right)\phi_i(r,t) = i\frac{\partial\phi_j(r,t)}{\partial t}$$

where $v_{ext}(r,t)$, $v_H(r,t)$ and $v_{xc}(r,t)$ are the TD external, the TD Hartree and the TD exchange correlation potentials. For the case of ground state DFT, the variation minimum principle is used for finding the total energy while in TD-DFT a stationary point of the action integral A needs to be found,

$$A = \int_{t_0}^{t_1} dt \left\langle \Psi(t) \left| i\frac{\partial}{\partial t} - H(t) \right| \Psi(t) \right\rangle$$

***Exchange Correlation Functionals***

The main disadvantage of the KS theory is that an exact XCF is only known for the free electron gas. Therefore, approximations need to be made for all the rest of the molecular systems. The first of these approximations to arise was the Local Density Approximation (LDA), which states that the system can be described by an electron gas whose density is equal to the local density of the molecular system. LDA performs well in systems with slow varying electron densities, like

metals. On the other hand, the rapid changes in electron density observed in molecules make this approximation fail. However, in this case the performance of LDA can be greatly improved through the use Generalized Gradient Approximations (GGA), that contemplate not only the electron density but also its gradient. In addition to these two approximations, in the 1990s Becke [4, 5] proposed to incorporate HF exchange into the XCF, and developed the first series of hybrid functionals. After Becke's initial work, many different hybrid functionals have been developed in order to satisfy the needs of different molecular systems. Throughout this dissertation only two hybrid functionals were used. First, the popular Becke three-parameter Lee Yang Parr (B3LYP) [4-6] and then its Coulomb Attenuated variant know as CAM-B3LYP. [7, 8] B3LYP has the following form,

$$E_{xc}^{B3LYP} = E_x^{LDA} + E_c^{LDA} + a_0\left(E_x^{HF} - E_x^{LDA}\right) + a_x\left(E_x^{GGA} - E_x^{LDA}\right) + a_c\left(E_c^{GGA} - E_c^{LDA}\right)$$

where the parameters $a_0 = 0.2$, $a_x = 0.72$ and $a_c = 0.81$, were obtained from fitting to experimental data. CAM-B3LYP modifies B3LYP in such a way that it accounts for long-range exchange, this modification is needed for molecules exhibiting Rydberg or charge transfer states, were the electrons usually have the ability to travel far away from the nuclei. In the CAM-B3LYP [7] functional the short- and long-range exchange are adjusted through the use of the parameters, using the following equation,

$$\frac{1}{r_{12}} = \frac{1-\left[\alpha + \beta \cdot \mathrm{erf}\left(\mu r_{12}\right)\right]}{r_{12}} + \frac{\alpha + \beta \cdot \mathrm{erf}\left(\mu r_{12}\right)}{r_{12}}$$

In this dissertation work the standard parametrization ($\alpha = 0.19$, $\beta = 0.46$, $\mu = 0.33$) has been employed.

**References**


1. Hohenberg, P.; Kohn, W., Inhomogeneous electron gas. *Physical review* **1964,** *136* (3B), B864.
2. Kohn, W.; Sham, L. J., Self-consistent equations including exchange and correlation effects. *Physical Review* **1965,** *140* (4A), A1133.
3. Runge, E.; Gross, E. K. U., Density-Functional Theory for Time-Dependent Systems. *Phys. Rev. Lett.* **1984,** *52* (12), 997-1000.
4. Becke, A. D., Density-Functional Exchange-Energy Approximation with Correct Asymptotic Behavior. *Phys. Rev. A* **1988,** *38*, 3098-3100.
5. Becke, A. D., Density-Functional Thermochemistry. III. The Role of Exact Exchange. *J. Chem. Phys.* **1993,** *98*, 5648-5652.
6. Lee, C.; Yang, W.; Parr, R. G., Development of the Colle-Salvetti Correlation-Energy Formula into a Functional of the Electron Density. *Phys. Rev. B: Condens. Matter* **1988,** *37*, 785-789.
7. Yanai, T.; Tew, D. P.; Handy, N. C., A new Hybrid Exchange-Correlation Functional using the Coulomb-Attenuating Method (CAM-B3LYP). *Chem. Phys. Lett.* **2004,** *393*, 51-57.
8. Peach, M. J. G.; Helgaker, T.; Sałek, P.; Keal, T. W.; Lutnaes, O. B.; Tozer, D. J.; Handy, N. C., Assessment of a Coulomb-attenuated exchange-correlation energy functional. *Phys. Chem. Chem. Phys.* **2006,** *8*, 558-562.

# APPENDIX E: **TPA AND TPCD SPECTRA OF R-BINOL, R-VANOL, AND R-VAPOL CALCULATED WITH B3LYP (CHAPTER 2)**

Experimental (black scattered squares) and theoretical TPA spectra of R-BINOL (top), R-VANOL (middle), and R-VAPOL (bottom) *in vacuo* using Dalton 2013. TPA was computed for the first 48 electronic excited states (colored scattered symbols) for all the molecules. The Lorentzian convolutions were obtained using a linewidth Γ = 0.2, 0.1, and 0.15 eV for R-BINOL (top), R-VANOL (middle), and R-VAPOL (bottom), respectively. The theoretical spectra were calculated with B3LYP/6-311++G(d,p). The theoretical shifts are: R-BINOL (+10 nm), R-VANOL (-5 nm), and R-VAPOL (-20 nm). All the experimental spectra were taken in THF solutions.

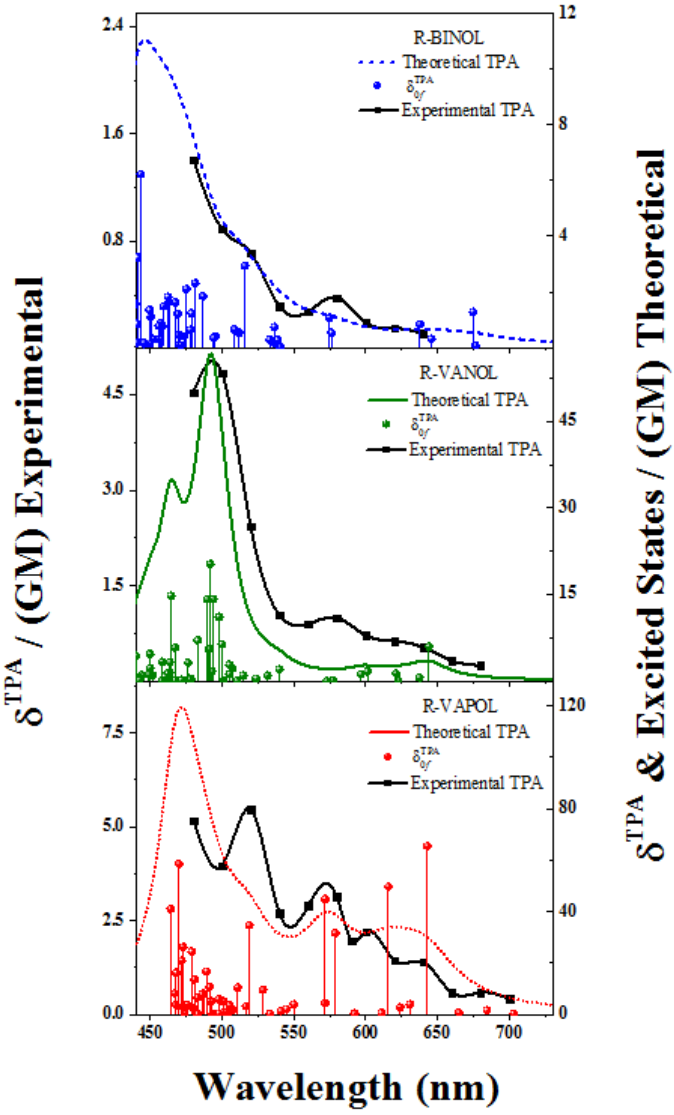

Experimental (black scattered squares) and theoretical TPCD spectra of R-BINOL (top), R-VANOL (middle), and R-VAPOL (bottom) *in vacuo* using Dalton 2013. TPCD was computed for the first 48 electronic excited states (colored scattered symbols) for all the molecules. The Lorentzian convolutions were obtained using a linewidth Γ = 0.2, 0.1, and 0.15 eV for R-BINOL (top), R-VANOL (middle), and R-VAPOL (bottom), respectively. The theoretical spectra were calculated with B3LYP/6-311++G(d,p). The theoretical shifts are: R-BINOL (+77 nm), R-VAPOL (+25 nm), and R-VAPOL (+45 nm). All the experimental spectra were taken in THF solutions.

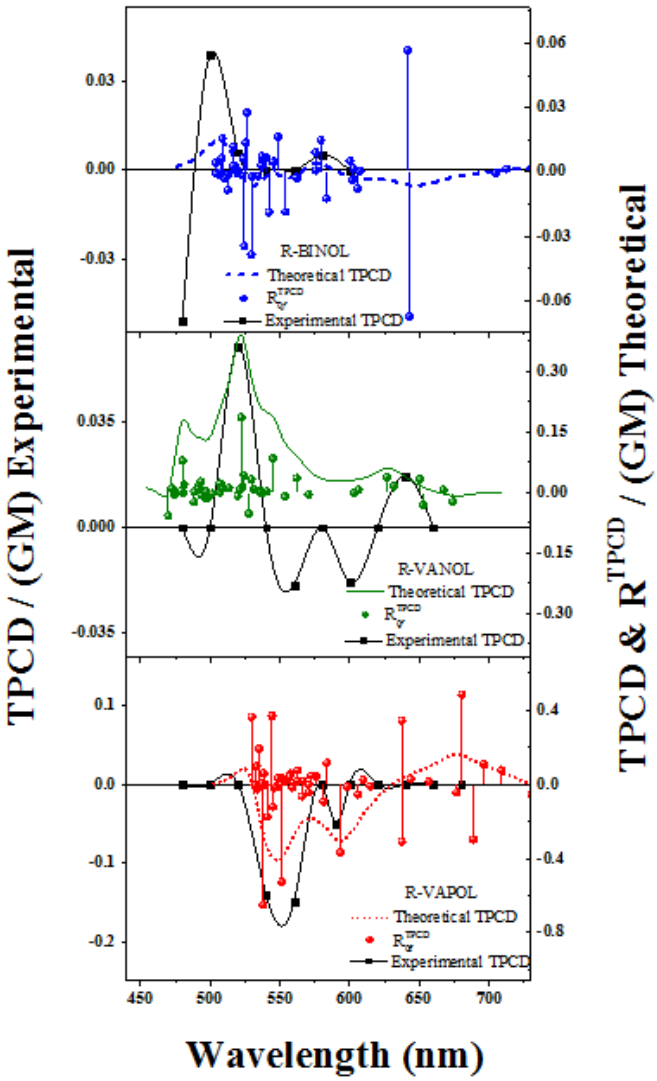

# APPENDIX F: **EXPANSION OF GRAPHS AND COMPARISON OF L-TRYPTOPHAN, L-HISTIDINE, L-PHENYLALANINE, AND L-TYROSINE (CHAPTER 4)**

Comparative plots of TPA (top left), TPCD (top right), OPA (bottom left), and ECD (bottom right) spectra of all six Trp residues in their corresponding random-coil (red dotted line), α-helix (black solid line) and β-strand (blue dashed line) conformations for the lowest 80 electronic excited states of all optimized structures were computed with TD-DFT/ CAM-B3LYP/6-311G(d). Shaded area indicates where ECD is truly functional.

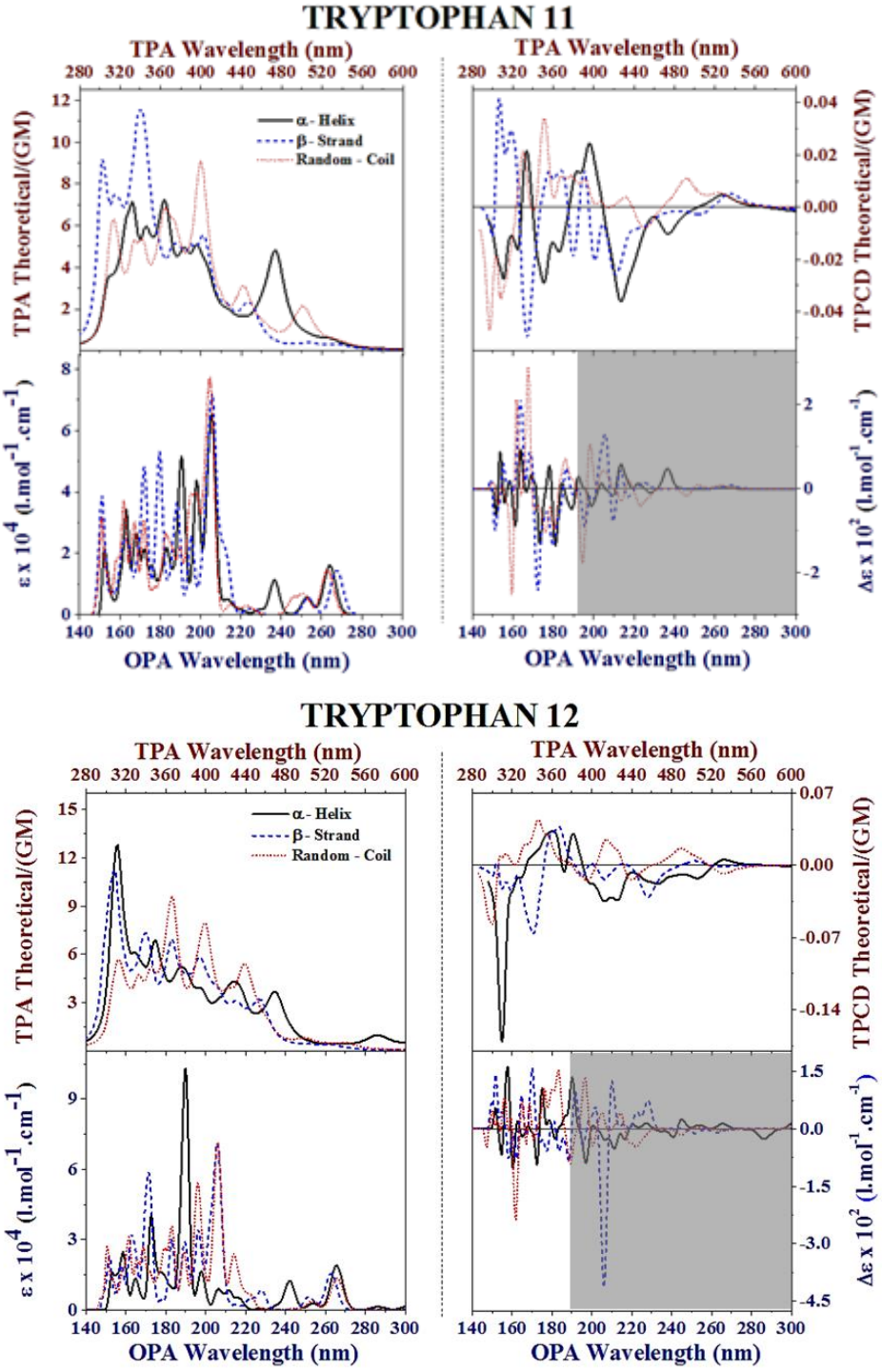

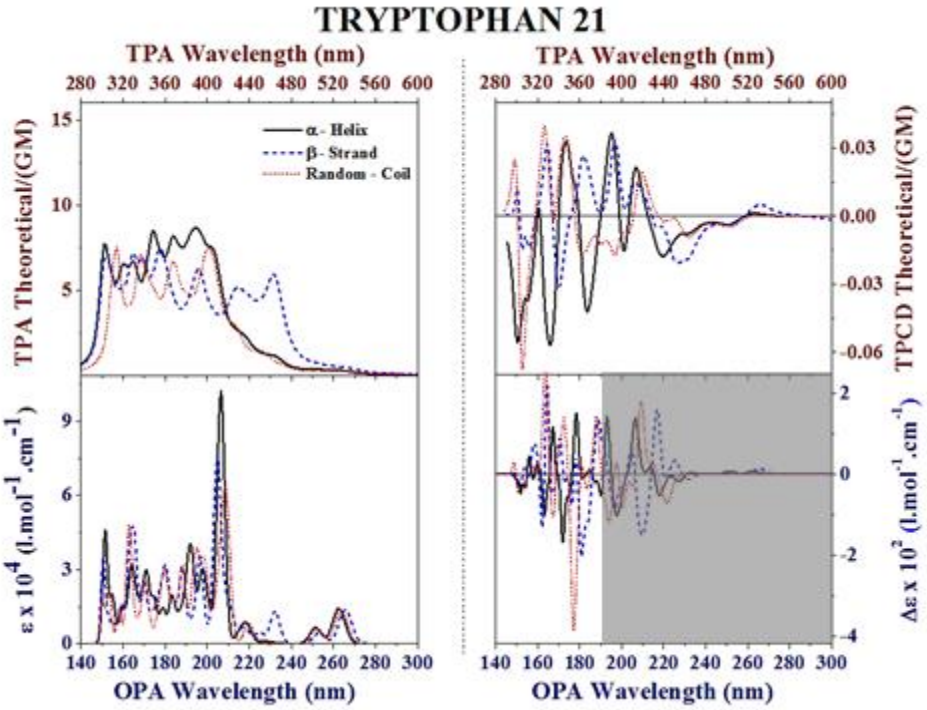
TRYPTOPHAN 21
TPA Wavelength (nm)
280 320 360 400 440 480 520 560 600
α - Helix
β - Strand
Random - Coil
TPA Theoretical/(GM)
ε x 10^4 (l.mol^-1.cm^-1)
OPA Wavelength (nm)
140 160 180 200 220 240 260 280 300
TPCD Theoretical/(GM)
Δε x 10^2 (l.mol^-1.cm^-1)

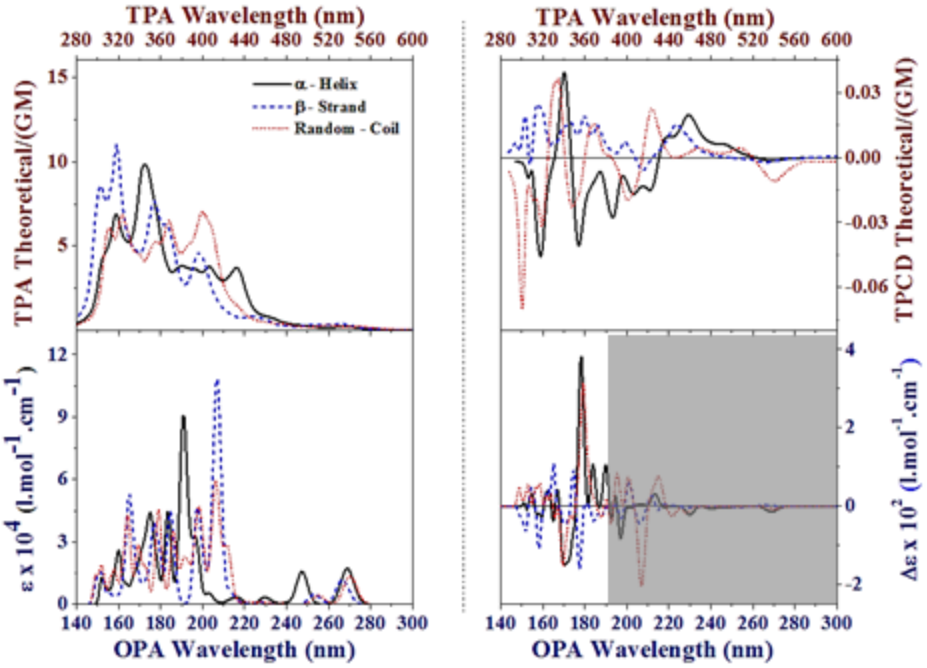
TRYPTOPHAN 22
TPA Wavelength (nm)
280 320 360 400 440 480 520 560 600
α - Helix
β - Strand
Random - Coil
TPA Theoretical/(GM)
ε x 10^4 (l.mol^-1.cm^-1)
OPA Wavelength (nm)
140 160 180 200 220 240 260 280 300
TPCD Theoretical/(GM)
Δε x 10^2 (l.mol^-1.cm^-1)

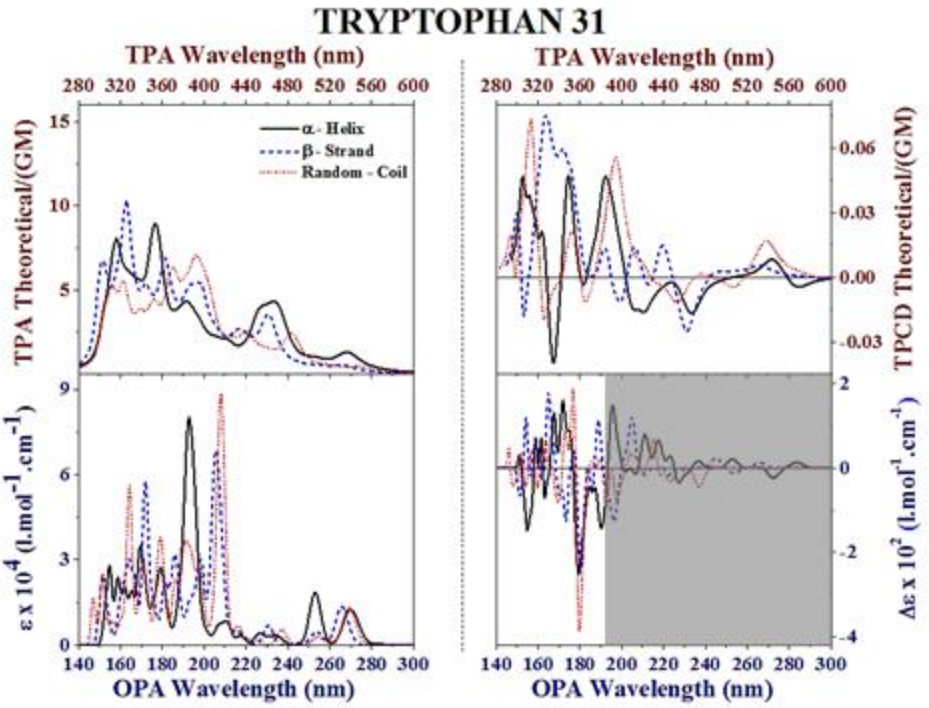
TRYPTOPHAN 31
TPA Wavelength (nm)
TPA Wavelength (nm)
α - Helix
β - Strand
Random - Coil
TPA Theoretical/(GM)
TPCD Theoretical/(GM)
ε x 10^4 (l.mol^-1.cm^-1)
Δε x 10^2 (l.mol^-1.cm^-1)
OPA Wavelength (nm)
OPA Wavelength (nm)

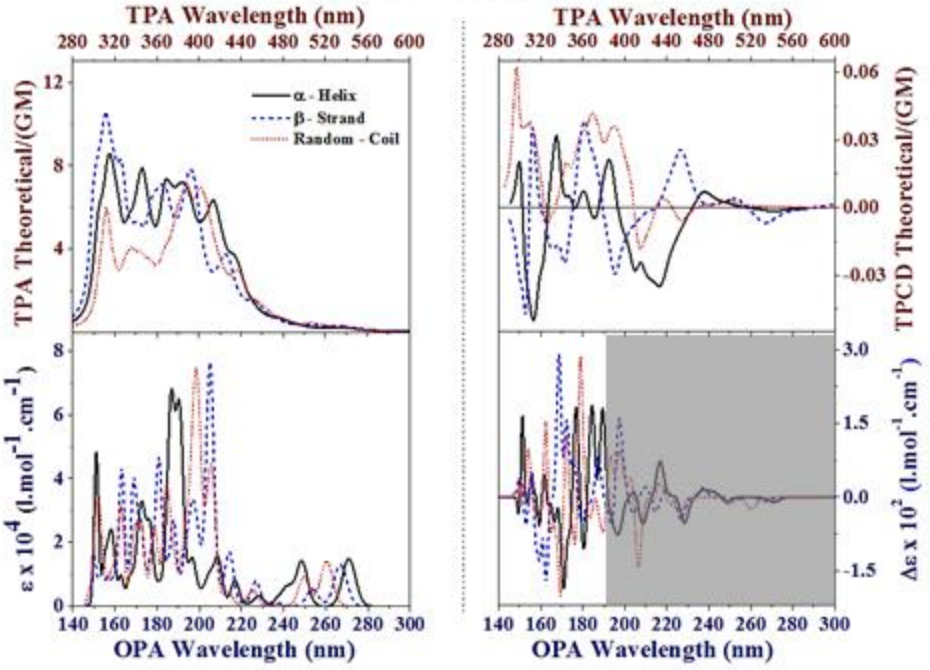
TRYPTOPHAN 32
TPA Wavelength (nm)
TPA Wavelength (nm)
α - Helix
β - Strand
Random - Coil
TPA Theoretical/(GM)
TPCD Theoretical/(GM)
ε x 10^4 (l.mol^-1.cm^-1)
Δε x 10^2 (l.mol^-1.cm^-1)
OPA Wavelength (nm)
OPA Wavelength (nm)

Comparative plots of TPA (top left), TPCD (top right), OPA (bottom left), and ECD (bottom right) spectra of all six His residues in their corresponding random-coil (red dotted line), α-helix (black solid line) and β-strand (blue dashed line) conformations for the lowest 80 electronic excited states of all optimized structures were computed with TD-DFT/ CAM-B3LYP/6-311G(d). Shaded area indicates where ECD is truly functional.

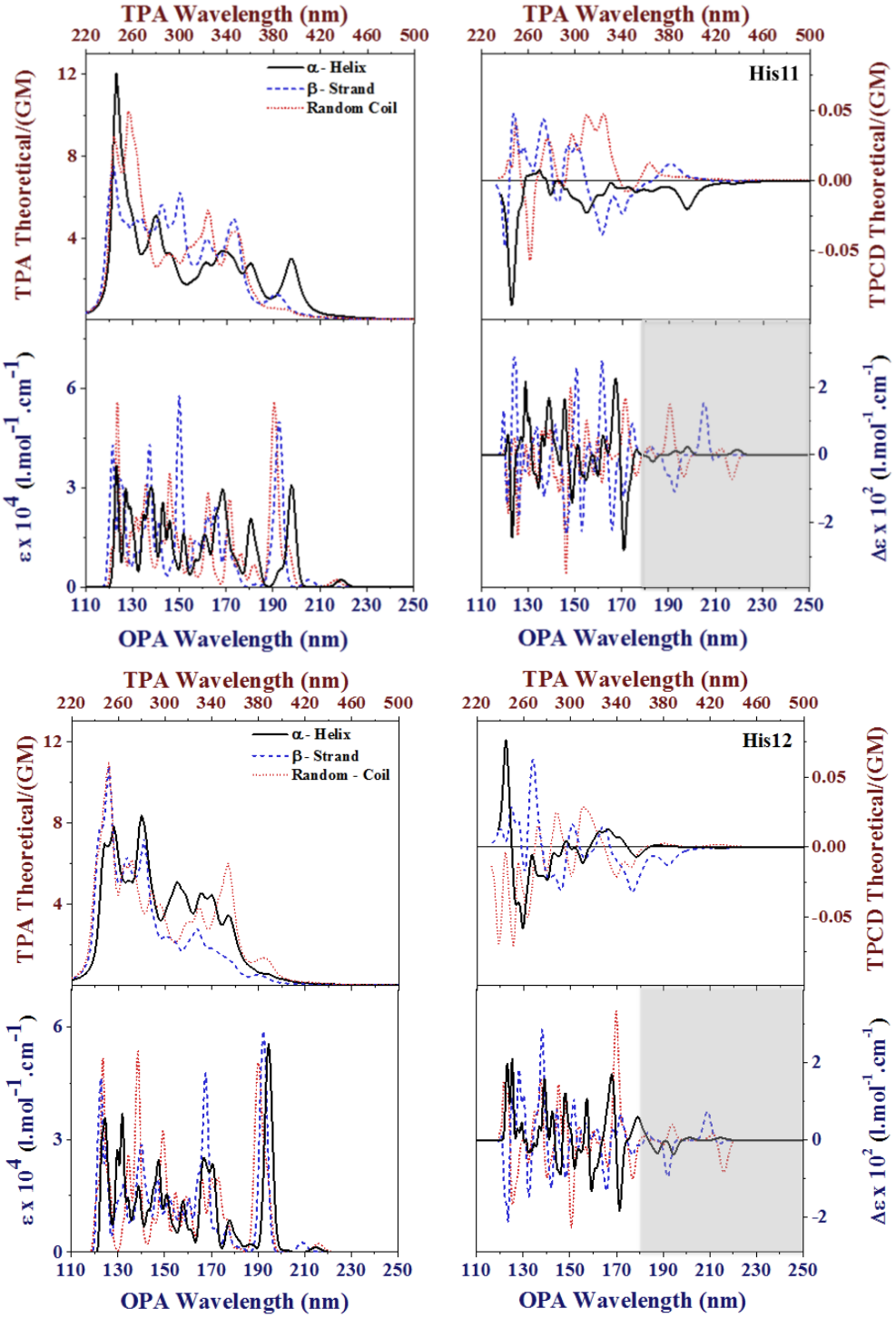

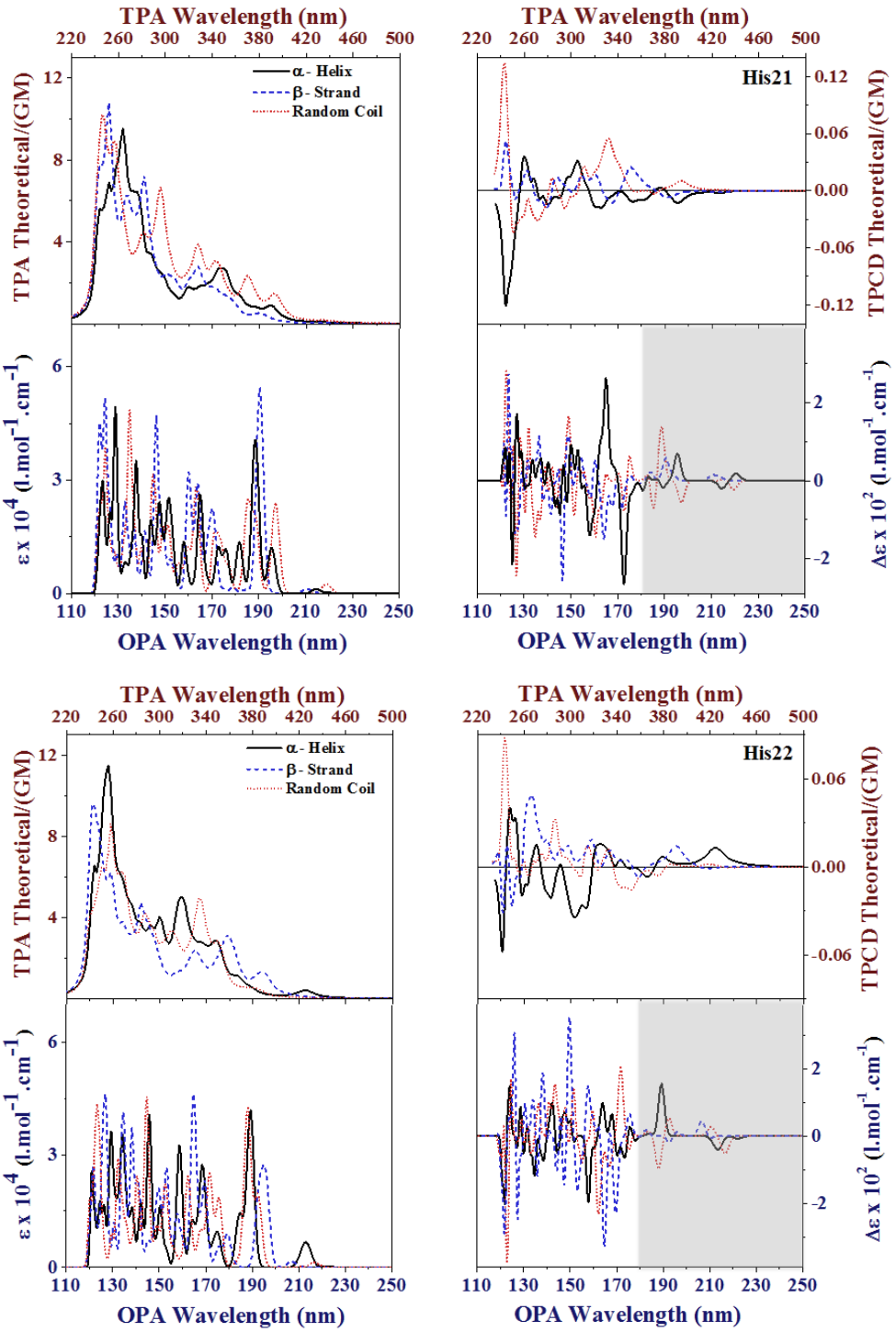
TPA Wavelength (nm)
TPA Theoretical/(GM)
α- Helix
β- Strand
Random Coil
ε x 10^4 (l.mol^-1.cm^-1)
OPA Wavelength (nm)
His21
TPCD Theoretical/(GM)
Δε x 10^2 (l.mol^-1.cm^-1)
His22

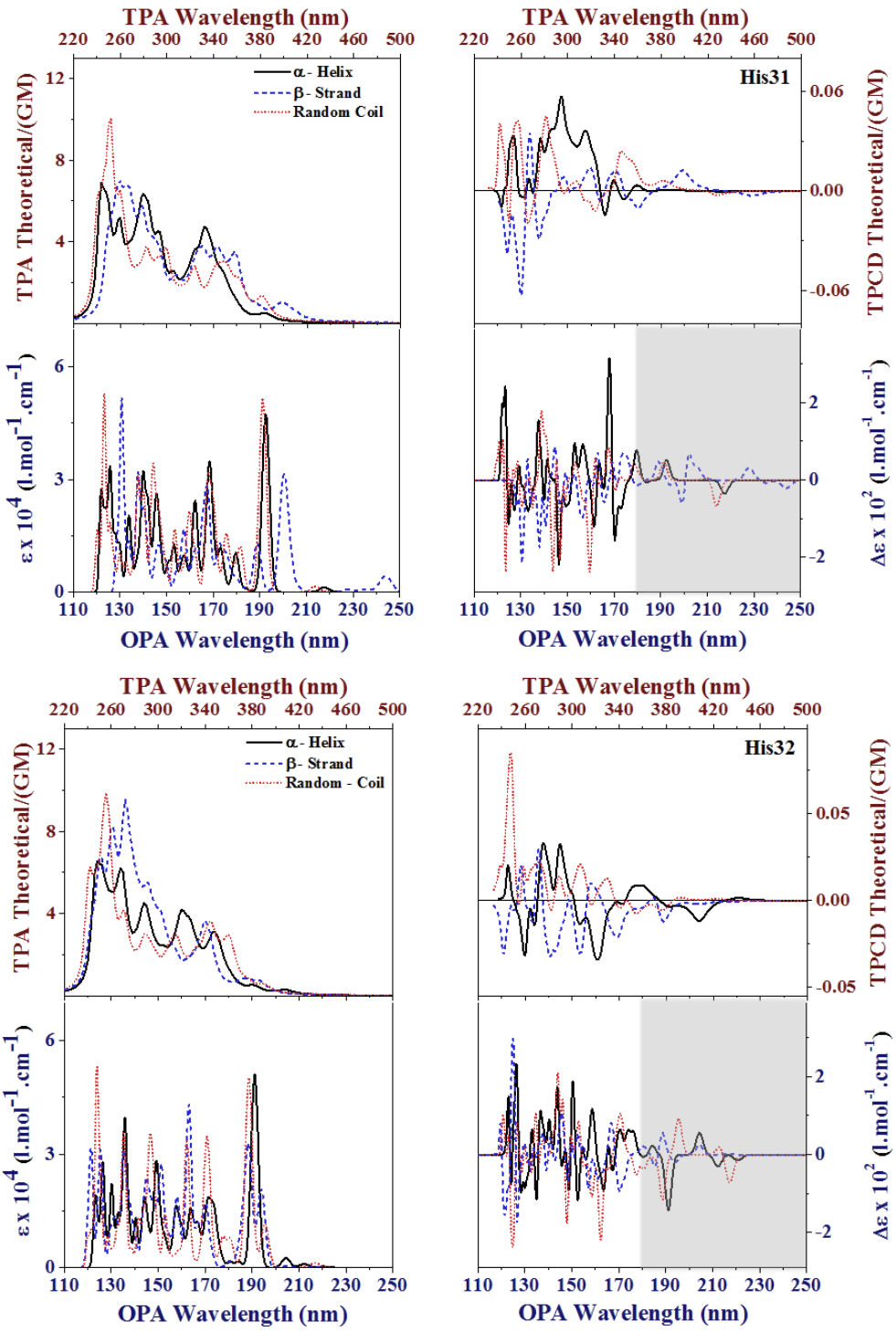
TPA Wavelength (nm)
TPA Theoretical/(GM)
α - Helix
β - Strand
Random Coil
His31
TPCD Theoretical/(GM)
ε x 10^4 (l.mol^-1.cm^-1)
Δε x 10^2 (l.mol^-1.cm^-1)
OPA Wavelength (nm)
His32
Random - Coil

Comparative plots of TPA (top left), TPCD (top right), OPA (bottom left), and ECD (bottom right) spectra of all six Phe residues in their corresponding random-coil (red dotted line), α-helix (black solid line) and β-strand (blue dashed line) conformations for the lowest 80 electronic excited states of all optimized structures were computed with TD-DFT/ CAM-B3LYP/6-311G(d). Shaded area indicates where ECD is truly functional.

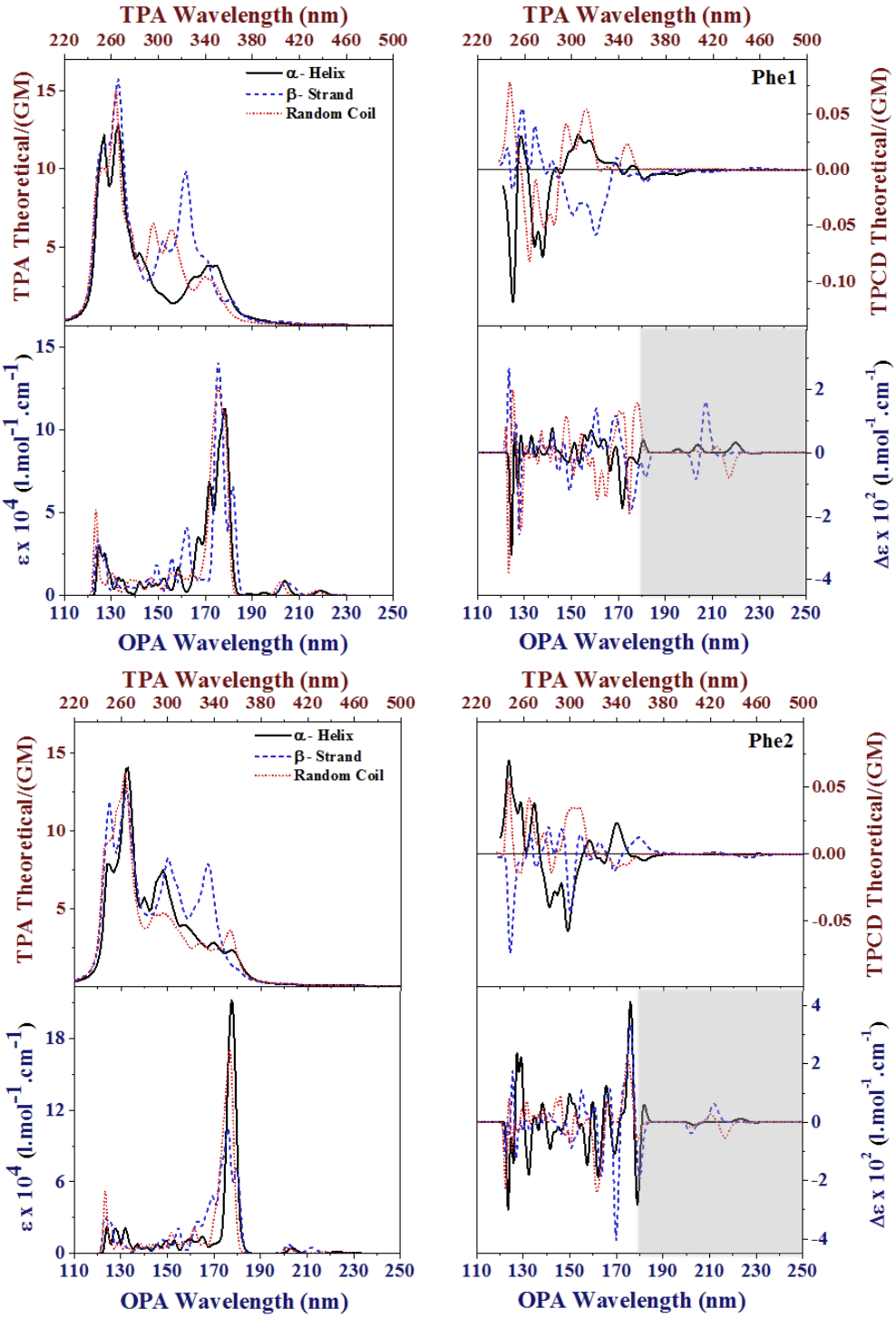

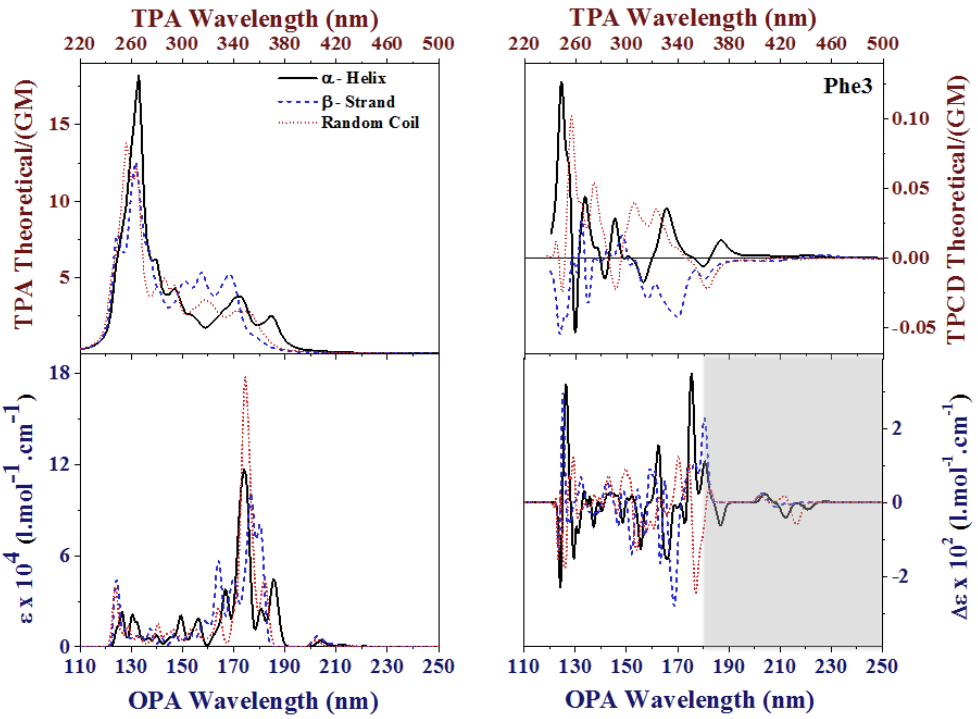
TPA Wavelength (nm)
220 260 300 340 380 420 460 500
α- Helix
β- Strand
Random Coil
TPA Theoretical/(GM)
15
10
5
ε x 10^4 (l.mol^-1.cm^-1)
18
12
6
0
110 130 150 170 190 210 230 250
OPA Wavelength (nm)
TPA Wavelength (nm)
220 260 300 340 380 420 460 500
Phe3
0.10
0.05
0.00
-0.05
TPCD Theoretical/(GM)
2
0
-2
Δε x 10^2 (l.mol^-1.cm^-1)
110 130 150 170 190 210 230 250
OPA Wavelength (nm)

Comparative plots of TPA (top left), TPCD (top right), OPA (bottom left), and ECD (bottom right) spectra of all six Tyr residues in their corresponding random-coil (red dotted line), α-helix (black solid line) and β-strand (blue dashed line) conformations for the lowest 80 electronic excited states of all optimized structures were computed with TD-DFT/ CAM-B3LYP/6-311G(d). Shaded area indicates where ECD is truly functional.

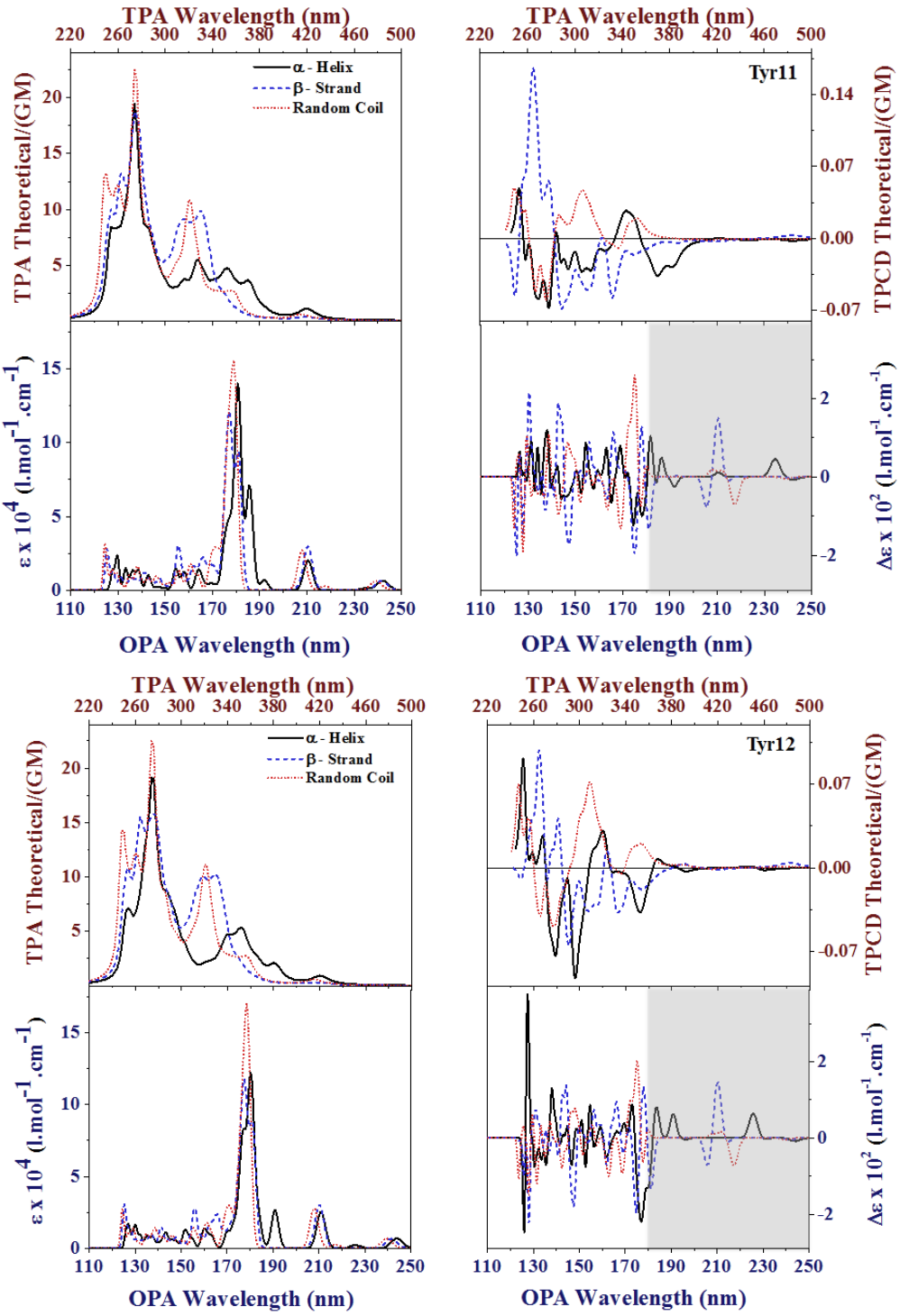

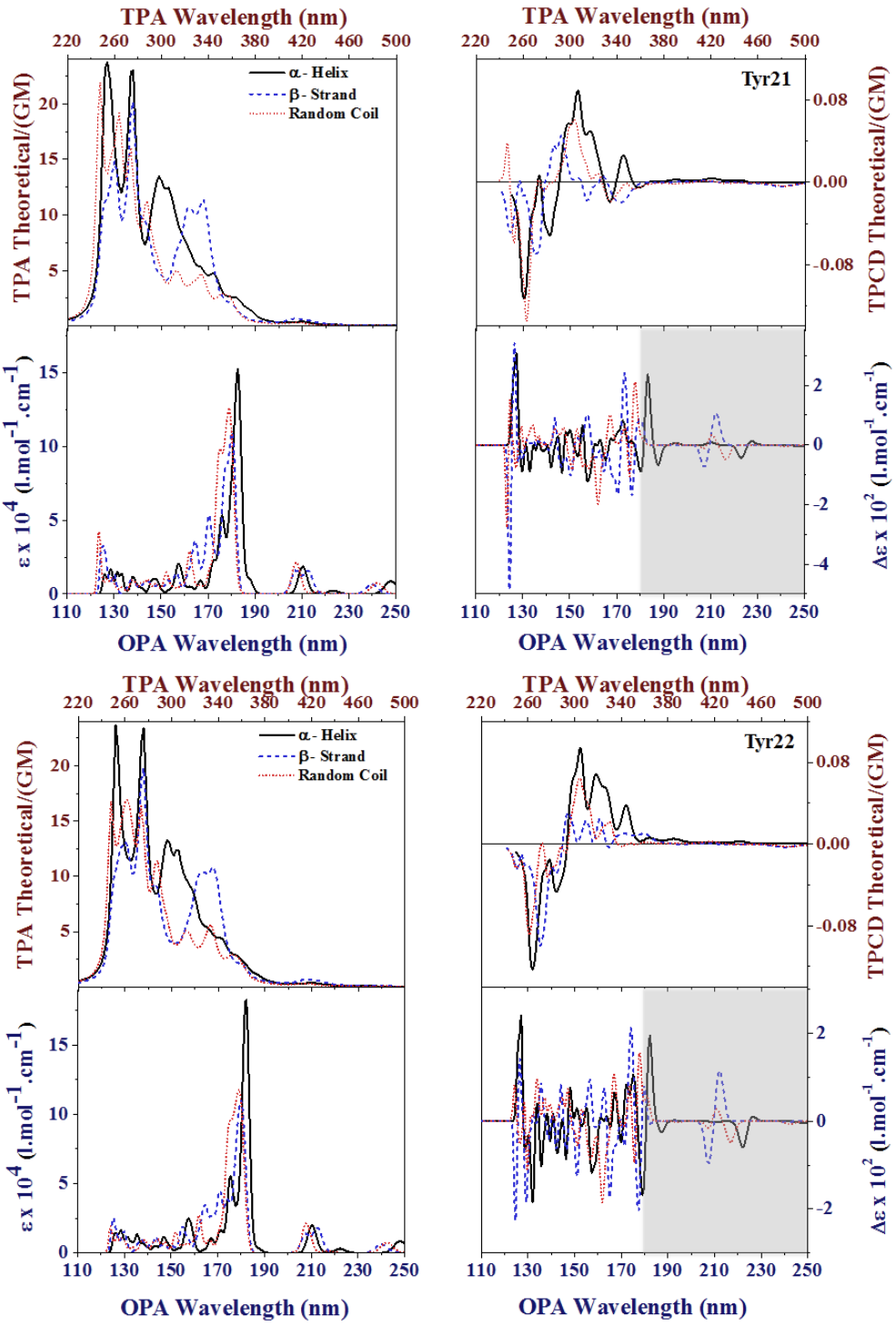
TPA Wavelength (nm)
TPA Theoretical/(GM)
α- Helix
β- Strand
Random Coil
ε x 10^4 (l.mol^-1.cm^-1)
OPA Wavelength (nm)
Tyr21
TPCD Theoretical/(GM)
Δε x 10^2 (l.mol^-1.cm^-1)
Tyr22

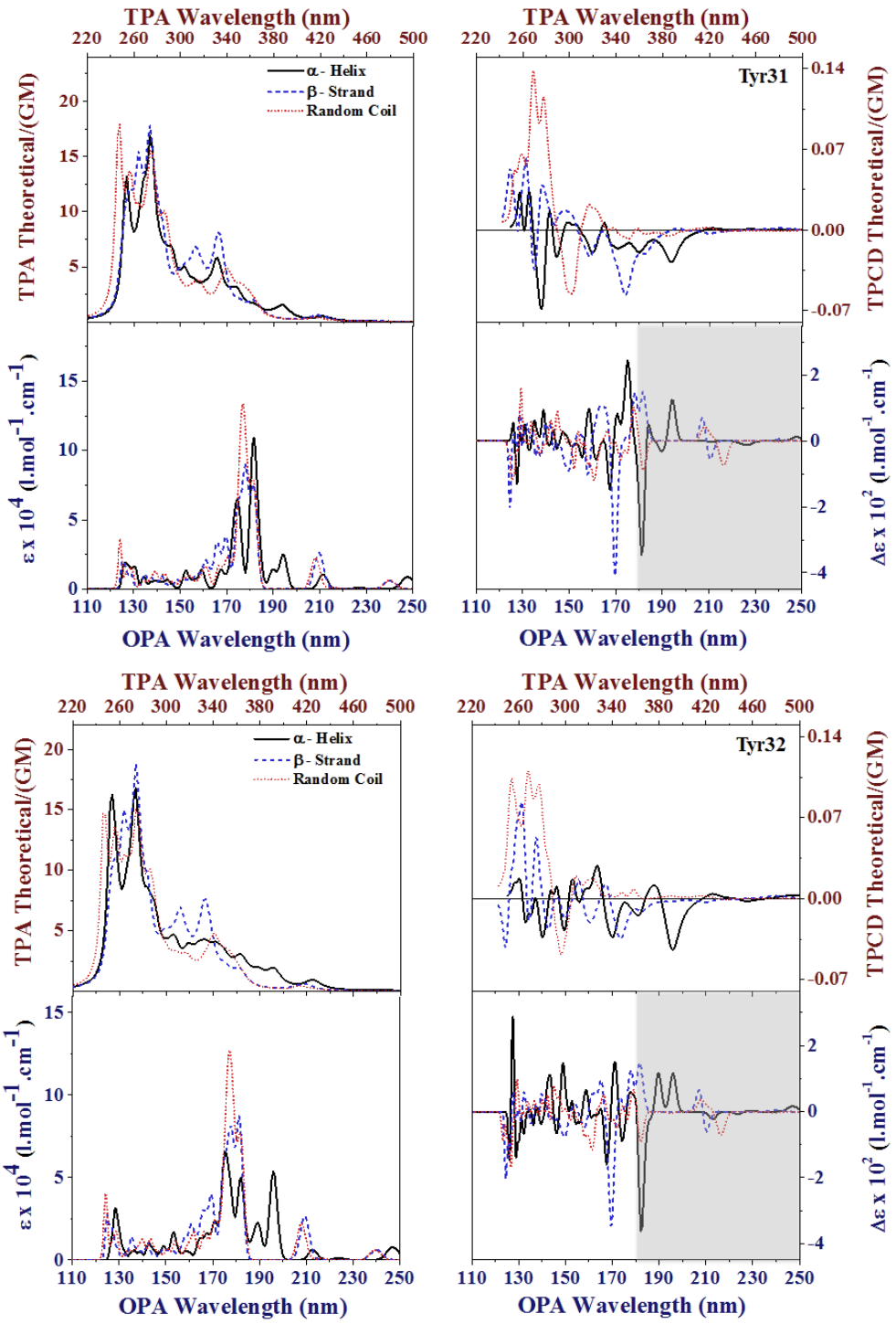
TPA Wavelength (nm)
TPA Theoretical/(GM)
α - Helix
β - Strand
Random Coil
ε x 10^4 (l.mol^-1.cm^-1)
OPA Wavelength (nm)
Tyr31
TPCD Theoretical/(GM)
Δε x 10^2 (l.mol^-1.cm^-1)
Tyr32

Comparative theoretical-experimental fitting performed with B3LYP/6-311G(d) and CAM-B3LYP/6-311G(d) over the first 20 excited states on the experimental measurements of the FUV-ECD spectrum down to 140 nm of L-alanine (bottom), B3LYP spectrum blue shifted +30 nm and CAM-B3LYP spectrum blue shifted +40 nm. L-leucine (middle), B3LYP spectrum blue shifted +8 nm and CAM-B3LYP spectrum blue shifted +28 nm. L-valine (top), B3LYP spectrum blue shifted +20 nm and CAM-B3LYP spectrum blue shifted +40 nm. Experimental data was imported form reference 11 in chapter 4.

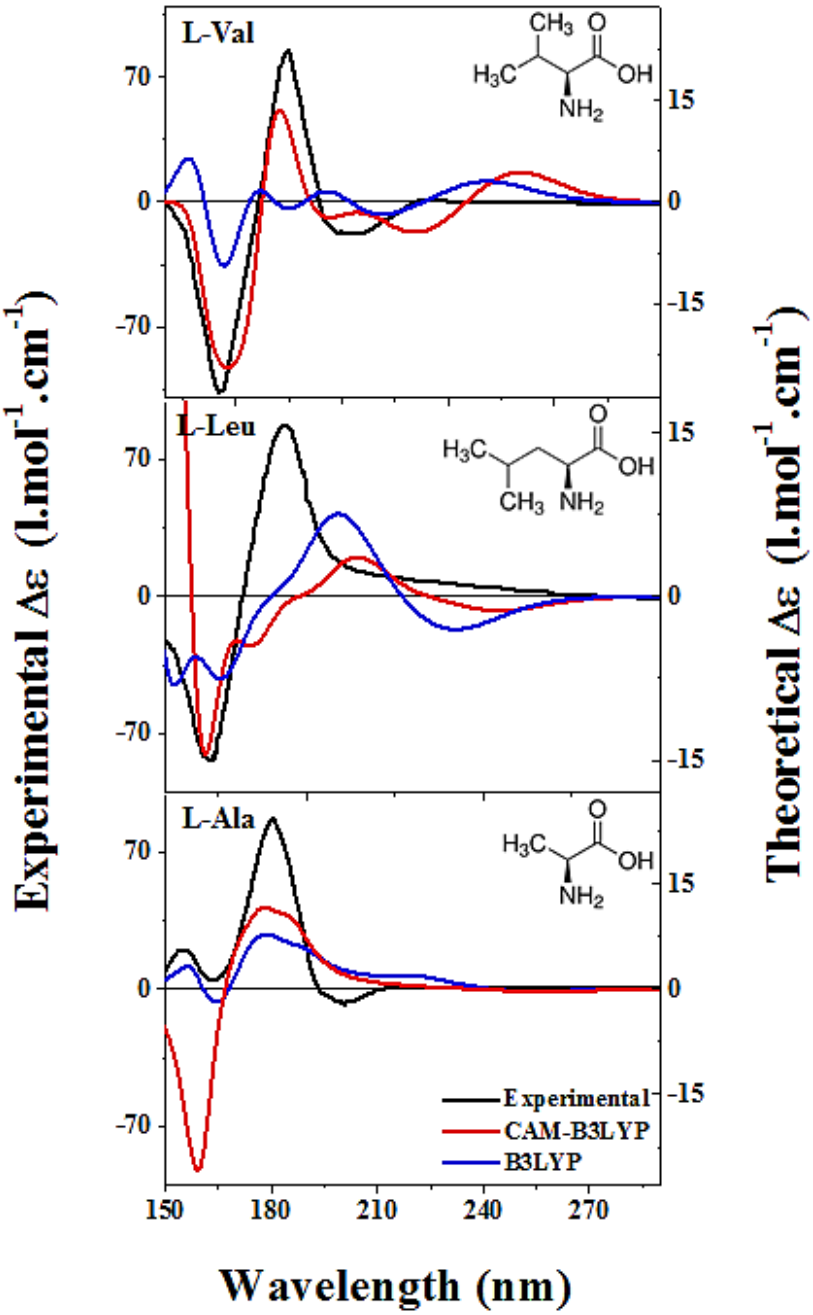

Comparative plots of TPA (left) and TPCD (right) spectra of all six Trp residues in their corresponding random-coil, β-strand and α-helix conformations. TD-DFT/B3LYP/6-311G(d)/80 excited states.

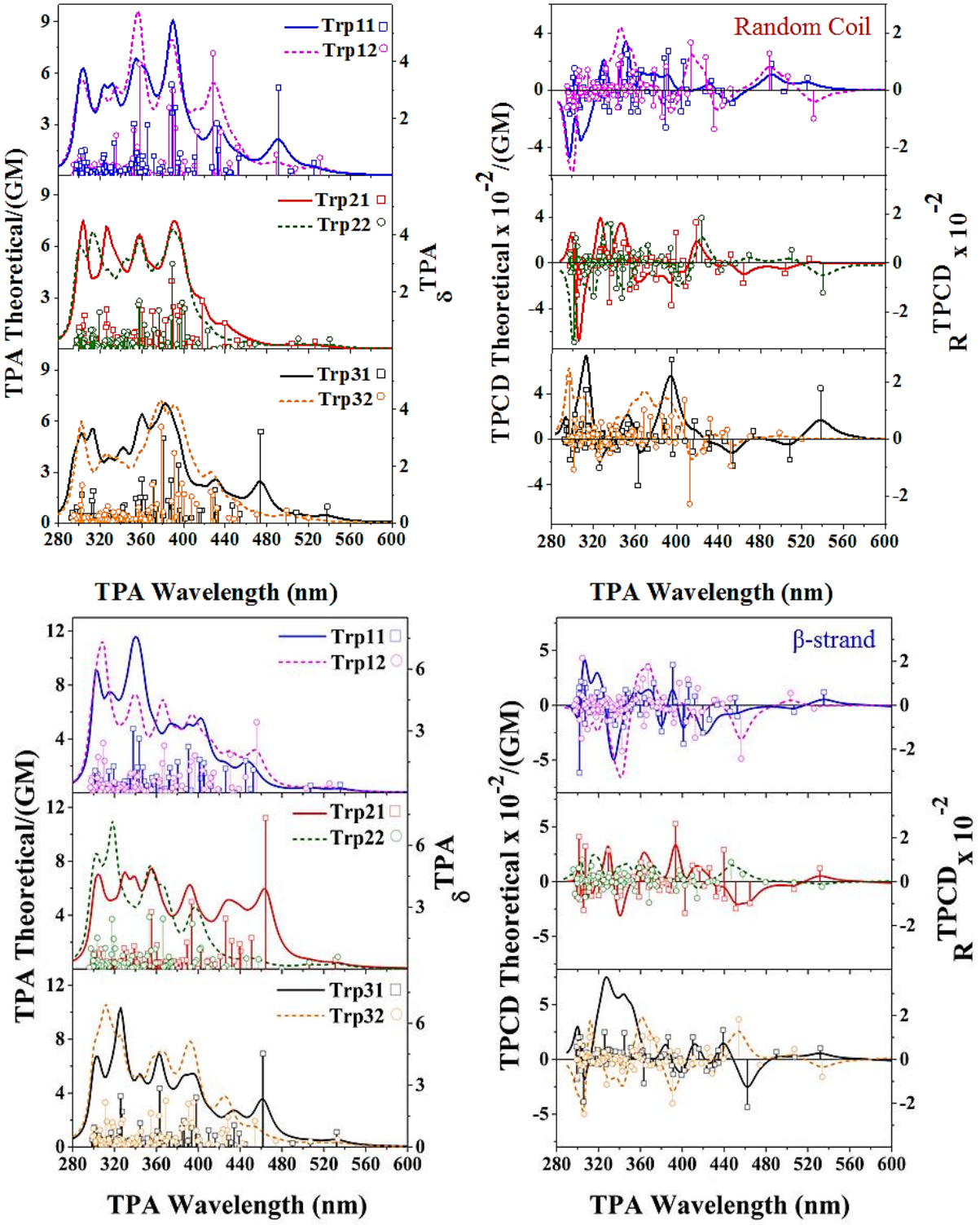

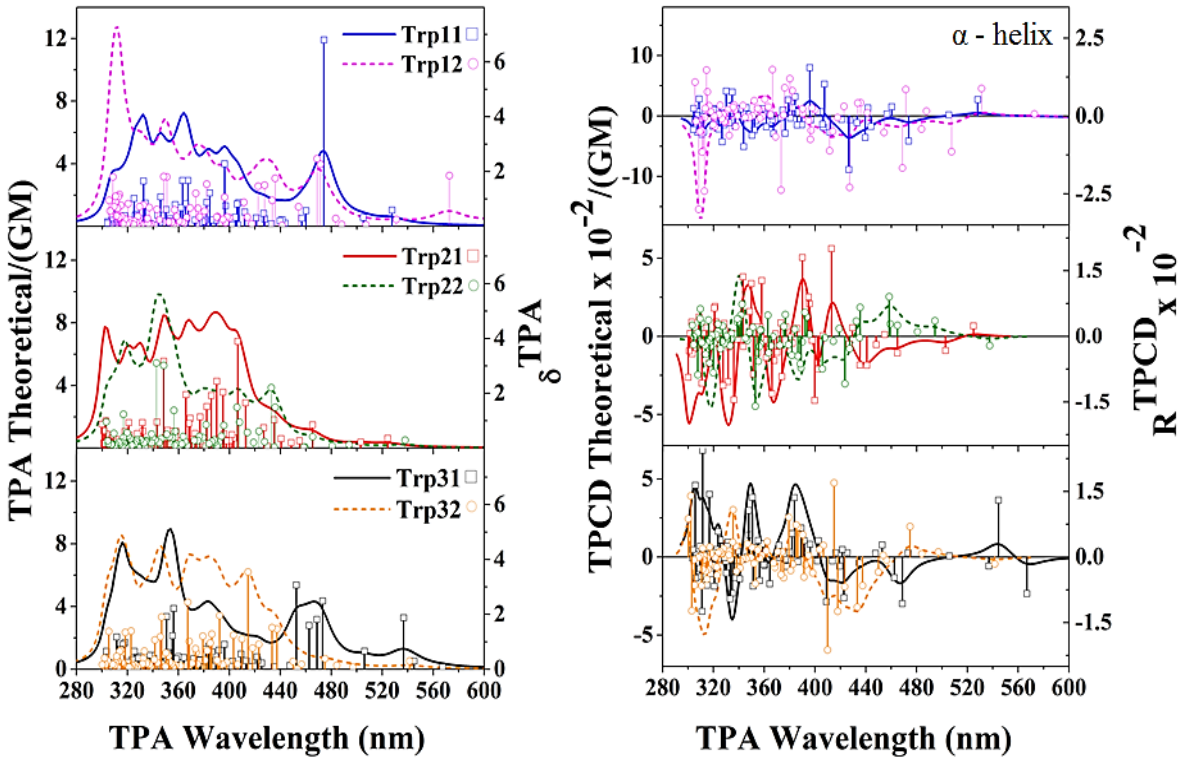
Trp11
Trp12
Trp21
Trp22
Trp31
Trp32
TPA Theoretical/(GM)
δTPA
TPA Wavelength (nm)
α - helix
TPCD Theoretical x 10-2/(GM)
RTPCD x 10-2
TPA Wavelength (nm)

Comparative plots of TPA (left) and TPCD (right) spectra of all six His residues in their corresponding random-coil, β-strand and α-helix conformations. TD-DFT/B3LYP/6-311G(d)/80 excited states.

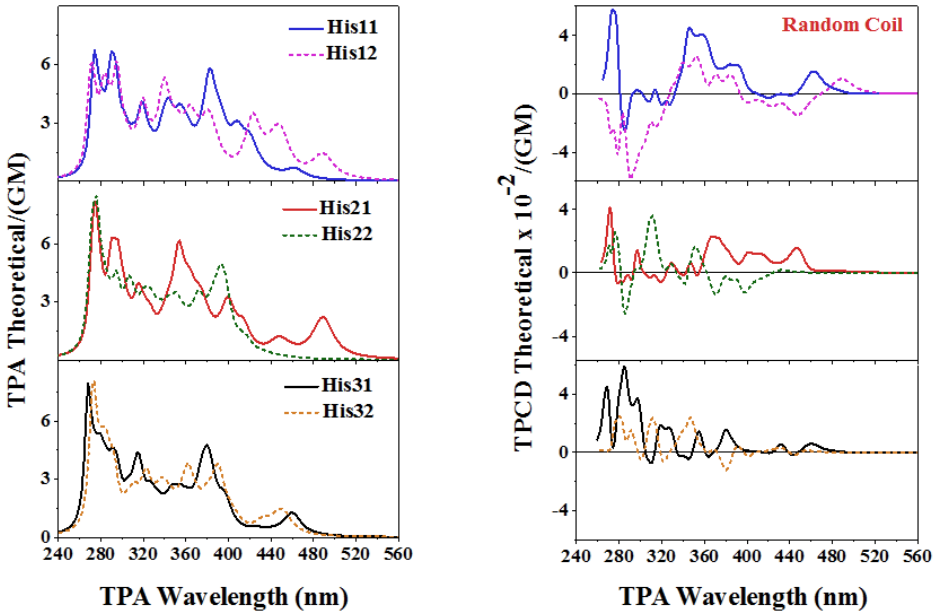


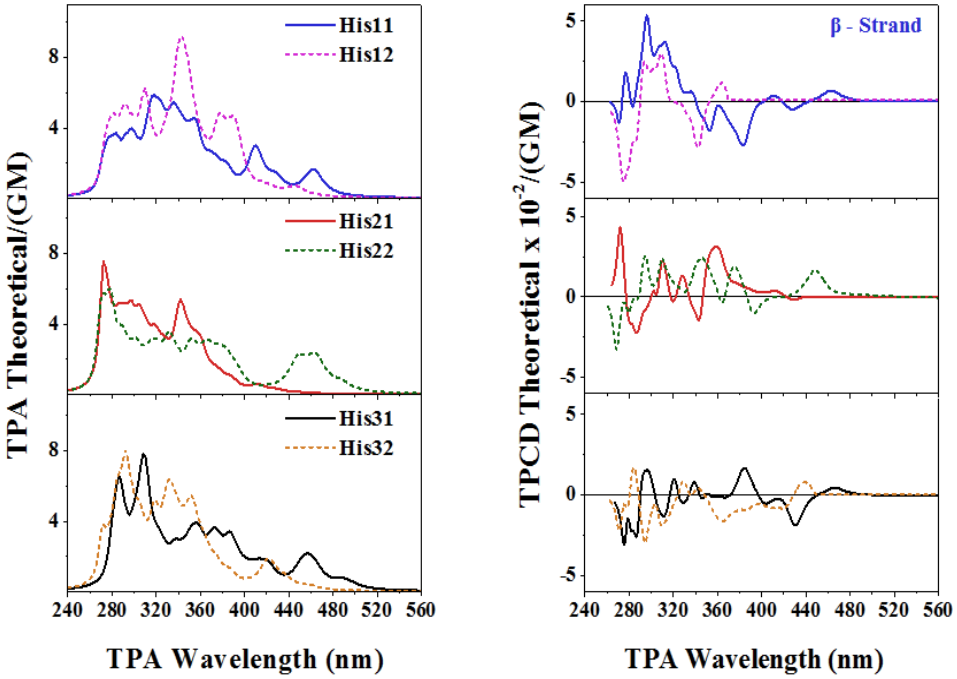

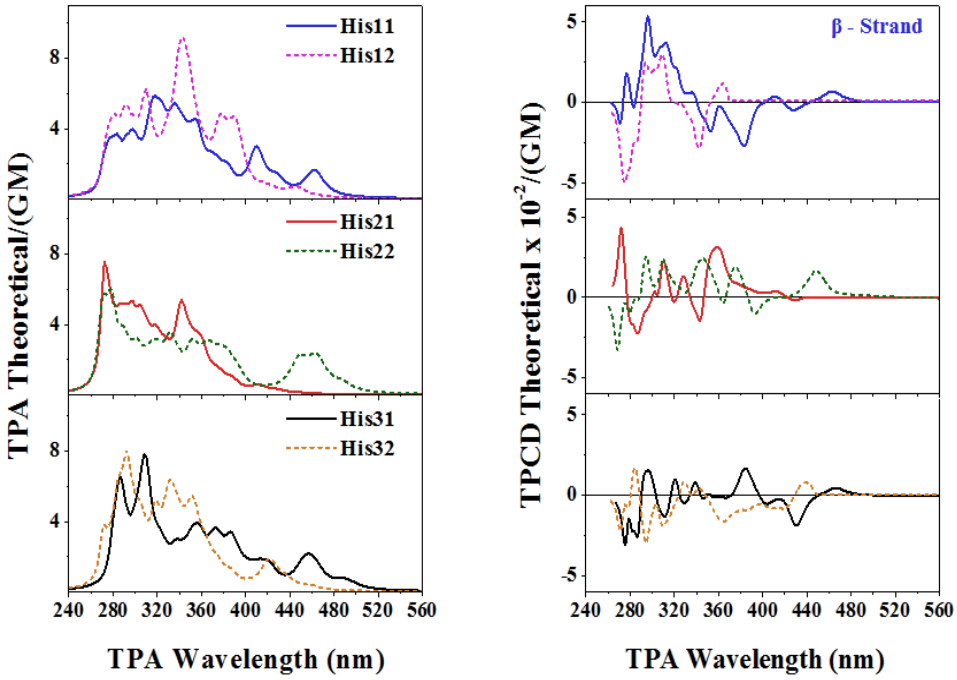
His11
His12
His21
His22
His31
His32
TPA Theoretical/(GM)
TPA Wavelength (nm)
β - Strand
TPCD Theoretical x 10-2/(GM)
TPA Wavelength (nm)

Comparative plots of TPA (left) and TPCD (right) spectra of all three Phe residues in their corresponding random-coil, β-strand and α-helix conformations. TD-DFT/B3LYP/6-311G(d)/80 excited states.

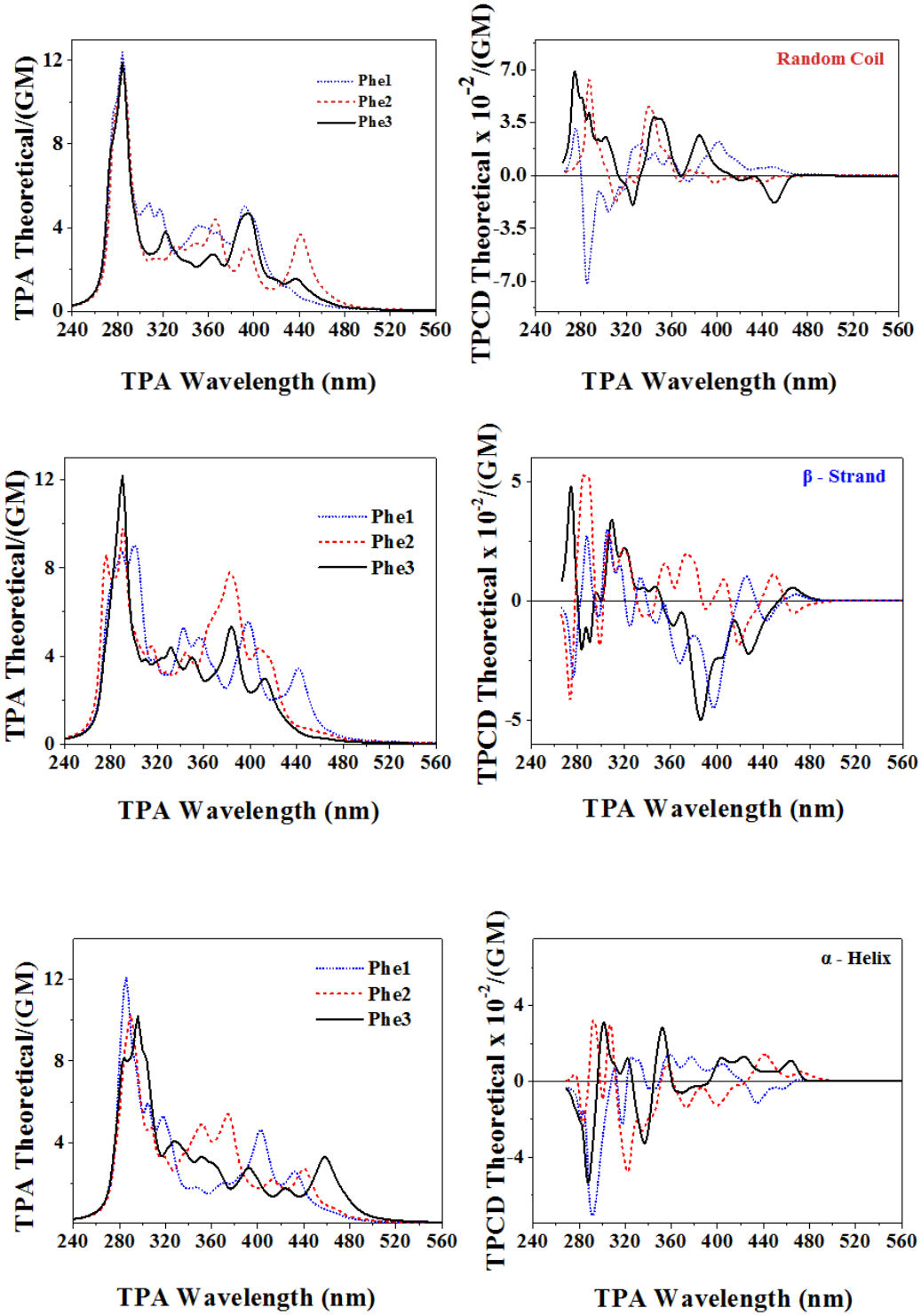

Comparative plots of TPA (left) and TPCD (right) spectra of all six Tyr residues in their corresponding random-coil, β-strand and α-helix conformations. TD-DFT/B3LYP/6-311G(d)/80 excited states.

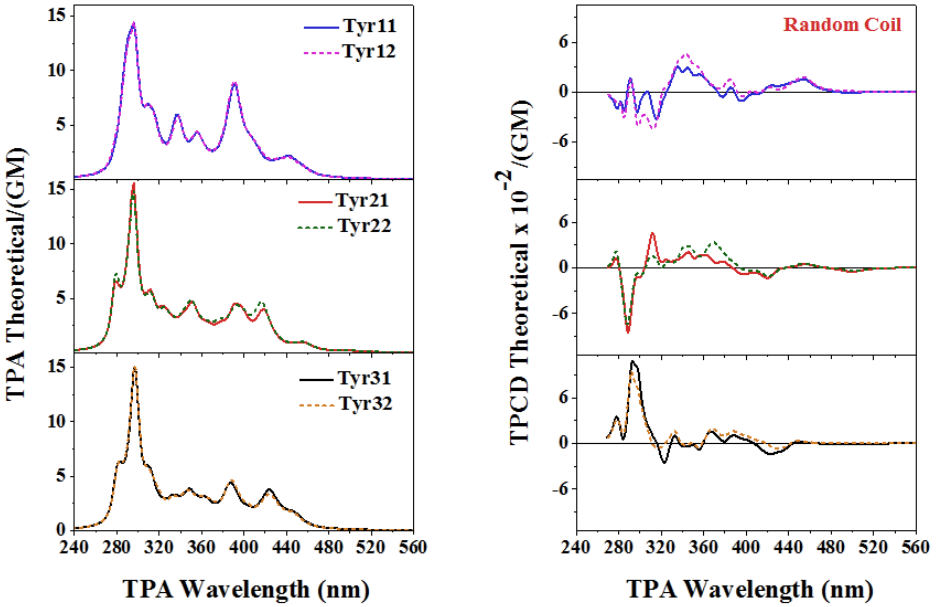


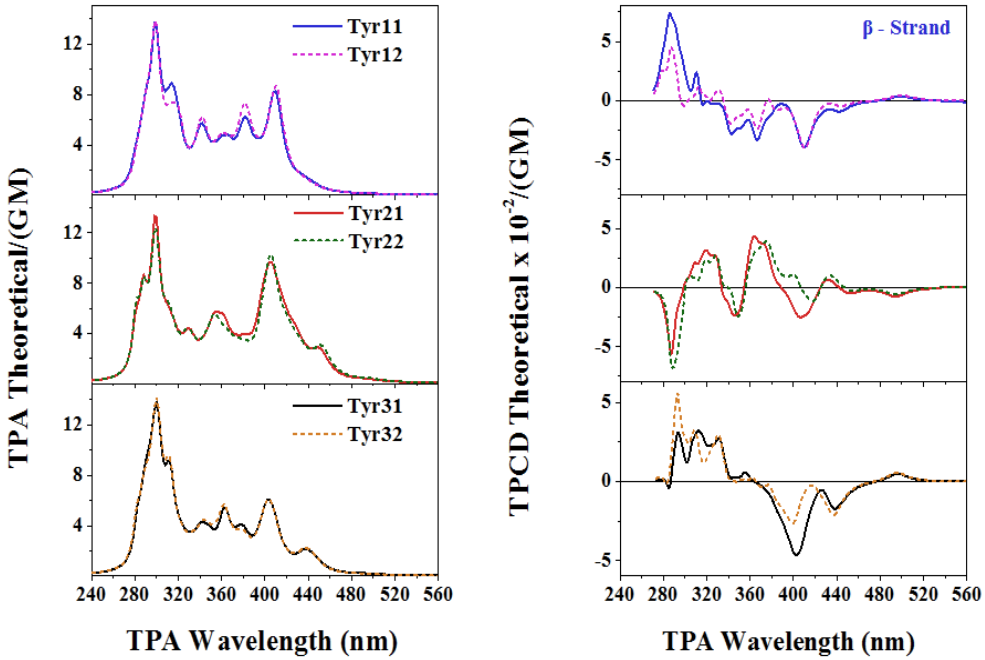

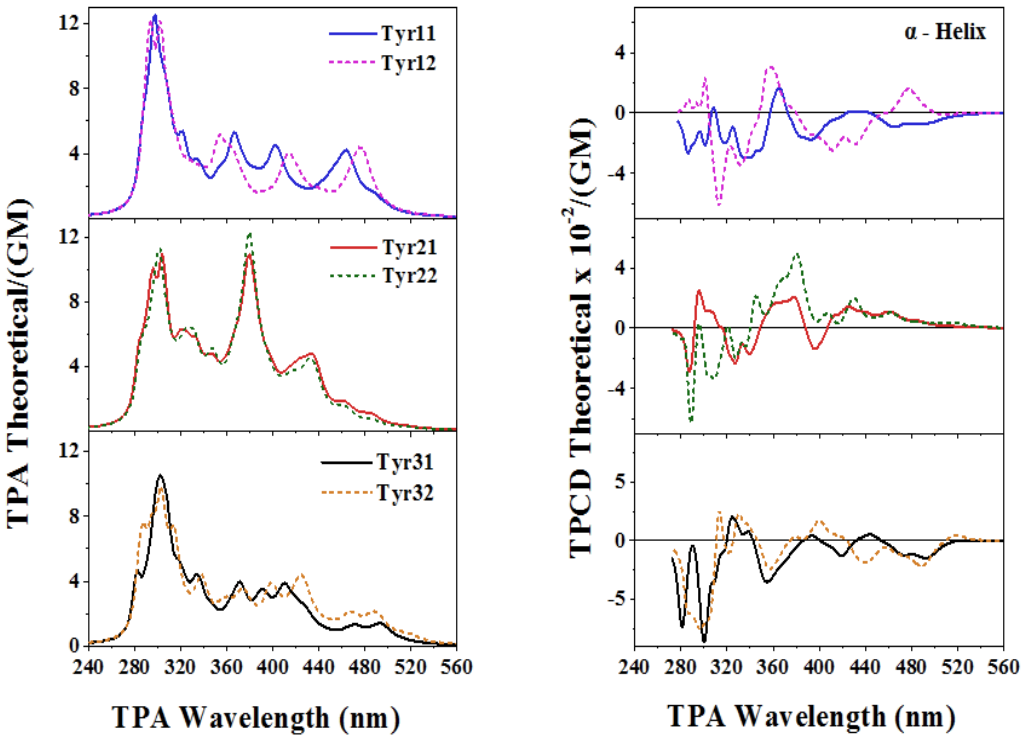
TPA Theoretical/(GM)
Tyr11
Tyr12
Tyr21
Tyr22
Tyr31
Tyr32
TPA Wavelength (nm)
α - Helix
TPCD Theoretical x 10^-2/(GM)
TPA Wavelength (nm)

Comparative plots of TPA (top left), TPCD (top right), OPA (bottom left), and ECD (bottom right) spectra of all six Trp residues in their corresponding random-coil (red dotted line), α-helix (black solid line) and β-strand (blue dashed line) conformations. TD-DFT/ B3LYP/6-311G(d)/80 excited states. Shaded area indicates where ECD is truly functional.

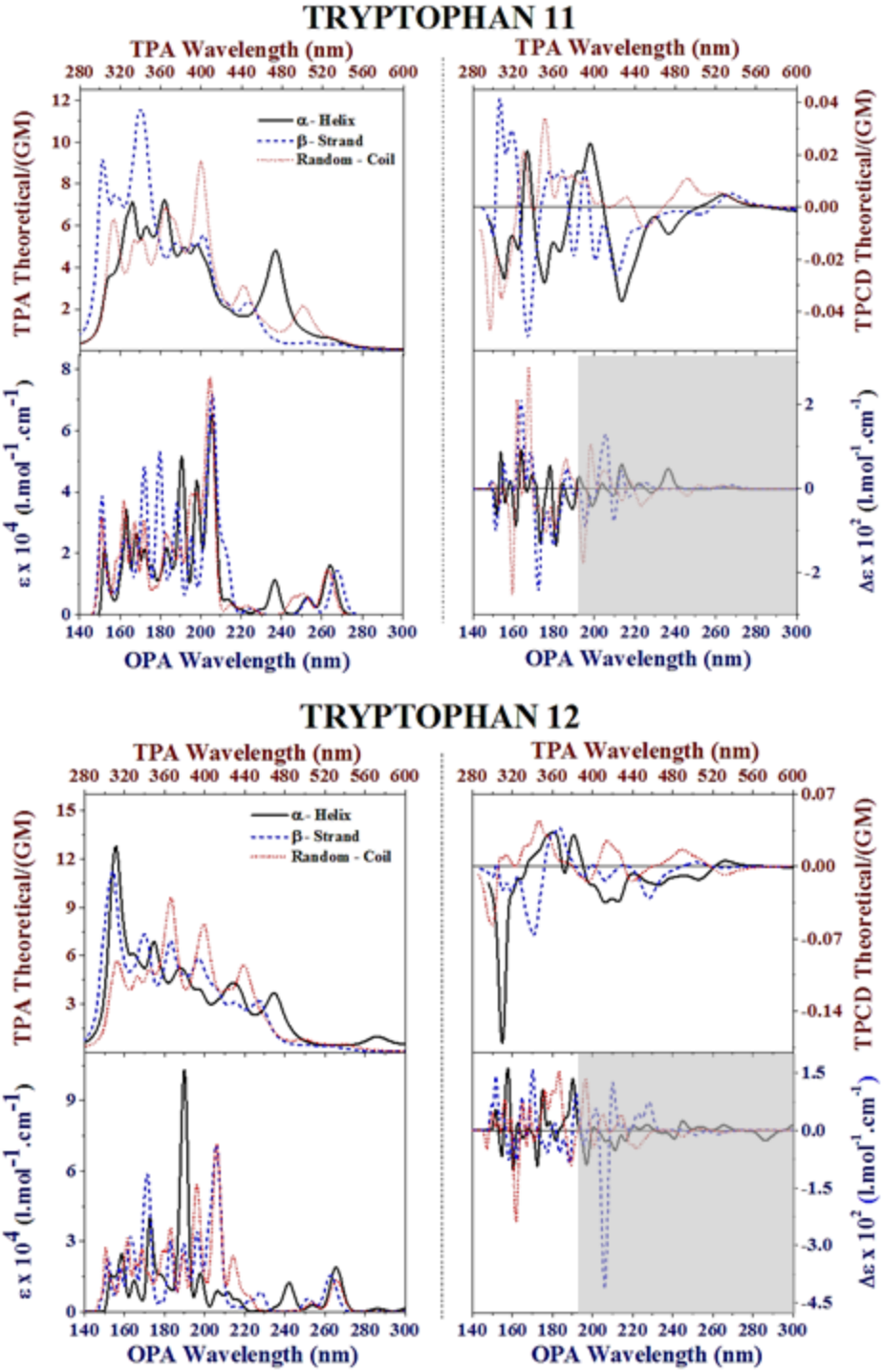

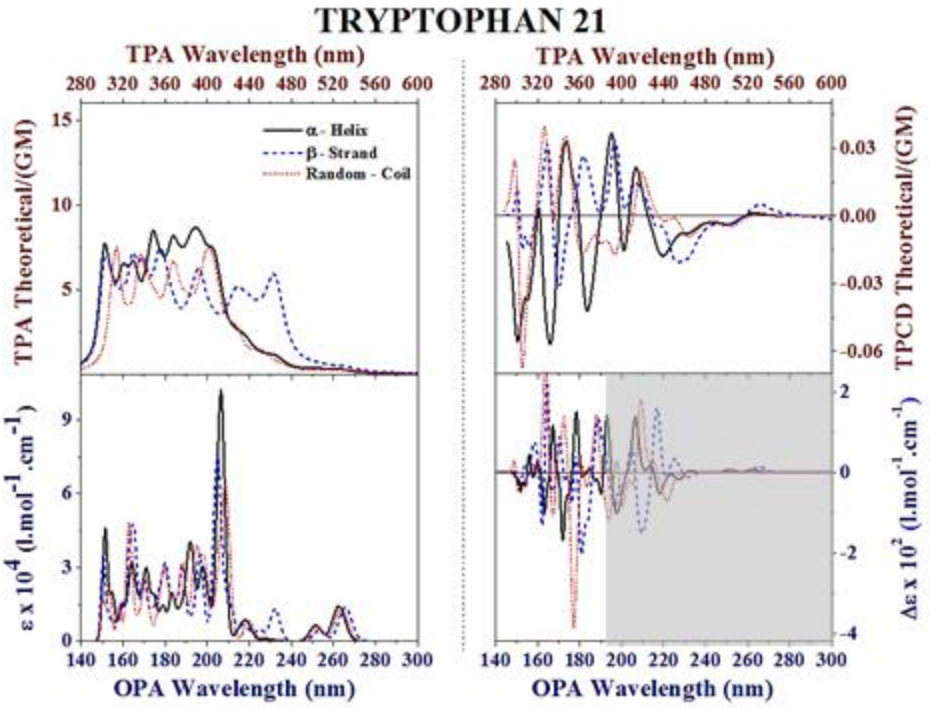
TRYPTOPHAN 21
TPA Wavelength (nm)
280 320 360 400 440 480 520 560 600
α - Helix
β - Strand
Random - Coil
TPA Theoretical/(GM)
ε x 10^4 (l.mol^-1.cm^-1)
OPA Wavelength (nm)
140 160 180 200 220 240 260 280 300
TPCD Theoretical/(GM)
Δε x 10^2 (l.mol^-1.cm^-1)

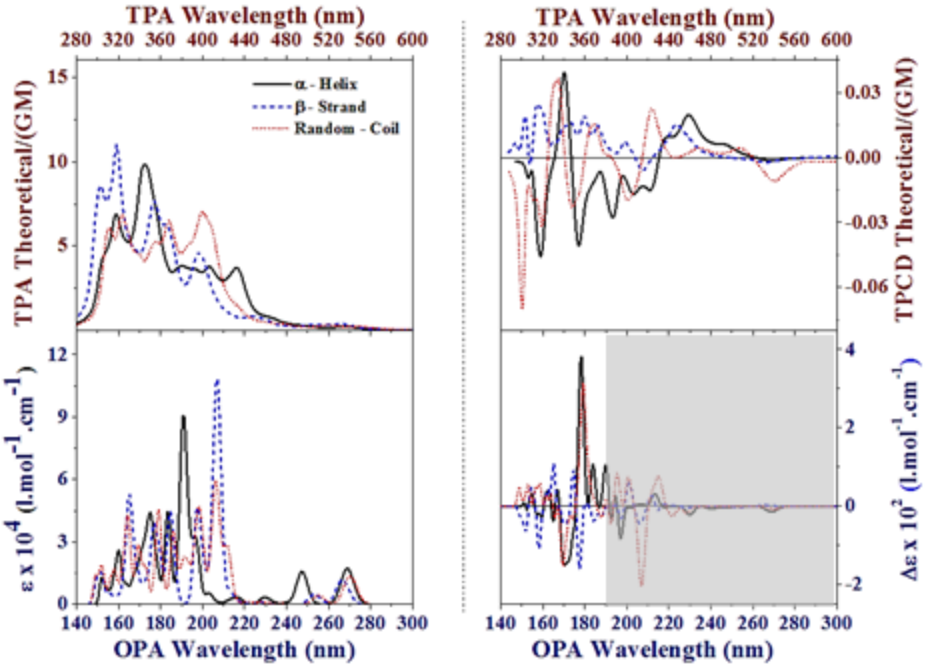
TRYPTOPHAN 22
TPA Wavelength (nm)
280 320 360 400 440 480 520 560 600
α - Helix
β - Strand
Random - Coil
TPA Theoretical/(GM)
ε x 10^4 (l.mol^-1.cm^-1)
OPA Wavelength (nm)
140 160 180 200 220 240 260 280 300
TPCD Theoretical/(GM)
Δε x 10^2 (l.mol^-1.cm^-1)

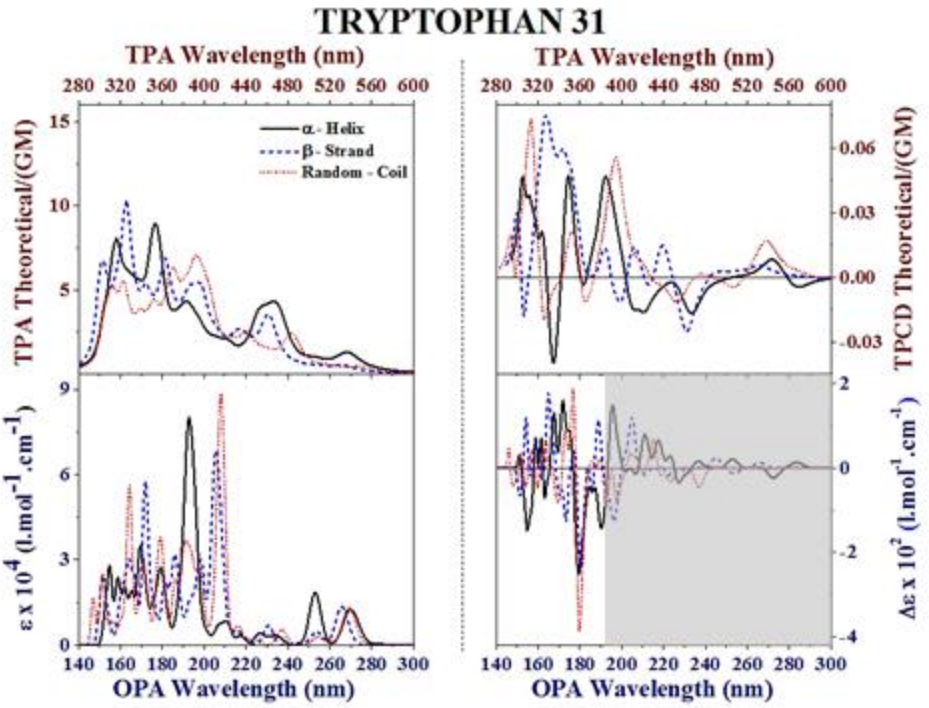
TRYPTOPHAN 31
TPA Wavelength (nm)
TPA Wavelength (nm)
α - Helix
β - Strand
Random - Coil
TPA Theoretical/(GM)
TPCD Theoretical/(GM)
ε x 10^4 (l.mol^-1.cm^-1)
Δε x 10^2 (l.mol^-1.cm^-1)
OPA Wavelength (nm)
OPA Wavelength (nm)

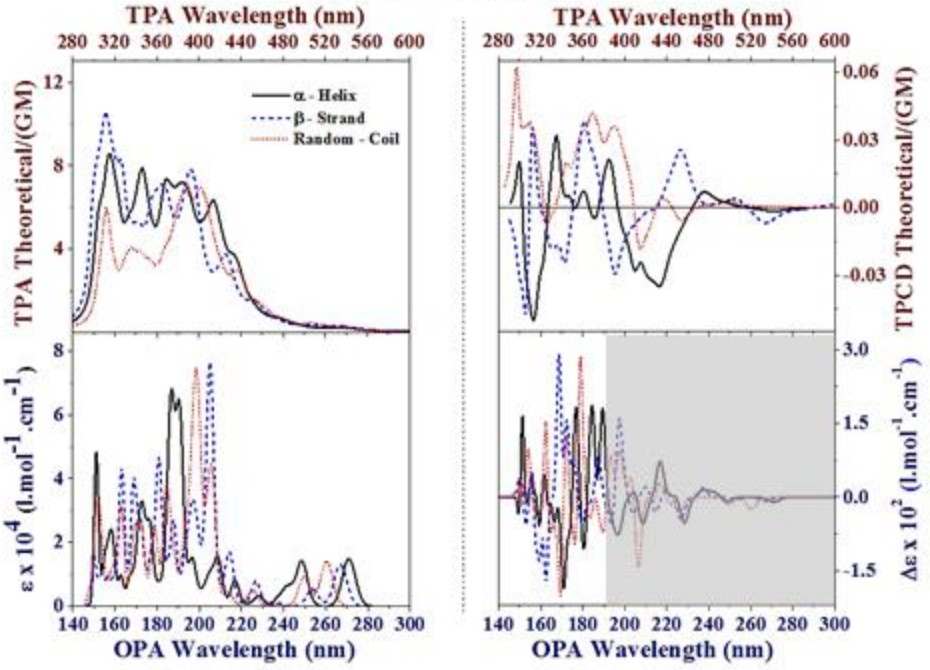
TRYPTOPHAN 32
TPA Wavelength (nm)
TPA Wavelength (nm)
α - Helix
β - Strand
Random - Coil
TPA Theoretical/(GM)
TPCD Theoretical/(GM)
ε x 10^4 (l.mol^-1.cm^-1)
Δε x 10^2 (l.mol^-1.cm^-1)
OPA Wavelength (nm)
OPA Wavelength (nm)

Comparative plots of TPA (top left), TPCD (top right), OPA (bottom left), and ECD (bottom right) spectra of all six His residues in their corresponding random-coil (red dotted line), α-helix (black solid line) and β-strand (blue dashed line) conformations. TD-DFT/ B3LYP/6-311G(d)/80 excited states. Shaded area indicates where ECD is truly functional.

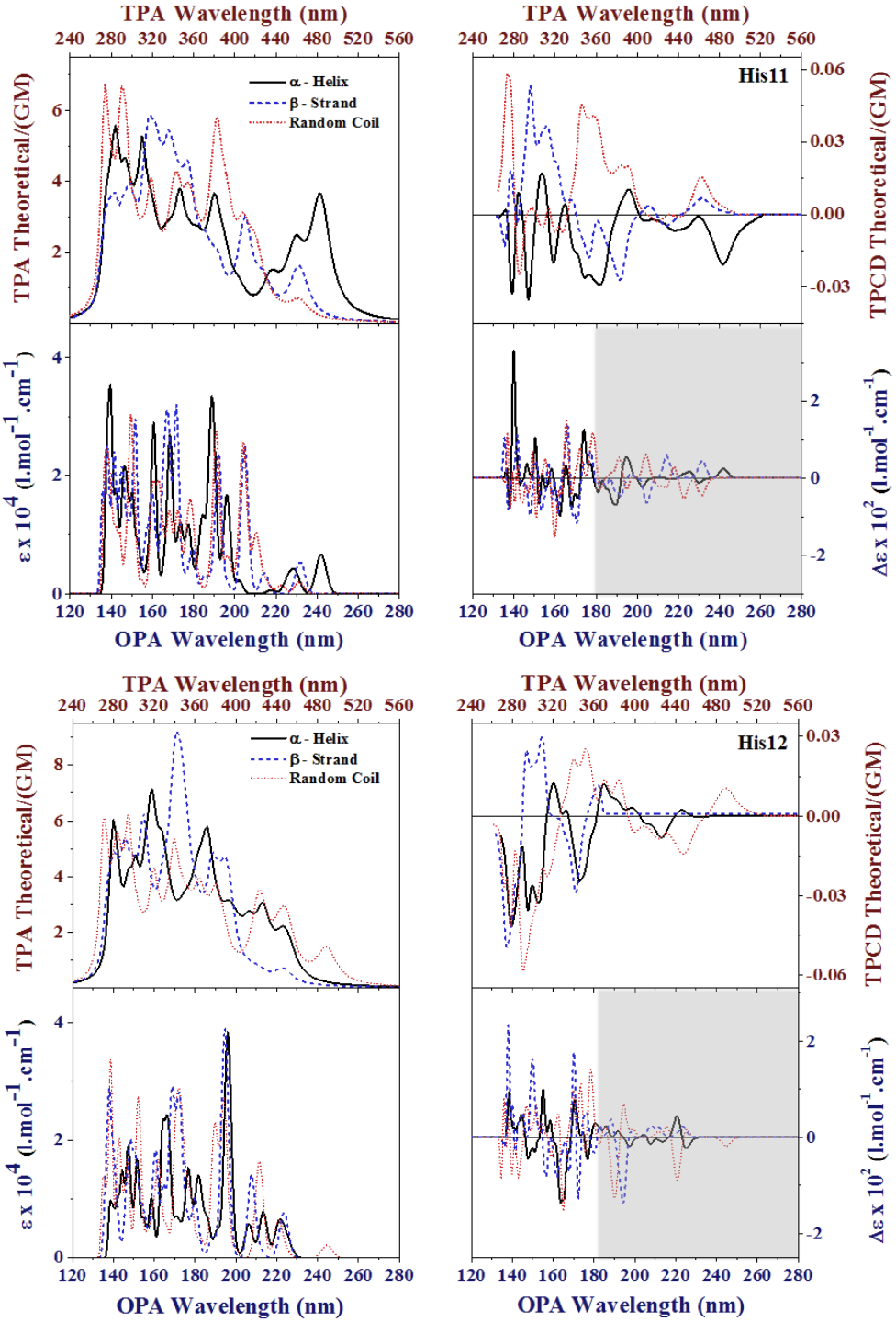

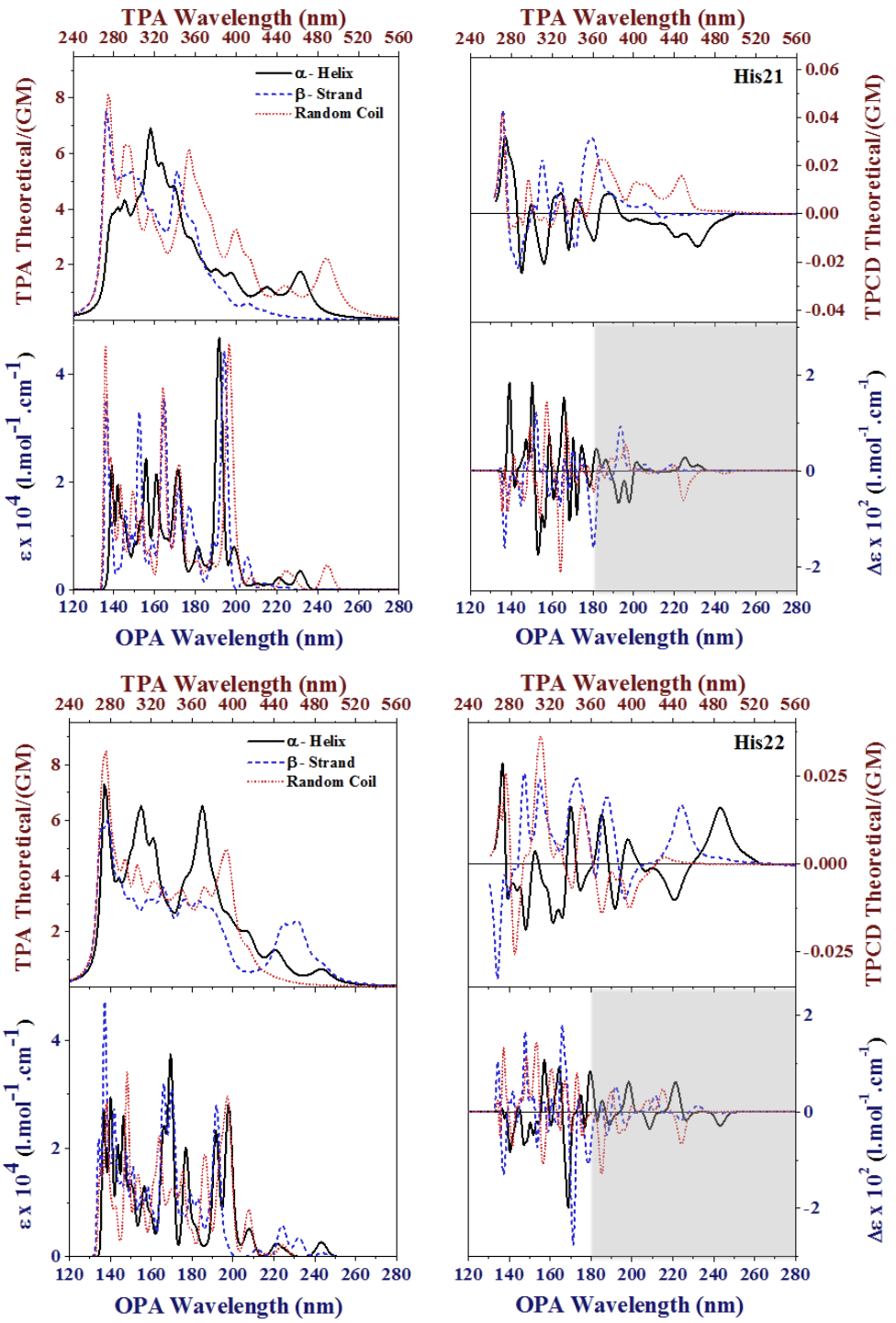
TPA Wavelength (nm)
240 280 320 360 400 440 480 520 560
α - Helix
β - Strand
Random Coil
TPA Theoretical/(GM)
ε x 10^4 (l.mol^-1.cm^-1)
120 140 160 180 200 220 240 260 280
OPA Wavelength (nm)
His21
TPCD Theoretical/(GM)
Δε x 10^2 (l.mol^-1.cm^-1)
His22

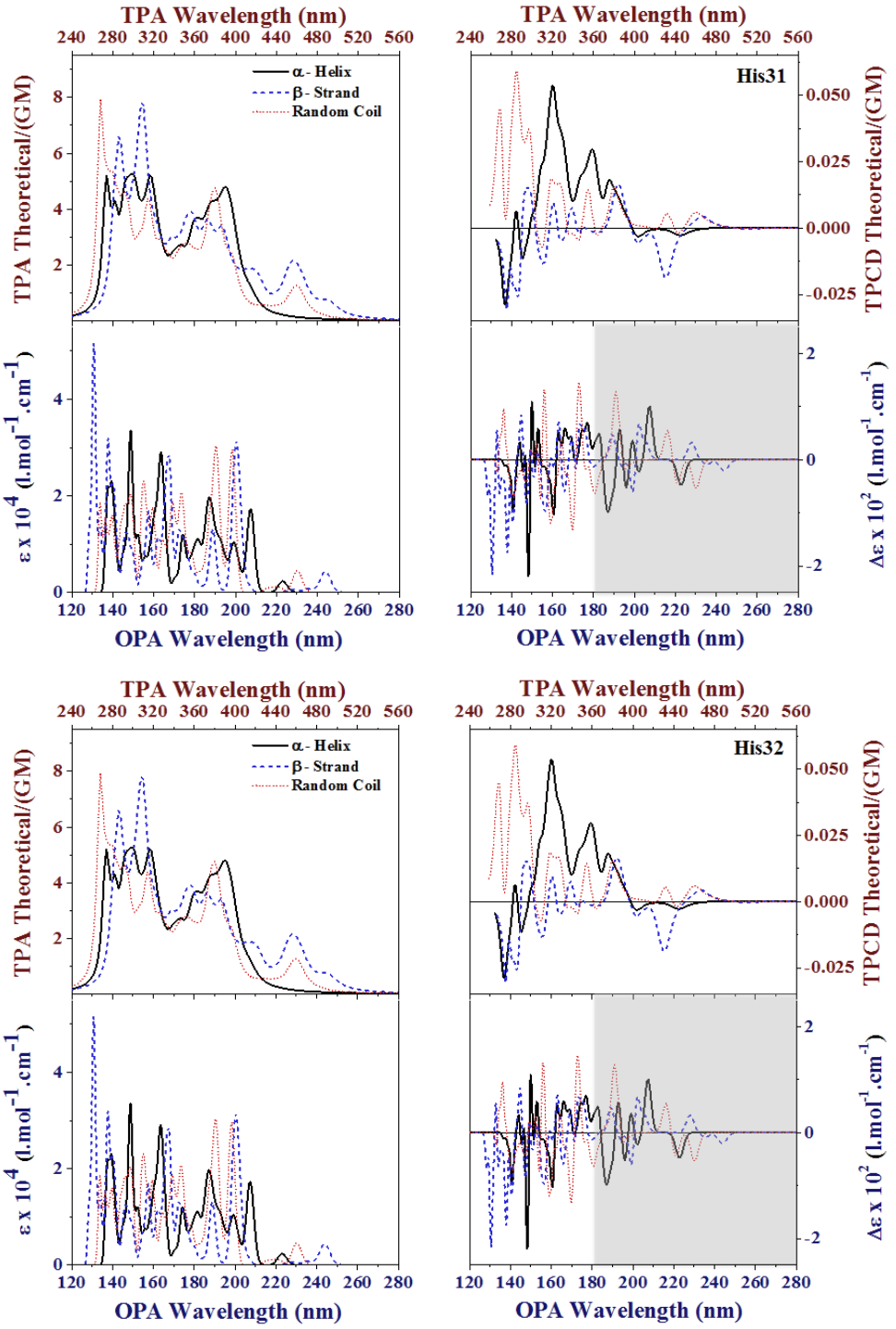
TPA Wavelength (nm)
TPA Theoretical/(GM)
α - Helix
β - Strand
Random Coil
ε x 10^4 (l.mol^-1.cm^-1)
OPA Wavelength (nm)
His31
TPCD Theoretical/(GM)
Δε x 10^2 (l.mol^-1.cm^-1)
His32

Comparative plots of TPA (top left), TPCD (top right), OPA (bottom left), and ECD (bottom right) spectra of all three Phe residues in their corresponding random-coil (red dotted line), α-helix (black solid line) and β-strand (blue dashed line) conformations. TD-DFT/ B3LYP/6-311G(d)/80 excited states. Shaded area indicates where ECD is truly functional.

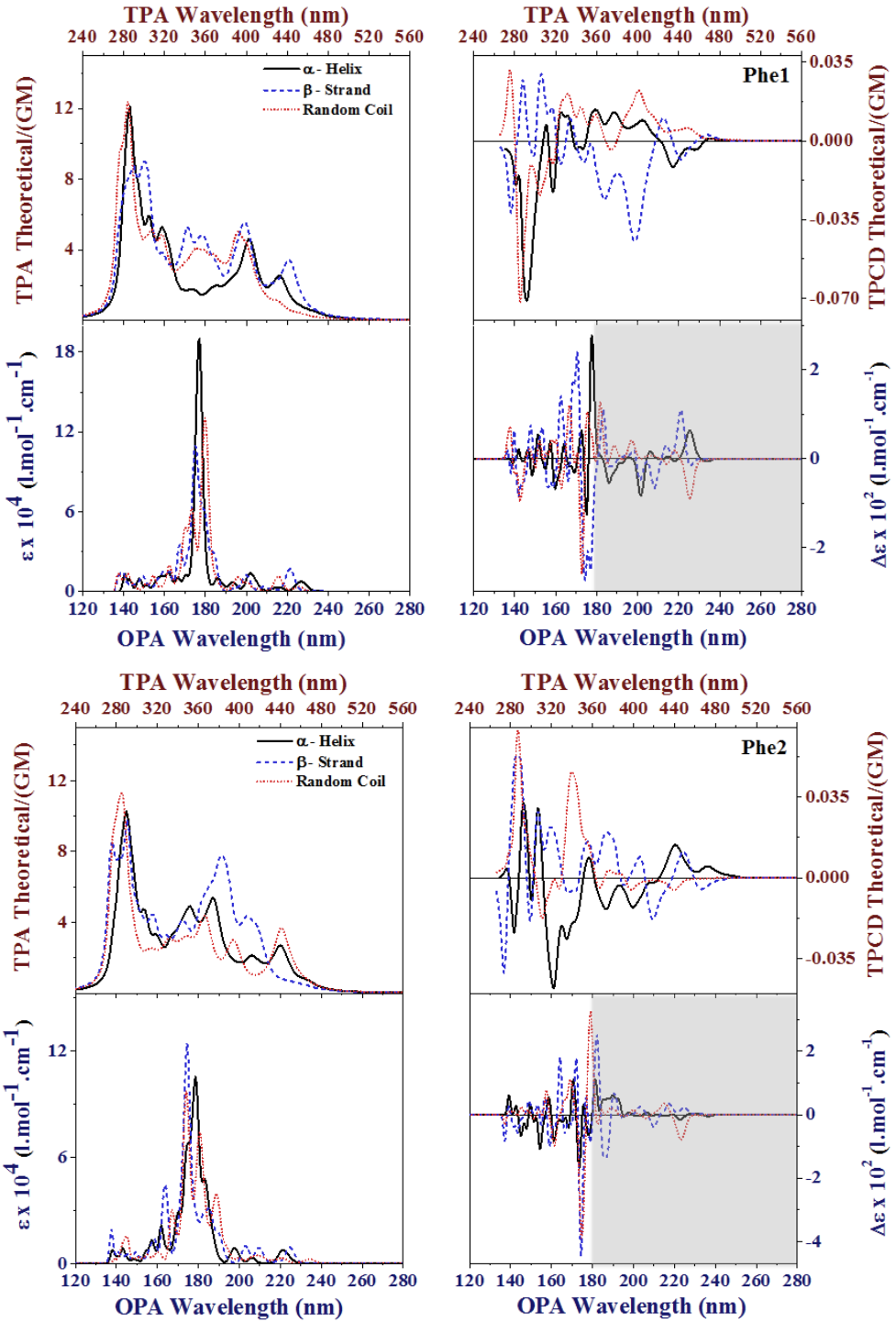

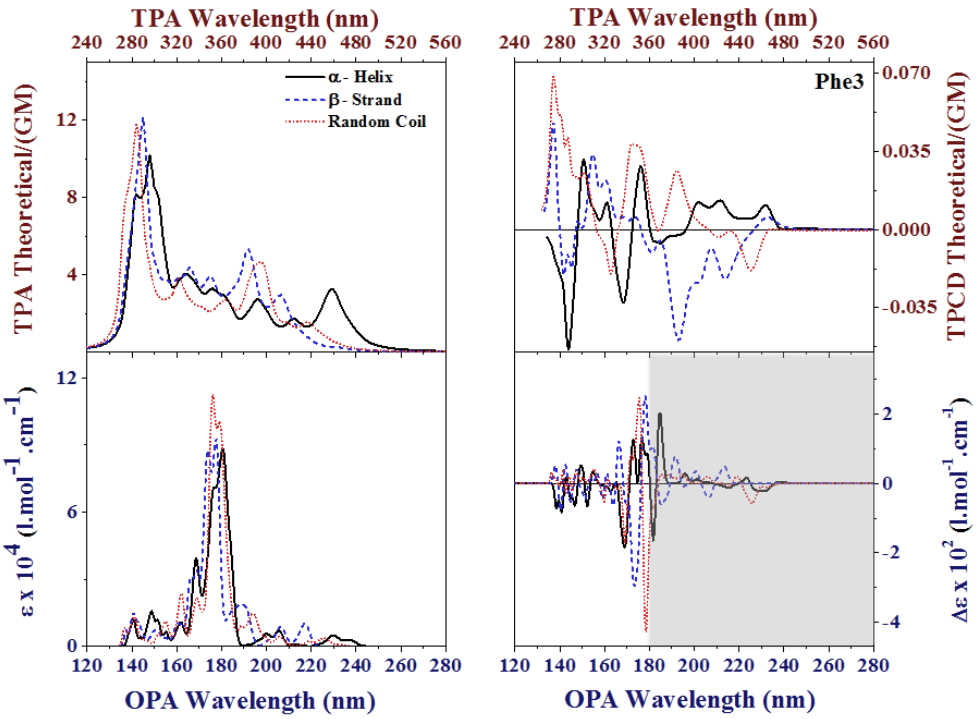
TPA Wavelength (nm)
240 280 320 360 400 440 480 520 560
α - Helix
β - Strand
Random Coil
TPA Theoretical/(GM)
12
8
4
ε x 10^4 (l.mol^-1.cm^-1)
12
6
0
120 140 160 180 200 220 240 260 280
OPA Wavelength (nm)
TPA Wavelength (nm)
240 280 320 360 400 440 480 520 560
Phe3
0.070
0.035
0.000
-0.035
TPCD Theoretical/(GM)
2
0
-2
-4
Δε x 10^2 (l.mol^-1.cm^-1)
120 140 160 180 200 220 240 260 280
OPA Wavelength (nm)

Comparative plots of TPA (top left), TPCD (top right), OPA (bottom left), and ECD (bottom right) spectra of all six Tyr residues in their corresponding random-coil (red dotted line), α-helix (black solid line) and β-strand (blue dashed line) conformations. TD-DFT/ B3LYP/6-311G(d)/80 excited states. Shaded area indicates where ECD is truly functional.

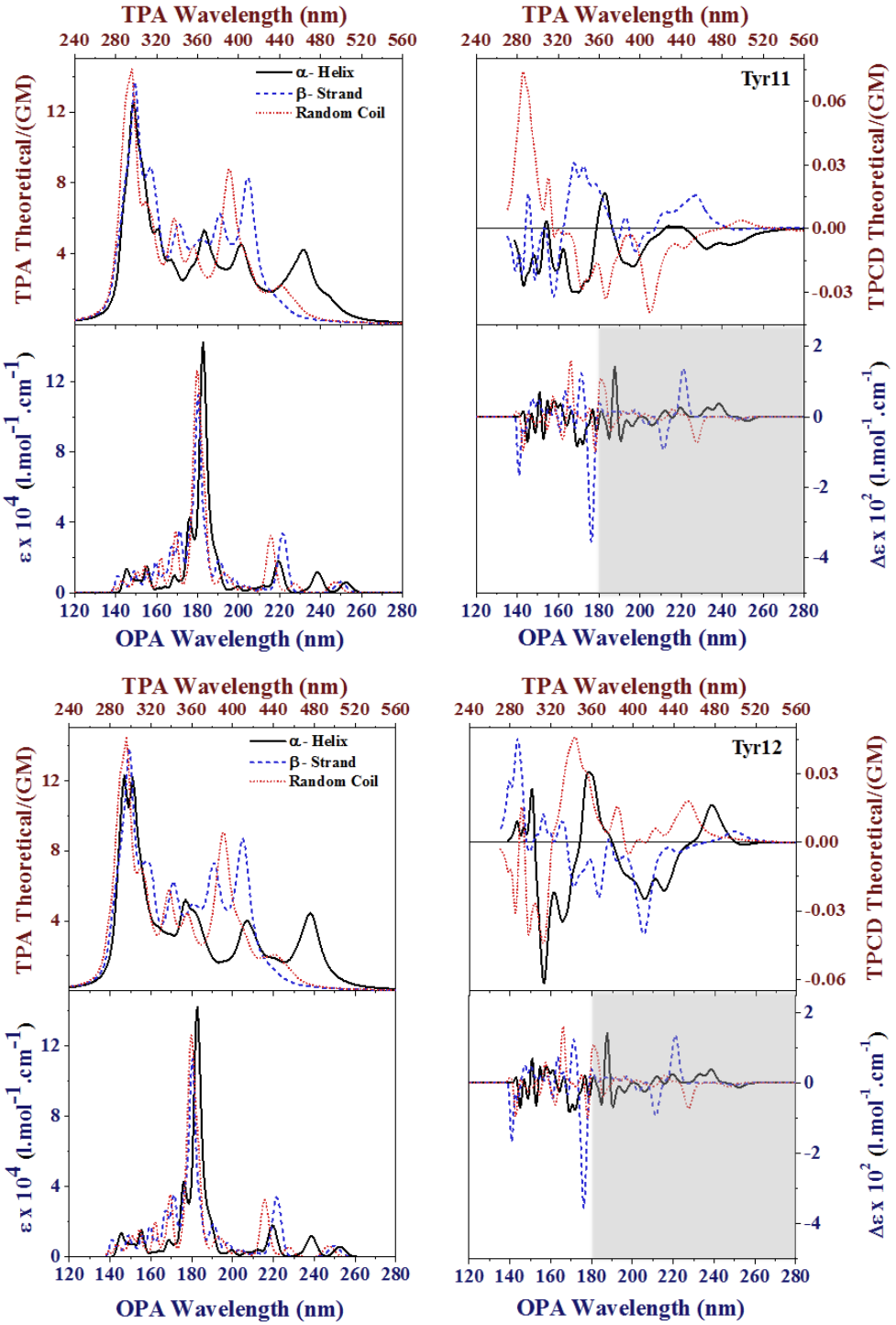

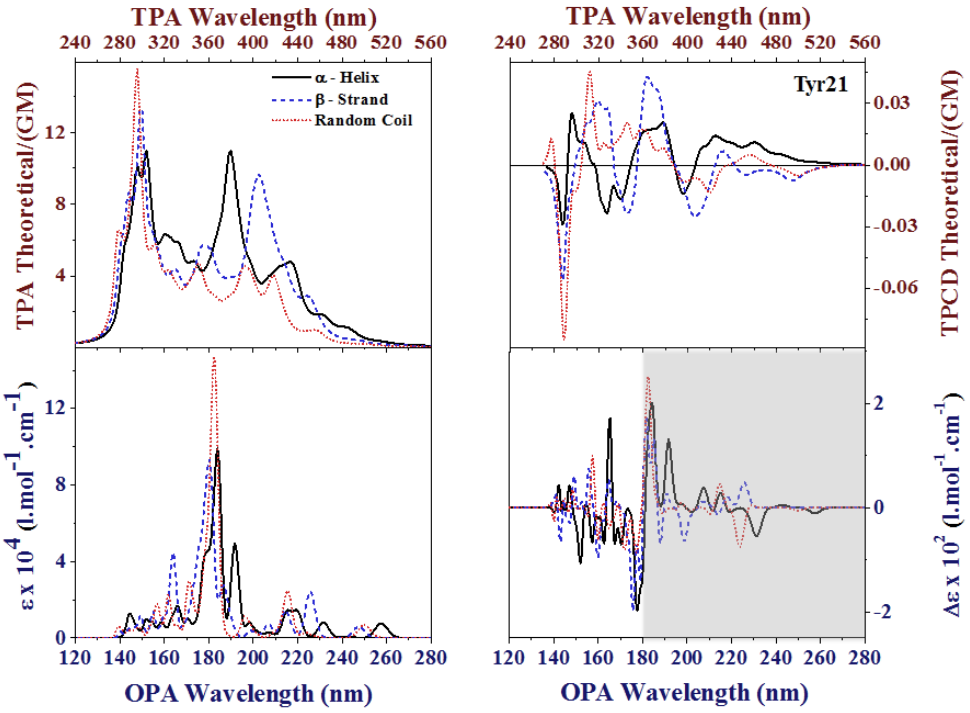
TPA Wavelength (nm)
240 280 320 360 400 440 480 520 560
α - Helix
β - Strand
Random Coil
TPA Theoretical/(GM)
ε x 10^4 (l.mol^-1.cm^-1)
120 140 160 180 200 220 240 260 280
OPA Wavelength (nm)
Tyr21
TPCD Theoretical/(GM)
Δε x 10^2 (l.mol^-1.cm^-1)

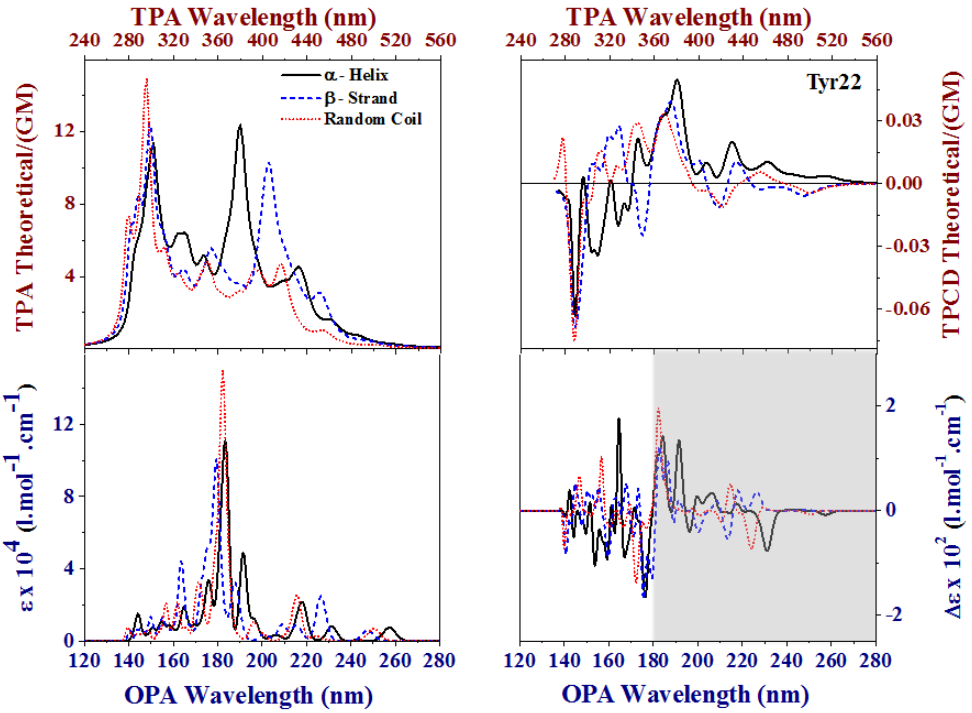
TPA Wavelength (nm)
240 280 320 360 400 440 480 520 560
α - Helix
β - Strand
Random Coil
TPA Theoretical/(GM)
ε x 10^4 (l.mol^-1.cm^-1)
120 140 160 180 200 220 240 260 280
OPA Wavelength (nm)
Tyr22
TPCD Theoretical/(GM)
Δε x 10^2 (l.mol^-1.cm^-1)

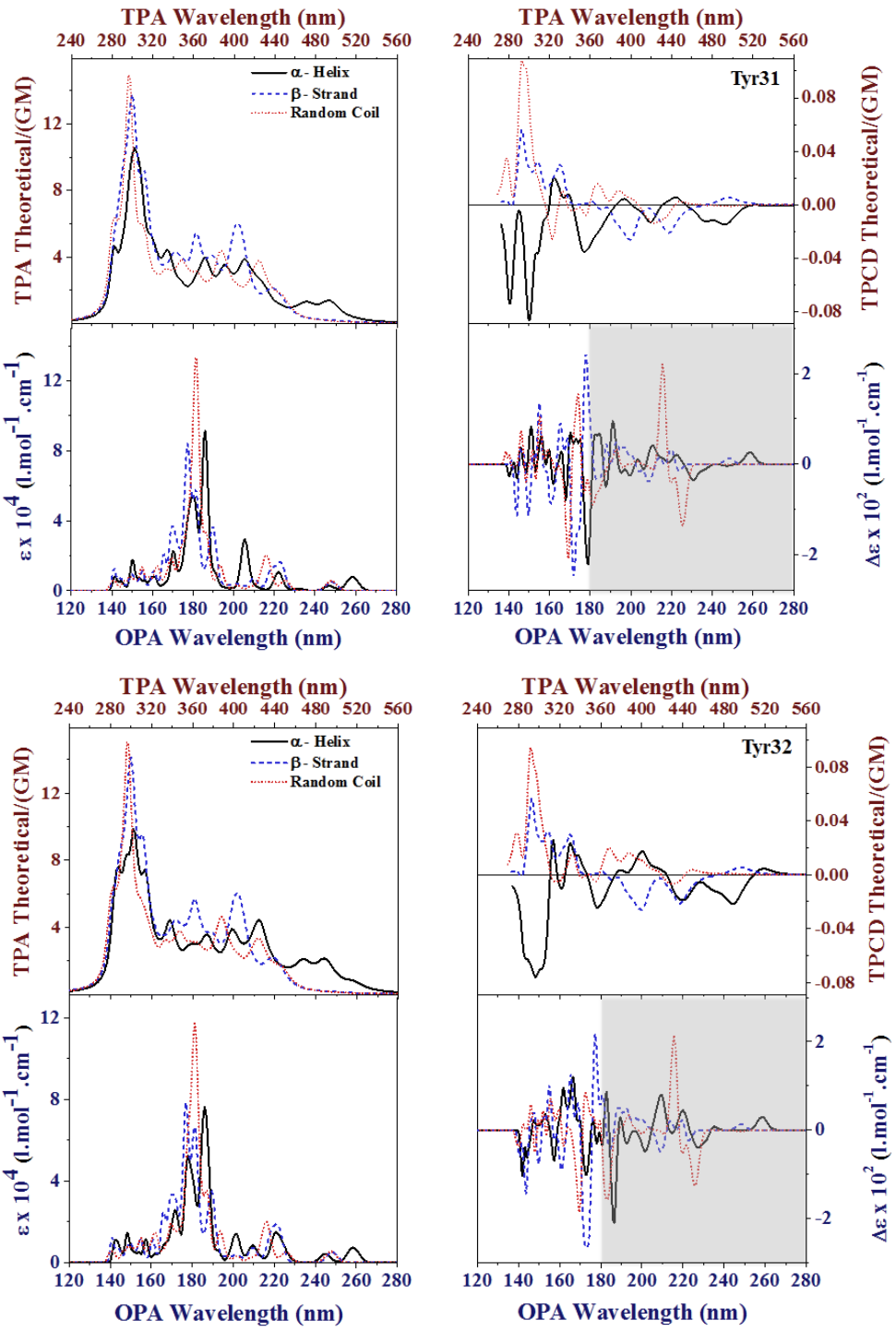
TPA Wavelength (nm)
240 280 320 360 400 440 480 520 560
α - Helix
β - Strand
Random Coil
TPA Theoretical/(GM)
ε x 10^4 (l.mol^-1.cm^-1)
OPA Wavelength (nm)
120 140 160 180 200 220 240 260 280
Tyr31
TPCD Theoretical/(GM)
Δε x 10^2 (l.mol^-1.cm^-1)
Tyr32

Stereochemical structures of L-tryptophan models in β–strand (left) and α–helix (right) conformation.

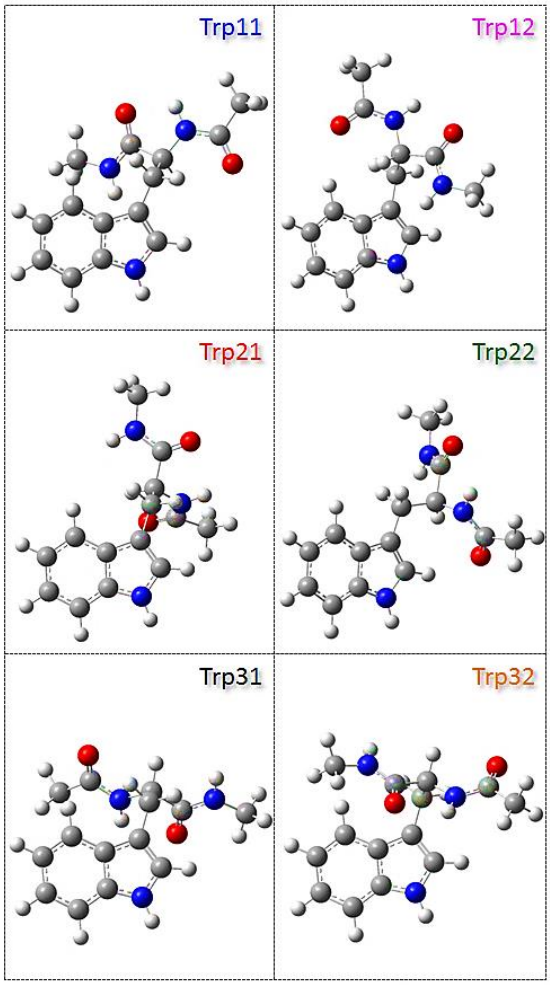


β-strand

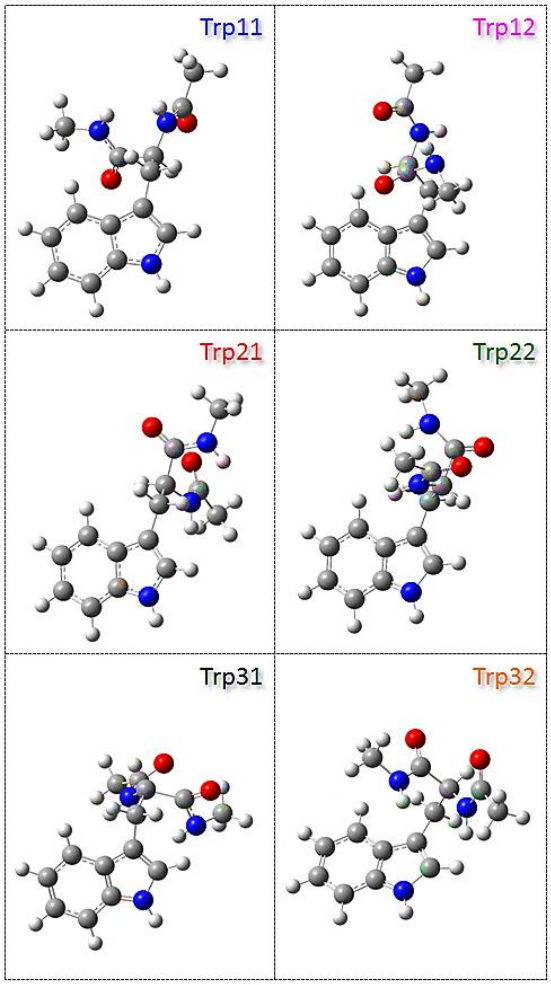


α-helix

Stereochemical structures of L-histidine models in β–strand (left) and α–helix (right) conformation.

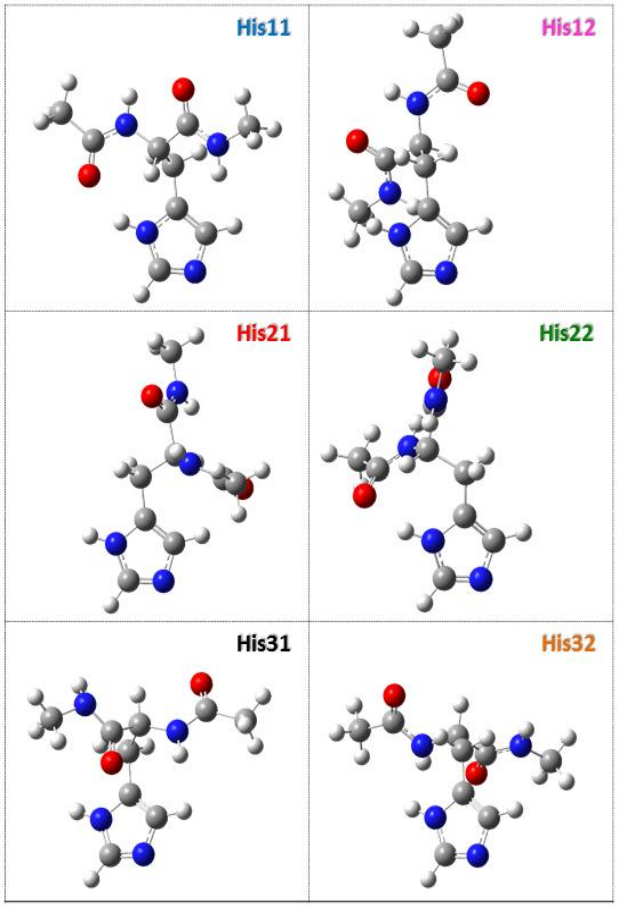


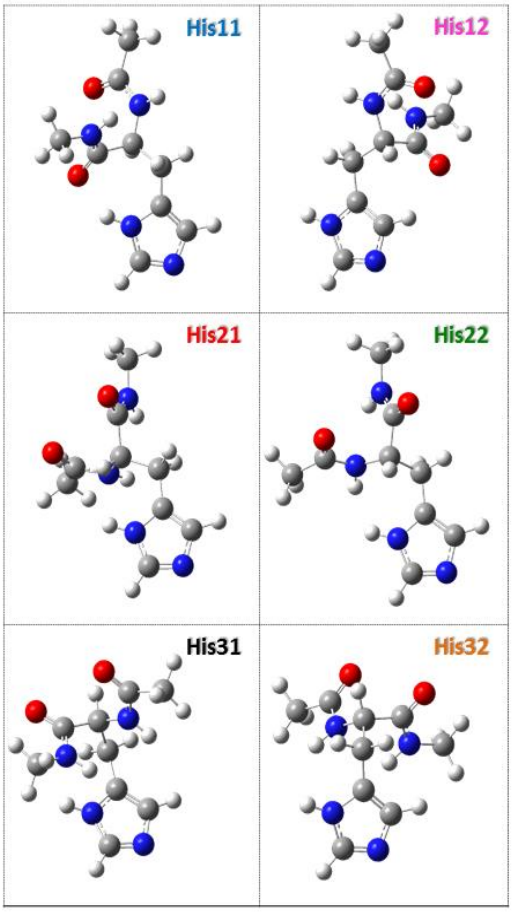

Stereochemical structures of L-phenylalanine models in β–strand (top) and α–helix (bottom) conformation.

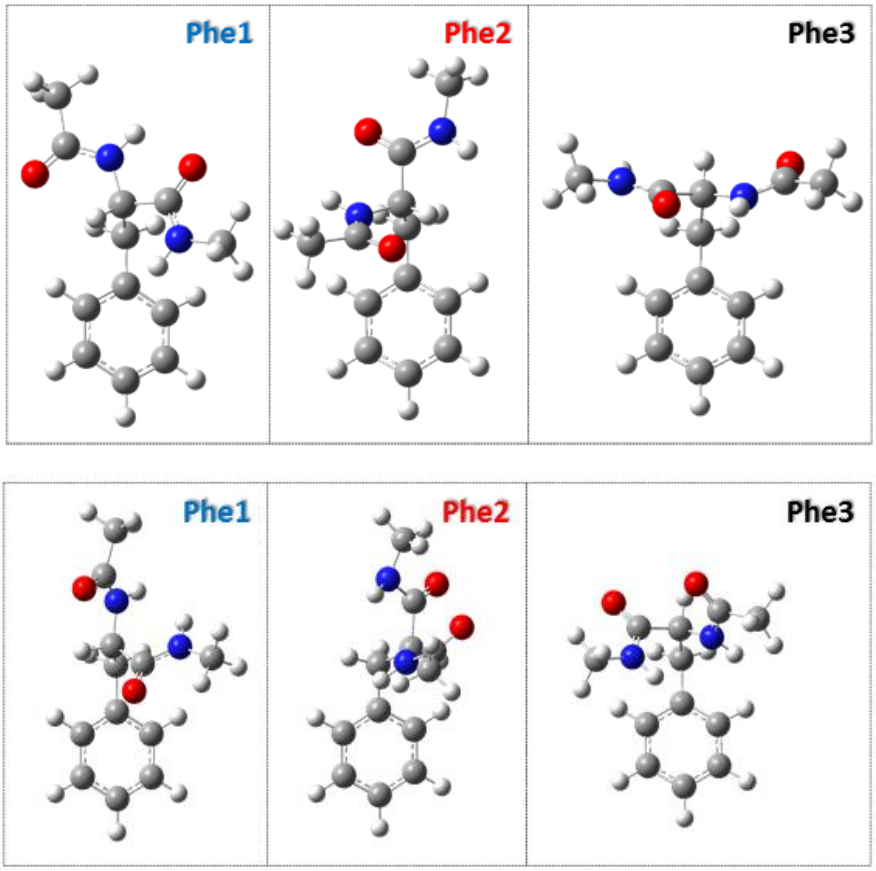

Stereochemical structures of L-tyrosine models in β–strand (top) and α–helix (bottom) conformation.

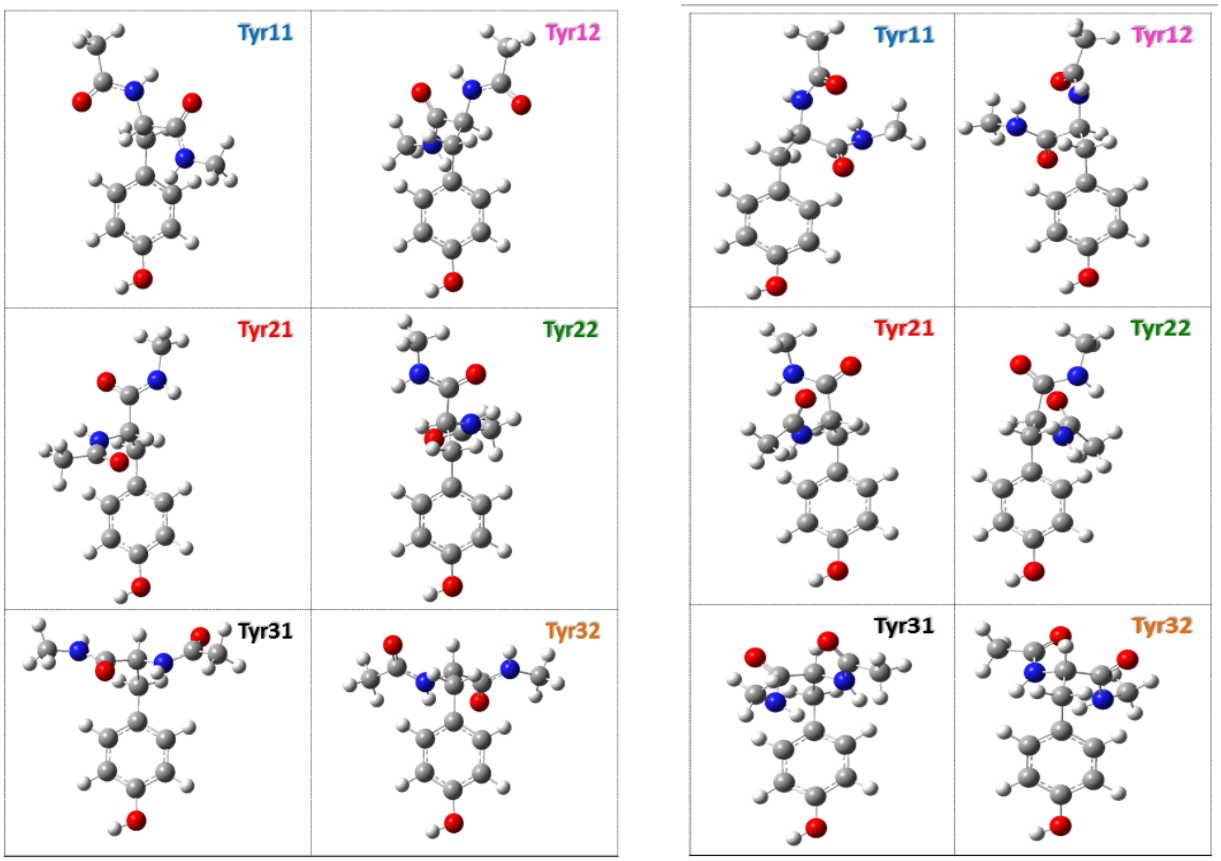

# APPENDIX G: **AUTHORIZATIONS FROM EDITORIAL OFFICES FOR USE OF COPYRIGHTED MATERIAL**

# Chapter 2. J. Phys. Chem. A. 2016. (American Chemical Society)

# Chapter 4. Chem. Phys. Lett. 2014, 601 (0), 6-12.






**Title:** Two-photon circular dichroism of molecular structures simulating l-tryptophan residues in proteins with secondary structures

**Author:** Yuly Vesga,Carlos Diaz,Mary Higgs,Florencio E. Hernandez

**Publication:** Chemical Physics Letters

**Publisher:** Elsevier

**Date:** 9 May 2014





## Order Completed

Thank you for your order.

This Agreement between Yuly Vesga ("You") and Elsevier ("Elsevier") consists of your license details and the terms and conditions provided by Elsevier and Copyright Clearance Center.

Your confirmation email will contain your order number for future reference.

Get the printable license.

| | |
|---|---|
| License Number | 3900390350805 |
| License date | Jul 01, 2016 |
| Licensed Content Publisher | Elsevier |
| Licensed Content Publication | Chemical Physics Letters |
| Licensed Content Title | Two-photon circular dichroism of molecular structures simulating l-tryptophan residues in proteins with secondary structures |
| Licensed Content Author | Yuly Vesga,Carlos Diaz,Mary Higgs,Florencio E. Hernandez |
| Licensed Content Date | 9 May 2014 |
| Licensed Content Volume | 601 |
| Licensed Content Issue | n/a |
| Licensed Content Pages | 7 |
| Type of Use | reuse in a thesis/dissertation |
| Portion | full article |
| Format | electronic |
| Are you the author of this Elsevier article? | Yes |
| Will you be translating? | No |
| Order reference number | |
| Title of your thesis/dissertation | Measurement of FAR-UV TPCD |
| Expected completion date | Dec 2016 |
| Estimated size (number of pages) | 200 |
| Elsevier VAT number | GB 494 6272 12 |
| Requestor Location | Yuly Vesga<br>9319 Strongbark Ln<br><br>ORLANDO, FL 32832<br>United States<br>Attn: Yuly Vesga |
| Total | 0.00 USD |

## Chapter 4. RSC Advances 2014, 4 (105), 60974-60986.



# Theoretical study of two-photon circular dichroism on molecular structures simulating aromatic amino acid residues in proteins with secondary structures

Y. Vesga, C. Diaz and F. E. Hernandez, *RSC Adv.*, 2014, 4, 60974
**DOI:** 10.1039/C4RA08383K